INNOVATIVE ADSORPTION HEAT EXCHANGERS FOR DESICCANT COOLING AND ATMOSPHERIC WATER HARVESTING

POLITECNICO
DI TORINO

Vincenzo Maria Gentile

Index

Nomenclature

Variables

a	surface area	[m^2 m^{-3}]
a_s	surface area silica bed	[m^2 m^{-3}]
a_L	lateral surface of packed bed	[m^2]
a_F	fin surface area	[m^2]
c_p	specific heat at constant pressure	[kJ kg^{-1}]
D_{eff}	global effective diffusion	[m^2 s^{-1}]
D_i	Inner pipe diameter of the finned coil	[m]
D_{Kn}	Knudsen diffusion	[m^2 s^{-1}]
D_m	molecular diffusivity	[m^2 s^{-1}]
D_o	outer pipe diameter of the fined coil	[m]
D_S	surface diffusion	[m^2 s^{-1}]
d	diameter	[m]
$d_{x,y,z}$	finite spatial difference	[m]
d_V	finite spatial volume of dimension $d_x d_y d_z$	[m^3]
E	energy	[Wh] [J]
f_D	friction factor	
$\dot{G}$	global mass transfer	[kg m^3 s^{-1}]
H_a	adsorption heat	[kJ kg] [J mol^{-1}]
H_{lat}	latent heat	[m
h	heat transfer coefficient	
h_m	convective mass transfer coefficient between air and packed bed	[kg m^{-2} s^{-1}]
h_t	heat transfer coefficient	[W m^3 K^{-1}]
k	Thermal conductivity	[W m^{-1} k^{-1}]
K_G	global mass transfer coefficient	[kg s^{-1}]
K_p	intraparticle mass transfer coefficient	[m s^{-1}]
K_0	equilibrium constant $(\rho_s\ w)/(\rho_a\ x_a)$	-
L	length	[m]
$\dot{m}$	mass flow rate	[kg s^{-1}]
m, M	mass	[kg]
Nu	Nusselt number	[-]
p	fin path	[mm]
P	gas or vapor pressure	[Pa]
P	Power	[W]
Pr	Prandtl number	[-]
$\dot{Q}$	volumetric flow rate	[m^3 h^{-1}] [liter min^{-1}]
Q_{sol}	solar energy	[kWh]
R	universal constant of gases	[J mol^{-1} K^{-1}] [J kg^{-1} K^{-1}]
R	latent heat of water vaporization	[J mol^{-1}] [J kg^{-1}]
RH	relative Humidity	[%] [-]
Re	Reynolds number	[-]
r	radius	[m]
Sc	Schimdt number	[-]
STE	specific thermal energy	[kWh kg_w^{-1}]
T	temperature	[°C] [K]

T^*	equilibrium temperature	[°C] [K]
t	time	[s] [min] [hours]
U, U_L	global heat exchange coefficient	[W m^{-2} K^{-1}]
V_n	net volume	[m^3]
v	volume	[m^3] [liter]
W	weight	[kg] [g]
w	water content	[g_{H2O} $g_{dry\ mass}^{-1}$] [g_{H2O} $kg_{dry\ mass}^{-1}$]
x	air moisture content; Humidity ratio	[g_{H2O} $g_{dry\ air}^{-1}$] [kg_{H2O} $kg_{dry\ air}^{-1}$]
x^*	equilibrium air moisture content	[g_{H2O} $g_{dry\ air}^{-1}$] [kg_{H2O} $kg_{dry\ air}^{-1}$]
z	air flow longitudinal direction	[-]

83 Symbols

@	At	
#	number	
$\bar{}$	Average	-
α_{OH}	Number of OH groups per unit surface area	[nm^{-2}]
Δ	Delta, difference	
∂/∂	partial derivative	
$\varepsilon, \varepsilon_b$	empty degree of a granular packed bed	[-] [%]
ε_p	mean particle empty degree	[-] [%]
η	efficiency	[-] [%]
μ_a	air dynamic viscosity	[Pa s]
ξ	Concentration of calcium chloride	[kg_{CaCl2} $Kg_{solution}^{-1}$]
ρ	Density	[kg m^{-3}]
$\sum$	Sum	
τ_p	adsorbent pore tortuosity	[-]
τ_s	adsorbent surface tortuosity	[-]
$\omega(r)$	Intraparticle distant dependent potential	[J]

Subscripts

a	air
amb	external environment
avg	average
b	bed
cool	cooling
cond	condenser
dew	dew point
el	electrical
L	external thermal losses
in	inlet
out	outlet
rec	recovery heat exchanger
reg	regeneration
s	silica gel, silica particle
sat	saturation
th	thermal
tot	total
v	vapor
w	water

Acronyms

ADS	Adsorption
BET	Brunauer-Emmet-Teller adsorption theory
CAGR	Compound Annual Growth
DIW	Deionized Water
DEC	Desiccant Evaporative Cooling
EDS	Energy Dispersive Spectroscopy
EER	Energy Efficiency Ratio
FWS	Fossil Water Source
ICZ	Intertropical Convergence Zone
HX	Heat Exchanger
LDF	Linear Driving Force
MODIS	Moderate Resolution Imaging Spectroradiometer
MOF	Metallic Organic Framework
MENA	Middle East North Africa regions
PEO	Polyethylene glycol, Polyethylene oxide
PDMS	Polydimethylsiloxane
PM	Molecular weight
PV	photovoltaic
REG	Regeneration
RWS	Renewable Water Source
SAPO	SiliconAluminiumPosphateOxide
SAWG	Solar Atmospheric Water Generator
SDG	Sustainable Development Goal
SEM	Spectrum Electron Microscopy
TPW	Total Precipitable Water
VDC	Volt Direct Current
WSI	Water Stress Indicator

1 INTRODUCTION

The phenomenon of water evaporation and condensation is a fundamental pillar on which natural and anthropic processes are built. The energy density associated to the phase change from liquid to vapor, and vice versa, is one of the highest among many different substances and, for sure, the highest occurring at low temperatures. This characteristic confers to the water liquid/vapor phase transition a role of main character in the field of thermoregulation processes. For example, the human body temperature regulation works on the phenomenon of evapotranspiration of water through the skin. A similar approach is present in most of the mammals and animals. The same role is played at planet level. Evaporation from free water surface, and condensation in the upper layers of the troposphere, are fundamental phenomena influencing the temperature of the planet.

Despite its positive relevance, the presence or absence of water vapor has a dichotomous nature. Too much water vapor in the air is a problem, especially for the indoor environment, negatively affecting thermal comfort of people. At the same time, the presence of water vapor in the air it has to be considered as a resource, especially for those regions affected by drought.

The response to the problem of thermal comfort is an intensive power solution called air conditioning. The forecasted increase of energy demand for cooling in the next future defined the new term “cold crunch”, to identify a dangerous scenario in which 2/3 of the world’s households could have an air conditioner. The consequences will be a further intensive use of fossil fuels to satisfy this incremented energy demand for thermal comfort[1].

On the contrary, the prospective of using atmospheric water vapor is a fascinating solution, especially for that country lacking any access to conventional fresh water sources. Machines converting water vapor into liquid fresh water are typically called atmospheric water harvesting generators. Again, the biggest share of technological solutions is occupied by very power intensive systems.

In both cases, the most applied solution is to use vapor compressing units to cool down the air up to the dew point, obtaining then the condensation of water vapor and the separation from treated air streams. Main energy consumptions are generated from the vapor compressor, resulting in an intensive use of electric power.

The alternative solution explored within this research his based on the iteration between water vapor and hygroscopic materials. The use of sorbents translates the problem of water vapor treatment, from an original consumption of electrical energy to the need of heat.

The alternative approach here investigated considers the use of hygroscopic materials through the phenomenon of physic sorption. The thermal power, required for the regeneration of the material to activate cycle of sorption/regeneration, if provided at temperature below 90°C, enables the use of cheap technology and sustainable sources such as solar energy and waste heat.

The alternative solutions here explored aim to shift the request of electrical power for the separation of water vapor from air to a thermal power need, with potential benefits in terms of carbon footprint and for the electric network. However, the competition with conventional technologies is not only a matter of energy saving, problems related to cost of materials and components manufacturing, together with maintenance issues, are usually the bottle neck for that kind of systems.

Theoretical studies, numerical modelling and experimental activities carried out in this research are strongly grounded in the set of sustainable development actions for the sectors of cooling and clean water solutions, enclosed in the set of action called Sustainable Development Goals (SDG 6 and 7).

In brief, aspects that have been investigated are ordered in the following list:

i) knowledge improvement on adsorption phenomenon.

ii) experimental activities to test performances of innovative adsorption heat exchangers (ADS-HX) for air conditioning

iii) definition of an improved method to produce freshwater from air, using renewable sources, demonstrating the validity with experimental testing and numerical modelling

iv) designing new materials and configurations of ADS-HX to be applied in the sectors of water harvesting and air dehumidification.

2. ADSORPTION and SORBENTS

Abstract

Fundamental characteristics of physical adsorption are the main pillars of the phenomena and applications investigated in this research project.

Functional hydrophilic groups such as hydroxyl, silanols and carbonyl are the basic bricks that builds the water uptakes curves of materials such as Silica gel and Zeolites. The knowledge of intrinsic properties together with equilibrium thermodynamic behaviour are fundamentals for the correct exploitation of these materials in air dehumidification and water harvesting sectors.

A particular effort was carried out to investigate water uptakes of a silica gel provided by the Oker Chemie producer, and a zeolite of improved performances, the SAPO-34, provided by the ITAE-CNR of Messina.

The equilibrium curves obtained from the fitting of the silica gel equilibrium tests is useful for the numerical model realized in the next chapters.

2.1 Adsorption theories and models

The capability of porous solids to uptake large quantities of vapor is a phenomena deeply studied in science since the end of the eighteenth century[2]. First applications in the industrial sector started in the early 1950s as an emerging alternative and competitive process to hydrocarbon distillation (higher effectiveness), for the removal of undesired impurities from natural gas (such as moisture, H_2S and mercaptans) or the recovery of aromatic hydrocarbons [3–5].

Materials porosity is one of the key parameters influencing adsorption processes and, according to IUPAC classification [6–8], it includes micropores (<2nm), macropores (>50nm) and mesopores in between. Anyway, this classification is not strict or an absolute scale, indeed Dubinin fixed the upper limit at 200nm and the lower at 1.2nm, with the mesopore region in the between of 3÷200nm.

The interaction between the vapor and porous solids belong to the category of physic adsorption, the general set of weak intermolecular interactions based on van der Waals forces (dispersion-repulsion) and electrostatic iterations (polarization, dipole and quadrupole) [2]. The iterations potential between sorbent and sorbate belong to the pair potential family proposed by Mye [9] in 1903 that has, in the empirical formulation of Lennard-Jones 12-6, the best known form of intraparticle distant dependent potential:

$$\omega(r) = -\frac{A}{r^6} + \frac{B}{r^{12}} \quad (2.1)$$

where $A \approx 10^{-77}$ J m^6 and $B \approx 10^{-134}$ J m^{12} for two interacting particles and r is the distance between them. The first term on the right of the equation describes the attractive component of van der Waals and, the second is the

short-range repulsive energy related to the finite size of molecules [10],[11]. The order of magnitude of intermolecular distance of reference is comparable with atoms and small molecules size, indeed the minimum of $\omega(r)$ for the interaction of two molecule has a distance $r_e \approx$ 0.35nm[11].

The progressive coverage of available site for an attractive iteration between sorbent and sorbate lead to the saturation of the first available layer, over which multiple layers can overlap until the full saturation of pores. This has a direct effect on the shape of adsorption isotherms, as described with the BET theory[12][13], with the classic classification of 5 different types. Differently from what is described by the Langmuir[14] model[i], in the BET theory a multimolecular adsorption (also multilayer adsorption, molecules adsorbed in the first layer become available site for a second layer and any successive one) is justified by the intermolecular interaction driven by the same forces that generate condensation[15]. Further one, when sorbate molecules have much more contacts between each other than with some surface spots, equilibrium constants change with macroscopic evidences on the isotherm's shapes. In addition to Langmuir and BET descriptions of adsorption isotherm shape, there's a third phenomenon occurring in continuous progression with the multilayer adsorption, the capillary condensation[16]. This occurs only for high level of coverage, and is comparable with a complete liquid filling of pores, due to the reduction of saturation pressure by the effect of surface tension, as described by the Kelvin equation [17–19].

$$\frac{P}{P_{sat}} = \exp\left(\frac{-2\sigma V_m \cos\vartheta}{rRT}\right) \quad (2.2)$$

Again, the phenomenon is strongly connected to the pore dimensions, as highlighted by the pore radius r. Indeed, in case of micro porosity the filling process can be wrongly imputed to capillary condensation when, actually, the phenomenon maybe more coherent with the monolayer formation and the Langmuir description of Type 1 [20]. Ramsay et al.[21],[22] demonstrated this difference analysing the distribution of water in different samples of mesoporous and microporous silica gel. With neutron scattering authors detected traces of water film only in the mesoporous configuration.

The three described theories, Langmuir, BET and capillary condensation gave a good approximation of adsorption isotherms only in a reduced range of the relative pressure. For example, Langmuir is suitable for P/P_s<0.05; BET models give a good approximation in the range of 0.1<P/P_s<0.4, while capillary condensation is suitable for P/P_s>0.8. There's another family of models, based on the empirical Polanyi potential theory [14],[23], [24], capable of fitting adsorption isotherms in a wider range. For example the Dubynin-Astakhov

[i] Langmuir theory is suitable only for monolayer of undisturbed molecules, condition that is more realistic for chemisorption than physic[14]. The monolayer fractional coverage Θ is proportional to bp/(1+bp), where b is the ratio of adsorption over desorption rate constant, and dependent by temperature following the vat Hoff model $b_0 * exp\left(\frac{-\Delta H}{RT}\right)$. The assumptions of energy equivalent spots, and no interaction with other molecules, implies the independency of adsorption heat from Θ.

[23],[25] equation, with an exponential dependence from the adsorption potential A (derived from the Polanyi theory) and an affinity constant E:

$$\frac{W}{W_0} = e^{-\left(\frac{A}{E}\right)^n} \quad (2.3)$$

Where W is the volume occupied by the adsorbent, W_0 the maximum available one. According to Polanyi theory the adsorption potential A is independent from the presence of other molecules and uniquely determined by the spatial position of the molecule. Furthermore, the gas is coherent with its equation state, and if compressed to its normal vapor density, it condenses into liquid [14]. In definitive:

$$A = k\,RT \ln\left(\frac{P_{sat}}{P}\right)_T \quad (2.4)$$

When n is equal to 2 the isotherm equation of Radushkevich is obtained[26]. In addition to what is covered by the theories of adsorption just summarized, a special role in the systems studied in this work is played by the hydroxyl group on sorbent surface and the hydrogen bond, especially in the adsorption of water. A higher concentration of OH groups on sorbent surface is generally associated to an increase of adsorption activity [27]. As Hontoria-Lucas et al.[28] observed on oxidized graphite with the adsorption of N_2 and CO_2, imputing the increase of adsorption intensity to the hydroxyl group instead to the carbonyl. The hydroxyl influence on the enhancement of adsorption properties on material surfaces is not only for the vapor phase but also at the liquid [29],[30]. The hydrophilic influence of the hydroxyl is associated also to the silanol group ($\equiv SiOH$). This is another functional group, imputed as main responsible for water interaction at molecular level [29],[31].

2.2 Conventional Sorbents

2.2.1 Silica gel

Silica gel is the common name of the amorphous and porous polymer of silicon dioxide, an old and deeply studied material, since the begin of '900. Between 1934-36 Hofmann et al [32], Rideal [33], and Kiselev[31],[34] were the main authors studying the interaction between the sorbent and water. At the begin research was focused on the physics and chemistry behind the formation of chemical groups, especially the hydroxyl, during the silica synthesis. Through condensation polymerization [35],[36] process, spherical colloidal particles are obtained starting from the Silicic Acid, $Si(OH)_4$. These particles are assembled as spherical colloid through siloxane bridges (SiO_2), exhibiting silanol protuberance ($\equiv SiOH$) on the external surface with the OH chemically held by the silicon atoms. First experimental proof of this structure, especially the presence and distribution of the hydroxyl groups, arrived many years later (1948-50) with the application of infrared spectroscopy methods [16],[37–40].

The presence and distribution of different OH groups on the external surface, usually defined as the chemisorbed water, together with the porosity of the structure, determines the activity and performances of the material as

sorbent, especially its capacity and the dynamic behaviour of water adsorption. Indeed, over the external surface of the colloid are coexisting different combinations of the mentioned groups as sketched in Figure 2.1: *i*) single and isolated free silanols $\equiv SiOH$; *ii*) single free silanediols $= Si(OH)_2$; *iii*) the combination of neighbour silanols and silanediols; *iv*) siloxane bridges with an oxygen atom on the external surface [16],[31],[37]. Thermogravimetric analysis [16],[31] on different silica type showed that the higher mass variation is at temperatures lower than 150-180°C, the upper limit is called critical temperature (T_B). Below this value water can be physically adsorbed, and this interval is called dehydration phase. At higher temperatures the loss of mass is imputed to the de-hydroxylation process: the chemisorbed water, in the form of OH groups, starts to desorb from the external surface, while the water structured into the SiO_2 bulk also starts to evaporate. Within the interval of dehydration zone, the activation energy of desorption (E_D) varies between 26-44 kJ mol^{-1}, as the spatial configuration of the physic-adsorbed water on silica surface, in particular in proximity of the monolayer configuration E_D lies in the interval of 37-44 kJ mol^{-1} [31],[41]. These values are comparable with adsorption heat of water vapor (Q_A): the activation energy for physical adsorption of water vapor on the hydroxylated surface of silica is null and, as result, the way in which water vapor molecules approach target surfaces is the only influencing factor for the adhesion process [31],[42]. The amount of silanol groups over sorbent surface is an extreme and important parameter determining water uptake capacity of the material [16]. Zhuravlev [31] determined that the concentration of the surface hydroxyl groups, defined as the silanol number α_{OH}[i] (number of OH groups per unit surface area, to assess the degree of covering of hydroxyls over the SiO_2 skeleton), over 100 silica sample as a constant mean value equal to 4.6-4.9 OH nm^{-2}, independently by the fabrication[ii] method of samples and by the temperature (only for $T<T_B$).

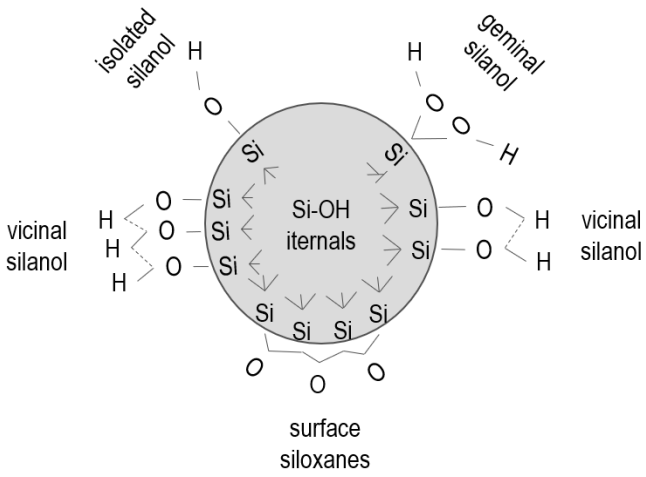

Figure 2.1: Surface chemistry structure of a silica colloid [31]

[i] number of OH groups per nm^{-2}, as the ratio between total number of silanol group over the specific surface area S in m^2 g^{-1}

[ii] on the contrary the water structure within the porous structure is strongly dependent from the production method

Indeed, increasing the temperature lead to a progress and linear reduction of α_{OH}, becoming lower than 1 OH nm^{-2} after 600°C, and negligible at 900°C. As the opposite E_D linearly increase from 50 to 200 kJ mol^{-1} as the temperature ranges between T_B-600°C.

The affinity with water is exploited in different technical applications, using the heat as primary driver for the reversible dehydration process within temperature of operational environment and T_B. A list of some typical application of silica gel and material properties are reported in Table 2.1 and 2.2.

Application	Reference
As catalyst carriers for water treatment	[43],[44]
Thermo chemical storage	[45]
Adsorption chillers	[46]
moisture proof packaging	[47]
petrochemical	[48]
Soil science	[49][50][51]

Table 2.1: Example of industrial application of silica gel for physical adsorption.

Type		S_{area}	D_{pore}	pH	c_p	K	Q_A	ρ_{app}	ρ_{bulk}	D_{s0}
name	Structure	m^2 g^{-1}	A	-	kJ kg^{-1} K^{-1}	W m^{-1} K^{-1}	kJ mol^{-1}	kg m^{-3}		m^2 s^{-1}
A	amorphous	650[41][52] 710[16] 864[53][54]	22[41][52][53]	4[53] 5[41][52]	0.921[41][52-54]	0.128-0.168[55][56] 0.174[41][52] 0.198[53] 0.18-0.2[57]	45.5-50[58] 3.1[53]	700[53] 730[41][52]	1306[52]	2.5x10^{-4} [53][54]
3A	amorphous	606[41]	30[41]	3.9[41]	0.921[41][52]	0.174[41]		770[41]		
RD	amorphous	636[54] 650[41] 716[59] 720[52] 820[10] 838[16]	14[60] 21-22[10][37][41][52] 23[45]	4[41][52]	0.921[41][52] [54] [59-61]	0.198[41] [45] [52] [61][60] 0.12[62]	41.5[10] 48.4[45] 48.6[60] 50.2[59]	800[41] 700[52] 740[60]	1158[52][62] 1220 [59]	2.54x10^{-4} [54] 2.9x10^{-4} [10]
MCM-41	ordered	[16]	15-100[63]	[16]	[16]	[16]	[16]	[16]	[16]	[16]

Table 2.2: Properties of the different types of silica gel

The widespread diffusion of this material together with the relative low cost, make it still interesting to consider for applications of desiccant cooling and water harvesting, despite the fact that some new and better performing materials are under development. Of particular interest is the compatibility with human health, indeed being non-toxic and odourless, U.S. FDA approved in 2019 the use for food addiction with a maximum amount of 2% by weight of food, by the 21FR172.480 [64], as stabilizer [65], anti-caking agent, defoaming, emulsifier and settling agent.

The silica gel studied in this research has been produced by Oker-Chemie GmbH with a pseudospherical geometry and used without any precaution or post treatment. It consists of amorphous silica beads, registered as Siogel ®, 99.5% purity, average diameter of 2-3 mm, surface area of 800 m^2 g^{-1} and bulk density in the range of 680-780 kg m^{-3}, as provided from producer.

A complete characterization of the material has been carried out measuring equilibrium isotherms in the temperature range of 20-60 °C and of RH 10-90% at ambient pressure. Equilibrium points have been obtained measuring the weight of a samples (100 g dry basis, accuracy of measurement ±0.1 grams) inside a climatic chamber, model DiscoveryMyDM340, at a fixed air temperature and humidity for at least two days. This offered

the possibility to explore sorbent uptake in real operative conditions with ambient air, and all its constituents. The equilibrium points have been defined, according to the standard UNI EN ISO 12571: equilibrium is considered to be established when the variation on weight measurement is lower the 0.1% of the dry basis, in a series of 3 different measurements. over 24 h time frame. Results of measurements are listed in table below.

T [°C]	RH [%]				
	10%	30%	50%	70%	90%
30	0.021	0.056	0.107	0.233	0.287
40	0.016	0.052	0.108	0.227	0.287
50	0.011	0.044	0.077	0.221	0.289

Table 2.3: Water uptake data of silica gel testing in the climatic chamber

Dubinin Radushkevich [26]	$w^* \exp\left(-\beta\left[\frac{RTln\left(\frac{P_{sat}}{P}\right)}{\Delta H}\right]^2\right)$	$\beta = 550$
modified Dubinin Astakov [23]	$w^* \exp\left(-\beta\left(\frac{T}{T_s}-1\right)^n\right)$	$\beta = 160$
Henry-vant Hoff [66].	$2.2\text{x}10^{-12} \exp\left(\frac{\Delta H}{RT}\right) P$	

Table 2.4: Different model for the definition of the adsorption isotherm curves

Datapoints collected with the described method have been compared with adsorption isotherm models described in the previous paragraph. Purpose of this comparison is the validation of an analytical method for an accurate prediction of the maximum water uptake, at determined condition of temperature and humidity, as required in the Chapter 4. As example in Figure 2.2, obtained equilibrium data @40°C were compared with mentioned adsorption isotherm models and plotted with the fitting parameters reported in Table 2.4.

The graph gives the evidences of what is discussed in the previous paragraph. Models based on Langmuir theory such as the Henry-vant Hoff (obtained using the Henry's law for the description of the adsorbate at low concentrations and the vant Hoff equation for the isotheric heat of adsorption dependeny from temperature and pressure), fail to describe silica gel behaviour, as a shortcoming of the assumption of a monolayer and homogenous distribution[66]. An idealization of the phenomenon that looks far from the reality of this specific silica's behaviour. Polanyi based models, the Dubinin-Astakov and Dubinin-Radushkevich, give a good estimation of the adsorption curve in the interval of $0.4<P/P_{sat}<0.9$, nonetheless there's a consistent underestimation of water uptakes at low relative humidity. The error committed is relevant and not acceptable, especially for the modelling purpose of the exchanger based on this material, as showed in the Chapter 4. Indeed, for the simulation model equilibrium curves represent an input for the definition of the maximum potential achievable, at defined thermodynamic conditions. Failing in the prediction of this number, will highly affect all the mass transfer equations defined in the next chapters. Reasons behind this discrepancy can be different. First of all these experiments were carried out in an environment that is far from an ideal lab environment, is instead closer to a real and operative environment of *"open air systems"*, as in desiccant cooling. This means that some competing mechanisms with other gas components may occur. Secondly, a precise estimation would require more investigations on intrinsic properties such as pores size distribution, adsorption heat, surface area.

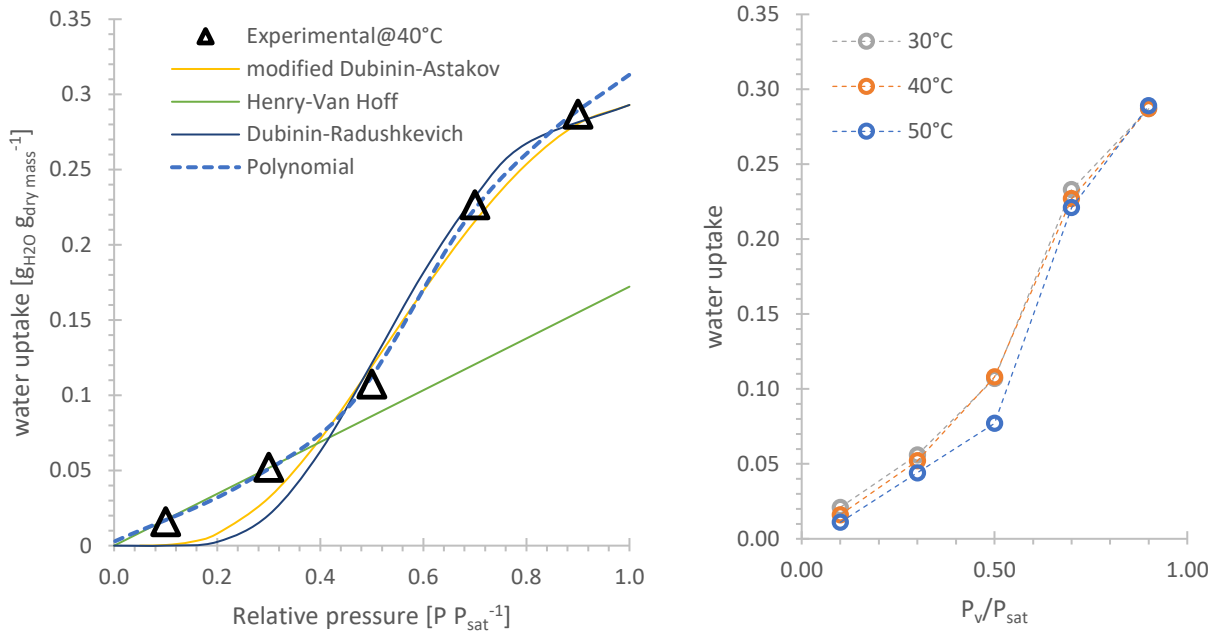

Figure 2.2: On the left a comparison between experimental data of tested silica gel in the climatic chamber @40°C and most diffused model of adsorption isotherms. On the right the graphical representation of numerical values contained in Table 2.3

A pure empirical approach can overcome these problems reaching the same goal, a mathematical function giving as an outcome the relative pressure of water vapor in equilibrium with the sorbent at defined water content and temperature.

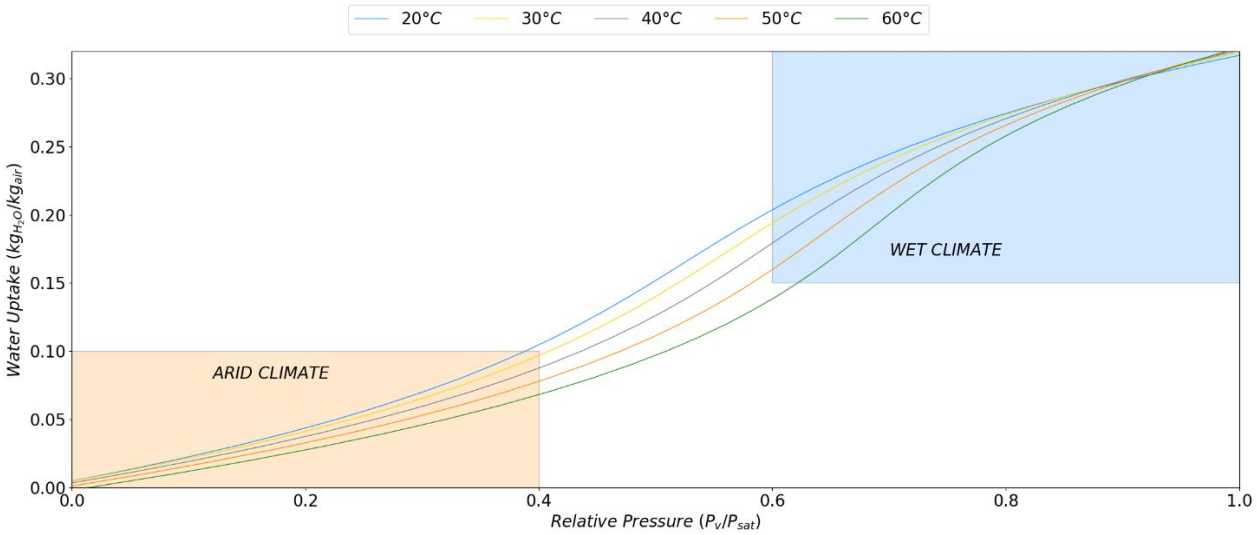

Figure 2.3: Equilibrium data can be fitted with a polynomial that correlate the variation of relative humidity as a function of water content and temperature.

The price paid will be the loss of any physical meaning for the equation, and parameters. For this purpose, a multivariate regression based on the Sherman-Morrison formula, has been applied [67]-[68] obtaining the following equation:

$$RH^* = S_1\,T^* + S_2\,T^{*2} + S_3\,w^* + S_4 w^*\,T^* + S_5\,w^*\,T^{*2} + S_6\,w^{*2} + S_7\,T^*\,w^{*2} + S_8\,w^{*3} + S_9\,T^{*3} \quad (2.5)$$

Where coefficients are respectively S1=-0.00249434; S2=0.0000529632; S3=5.65527;

S4=0.0360887; S5=-0.0000713679; S6=-24.9044; S7=-0.112424; S8=54.8088; S9=-0.000000123558. This it will be used in the next chapter for the evaluation of the equilibrium conditions in a temperature range of 20-70°C, as depicted in the next figure.

This formulation still has some problems on the very extreme conditions: in very humid conditions, RH close to 1, different curves can overlap. The difference between resulting values is very low and has been neglected. In very arid conditions, when RH is close to zero, especially at higher temperatures, the water uptake can result in negative values. This problem was simply solved in the numerical model of the Chapter 4 imposing a saturation lower limit of 0. These extreme conditions are very rare in the experienced adsorption/regeneration tests, the weight and importance for the entire process of simulation is very low.

The structure and the elemental composition of the silica gel particles were analysed using Scanning Electron Microscopy (SEM) using a FEI Quanta 200 coupled with Energy Dispersive X-Ray Spectroscopy (EDS) (Oxford Instruments), at the imaging and analysis center of the Andlinger Center for Energy and the Environment, Princeton University. The picture in Figure 2.4 shows particles with an overall a smooth surface, but the brittle nature of these structures results in the formation of fracture points in certain regions, Figure 2.5. This may create problems in the final applications. Indeed, the fine powder generated from these fractures, and connected to its handling, can be an issue in the final applications especially in open air systems. The correct use in this case should anticipate the problem with a correct filtering of the air transporting the powder, especially in the break-in phase. The spectrum analysis in Figure 2.6 and Figure 2.7 has detected 7 relative peaks, out of which the 0 keV one is not representing any atomic species but only the background noise from the x-ray diffraction. The tallest peaks are at 1.74 keV and 0.53 keV, identifying respectively silicon and oxygen atoms as the main constituents of silica gel structure. Smaller peaks identified components with a concentration smaller than 1%, the Na at 1.04keV and Al at 1.49 keV. Their presence is justified by the original composition of the material: sodium aluminate silicates are precursors for the formation of the silicic acid $Si(OH)_4$, structural element of the polymeric condensing process that leads to the formation of silica gel colloids. Remaining peaks at 0.28 and 2.31 keV are respectively atoms of carbon and sulphur. The sulphur peak is smooth and less sharp, meaning that doesn't belong to a crystalline structure. Its presence can be justified as corresponding belonging to some hydrocarbon molecule, as supported by the presence of carbon, and chemically held to OH group[i]. Anyway this hypothesis cannot be verified, and the possibility that carbon and sulphur came from some contamination of the instrument cannot be totally excluded.

[i] It's resistance to the vacuum (2.3×10^{-1} Torr) cannot be justified as a physical adsorbed molecule. The strength of the link can sound more as a chemisorbed molecule, irreversibly linked to the structure (at least always present in the dehydration phase).

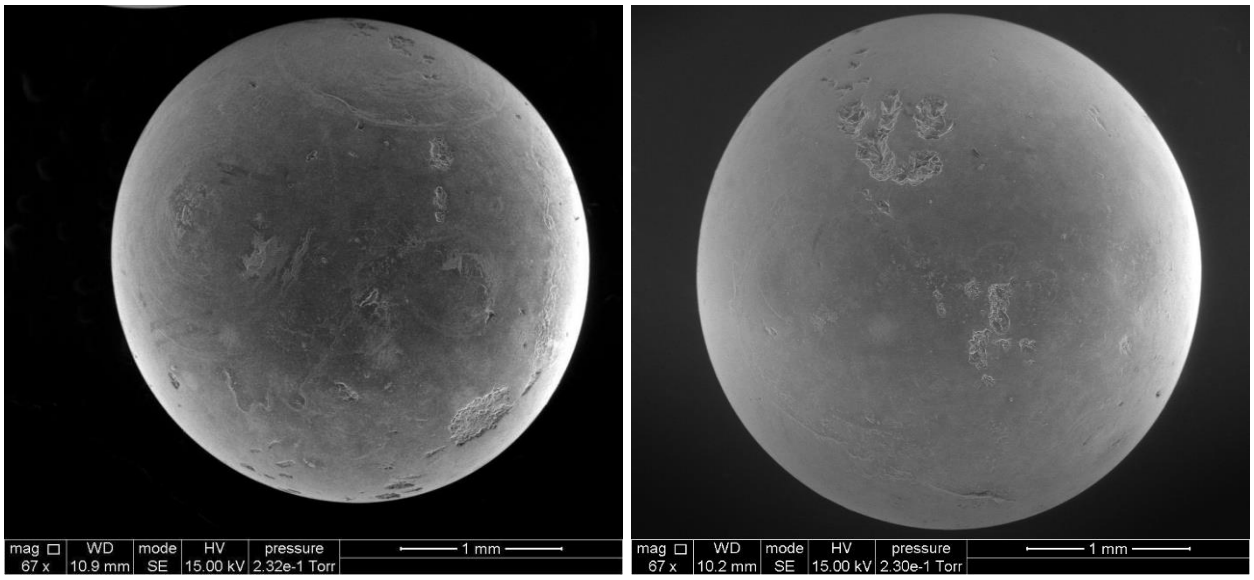

Figure 2.4:. Overall image of a silica gel bead magnified with SEM microscope. Particles showed an average size around 2-3 mm, with overall a smooth surface.

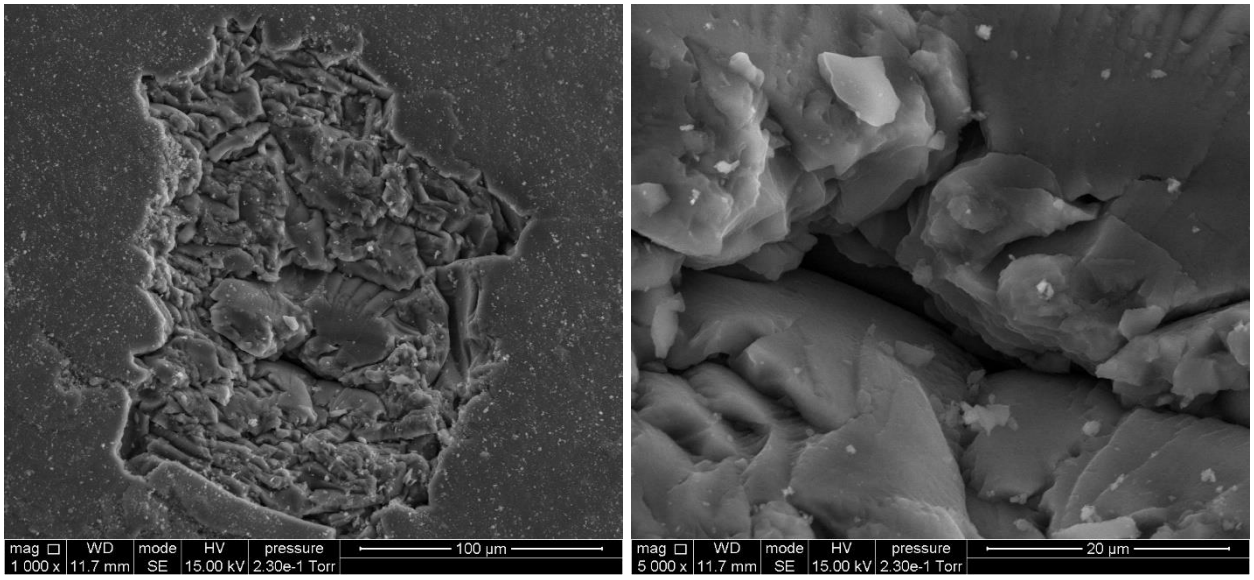

Figure 2.5: 1000x magnification of a fractured point on the smooth surface of silica gel particle (left). 5000x magnification of the fracture on the left (right).

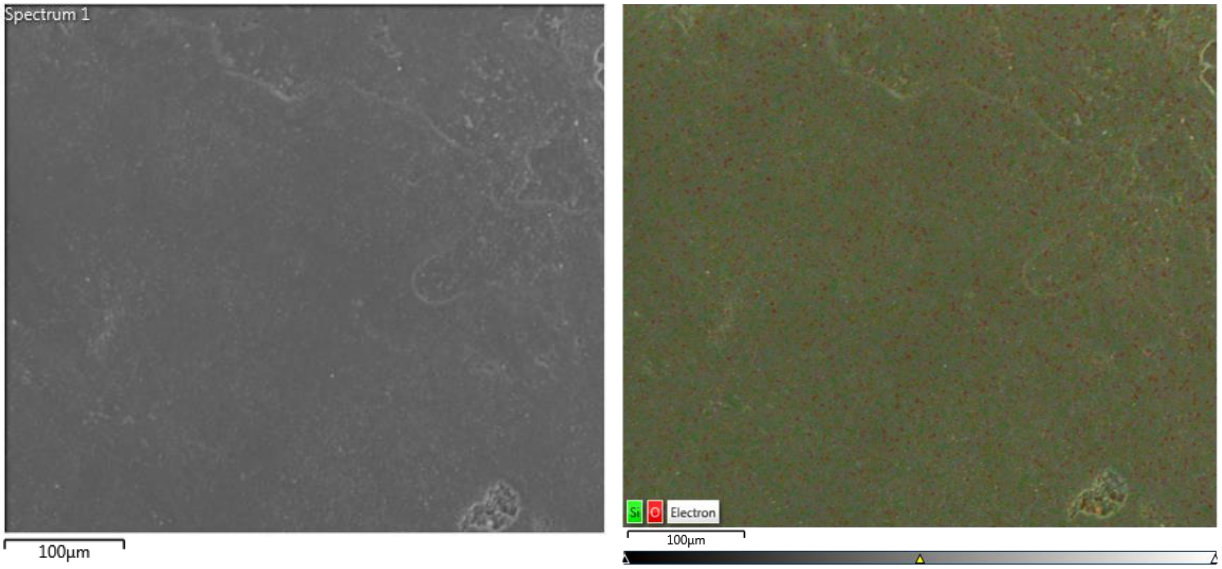

Figure 2.6: The SEM-EDS analysis of the image () (left). The spectrum analysis (right) of the element in the composite mass of the silica particle, visualized in the relative voltage range 0-12 keV, counted per second per electron-volt cps/eV. The silica particles indicate traces of Na lower than 1 atomic %

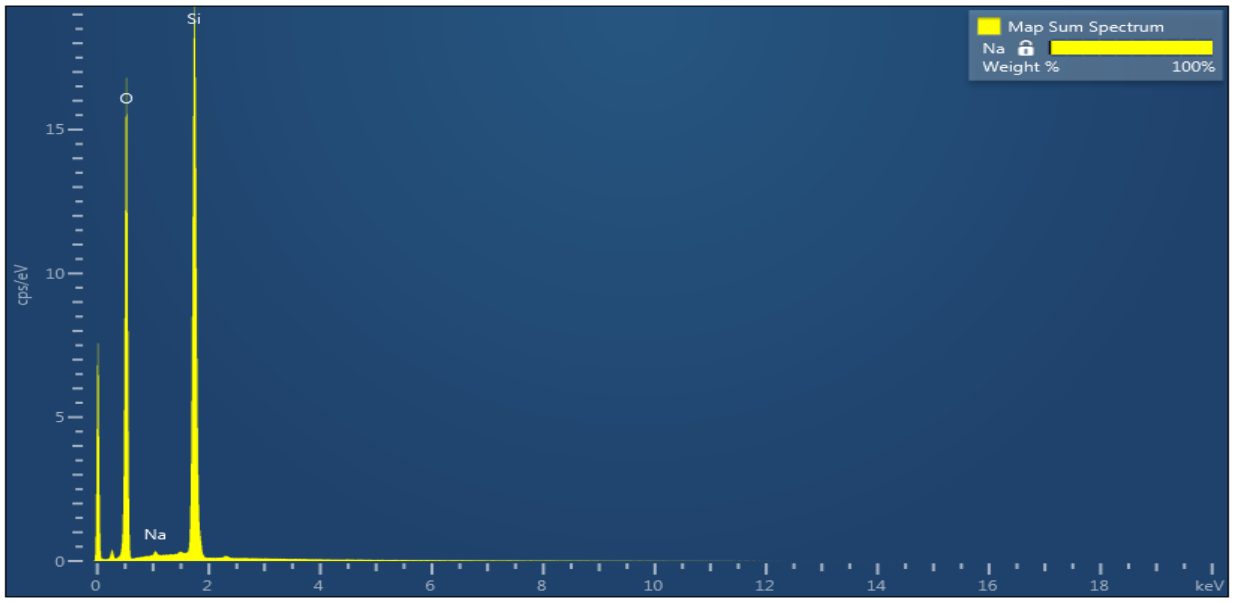

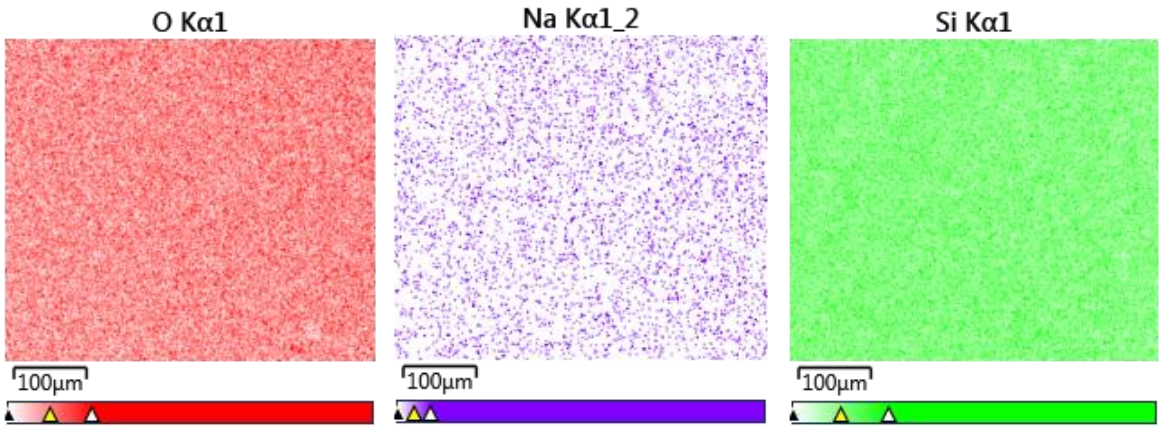

Figure 2.7: Elemental analyses on the silica particles indicate traces of Na lower than 1 atomic %

2.2.2 Zeolite

Zeolite is the family name of a large group of microporous aluminosilicate minerals and synthetic cristals. Etymology of the word is Greek, ζέω (zéō) *to boil* and λίθος (líthos) *stone*, defined the first time by the mineralogist Cronstedt[69], resulting from his experimental observation of a literary boiling stone after heating the mineral Stilbite . More of the 50% of the global market of natural zeolite is applied in the construction industry, especially to improve fire resistance, straight and sound absorption of lightweight concrete[70]. Another very spread application is the use as additive of animal feedings [71], mineral such as kaolin, bentonite and other zeolites, are used for the prevention of intestinal diseases [72], especially for the absorption of mycotoxin contaminating animal feedings [73][74]. Other interesting expanding sector is the application for soil remediation [75] and wastewater treatment [76], for the removal efficacy of heavy metals and nitrogen-based components and the very low cost [76],[77]. The association between zeolites and the term *"molecular sieve"* is typical for the ability to selectively sort molecules by their dimension. This is due to a very regular pore structure of molecular dimensions, that can specifically synthetized in order to have definite pore dimension and a preferential affinity towards specific molecules [8],[78].

General structure of a microporous zeolite is a hosting framework of negatively charged aluminosilicates counter balanced by different cations: $(AlO_2)^-(SiO_2)^- + Cations$ [16],[79]. As for the silica gel, hydrophilic properties are proportional to the concentration of active sites, but a relevant role is played by the extra-framework cations this time, in addition to the aluminosilicate. The type of the cations binding the aluminosilicate group identifies typically the family name: ALPO family contains aluminophosphates cations; MEAPO family contains metal-aluminophosphates; SAPO family contains silico-aluminophosphates [80]. These aluminophosphates families have a regular pores system, a three-dimensional network similar to zeolites and improved adsorption affinity with polar molecules, exhibiting a typical type V adsorption isotherm when paired with water [16]. SAPO materials generally show higher capacity then other families because the extra presence of the active site (SiO_4^{4-})[8],[16],[78].

Material	W @25°C	H_{ads}	T_{rig}	Ref
	$kg_w\,kg_s^{-1}$	$kJ\,kg^{-1}$	°C	
SAPO-34	0.313		66-90	[80]
13X	0.3	3500-6000	150	[81][82]
MgY	[80]	3000-6000	150	[81]

Table 2.5: Some characteristic properties of the most spread zeolites

Among the different options, SAPO-34 is a very promising adsorbent with a CHA type 3D-structure and 0.38 nm window dimension, which is able to combine a moderate hydrophilicity with a high capacity of adsorption of water vapor, resulting in moderately low regeneration temperature (60–100 °C) and a reduced desorption heat, while maintaining high performance within the adsorption cycle [83]. Within the framework of the experimental investigation of this material for desiccant cooling exploiting natural buoyancy, the National Research Center of

Messina provided an important contribution for the evaluation of adsorption equilibrium curves of the material reported in Figure 2.8, and the manufacturing the adsorption heat exchanger with a coating technique[83]. The cited paper contains all the information about the thermogravimetric method used for the evaluation of water uptake, and the coating techniques adopted for the strong adhesion of the zeolite SAPO34 over the metallic surface of a typical finned coil heat exchanger.

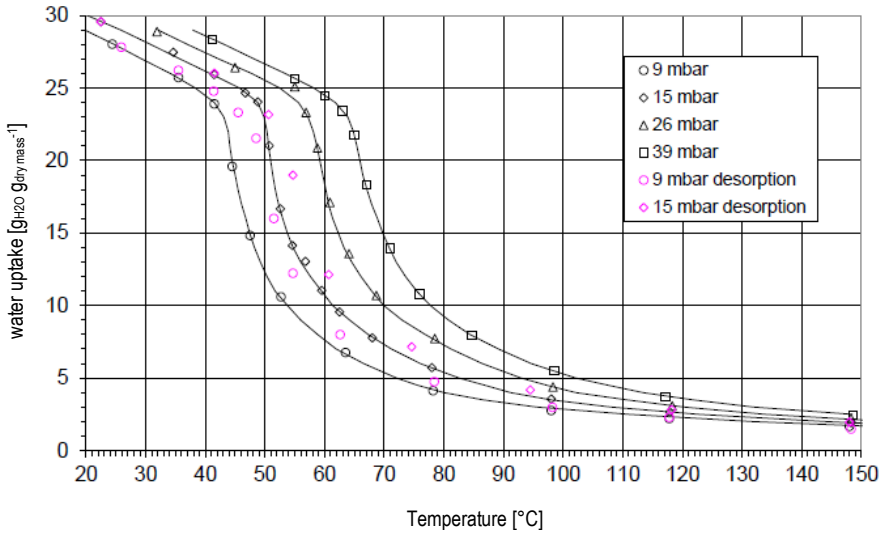

Figure 2.8: Iso-pressure adsorption characteristics of the pair Zeolite SAPO34-water vapor, within the temperature range of 20-150°C

2.2.3 Composite sorbents

In addition to the two reference sorbents, the industry of adsorption found interesting application with composite media, obtained with the combination of a conventional sorbent (as hosting matrix) and an hygroscopic salt (such as $CaCl_2$, LiBr, LiCl, $MgCl_2$). Lithium chloride, for example is used in rotating wheels, impregnating a porous media with the typical corrugated structure of desiccant wheels. Some companies (e.g. Klingeburg, Munters, Engelhar HexCore) produced desiccant wheels using as porous media typical honeycomb cells of silicates, cellulose.[84],[85]

The combination of different host matrices (e.g. mesoporous o microporous silica gels, alumina, porous carbon or polymers) and salt (e.g. $CaCl_2$, LiBr, LiCl, $MgCl_2$) change consistently properties of the sorbent itself, usually improving water capacity and diffusivity. For example in [85][86] the addition of lithium chloride to typical silica rotors, improved dehumidification capacity of 3 g/kg and dehumidification efficiency up to 90%.

In [87], Aristov et al. experienced a composite obtained from the combination of loose grains (particle radius 0.355-1.4 mm) of mesoporous silica and with $CaCl_2$, within the operative range of Pv_{H2O}=0.8-7kPa and T=33-69°C.

The realization of the composite is based on an impregnation process requiring few steps: i) drying of the hosting matrix (T=120-180°C); ii) immersion and impregnation of the matrix with the selected water/salt solution; iii) removal of salt excesses and heating again the material, eventually activating calcination process. Sorptive

properties of the final composite depend by multiple factors and are not the linear superposition of matrix and salt properties but are rather influenced by their mutual interaction.

Observed dependencies are connected to the chemical composition of the salt; the concentration of the salt during the impregnation; the chemical composition and porous geometry of the host matrix; the condition of temperature and pH during the synthesis. For example in [88] is shown as using the same silica gel matrix and salt concentration (33wt%), LiBr shown much higher water uptakes than $CaCl_2$ at low temperatures meanwhile required regeneration temperatures are higher.

The improvement of water capacity was found to be driven mostly by “liquid absorption” (characteristic of the hydrated salts) rather than the “solid absorption” (connected to the passage from the anhydrous to the hydrated configuration of salt crystals). Further, as demonstration of the matrix/salt mutual influences, the occurrence of the dihydrate configuration of the calcium chloride ($CaCl_2$*$2H_2O$) shifted down at much lower water vapor relative pressure than the value of the bulk (2% against 13%). Meanwhile, the hexahydrate form ($CaCl_2$*$6H_2O$) was not found in the composite despite, is well known its presence in the bulk especially at higher relative pressure [88], [89].

These considerations, at least for the couple silica gel/$CaCl_2$ are more coherent with the concept of pore volume filling at the basis of the Dubinin theory that, especially for high values of relative pressure, can evolve in the phenomena of capillary condensation. Disadvantage in this case is an eventual diluition of the salt deposited within the pore volume that, migrating throughout the mesoporous structure, may define a degradation of performances [90],[91].

3. AIR DEHUMIDIFICATION VIA ADSORPTION

Abstract

As discussed in the previous chapter peculiarity of adsorption materials is the possibility to reversibly switch between adsorption and desorption within the dehydration operative zone, without affecting its properties. The limit is defined by the critical temperature T_B that, in most of the cases, doesn't exceed 200°C. To invert the mass transfer during desorption an external energy input is required, supporting the break of the attractive iteration between the adsorbed molecules with the sorbent surface traps (hydroxyl; silanol; silicate, etc…) first, and second to assist the diffusive transportation of water molecules through the internal porosity of the material up to the external bulk side. The way the adsorption/desorption cycles are operated gives typically the name of the category. Thermal swing adsorption use the heat as energy source, and regenerate the sorbent rising the temperature. Pressure swing adsorption uses the gradient pressure of gas species as unique driving force for the process, and regeneration is carried out reducing the total pressure within the sorbent bed. In addition to these two methods, sorbent regeneration may also be assisted by ultrasounds[92–95]. This technique is mostly experienced at research level, with the advantage to increase the diffusion transport of the sorbate through the pores of the sorbent. Among different applications in the chemistry sectors for gas separation and chemical removal, or in the petroleum sector as a more efficient alterative to standard distillation, air conditioning sector had different example of experimental and industrial/commercial applications. In this case the adsorption/desorption swing belongs to the thermally driven category. The rationale is quite simple: the application of adsorption phenomena in air conditioning and refrigeration rises as potential competitor to electrically driven vapor compression units. The use of pressure swing and ultrasounds require, necessarily, mechanical energy generated from an electrical conversion, failing then the original scope to be an alternative solution. In the following chapter the experimental testing of improved solutions shows the advantages of the application of *conjugated heat and mass transfer* for air dehumidification in the indoor environment. Three different studies published by the author report performances, advantages and drawbacks of the application of sorption techniques to manage the latent part of a typical air treatment carried out for ventilation of buildings.

Keywords: regeneration temperature; conjugate heat and mass transfer; desiccant evaporative cooling

Most of this chapter is based on following papers

"Experimental results on adsorption beds for air dehumidification"

Finocchiaro, P., Beccali, M., **Gentile, V**. (2016). *International Journal of Refrigeration*, Vol 63, pages 100-112. doi:10.1016/j.ijrefrig.2015.10.022

"Experimental testing of the buoyant functioning of a coil coated with SAPO34 zeolite, designed for solar DEC (desiccant evaporative cooling) systems of buildings with natural ventilation"

Simonetti, M., **Gentile, V.**, Fracastoro, G. V., Freni, A., Calabrese, L., & Chiesa, G. (2016). Applied Thermal Engineering, Vol 103, pages 781-789. doi:10.1016/j.applthermaleng.2016.02.072

"Experimental analysis of "NAC-wall" for hybrid ventilation mode"

Simonetti, M., **Gentile, V.**, Liggieri, L., Fracastoro, G. V., & Carrabba, M. G. (2017). *Energy and Buildings,* Vol 152, pages 399-408. doi:10.1016/j.enbuild.2017.07.047

"Optimized low pressure solar DEC with zeolite based adsorption"

Simonetti, M., **Gentile, V.**, Fracastoro, G. V., & Belmonte, R. (2017). Paper presented at the *Energy Procedia,* Vol 122, pages 1033-1038. doi:10.1016/j.egypro.2017.07.472

"Preliminary study of the hybrid solar DEC "NAC wall" system integration in building façades in urban context"

Simonetti, M., **Gentile, V.**, Chiesa, G., & Nigra, M. (2017). Paper presented at the *Energy Procedia,* Vol 134, pages 588-597. doi:10.1016/j.egypro.2017.09.570

"Monitoring results and energy performances evaluation of Freescoo solar DEC systems"

Finocchiaro, P., Beccali, M., Brano, V. L., **Gentile, V**. (2016). Paper presented at the *Energy Procedia,* Vol 91, pages 752-758. doi:10.1016/j.egypro.2016.06.240

"Monitoring and energy performance assessment of an advanced DEC HVAC system in Morocco"

Beccali, M., Finocchiaro, P., **Gentile, V.**, Muscherà, M., Motta, M. (2017). Paper presented at the Solar World Congress 2017 - IEA SHC International Conference on Solar Heating and Cooling for Buildings and Industry 2017, Proceedings, pages 1644-1654. doi:10.18086/swc.2017.28.01

3.1 Air Dehumidification and Cooling

The increased demand for thermal comfort of indoor occupants is leading an impressive growth of installed air conditioning appliances and a consequently sharp rising of energy consumptions, condition that will be exacerbated in the next future, basing on global warming scenarios [96–99].

Adsorption technologies since different decades are envisioned as interesting and fascinating solution, offering the possibility to shift the cooling demand for indoor environmental control from power heat [100–105]

Of particular interest, is the integration of these type of systems with sustainable sources of heat. For example, waste heat coming from thermal cascade of industrial activities or production processes. Another good example is the use of heat from solar energy. This is particularly fascinating giving the seasonal synchronization between irradiation and cooling needs.

The application of thermally driven adsorption technologies for refrigeration and air conditioning are classified in two main categories: *closed loop* and *open loop*. In both cases the cooling effect is obtained working on the variation of pressure of water vapor: *i*) evaporation of water generates a cooling effect and increases vapor pressure; *ii*) drying the air/water vapor mixture with adsorption to equalize/reduce related partial pressure of water vapor; *iii*) reject the adsorbed vapor at higher pressure than the evaporation and adsorption phases, using the external environment as sink.

Despite the general concept is similar for all the categories, there are substantial differences: in *closed loop systems* the air/water mixture is always the same because there's no direct communication between the sorbent and the external environment. The only exchange mechanism is based on the thermal transfer at the evaporator/condenser. Closed loop is mainly applied for refrigeration. On the contrary *open loop systems* treat directly outdoor air and provide the required thermo-hygrometric for a correct indoor ventilation. The second substantial difference is about the absolute pressure: *closed loops* may work at different absolute pressures and under vacuum; *open loops* work only at the atmospheric pressure level. This research focuses the interest on *open loops*, and the next paragraph will describe main characteristics and problems.

3.1.1 Open Loop Desiccant Evaporative Cooling

Desiccant Evaporating Cooling (DEC) systems have been used for the direct treatment of external air to satisfy thermo-hygrometric requirements of ventilation for indoor comfort of the occupants. For this purpose, either solid or liquid desiccants have been employed.

The most applied solution is based on the Pennington cycle [106–108] realized through a rotary wheel exchanger coated with a sorbent material. Sometimes these wheels are called enthalpic exchanger, because they operate on the entire enthalpic content of the air. In most common and used DEC systems, the desiccant wheel is based on silica gel or lithium chloride as adsorbent materials. This is the most crucial component while the remaining

parts are conventional technologies (the heat recovery unit; humidifiers; fan; water/air heat exchangers, water pumps) used for many other applications of the same sector and generally in the industry. Anyway, desiccant wheels have been not used only for building air conditioning. They found also application in the industrial sector including pharmaceuticals, chemicals, food and beverages, and many others requiring a very fine and accurate humidity control of the operative and working environment. Especially the pharmaceutical, chemical and electronic sectors are driving the global growth for the application of this technology that, in 2016, was mainly dominated by silica gel desiccant wheels, covering more than 60% of the global market, with an estimated CAGR (Compound Annual Growth Rate) for the next 10 years of 5.3% [109][110].

The original cycle had many improvements over the years [111–116], and in Figure 3.1 is reported a schematic diagram of how a DEC cycle can be assembled, to provide indoor ventilation in both summer and winter season. On the right, different steps are depicted over the psychrometric diagram.

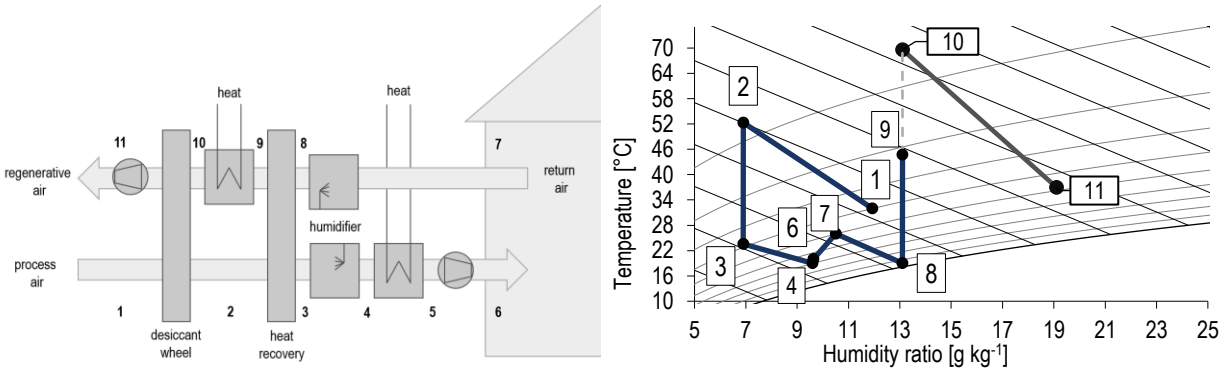

Figure 3.1: Schematic diagram of a DEC system (left up). Qualitative behaviour of process air in terms of temperature and moisture content (left down). Thermodynamic transformations on process and regeneration air (right).

Two main air flows, *process* and *regenerative* air flow, cross at the same time and in counter current the wheel. *Process air* defines the primary air flow going from the external environment to the building, *regenerative air* is instead the opposite flow, from the building to the external environment. Fundamental steps for the treatment of process air are performed as following:

- **Dehumidification**. The process air, directly taken from external environment, flows through the desiccant wheel, reducing the moisture content (reducing also vapor pressure). The heat generated through the adsorption phenomenon causes an increase of temperature for both sorbent and air. Outlet conditions of process air are hotter, and drier than inlet ones
- **Thermal recovery**. Outlet stream has a relevant sensible energy content. This is recovered through a counter current heat exchanger (alternative configurations employ thermal recovery wheel) and transferred to the *regenerative air*. The recovery unit is an essential component reducing the total energy required for regeneration of the sorbent and reducing the temperature of *process air.* Main effect of this step is the increase of energy and power performances. The regenerative air, before encountering the

desiccant wheel, is heated firstly through the thermal recovery step, with an external heat supply eventually;

- **Humidification**. After the thermal recovery step, a water stream is sprayed through atomizing nozzles over the air. Water evaporation cools down the air, and the moisture content increases. This is a crucial step for the determination of the final delivery condition in terms of temperature and humidity. Water flow rate, surface area of exchange, and degree of atomization are crucial parameters for this step.

The desiccant wheel is continuously rotating, and the portion area exposed to the *process air* move up to the *regenerative air* active zone. Now the wetter sorbent is exposed to a hotter and drier environment, that drives the opposite phenomena, the desorption. With this approach, the combined rotation and counter current/parallel flows, what was a batch process of adsorption/desorption stages becomes a continuum, guaranteeing the effectiveness and the continuity of the entire cycle.

The location of components, as sketched in Figure 3.1, allows to perform a full air treatment satisfying both the winter and summer season requirements. The resulting cycle depicted in the psychrometric diagram is stepped in:

1-2 quasi adiabatic dehumidification of *process air*. Resulting air is hotter and drier;

2-3 pre-cooling of *process air.* This regenerative heat exchange, performed through an air-to-air counter current device or a regenerative wheel, recovers the sensible cooling potential contained within the indoor environment;

3-4 evaporative cooling of *process air*. Thermal comfort requirements define the final moisture content of the air exiting this step;

4-5 post heating of *process air*. This heat exchange is enabled only during the winter season. Instead in the summer season it will be bypassed and not used;

5-6 parasitic temperature increase due energy dissipation of the fan for the air circulation;

6-7 at 6 air is delivered to the indoor environment. Temperature and humidity increase up to point 7 because the latent and sensible gains of the indoor environment;

7-8 *regenerative air* is initially cooled through a parallel evaporative cooling step. Reaching the relatives wet bulb conditions. This stage is necessary to improve the cooling step performed at 2-3;

8-9 *regenerative air* is pre-heated. Recovered heat from *process air* is the parallel result of process 2-3;

9-10 *regenerative air* is heated with the external heat source (solar energy or other conventional heaters such as a gas boiler);

10-11 adiabatic regeneration of the desiccant wheel. Water vapor contained in the sorbent pores desorbs while absorbing the sensible energy content of the *regenerative air*. As result of this step outlet air is colder and moister. This air flow is then rejected to the external environment.

The interesting outcom of the application of this cycle is obviously the low impact in terms of power intensity and the possibility to couple more sustainable sources with the cooling demand:

- The cooling effect is not directly generated by an electricity use. Indeed, the pressure variation is thermally activated. The only power consumptions are generated by auxiliary components (air fan, water pumps, damper actuators);
- The highest temperature of the cycle, at the inlet of the desorption step 10-11, in most of the cases, is close to 70°C [i]. This temperature level is compatible with low exergy sources such as solar thermal energy, cogeneration or waste heat from industrial process.

Anyway, there are some shortcoming connected to the use of the desiccant wheel, affecting performances and limiting the effective exploitation of solar thermal energy:

- progressive heating of the sorbent is occurring within the dehumidification step 1-2. The cause is the release of the adsorption heat;
- the heat released to the process heat is amplified by a "*thermal-carry-over*" phenomena. Indeed, through the rotation of the wheel, a certain amount of the sensible heat from desorption sector, moves down to the adsorption sector.

The combined effect of these two phenomena is the rise of the average temperature of the step 1-2, and resulting slope of the transformation is higher than the adiabatic line, as in an ideal process. Consequently, the operative equilibrium water uptake is lower than the potential value if considering outdoor conditions as equilibrium environment, as point 1. In the end, this reduces the dehumidification effectiveness of the sorbent and the device. At the same time an inverse problem is occurring during regeneration. Indeed, the adiabatic process is occurring also through the desorption step 10-11, causing a consistent temperature drop. This time, the minimum achievable water uptake is higher if compared to the potential value achievable supposing an equilibrium potential equivalent to the inlet temperature of 10.

In the end:

- the increase of air temperature during the contact with the porous sorbent reduces relative humidity and limits maximum water uptake of material;
- higher temperature over the adsorbent layer during dehumidification leads to the further increase of the regeneration temperature, reducing in particular the effective exploitation of solar energy[ii];

Within this research all these aspects have been considered as an issue to be solved, opening the chance to the study and testing of an alternative possibility: driving adsorption and desorption through ***conjugate heat and***

[i] The effective value depends typically by local climate, and by desired delivery air conditions. Real application actually have shown that the good performances of the cycle are achieved at higher temperatures

ii Hottel- Whillier equation shows that the increase of mean operative temperature of a solar thermal collector reduces the energy efficiency of the device. For flat panel there's a linear correlation, for evacuated tube this is quadratic.

mass transfer, instead of an ideal adiabatic process, through what is called adsorption heat exchanger (for the sake of brevity ADS-HX). Different authors [117–119] tried to implement this concept on the existent configuration, resulting in very complex systems caused by the intensive use of auxiliaries (dumpers and actuators) and consequently increasing costs and complexity. A more practical alternative is the substitution of the desiccant wheel with a static heat exchanger.

Bongs et al. [120],[121] have approached a configuration of ADS-HX gluing silica gel beads (Grace 123B) over the primary channel of an air-to-air cross flow heat exchanger. In parallel evaporative cooling is driven on the secondary channels of the heat exchangers. Matching latent heat of evaporation with adsorption heat is indeed a smart solution, being the adsorption heat and water evaporation quantitatively comparable, an ideal isothermal adsorption could be approached. On the other hand the double air flow management is very complex, both for the adsorption and regeneration, complexity that at the end strongly affected the practical application of this device [122]. Further on, air has a very low specific heat, affecting the power density of the entire device. A more practical solution has been experienced by the author using finned coil heat exchangers, as heat transfer media, and supply and reject heat through heat transfer fluids with higher energy density, such as water.

In the next paragraph two tested solutions are compared, highlighting the main characteristics behind the conceptual design: an **inertial device** versus a more **responsive** solution.

3.2 Experimental setup

A schematic diagram of the experimental setup is drawn on Figure 3.2. The experimental facility is based on two AHUs (Air Handling Units), which can supply air flow rate in the range 100÷1500 $m^3\ h^{-1}$, equipped with a set of sensors and control devices to manage the outlet temperature, outlet humidity and air flow rate, according to user inputs. Each AHU includes an electrical heating battery (H2), a humidifier and calibrated flanges with the airflow rate measurements. Table 3.1 reports the list of monitoring sensors, position, typology, and related accuracy employed for the entire experimental campaign. The heat for regeneration is provided to the ADS-HX flowing the hot water produced with 10 m^2 of evacuated solar thermal collectors and installed on the roof of the lab. The solar thermal circuit is connected to 500 liters of thermal storage, equipped with an auxiliary electrical resistance (H1) of 3 kW as backup system.

Two water pumps (P1, P2), with a 3-level fixed velocity and a maximum absorbed power of $60W_{el}$, control the water flow through the primary loop (solar field-storage) and secondary loop(storage-ADS-HX). Through the three-way membrane valves V1/V2, powered at 24 VDC is controlled the switching between the hot closed loop, and the heat rejection loop open with the water network. Valves V3-V4-V5-V6 selects and enable the water flow only in one exchanger per time. An electromagnetic flow meter measures the water flow (m_w) through the ADS-HX loop. Air temperature, relative humidity and water temperature sensors are distributed along the test rig, as showed in the sketch above.

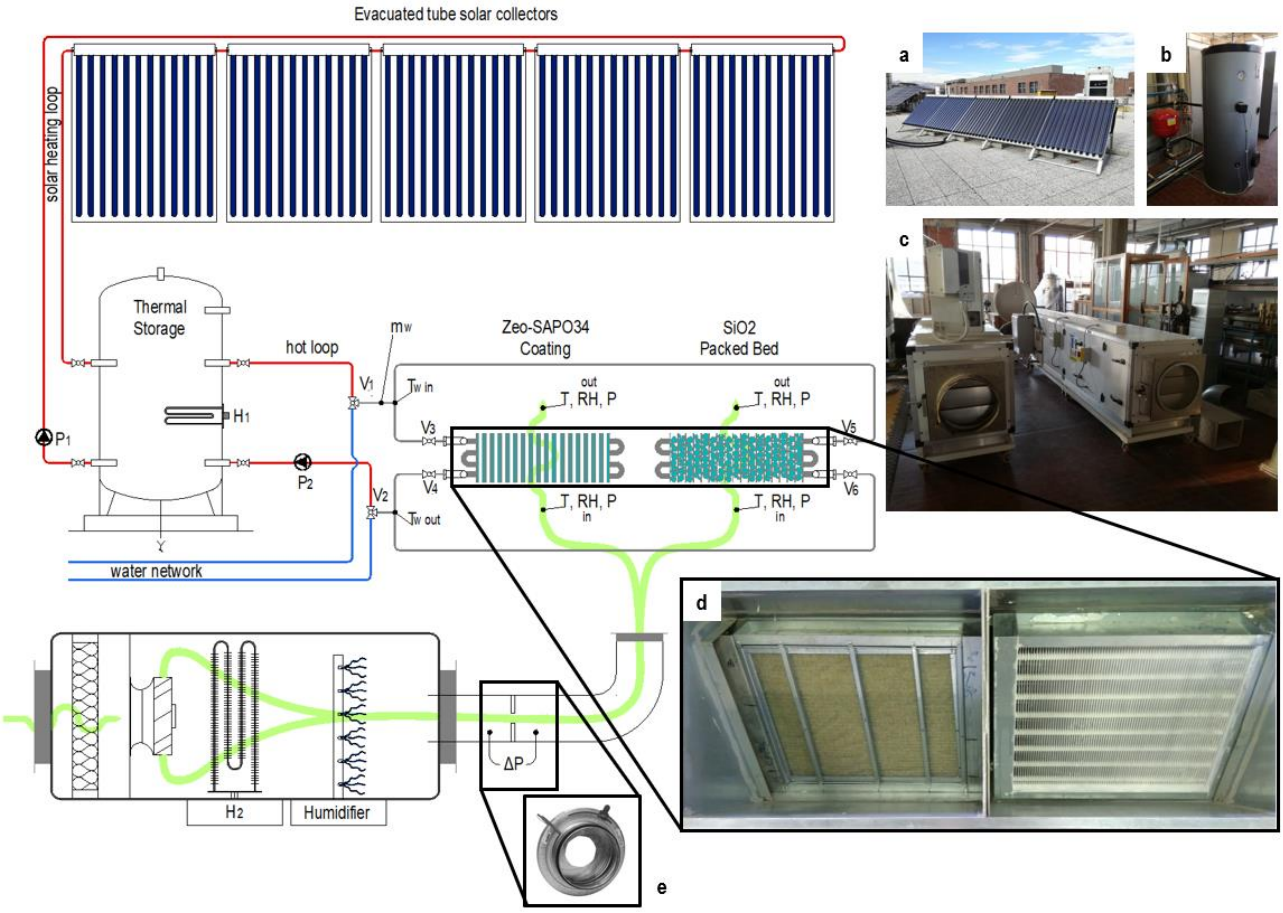

Figure 3.2: Scheme of the experimental setup. 10 m^2 of evacuated tube solar collector installed on the roof of the Lab (a), provides the thermal energy for the regeneration of the two ADS-HX (d). The energy is stored in an insulated water vessel (b) of 500L equipped with auxiliary backup heater (H1) to guarantee always the availability of heat. Two HVAC units (c) provide the air flow with a constant rate, measured with a calibrated flange (e) at the desired thermo-hygrometric conditions.

Physical value	Accuracy	Unit	Position	N°	Typology	Signal
air pressure	±0.2%	Pa	P_{in}; P_{out}; ΔP	3	3-wire differential pressure transducer	0-10VDC, 100ms response
air temperature	±0.4%	°C	T_{in}; T_{out}	4	2-wire NTC	1.8kΩ 25°C
water Temperature	±0.3°C	°C	Tw_{in}; Tw_{out}	2	4-wire Pt100	100Ω 0°C
relative humidity	±2%	%	RH_{in}; RH_{out}	4	thermoset capacitive polymer	0-10VDC
water rate	±1.5%	kg s^{-1}	m_w	1	electromagnetic flow meter	0-10VDC

Table 3.1: List of different sensors used to measure air temperature and humidity, water temperature and flow rate and pressure drops.

Most of the installed sensors didn't require specific precautions during the installation, and were provided with the calibration curve from the producer, except for the NTC and Pt100 thermistors. These have been calibrated comparing resistance measurements with a reference Pt1000 thermometer in a thermostatic calibration bath, within the temperature range of 20-90°C. The measurement at 0°C was obtained using melting ice instead of the calibration bath. Data collected in the tables below, were used to build the characteristic conversion curves of each sensor. From NTC thermistor calibration procedure is obtained a polynomial curve of 4th power, with fitting coefficients p1=2.022x10^{-4}, p2=-4.853x10^{-2}, p3=4.5893, p4=-220.447 ad p5=5090. For the Pt100 the relation is linear, with inclination at 0.1004 and intercept equal to 0.01376. The fitting of this function is showed in Figure 3.3 and 3.4. All the sensors provide an analogical output directly correlated to the physical observed quantity, except for the air flow measurement. Through the calibrated iris shutter shown in Figure 3.2(e), the aperture is regulated according to the desired flow range.

Ta in sx		Ta out sx		Ta in dx		Ta out dx	
T (°C)	Ω	T (°C)	Ω	T (°C)	Ω	T (°C)	Ω
84	257	84	258	84.1	255	84.1	258
60	523	59.9	526	60	522	60.1	526
30	1462	30	1460	30	1460	30	1462
21.9	2000	21.7	2020	21.9	2000	21.7	2020
0	5080	0	5010	0	5090	0	4990

Table 3.2: Electrical resistance values of calibrated NTC thermistors for air temperature measurements.

Tw in		Tw in	
T (°C)	Volt	T (°C)	Volt
0	0	0	0,01
25	2.53	25	2.55
30	3.04	30	3.05
60	6.04	60	6.05
84.1	8.45	84,1	8.47

Table 3.3: Electrical resistance values of calibrated Pt100 thermistors for air temperature measurements.

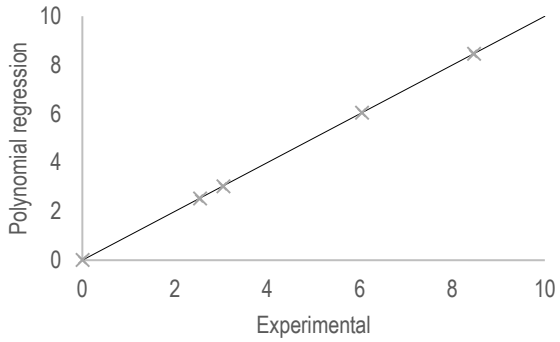

Figure 3.3: Verification of the polynomial fitting for the NTC air temperature sensors.

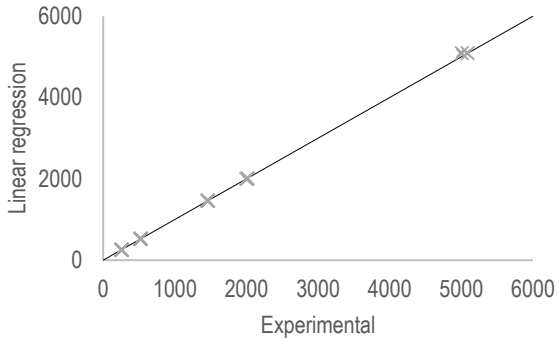

Figure 3.4: Verification of the linear fitting for the Pt100 water temperature sensors.

The differential pressure transducer provides a tension signal proportional to the pressure drop across the flange, correlating the measured ΔP[Pa] to the volumetric air flow with the following equation:

$$Q = \frac{k}{3.6}\sqrt{\Delta P} \quad \left[\frac{m^3}{h}\right] \qquad (3.1)$$

Where k is a correlation coefficient ranging between 1.5-15, linked to the actual opening of the iris shutter.

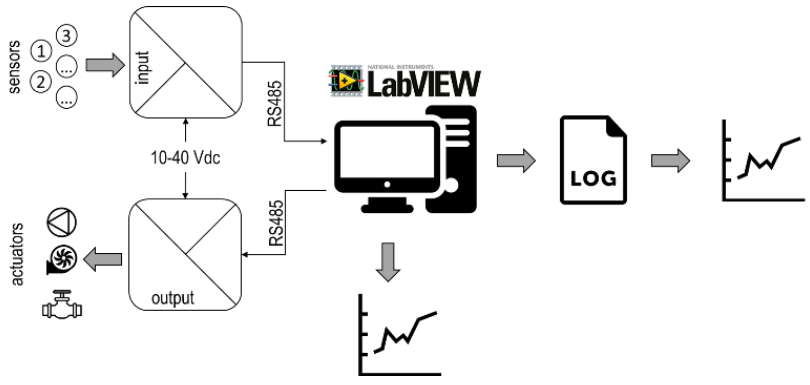

Figure 3.5. Architecture of the data real time monitoring and logging.

All the analog outputs were acquired with the architecture sketched in Figure 3.5. Analog/digital conversion is realized with a 16bit resolution modules from Seneca producer (Z-8AI; Z-8NTC). These, via a RS485 Modbus protocol, communicate digital values to the master module Z-GPRS2, that finally send the data stream containing each measured point, to the Lab desktop PC. The monitoring interface is realized though Labview software that,

first interrogates the Z-GPRS2 with a frequency of 0.01 seconds and later averages the 100 collected data every second. The averaged value is then considered the final measurement and plotted real time for the user monitoring. Finally, this is logged with a temporal discretization decided by the user and typically between 10 seconds to 1 minute. Log file are then used to do the post processing, for the evaluation of indirect values and any coefficient performances. Air moisture content has been evaluated starting from the couple of air temperature and RH measurements and the following equation:

$$x = 0.622 \frac{RH\ P_{sat}(T_a)}{P_{atm} - RH\ P_{sat}(T_a)} \quad \left[\frac{kg_{water}}{kg_{dry\ air}}\right] \quad (3.2)$$

where 0.622 is the molecular weight ratio between water vapor (18.02 g mol^{-1}) and dry air (28.97 g mol^{-1}). P_{atm} is the local atmospheric pressure, and P_{sat} is the saturation pressure of water vapor at the temperature T_a(°C), approximated with equation (3.3):

$$P_{sat}(T) = 611.85\ e^{\left(\frac{17.502*T}{240.9+T}\right)} \quad [Pa] \quad (3.3)$$

The amount of adsorbed or released water per each timestep is evaluated as:

$$\Delta m_{H2O} = \frac{\dot{Q}_a}{3600}\ \overline{\rho_a}\ (x_{in} - x_{out})\ \Delta t \quad [kg_{H2O}] \quad (3.4)$$

Where the average air density is the result of the inlet and outlet temperature average and is considered constant during the timestep Δt. The cumulative value of adsorbed/released water between two intervals t_1 and t_2 value is evaluated as:

$$M_{tot}(t) = \sum_{i=t_1}^{t_2} \Delta m_{H2O_i} \quad [kg_{H2O}] \quad (3.5)$$

$$\Delta x = x_{in} - x_{out}; \qquad \Delta T_a = T_{a_{in}} - T_{a_{out}}; \quad (3.6)$$

The average thermal power exchanged between the air and the adsorption heat exchanger, during the timestep Δt is estimated as:

$$P_{th_{\Delta t}} = \overline{\rho_a} \frac{Q_a}{3600} \left[c_p(T_{in} - T_{out}) + R(x_{in} - x_{out})\right] \quad [kW_{th}] \quad (3.7)$$

Where R is the water latent heat (2501 kJ kg^{-1}), and c_p the specific heat of air, considered constant at 1.005 kJ kg^{-1} K^{-1}. Being the data logging discrete over time, and at fixed sampling time, the integral evaluation of energy flows, can be converted in a sum as:

$$E_{cool} = \Delta t \sum_{ADS} P_{th}\,; \quad E_{reg} = \left| \Delta t \sum_{REG} P_{th} \right|; \quad (3.8)$$

Where the two subscripts ADS and REG are referring to adsorption and regeneration phases. The module was used to avoid problems with the sign and to have always a positive number. In any case, is intended that versus of the heat transfer is from air to the ADS-HX for E_{cool}, and the opposite for E_{reg}.

3.2.1 SiO2 packed bed configuration

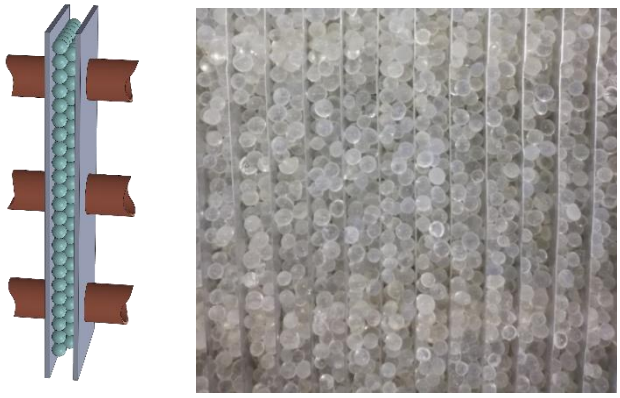

	d	n	p	L	A	B
	[mm]	-	[mm]	[m]	[m]	[m]
Fins	-	90	5	-	0.10	0.48
Tubes	15	24	-	0.45	-	-
Frame	-	-	-	0.74	0.10	0.54

Table 3.4: Characteristic dimensions of the finned coil used for the SiO_2 packed bed configuration.

Figure 3.6: On the left a schematic representation of the packed bed finned coil adsorption heat exchanger. On the right a picture showing the beads of 3 mm diameter, dispersed between the aluminum fins of the heat exchanger.

The packed bed configuration is realized simply pouring SiO_2 beads, with a pseudo-spherical geometry, into the air gap between fins of the finned coil. Then, the beads are enclosed ad blocked with a double mesh grid (fine and flexible; gross and rigid) to avoid the relative movements of the beads. The pouring procedure generates a stochastic distribution, usually called as random close packing (RCP), with a large number of empty interstices between each particle. The air, flowing between these interstices, enters in contact with a huge surface for the mass transfer. The parameter identifying a final configuration is the bed porosity ε, defined as the fraction between the volume of empty space and total available volume. In 1611 Kepler conjectured that in a Euclidean three-dimensional space the highest packing density is achieved with a face-centred cubic packing, consequently the minimum ε is equal to $1 - \pi/(\sqrt{3}/2) \sim 25.95\%$. In recent years Hales [123–125] gave the formal proof for this conjecture and the theoretical demonstration for this number, listed as the 18th of the 24 most important mathematical problems by Hilbert at the begin of the XX century. Anyway, the stochastic feature of the pouring process is affecting the final value and the density limit for hard spheres ore pseudospheres with RCP reduces up to 63.4%, meaning that minimum ε is increased up to 36.6%. A further element influencing the final configuration is the wall effect exerted by the aluminium fins, being the fin path (p) comparable with the beads diameter (d) cannot be neglected. Pistocchini[126] et al. defined an empirical correlation between packing density and the ratio p/d, showing as the final density values can be as much lower as far from the theoretical configuration, with ε up to 0.45. Based on Pistocchini's relation, and with the goal to maximize the beads surface

area, the selection of the coil together with beads diameter was carried out to approach the maximum packing density, according to the available configurations on the market, as reported in Table 3.4. Final values are $p/d \sim 1.67$ and $\varepsilon \sim 0.412$. Given the definition of ε, the surface area for the mass exchange, defined as the total particle surface over the exchanger volume can be estimated with the equation (3.9)

$$surface\ area = 6 * V_n * \frac{1-\varepsilon}{A * B * L * D_{avg}} \sim 2000\ \ [m^2\ m^{-3}] \quad (3.9)$$

Where V_n is the net available volume for the beads (the presence of fins and pipes reduces the total available volume); $A\ B\ L$ respectively the gross width, height and length of the finned coil (excluding frame size of the HX); and D_{avg} the average beads diameter (provided by the manufacturer). This last parameter can cause a considerable uncertainty on the final surface value because the beads are not completely spherical, and the distribution ranges between an equivalent diameter between 2-4 mm, with an average value of three as provided by the manufacturer. With this consideration final value of surface area is close to 2000 m^2 per m^3 of HX gross volume. Aluminum fins, together with copper tubes, generate instead a total surface for the heat transfer equal to 8.64 m^2, that in specific terms is equal to ≈200 m^2 per m^3 of gross volume of the HX.

3.2.2 SAPO34 coated coil configuration

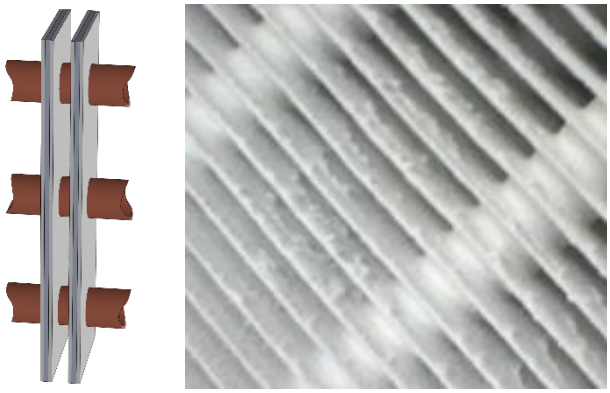

	d	n	p	L	A	B
	mm	-	mm	m	m	m
Fins	-	56	8	0.6	0.15	0.48
Tubes	15	24	-	0.45	-	-
Frame	-	-	-	0.74	0.15	0.54

Table 3.5: Characteristic dimensions of the finned coil used for the SiO_2 packed bed configuration.

Figure 3.7: On the left a schematic representation of the coated finned coil adsorption heat exchanger. On the right a picture showing final result of the coating process.

This configuration has been realized by ITAE-CNR of Messina, coating with zeolite SAPO34 a similar finned coil as the previous one but with bigger fin path. Coating procedure can be synthetically listed as following: *i*) preparation of a liquid SAPO-34/silane solution; *ii*) pretreatment of the heat exchanger surface; *iii*) spraying the coating over the metallic surface; *iv*) final drying and curing. A trifunctional silane compound, the N-propyl-trimethoxy-silane (PM=120.22 g mol^{-1}, ρ=0.88 g ml^{-1}, purity>97%) from Aldrich, was used as adhesive sealant to link the zeolite over the metallic surface. Hydrolysis was performed in presence of distilled water and ethanol (ethanol/water/silane 90/5/5 % v/v) and stirred for 24 h at room temperature. Then the SAPO-34 powder was

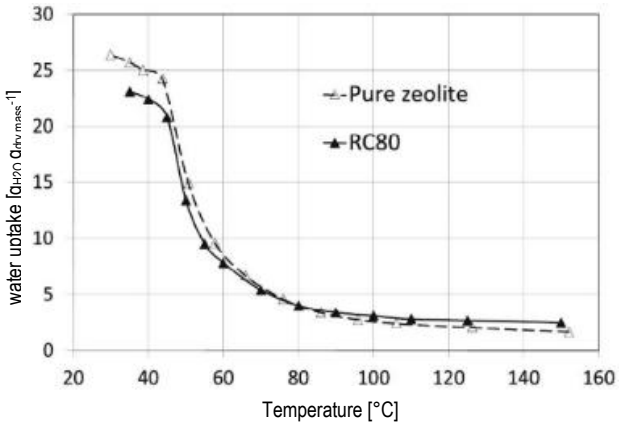

Figure 3.8: Comparison of water uptake between pristine SAPO-34 ad after the coating process, containing only 80% of sorbent on total amount. [83]

added to the silane solution in the ratio of 80-20 % of the weight, and continuously stirred for 15 minutes for to have a homogeneous solution before the spraying procedure. The surface of heat exchanger was degreased in a diluted alkaline solution (0.1 N NaOH), washed in distilled water and finally with acetone. After the first spraying of the silane solution, the sample was cured at 80 °C for 20 min. During the cure, the cross-linking reaction occurs, forming aluminum-siloxane bonds (Metal-O-Si) at the interface, increasing adherence of the silanes to the metallic substrates. Then, a second spray of a silane/zeolite solution was performed followed by a final curing step for 12 h at 80 °C. In Figure 3.7 a detailed view of final result of the coating process and the uniform distribution of the adsorbent over the fin surface [83]. The coating process affected water uptake characteristics, as shown in Figure 3.8. The water uptake of the 80% solution at the different equilibrium temperatures is slightly lower than that of the pure SAPO-34 sample at low temperature and higher for temperatures higher than 100°C. This result was expected as the adsorbent coating formulation consists of 80 wt.% of active material (the adsorbent itself) and 20% of binder solution, which can be considered as an inert mass in terms of water vapor adsorption. Moreover, repeated ad/desorption tests demonstrated that the water adsorption process is completely reversible and hysteresis phenomena are absent[83]. With the similar approach of the previous configuration, it is interesting to calculate also here the surface of respectively thermal and mass transfer. Here, being a thin coating over a flat surface, the ratio between the two contact-surface type is close to one and equal to 8.064 m^2, that in specific terms reaches a final value of 186.7 m^2 per m^3 of heat exchanger. Close to an order of magnitude lower than the previous configuration.

3.3 Experimental results

3.3.1 Pressure drop

The analysis of pressure drops on the air side of the ADS-HX is of fundamental importance. This, together with the pressured drops caused by the water circulation, are the only sources of mechanical energy degradation and, then, of electric power requirements. The focus was only on the air side being the two configurations practically equal from the water point of view (except for the different length of the coils), instead very different on the air point of view. The way in which the sorbent has been arranged over the metallic structure indeed affected the total value of surface area between air and sorbent of 1 order of magnitude.

Pressure drops characterization has been carried out measuring the difference of the static pressure between the inlet and outlet while the air was flowing and at volumetric rates (100-700 $m^3\ h^{-1}$). Pressure drops of Zeo-

SAPO34 ADS-HX are registered out of the average over 10 successive measurements, of 1 minute each one, and after the stabilization of the flow rate between each step of the total range. Moreover, also the dependency of air pressure drop from the stream temperature has been investigated, repeating this testing procedure at different air inlet temperature between 10-35°C, covering an extensive range of possible operative ambient temperatures. The air flow rate is varied changing the speed of the fan in the AHU, adjusting the frequency of the electric motor with a controlling inverter, and regulating the rotational speed between the 10 and 100% of the full speed. Finally, the flow rate is measured using the calibrated flanges and the pressure transducers, generating respectively a measurement error on the volumetric air flow rate of ±7%, and ±0.2 Pa on the static pressure measurements. Measured values are reported in tables of the Annex-A, and in Figure 9 are compared with the SiO_2 packed bed configuration , with the same configuration and methodology[127].

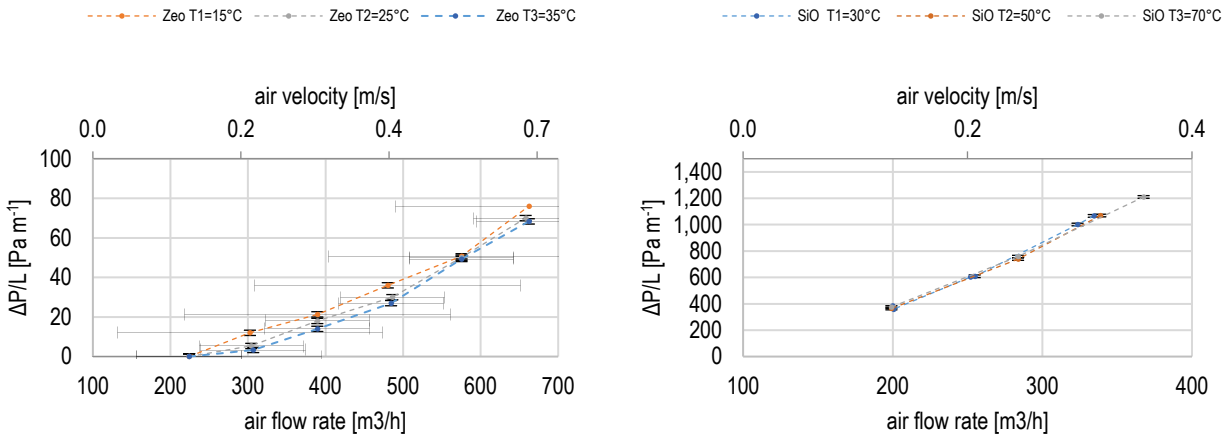

Figure 3.9: Comparison of air pressure drops measurements between the Zeo-SAPO34 coating configuration (left) and the SiO_2 packed bed configuration (right).

The huge difference between the surface area of the two configuration is evident also in terms of manometric characteristics. Indeed, as it changes of 1 order of magnitude, the same ratio is on measured pressure drops at fixed stream velocity. Temperature dependency is explicit using the Darcy-Weisbach empirical relationship between the pressure losses and the friction factor f_D:

$$\frac{\Delta P}{L} = f_D \frac{\rho_{air}}{D} \frac{v^2}{2} \quad \left[\frac{Pa}{m}\right] \quad (3.10)$$

Where the air density is evaluated with the correlation

$$\rho_T = 1.293 \frac{P_b}{P_0} \left(\frac{273.15}{273.15 + T[°C]}\right) \quad \left[\frac{kg}{m^3}\right] \quad (3.11)$$

P_0 is the atmospheric pressure at the sea e level and equal to 1.013 mbar. Instead P_b is the local barometric pressure, evaluated for the city of Turin (elevation over the sea level H=239 m) with the following relation:

$$P_b = -0.1125 * H + 1011.5 \quad [mbar] \quad (3.12)$$

The increase of air temperature leads to a reduction of the density, and consequently a proportional reduction of pressure drops at equal velocity. The 20°C temperature increase generate a pressure drop reduction between 10-35%, within the analyzed velocity range.

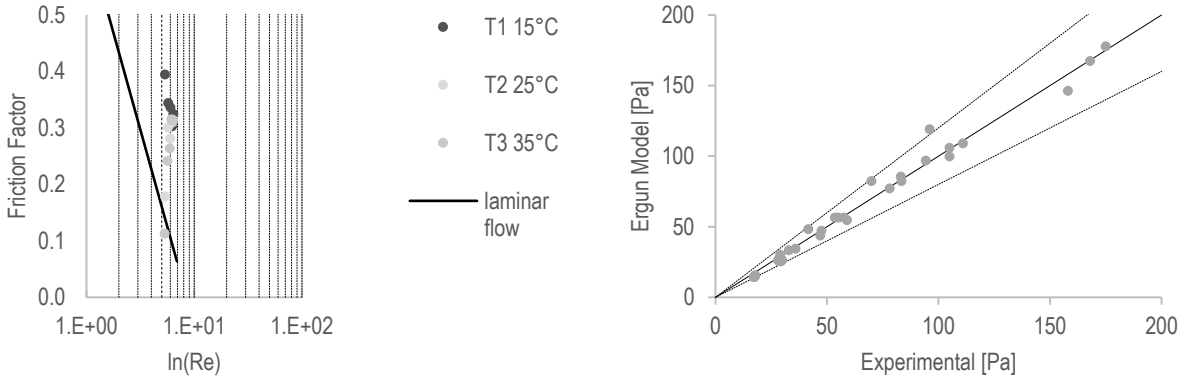

Figure 3.10: Graphical representation of experimental data on the moody diagram f_D-ln(Re), and comparison with the general formula for cylindrical smooth pipes with laminar flow (left). Calibration of pressure losses experimental data of SiO_2 packed bed against Ergun model.

Experimental value of the f_D are generally higher if compared with the theoretical values of circular ducts and laminar flow, $64/Re$, as in the graph of the left in Figure 3.10. This check is useful to verify the consistency of measured values being very low, and comparable to natural buoyancy regimes. Anyway, the flow cannot be considered totally laminar with a full developed parabolic velocity profile: the entrance losses and the relative small length of the reference channel don't allow the full development of the laminar flow that, in addiction, has to deal with a rectangular shape and not cylindrical (fin path of 6 mm considering the coating thickness of 1 mm per side, and a length of 15 cm). All these conditions justify f_D values higher than theoretical laminar flow, and an average over the different experimental tests of 0.29. On the right of Figure 3.10 is instead demonstrated how the Ergun model [128] is a suitable mathematical instrument for the evaluation of pressure drops in packed bed configurations, also when the RCP configuration includes considerable wall effects, increase the distance between the reality and a theoretical configuration of the Ergun model with the equation (3.13)[127].

$$\frac{\Delta P_{ERGUN}}{L} = \left(150\ \frac{1-\varepsilon}{Re} + 1.75\right)\left(\frac{1-\varepsilon}{\rho_a D_p \varepsilon^3}\right)(v\ \rho)^2 \quad \left[\frac{Pa}{m}\right] \quad (3.13)$$

Where the characteristic length for the evaluation of the Reynolds number considers the spherical particle of diameter D_p (3 mm in our configuration), and v is the mean velocity considered constant through the entire path and evaluated starting from the entire volumetric flow rate Q and the gross cross section of the heat exchanger, excluding frames. Despite these hypotheses, the error range within the interval of ±20%, in the experienced velocity range of 0.2-0.8 m s^{-1}.

3.3.2 Zeolite functioning with Hybrid ventilation

In this section are provided results on dehumidification performances of the Zeolite configuration tested in hybrid ventilation mode[83]. The term "hybrid" is referring to the mechanical aspects of the air motion. Indeed, despite the air flow for this system is mechanically driven with a fan, there's an important contribution on the total air flow rate, generated by the natural buoyance induced by the temperature difference between the air and the sorbent. The temperature difference, especially during regeneration, generates an air motion of up to 100 m^3h^{-1} [83]. The air temperature and relative humidity were monitored at both inlet and outlet conditions at increasing air flow rate. The AHU treats the external air in order to obtain air streams of typical summer conditions of hot and humid climates (T>31°C; RH>60%). The adsorption tests were carried out in the velocity range of 0.3-1.6 m s^{-1}, corresponding to an air flow rate of 150-800 m^3h^{-1}. Each of the adsorption tests was preceded by a regeneration of the zeolite coating, flowing hot water in the range of 80-90°C, for a period of time higher than 30 minutes. Testing conditions are recapped in Annex B in the tables B1 and B2, for both the regeneration and adsorption conditions of the inlet flow. Adsorption tests were carried out for more than 80 minutes, but in most of the case the dehumidification is not effective after only 30 minutes, as shown in the left graph of Figure 3.11, where all the dehumidification results are collected over the functioning time. The graph on the right shows instead the effect of the increase of air flow rate on the Δx, focusing on three different tests, respectively the #2, #12, #22, with similar inlet conditions (31-33°C and 65-75%) and an air flow rate of 210, 405 and 685 m^3 h^{-1}.

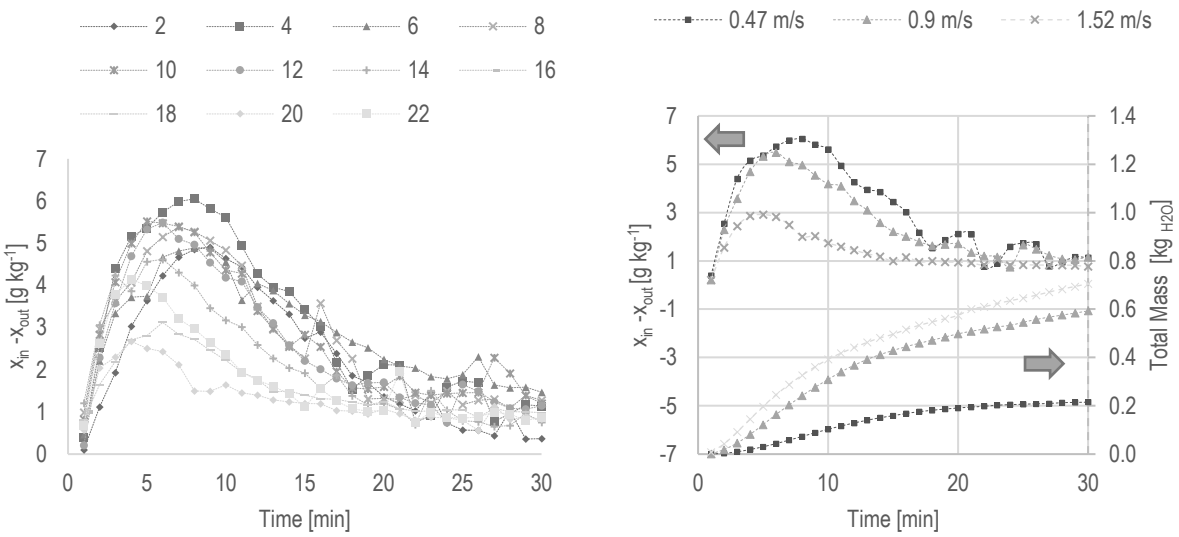

Figure 3.11: On the left the collection of all the dehumidification tests from #2-24. On the right only three tests have been selected #2, #12, #22, comparing the effect of stream velocity on the Δx and total adsorbed water. The selection has similar inlet conditions.

In general from both the two graphs is evident the typical shape of the adsorption transient, with three distinct phases: *i*) a rapid increase for the first 5-8 minutes; *ii*) a peak plateau between 8-12; *iii*) the decreasing phases. The first one is related to the presence of residual sensible heat from the previous regeneration. Indeed, the material is still hot and the gradual cooling (from 80°C to values lower than 50°C) is resulting in the increase of

the dehumidification rate, as the equilibrium uptake is moving towards favorable temperatures. In the second phase the benefits coming from the temperature reduction have reached the maximum potential, and the competition with the rising heat generation from the adsorption process, stabilize the dehumidification rate. Gradually the available sites for adsorption decreases, as the material saturation, reducing the dehumidification rate and becoming negligible after 30 minutes. Increasing the air flow rate, increases the convective cooling accelerating the first phase. Indeed, the peak time for the three curves shift progressively down at 8, 6 and 4 minutes after the begin of the test. At the same time, increasing the air velocity reduces the contact time, and the total dehumidification realized through the fin (0.15cm) is shifted down. If this is true in specific terms, from the total removed water mass the behaviour is the opposite. Indeed, on the bottom the three curves show as increasing the total flow rate leads to faster total water removal, especially for the first step when the air velocity is increased from 0.36 to 0.9 m s^{-1}. The further increase of air velocity reduces the incremental benefits of convective cooling, reducing the gain on the total removed water mass.

The analysis of thermal power exchanged between the air and the adsorption heat exchanger highlights the relevant contribution of the heat balance once both the residual and the adsorption heat are considered. As shown in Figure 3.12 during adsorption the two terms composing the total exchanged power, sensible and latent components, having an opposite sign, are in competition. Despite the latent part reach peaks value of 2 kW, and an average of 1 kW for the first 15 minutes, the increase of temperature, basically makes null this contribution for the total cooling power.

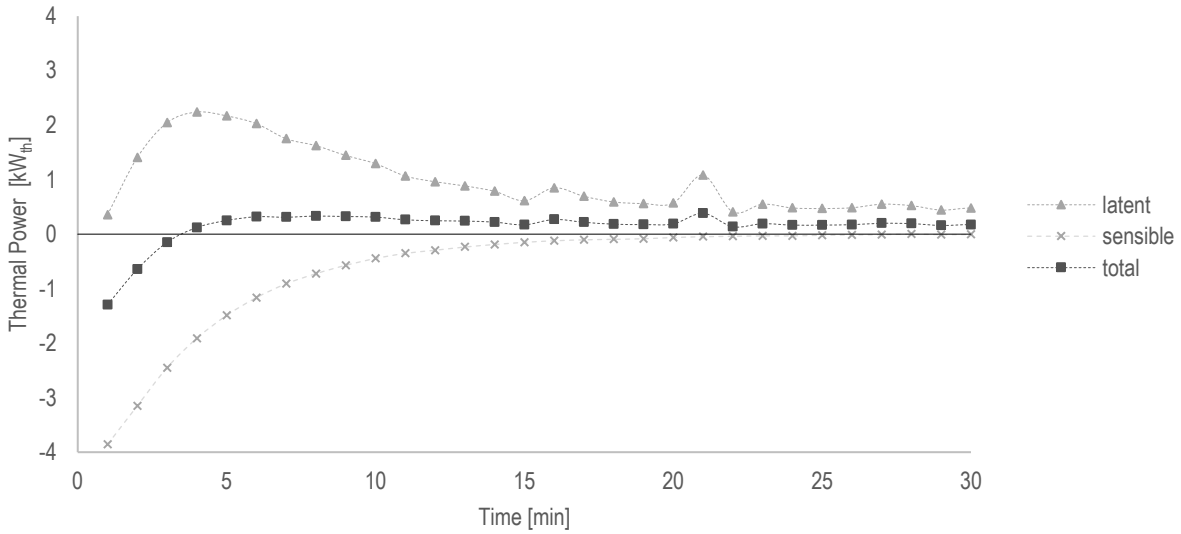

Figure 3.12. Behaviour of the two components composing the total power exchanged between the air stream and the zeolite adsorption heat exchanger. Data are related to the test #22, characterized by the highest value of P_{th} among the 24 tests carried out and reported in the Annex B.

Thermal power in y axis of figure 3.12 is the composition of latent and sensible contributions to the thermal power exchanged between the air and the ADS-HX, evaluated as in equation 3.7:

$$P_{th_{\Delta t}} = \overline{\rho_a}\frac{Q_a}{3600}\left[c_p(T_{in} - T_{out}) + R(x_{in} - x_{out})\right] \quad [kW_{th}] \quad (3.7)$$

Where signs of the inlet/outlet temperature difference and moisture content difference drive the global sign of the exchanged power. According to equation 3.7, when outlet temperature is higher than inlet the sensible term is negative (and viceversa). Instead, the latent part is positive during dehumidification and negative during regeneration. During dehumidification (latent positive), the heat generated through adsorption increases the temperature of the air (sensible is negative). Further on, being just finished the regeneration, the sorbent has higher temperature then air (residual heat), increasing the negative contribution to the sensible part. During the first 5 minutes the total thermal power exchanged between air and the ADS-HX is slightly negative. The stabilization of the sorbent temperature reduces contribution of the residual heat, and after 5 minutes the exchanged power is slightly positive (meaning cooling).

These experiments shown that rejection of heat during adsorption phase is a mandatory step to have effective contribution on the air treatment for ventilation, as explained in the successive paragraph.

3.3.3 Direct dehumidification and cooling

Testing procedure was modified to introduce the possibility of rejecting the heat during the adsorption phase, obtaining results that can be compared with the previous experience. The switching between the two water loops, hot and cold, is done by operating paired valves as mentioned in the setup description. The operations were performed with the temporal order as listed in the following bullet points:

- AHU inverter is regulated adjusting fan speed in order to provide the required air flow rate, as the previous tests;
- The adsorption phase begins, air flows through channel of the adsorption heat exchanger, and cold water from the network flows through the coil.
- After a priori determined time the operational is switched to regeneration. The electric valves V1 and V2 switches modifying the water circulation. Now hot water is flowing from the boiler trough the coils.
- This stage continues until the quasi-complete regeneration is obtained.

The comparative procedure was carried out also for the silica gel configuration. During the entire transient, air temperature (T_a), relative humidity (RH), water temperature (T_w), air flow rate (Q_a) and water flow rate (m_w) have been constantly measured at the inlet and outlet and logged with the architecture described before.

Figure 3.13 compares two tests on the SAPO34 ADS-HX, highlighting the difference between a not cooled and a cooled adsorption phase in terms of dehumidification and temperature difference. The reference inlet conditions are an air flow rate of ~320 m^3h^{-1} at 31.9°C and 69%, while the cooling temperature ~18°C. The behaviour during the transient didn't change the intrinsic shape but modified the absolute values. During the initial transient (t<10min) the heat rejection operated the highest benefits, anticipating the peak and intensifying the tilt of the Δx increment.

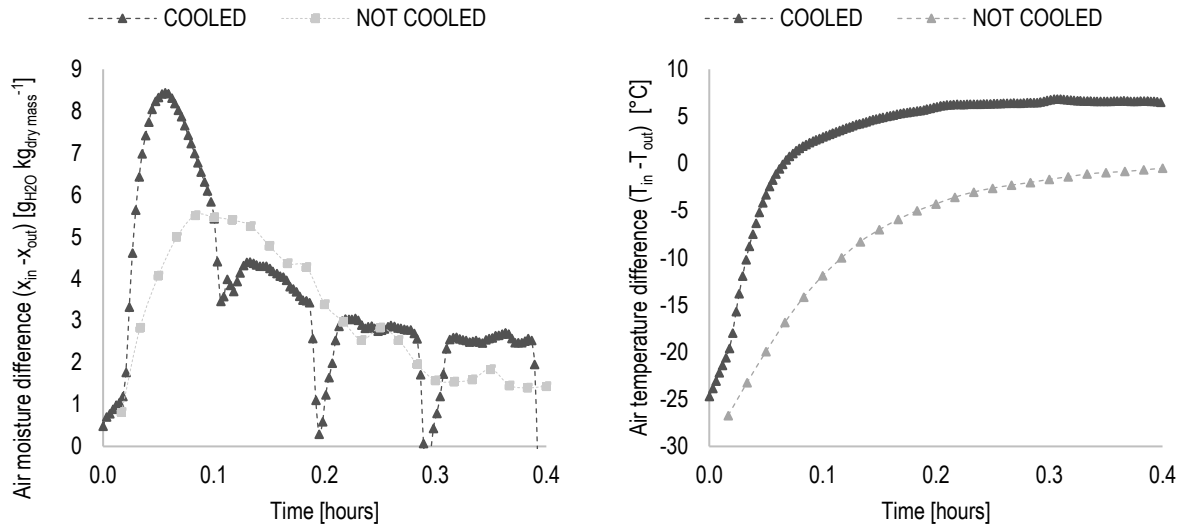

Figure 3.13: Comparison of two operational adsorption mode on the SAPO34-ADS HX: cooled adsorption versus adiabatic adsorption. On the left the graph compares the transient over time of the difference of air moisture content between inlet and outlet (positive values mean dehumidification). On the right the graph compares the transient over time of the air temperature difference between inlet and outlet (positive values means air sensible cooling, while positive values mean air sensible cooling.

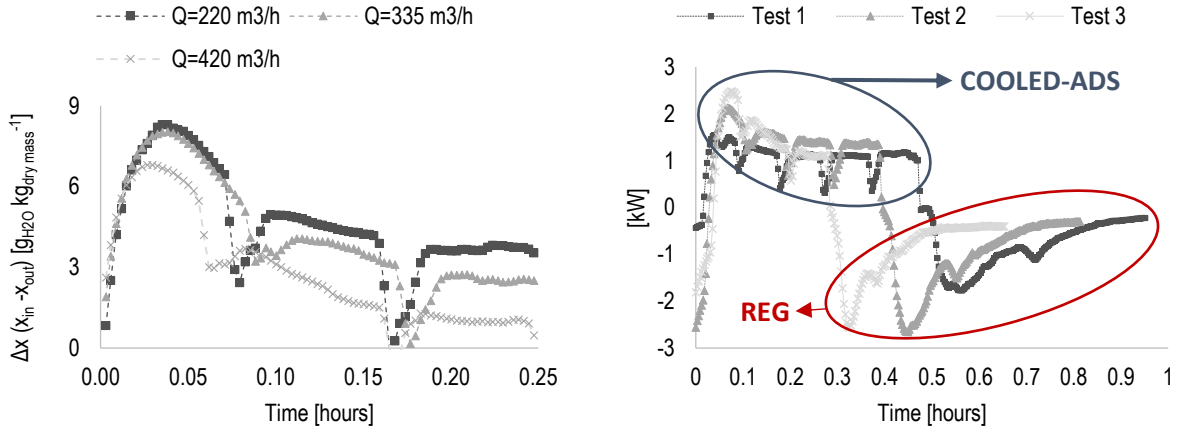

Figure 3.14: Effects of the air flow rate increase on air dehumidification (left) during cooled adsorption tests, Cool-1, Cool-2 and Cool3. On the right the thermal power exchanged between the air and the SAPO34 ADS-HX during both the adsorption and regeneration of the three tests.

Test		Time	Q	$T_{a\,in}$	RH_{in}	T_w
#	-	min	$m^3\,h^{-1}$	°C	%	°C
Cool-1	ads	27	196.2	31.9	68.4	18.1
	reg	29	61.4	28.7	48	61.5
Cool-2	ads	23	331.1	30.3	62	18.6
	reg	25	67	29.7	30.5	63.1
Cool-3	ads	15	412.7	30	58.3	20.5
	reg	22	83	29.8	27.4	62.7

Table 3.6

Maximum value increased of 55% and obtained in half of the initial time, further higher Δx are also obtained in the stabilization phase occurring after 15 minutes after the begin of the adsorption test. The most important

aspect is also that this time the air temperature is reducing, as showed in the graph on the right of the Figure 13, with a reduction of the outlet temperature in respect to inlet stabilized at 5°C. Realizing directly and at the same time a dehumidification of 6-9 g/kg and sensible cooling of the air, with a temperature difference of only 5 °C, instead of minimum of 15°C as required in the case of a typical dew condensation, with the same dehumidification rate. As done before, the influence of air flow rate has been investigated in terms of both dehumidification and absorbed thermal power. This time the inlet humidity was reduced to an average value between 15-20 g kg^{-1} (Table 3.6) to avoid the risk of an eventual condensation, invalidating the experiments. Increasing air flow rate among the three tests cool-1, 2 and 3 and similar air inlet conditions resulted in a reduction of the air dehumidification curve (Figure 3.14) similar to what observed in the previous paragraph. Maximum value is reduced from more than 9 to 6.5 g/kg, and an increase of the slope of the curve, as seen in Figure 3.14. As before, the higher air stream velocities on the coil, increase the number of interactions between water vapor molecules and the sorbent, leading to a faster saturation of the material and then to a progressive reduction of the duration of the adsorption phase, from 30 to around 20 minutes. These behaviours are depicted and summarized in the graph on the right of Figure 3.14, in which the total thermal power (latent plus sensible) exchanged between air and the adsorption heat exchanger is showed.

3.3.4 Comparison between the packed bed and coated coil configuration

Basing on the same approach and testing methodology of the previous paragraph, in this section a comparison between the two configurations, SiO_2 packed bed and SAPO34 coating is performed using the same performance indicators, Δx, ΔT and exchanged thermal power, with an inlet stream as reported in Table 3.6. Despite there's a slight difference in terms of inlet temperature, vapor pressure were similar as the inlet moisture content and the dew point, around 3250 Pa, 16 g kg^{-1} and 22°C. Adsorption was carried out cooling down the coil with at 18-19°C, while the average inlet temperature during regeneration was 61-62°C, in both cases.

	$T_{a_{in}}$	RH_{in}	x_{in}	T_{dew}	$T_{w_{in_{ADS}}}$	$T_{w_{in_{REG}}}$	$\dot{Q}_{a_{ADS}}$	$\dot{Q}_{a_{RIG}}$	$\dot{m}_{w_{ADS}}$	$\dot{m}_{w_{RIG}}$
	°C	%	g kg^{-1}	°C	°C	°C	m^3 h^{-1}	m^3 h^{-1}	L min^{-1}	L min^{-1}
Zeo	31.9	68.4	19.6	25.4	18.1	61.5	195.9	52.9	21.7	1.0
SiO	36.3	56.1	20.6	26.2	18.5	61.8	152.3	147.1	22.3	2.6

Table 3.6: Average inlet condition of air and water flows during both the two tests.

In Figure 3.15 are reported results of both the two configurations, respectively the zeolite on the left and silica on the right, together with the inlet water temperature $T_{w\,in}$ for the entire adsorption and regeneration cycle.
As result of the different design concept (packed bed versus coating) one large difference is on the water and air flowrates, in particular during the regeneration. Anyhow, in these systems the conditions for the adsorption and regeneration are indeed more dependent from temperature values than air velocity. The function of the air flow is reduced with respect to the adiabatic case: it provides the sufficient ventilation for the mechanical removal of released water vapor during the regeneration; during the adsorption phases it provides water vapor for the

sorbent. In the zeolite case, the contact surfaces between air/sorbent and sorbent/thermal support are basically equal. During the regeneration the heat for desorption is directly transferred to the sorbent mean from hot water through the metallic media (the same is for the removal of adsorption heat). The most important consequence of that is the possibility to operate the two stages, the one adsorbing and the one desorbing water, at very different air flow rates, preserving anyway the water removal rate, and obtaining similar time durations for both adsorption and regeneration. For example, measured air flow rate for the coating case (reported on left graph of Figure 3.16) was respectively 196 and 41 $m^3 h^{-1}$ during adsorption/regeneration.

For the packed bed configuration, the sorbent/thermal support contact is many times lower than the air/sorbent contact area, and the mechanism for the regeneration is different. Indeed, the thermal transfer is still mainly provided firstly through the convective transfer between the air and the fin, and successively between the air and the sorbent. This means that during the regeneration stage, an eventual reduction of the air flow will reduce the total amount of heat provided to the sorbent, and the regeneration will be slower. Eventually the process is still inherently iso-enthalpic, but the concomitant drop or increment of temperature due to the exo/endothermic behaviour of the transformation is continuously counter balanced with the fin thermal exchange, following the behaviour of a typical inter refrigerated or heated transformation. Hence, for packed bed configuration, a similar timing between the adsorption and regeneration stage (see the graph on the right of Figure 3.15) is achievable only providing an average constant air flow rate during both phases, respectively 152 and 147 $m^3 h^{-1}$.

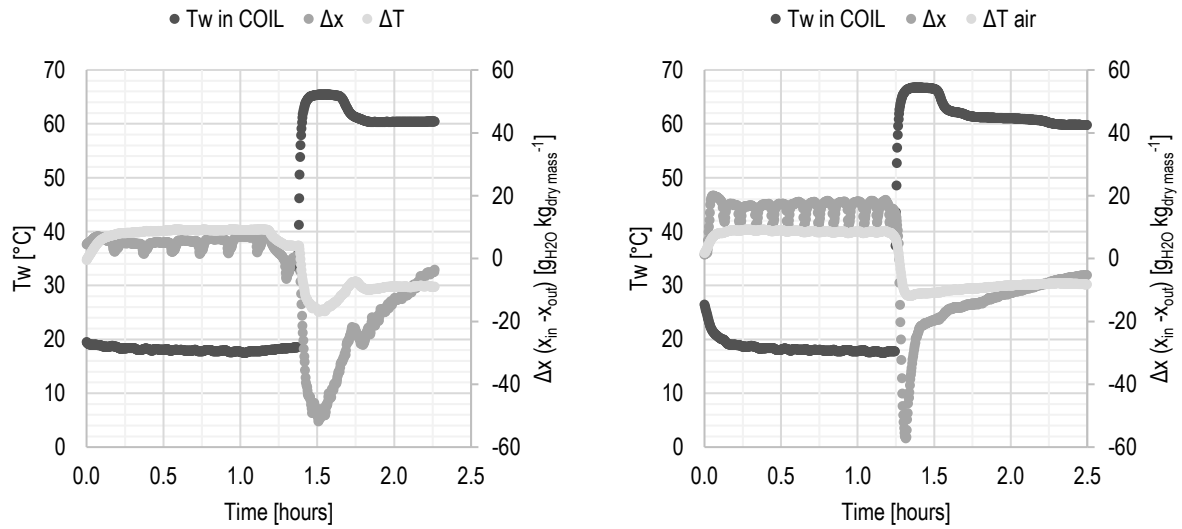

Figure 3.15: A complete Adsorption/Regeneration cycle thermally drive by cold/water circulation. On the left the cycle performed on the zeolite configuration, on the right the cycle performed on the silica configuration. Temperature of the water at the inlet of the coil, ,the difference in terms of moisture content between the inlet and outlet,and the air temperature difference between inlet and outlet are depicted to show physical transformation on air. The first half part is the adsorption phase; the second part is the regeneration phase.

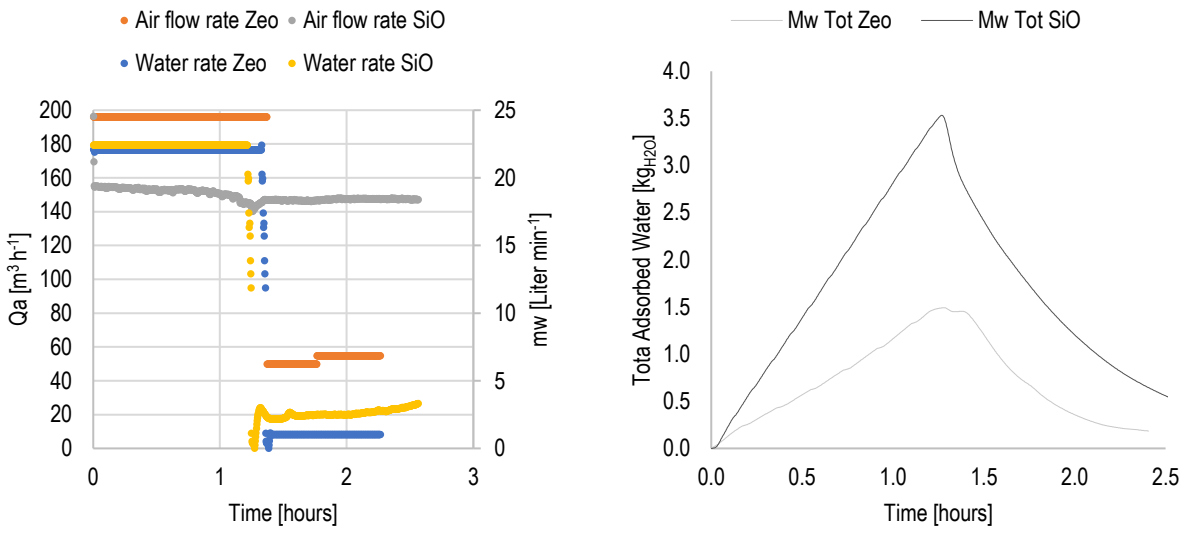

Figure 3.16 On the left the air and water flow rate on the silica and zeolite adsorption heat exchanger. On the right the evaluation of the total adsorbed mass through an entire cycle of adsorption/regeneration on both configuration, based on the balance of the inlet/outlet thermo-hygrometric conditions and the respective air flow rate.

A slight difference occurred also on water circulation during regeneration. Indeed, the fin length in the zeolite configuration is higher, being 15 cm against 10 cm. Water pressure drops measurements provided by the producer are 0.48 and 0.33 kPa, with a water velocity of 0.18 m s^{-1}. If during the adsorption, the cold water flow provided by the water network is not affected by the different pressure drops (a constant value of 22 L min^{-1}), during regeneration the fixed power of the water pump resulted in a reduction of water circulation when the circuit is switched from the silica finned coil to the zeolite one (2.6 against 1 L min^{-1}).The behaviour of Δx, as showed in Figure 3.15, is disturbed by the management of the humidifier that, to preserve a constant salinity to avoid the fouling of the steam generator, drives washing cycle of the water tank approximately every 10 minutes, reducing the total amount of produced steam, and then the inlet moisture content. In the zeolite configuration the outlet moisture content changes more rapidly in accordance with the inlet disturbance respect of the packed bed, where the bigger amount of sorbent mass creates a buffer for any type of inlet oscillation. As a result, Δx perturbations in the packed bed are more intense than in the other configuration. Anyway, despite the disturbance, the average Δx was pretty constant during the entire adsorption phase, with a mean value of 6-7 g kg^{-1} for the zeolite and around 16 g kg^{-1} for the silica, while the average ΔT was respectively 8.2 and 8.4 °C, for 82 and 74 minutes.

During regeneration the Δx has a different transient: Δx value becomes negative being the mass transfer inverted (from the sorbent to air) and the outlet moisture higher than inlet. At the same way the temperature difference follows this behaviour. Just after the thermal switch, Δx reaches rapidly a very high peak, -51 and -57 g kg^{-1} respectively for zeolite and silica, reducing progressively as the reduction of the water mass contained in the sorbent (as showed in the right graph of Figure 3.16). The value becomes negligible approximately after 62 and 79 minutes from the beginning of the regeneration.

The estimation of the water adsorbed mass shows that the mass transfer phenomena on the packed bed configurations are much higher than on the coated coil configuration. At the end of the adsorption stage the total adsorbed mass was 3.5 kg, 2.3 times higher than the case with zeolite. Further, despite we considered the test finished after 2.5 hours, because the Δx was negligible, in reality the residual water mass at this time shows as a certain amount of water is still contained in the porosity of the material, precisely 0.5 kg and 0.25 kg for the silica and the zeolite respectively.

It is interesting to analyze and compare performances for the two configurations also in terms of total cooling power realized on air, the total absorbed power for regeneration, and coefficients of performance.

In Figure 17 is reported the instantaneous value of thermal power exchanged between the air and the adsorption heat exchanger.

The disturbance generated by the humidifier on the air stream at the input of both adsorption heat exchangers is clearly visible also on the estimated power. Comparing the two configurations, as in the graph on the left, underlines the different power density of the two components. In the average during the phase of dehumidification and cooling the exchanged power was 2.4 kW for the packed bed, 1.9 times higher than the other configuration, with a similar ratio observed during the regeneration phase. Decoupling the sensible part from the latent one is possible by splitting the ΔT from the Δx proportional items. Clearly these are mostly devoted to work on the latent part, as showed in the graph on the right where the total delivered cooling and absorbed energy, and the relative distribution has been estimated computing the integral over the respective periods.

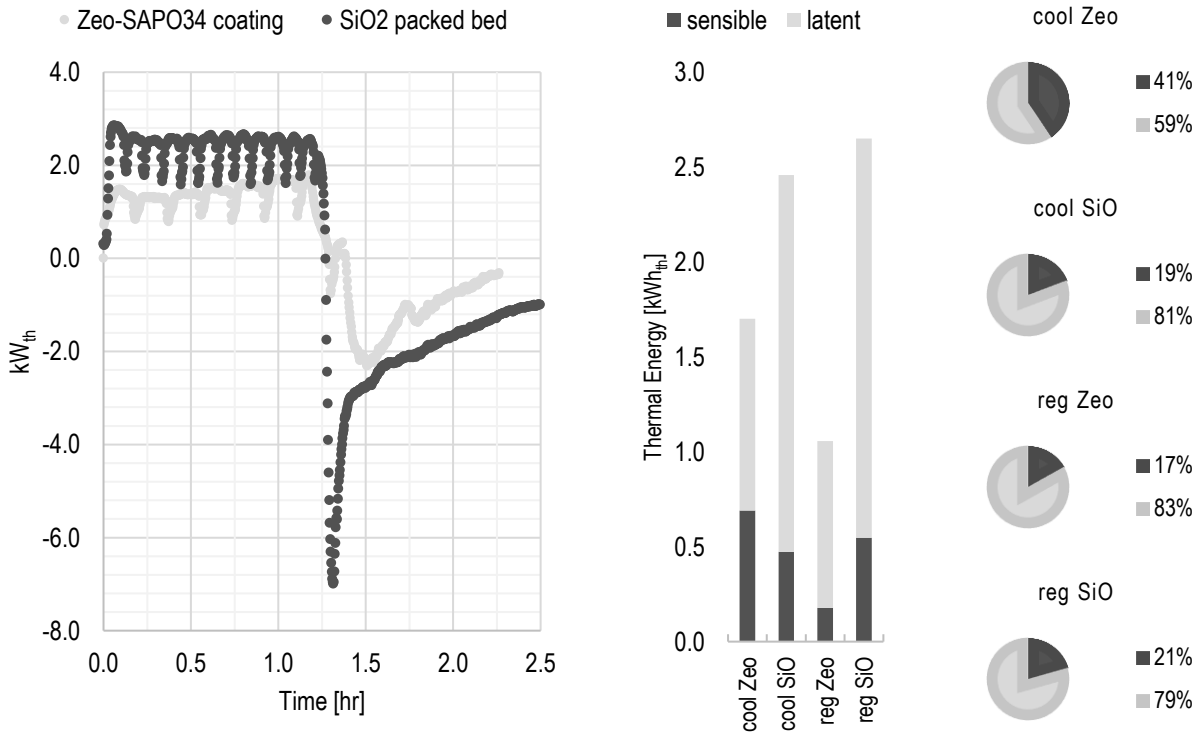

Figure 3.17. Thermal power and exchanged between air and the adsorption heat exchanger during the two tests.

In the packed bed configuration, the sensible part is 19-21% of total in both working modes, adsorption and regeneration. In the other instead, is evident an influence of the reduction of air flow rate, reducing the sensible part from 41% during the adsorption, to 17 in regeneration mode. This behaviour should be considered, in general, as an improvement and a good rule for control strategy. Indeed, if during the adsorption the sensible cooling is positive because provides delivery condition to the indoor environment at lower temperature, for the regeneration is the opposite. The sensible part in this case is just heat absorbed from the primary driving source, and then irreversibly rejected to the external environment. The lower it is, the better the efficiency would be.

The performance analysis needs to consider also specific performance indicators, such as the Energy Efficiency Ratio (EER) for the electrical point of view, and the Coefficient Of Performances (COP_{th}) for the thermal point of view. This evaluation has been done on the energy and not on power, because the different thermal and electrical flows are not simultaneous for both adsorption and regeneration. EER considers the entire cooling energy delivered during ADS, and the entire electrical energy in both ADS and REG, as:

$$EER = \frac{\Delta t \sum_{ADS} P_{th}}{\Delta t \sum_{ADS} P_{el_{PUMP}} + \Delta t \sum_{REG} P_{el_{PUMP}} + \Delta t \sum_{REG} P_{el_{FAN}} + \Delta t \sum_{REG} P_{el_{FAN}}} \quad (3.14)$$

$$COP_{th} = \frac{\int_{ADS_{in}}^{ADS_{fin}} (\dot{m}_a * R * (x_{inlet} - x_{outlet}))dt}{\int_{REG_{in}}^{REG_{fin}} (\dot{m}_w * c_{p_w} * (T_{w_{inlet}} - T_{w_{outlet}}))dt} \quad (3.14a)$$

Electrical power for water and air circulation were not directly measured. For the water pump was estimated considering, in a conservative way, the maximum power absorbed by the pump (P_{PUMP}=60W_{el}) constant for the entire process. The estimation of the power for the air circulation can be more precise, starting from the measured value of air flow rate, and related pressure drops, validated respectively with the Darcy-Weisbach model (average f_D=0.29) for the coating configuration, and the Ergun model for the packed bed.

$$P_{el_{FAN}} = \frac{\dot{Q}_a \, \Delta P}{3600 \, \eta_1 \, \eta_2} \quad (3.15)$$

Where the two efficiency considers respectively the electrical and transmission efficiency of the motor ($\eta_1 = 0.7$) and the mechanical conversion of pressure in motion ($\eta_2 = 0.5$).

The coating configuration, despite the lower power exchange, shows both higher EER (27 against 22) and COP than packed bed (1.6 against 1.2).

Despite these values are very high, and very encouraging for the use of this type of system for the environmental control of the indoor volumes, a final consideration is needed about the free use of the “cold source”. Indeed, this computation considers the heat rejection during the adsorption as free, and is not included both in the definition of EER and COP. There could be some cases in which this is true, such as the use of cold geothermal sources and/or efficient evaporative cooling systems. In this case the additional cost would be only on the water

pumping that, at the end, will not change significantly final values. For all the other cases the necessity of a refrigeration unit, based on the use of inverse cycle would be to be considered.

Conclusion

The experiments presented in this paper explored the feasibility of operating a fixed sorption bed for air dehumidification and cooling. Tested sorption beds are based on air/water finned coil heat exchanger, with two sorbent configurations: coated with a surface thin layer of Zeolite SAPO-34; a packed bed filled with silica beads of 3 mm. A flow of hot/cold water in the coil activates the two phases of non-adiabatic adsorption and regeneration. Cold water at 18°C is used to refrigerate the adsorption process to combine a conjugated dehumidification and cooling, providing a direct process that doesn't require to reach dew points temperatures. This enables the use of chilled water at higher temperature than in standard air conditioning systems, increasing the efficiency of cold sources.

Regeneration is driven at relative low temperature and compatible with solar thermal systems at low temperature.

Different configurations offer different properties: a massive sorbent configuration gives higher latent cooling power, but the increase of surface area for the mass transfer increases the power consumptions needed to overcome air pressure drop through the ADS-HX. Conversely, a coated coil configuration is more responsive, but reaches saturation conditions faster, requiring lower switching times between the regeneration and the adsorption.

In both cases, the power consumptions were substantially low if compared with the cooling power exchanged with the process air stream and as a result the demonstrated Coefficient of Performances (electric) has reached numbers as higher than 20

4. ATMOSPHERIC WATER HARVESTING

Abstract

The interesting outcome of regeneration tests reported in chapter 3, is the possibility to generate very high and consistent peaks of humidity, overcoming values of 60 g kg^{-1}, and dew points much higher then 40°C. The exploitation of this phenomenon led to the second investigated application: the Atmospheric Water Harvesting. The fundamental principle behind this application is that if the dew point of the hot and humid stream resulted from the regeneration is sufficiently higher then ambient temperature, considerable amount of water can be tapped out of the air without the use of any refrigeration system. This approach reduces drastically energy demand and ca be a potential solution for regions with drought problems and in which the problem of access to freshwater resources is a limiting factor for the economic and social development.

This study demonstrates the possibility of the effective use of the most spread renewable sources for water production: the water vapor atmosphere as primary source of water and the sun as primary source of energy.

A water harvesting prototype built and tested in the Lab demonstrated how also the inexpensive and less performing silica gel can be used if combined with an efficient cycle. Lab environmental conditions reproduced hot and arid climates (dew point below 10°C and ambient temperature above 30°C), demonstrating that water can be extracted from silica gel at a regeneration temperature of 57°C and condensed at ambient temperature with high thermal efficiencies and using solar grade thermal energy. The adopted solution is compared also with different studies at prototype level, aiming to solve the problem mostly with improvement on the material side, showing as an effective cycle led to comparable and even improved performances, in the same operational range. Experimental results demonstrated that the performance of the device reduces as the water uptake reduces and the severity of the climatic environment. In particular, the latter has a considerable effect on the first four hours of operation. This analysis has been carried out with help of some performance indicators, investigating on water production capacity and energy performances. Further on, a 1d numerical model of the packed bed ADS-HX used in this application has been developed based on different solution adopted in literature and checked with experimental data to demonstrate its accuracy. This model can be a useful tool for the design ADS-HX, or for the assessment of performances at different climatic conditions. The thermal energy required is comparable with the typical output of a solar thermal collector: a daily production of up to 2 L/day per square meter of the solar field is achievable with regeneration temperatures below 60°C, ambient temperature up to 35°C, and a consumption of thermal energy between 1-3 kWh per liter of harvested water.

Keywords: AWG; thermal cycle; low regeneration temperature; liter scale prototype;

Scientific contribution of the author on this topic is:

"Water Production from the Atmosphere in Arid Climates using Low Grade Solar Heat"

Gentile, V., M. Simonetti, P. Finocchiaro, and G. V. Fracastoro (2017). Paper presented at the ISES Solar World Congress 2017 - IEA SHC International Conference on Solar Heating and Cooling for Buildings and Industry 2017, Proceedings, pages 984-995.

doi:10.18086/swc.2017.17.02

“Method for production of water from air based on low-temperature heat, and machine and system thereof”

Gentile, V., Simonetti, M., Fracastoro, G.V. (2017). PCT Int Appl WO 2019/082000A1.

4.1 Topic Introduction

Water is the essential component for living organisms, society, agriculture and industrial processes. As a matter of fact, the amount of water consumed per day by an individual can easily exceed 100 L in developed countries. On the other hand water is the basic ingredient for production of essential consumed products, and its exploitation is very intensive: 30 g of bread require as much as 40 L of water, taking into account the whole production chain[129],[130]. Recent studies predict that the anticipated economic growth of developing countries combined with the uncontrolled increase of population worldwide will exacerbate stress on the natural cycle of water [131]. Indeed, we are currently intensively exploiting easily available surface and groundwater to satisfy all our needs in freshwater [132]. This is evidently not a sustainable path to follow as it has already shown its limits in the form of extreme drought situations accompanied with severe societal, economical, and political crises across the world[133–135].

To address the continuously growing water stress phenomenon throughout the world, research in academia and industry has been investing large amounts of resources into new technologies for more efficient processes for reclaimed water or desalination of seawater [136],[137]. Among various alternative technologies, membrane separation is being considered as the most promising solution to provide large volumes of water on a daily basis for humans and industry to respond to the forecasted water stress problem worldwide [138]. However, such a method suffers from high operation costs, intensive use of fossil fuels, limited life time of components (fouling, corrosion), and sustainability concerns related to concentrate disposal [139–142]. Moreover, the engineering complexity and geographical requirements of desalination techniques make their deployment difficult in certain regions of the world, such as dry climates and countries with no direct access to any surface or underground to brackish or seawater.

The atmosphere contains around 13,000 km^3 of freshwater, which is an order of magnitude higher than rivers (most exploited source of fresh water by human societies) and this water is also a widely accessible resource in all regions around the world [143]. Today this potential is under exploitation by a sector that is worldwide known as Atmospheric Water Harvesting. AWH is clearly an interesting research field that opens the way for novel science toward a sustainable environment.

AWH takes place when the air temperature reaches the dew point, and atmospheric water vapor condenses into liquid. In humid climates, this can be achieved spontaneously using passive systems such as fog nets. As an exposed surface cools by radiating its heat to the sky, water vapor condenses at a rate greater than that of which it can evaporate, resulting in the formation of water droplets. The phenomenon is favourable when the dew point is close to ambient temperature, and mostly observable on thin, flat, exposed objects including plant leaves and blades of grass. Research is investigating the effects on water harvesting performances at high humidity (RH>85%), optimizing both the wettability of materials and meshing patterns of the condensing substrate [144–

146]. This investigation area takes inspiration from the natural dewing happening over numerous plants and animals, exploiting textural and chemical features on their surfaces to harvest this precious resource [147–152]. Despite the limited operative conditions for this passive system reduce its feasibility mostly to humid and mountain regions, applications demonstrated productivity of the order of 1-2 L/day per meter square of the net [153–155].For less humid climates the approach is different and requires active systems based on refrigeration or desiccant materials. Active cooling based on mechanical vapor-compression refrigeration is an effective solution already exploited at commercial level. This solution becomes power intensive at higher temperatures, and especially in arid climates with low vapor pressure. The energy consumption indeed is proportional to the difference between ambient temperature and dew point [156]. Typical energy consumptions are in between 0.33-0.5 kWh_{el} L^{-1}, and most of the cost per unit of produced water are attributed to energy consumption than capital costs [156–158].

The use of conventional desiccant materials such as silica gel, which have discrete water storage capacity in most climate conditions is a promising approach for efficient atmospheric water harvesting. The regeneration of solid desiccants is typically done with heat, under which the ambient vapor pressure increases, as well as the dew point, and creates a spontaneous condensing environment for water. Most of the research carried out in past years, but especially in the last ones, focused the efforts on the improvement of sorbent uptake developing innovative materials and composites.

Metal-organic frameworks (MOFs) [159],[160] are an example of this research branch, that have demonstrated gram-scale water harvesting capabilities in the laboratory and the field. These organic and inorganic materials present several advantages in terms of water uptake capacity and atmospheric vapor pressure condition. In particular, MOFs offer the possibility to be synthesized with a desired molecular structure for specific adsorption characteristics with more or less stressed s-shape in the adsorption isotherm curves (types IV and V) [161],giving a competitive advantage in very dry climates (negative dew points).

Other explored solutions consist in the use of composite hydrogels [162–164], or in alternative the addiction of conventional sorbents (MCM, active carbon, silica gel, synthetic zeolites) with hygroscopic salts [165–169]. Despite all this activity are boosting the research on this topic it's hard to find the perfect combination that satisfies all the requirements for a real application. Although materials such as MOFs or hygroscopic salts have higher moisture uptake capacities than silica gel [52],[170],[171], they generally require much higher regeneration temperatures (around 100°C and above), they can be corrosive, and present risks of toxicity for the human body [161]. Similar concerns are about the use of hydrogels based on polymeric compounds that, up today, didn't demonstrate stable and safe water production over thousands of cycles as required for a real and feasible application.

Other major concerns that need to be addressed in this area include the energetic consumption of an AWH (Atmospheric Water Harvesting) device, and the overall capital costs of the technology [172]. Obviously, most

of the experienced solutions use solar energy for the regeneration of the material, but being mostly focused on demonstrating material potentials, the final prototype development presented some lacks affecting the correct and effective exploitation of the solar source.

In some of these studies solar radiation is directly used to heat the sorbent up to regeneration temperature. The limitation in this case is that an extensive water production will need a proportional surfaces extension of the device and secondly the copresence of two opposite phenomenon, regeneration and condensation, in the same location results in a not effective exploitation of the maximum potential of both processes. Most of the time regeneration temperature is higher than 90°C, requiring the indispensable use of concentration lens, reducing the overall efficiency of the system. In alternative an electric resistor, powered with photovoltaic panels, can be used to overcome the thermodynamic constraints on regeneration temperature. If this can be a practical solution to solve the problem, at the same time it is costing from the energetic point of view: PV technologies converts solar energy in the used form of power, and then into heat, with an efficiency of ~10-18% (commercial technologies). The same process done with a solar thermal technology (typical flat or evacuated tube solar collectors) has an overall efficiency ~50-70%, depending on the operative conditions. In the end the PV approach would require a more extended surface to produce an equivalent heat for the regeneration of the material, with potential issues on the capital cost increase and dimensional constraints.

Finally, most of concerns encountered in a real field application are about the condensation stage of the humid stream produced from the regeneration. High ambient temperatures reduce the effectiveness especially when a total passive approach is applied. On the contrary employing an active cooling to overcome, again, a temperature issue, will result in the rise of total energetic costs per produced litre of water.

An important part of this research is based on these premises, with the goal of designing an efficient process, one that optimizes the energy cost of produced water, maintains the temperatures levels compatible with the effective exploitation of both atmospheric water and solar energy. The following bullet points defined the guidelines of the research path:

- low regeneration temperatures compatible with the thermal conversion of solar radiation
- addressing the issue of condensing at ambient temperature
- reducing as much as possible the use of electric power
- compatibility of involved materials with health constraints

The next paragraphs will investigate on a global assessment to understand the potential available source for water harvesting and the definition of a good practice cycle. This is demonstrated with testing in the lab a water harvesting prototype using inexpensive silica gel. Based on experimental results, several litres can be produced in one day-night cycle, based on the energy consumption of a single solar thermal collector. The lab environment reproduced the conditions of hot and arid climates (dew point below 10°C and ambient temperature above 30°C) and demonstrated that water can be extracted from silica gel at a regeneration temperature of 57°C and

condensed at ambient temperature with a global maximum efficiency higher than what reported in by available literature.

4.2 Global assessment of atmospheric water

Despite current global withdrawals are below the total amount of water circulated through the natural hydrological cycle [143],[173–175], water-stressed regions across the world increased in the last decades and affected more than 2 billion of people [129],[176],[131]. Projections forecast a worsening picture of the globe that will induced mainly by the unequal distribution of renewable freshwater resources (RWS) across the world, for physical and economic factors [176]. Indeed, at global level, theoretical total renewable freshwater resources generated through the complete hydrological cycle, every year, accounts for more than $4.5*10^4$ km^3 per year, much higher than actual human withdrawals (3810 km^3/year of which ~10% used in dwellings, 70% for agriculture, and 20% in industry) [143]. In the reality the use of renewable water sources to satisfy human withdrawals is much lower than maximum potential for multiple reasons. The fluctuation over the year of RWS availability due to the climatic variation is consistent, daily and seasonal flow variations can be on the order 2-3 times [143],[173–175]. Moreover, lake, rivers or other surface water streams have a very sparse distribution that is strongly limited by the geography and climatic conditions of regions. Eventually, even in presence of great surface water sources, the entire potential reduces especially when upper streams affect downstream withdrawals due to water pollution and very high consumptive uses. Last consideration regards the entire ecosystem, the RWS potential cannot be entirely devoted for human uses, being the only sources for the rest of the ecosystem.

Alternative options to RWS are the exploitation of underground basins, desalination and water trade. Among them today the first approach is to dig deeper, exploiting underground reservoirs. For these type of water sources, the typical recharging rate are quite slow, with mean residential time order of 10^2-10^3 years. This is why usually they are called Fossil Water Sources (FWS) [143]. As second, desalination is generally suitable for places when instead of fresh aquifers, seawater or brackish sources are available at the surface or underground level. At the end of 2015 more than 18000 desalination plants were installed around the world, 44% in the MENA area, for a production capacity of 86.55 million m^3day^{-1} [177], with an energy costs that goes from 2-3 kWh m^{-3} up to 80 kWh m^{-3}, depending by the type of source (brackish of seawater) and technology (multistage flash, multiple effect distillation, membrane reverse osmosis and the hybrid combination of all of them) [178]. Water trade is a third approach and mainly adopted for drinking water. The long-distance connection between source and users is typically built on car/truck transportation [143],[173–175]. When transferred water units crosses regions and country, this water trades are considered as importation/exportation of water from foreign countries or in a real form (physical transportation of water by truck) or virtual (transportation and trade of food and goods is considered as a virtual importation of the water needed for their production [131],[179],[175].

Over all these bricks (RWS, underground, desalination, water trade) is built the water distribution infrastructure of nations and their weakness, caused by a defective reliability or source availability, can easily generate a water stress condition for people living in that regions. Among years engineers used an index identifying the overall stress on the natural water cycle, exacerbated by human activities at regional and local level. This is typically evaluated as the ratio between withdrawals (excluded the provision from recycled and desalination plants) and the RWS per year. This type of index, called Water Stress Indicator (WSI) is useful not only to have a current picture of the global situation as in Figure 4.1, but also to quantify and estimates effects and impacts of water policy makers, or to understand aspects related to climate change [179–181]. In Figure 4.1 the WSI was evaluated using the withdrawals of 2010, against available RWS between 1950-2008. High stress values indicate an increasing inability over time and at regional level to meet the rising water demand with existent supplies. Within this inability reasons are multiple and not strictly related to climatic drought conditions rather than extensive use of water resource. Indeed, if the chronic sufferance of MENA regions and the Asiatic inner land is mostly associated with the climatic and geographic severity, the rising stress of southern Europe and USA west coast, is mostly the consequence of the intensive use in agriculture, industry and civil use [129],[131],[143],[173–176],[179–181]. Evidence of these condition are the statistics about drought event, worldwide spread, and most of the time associated to heat wave, worsening of climatic conditions, and human pressure on the environment [135,182–186]The continuous research towards alternative water supply is a good approach to increase the human society resilience towards the worsening problem of water.

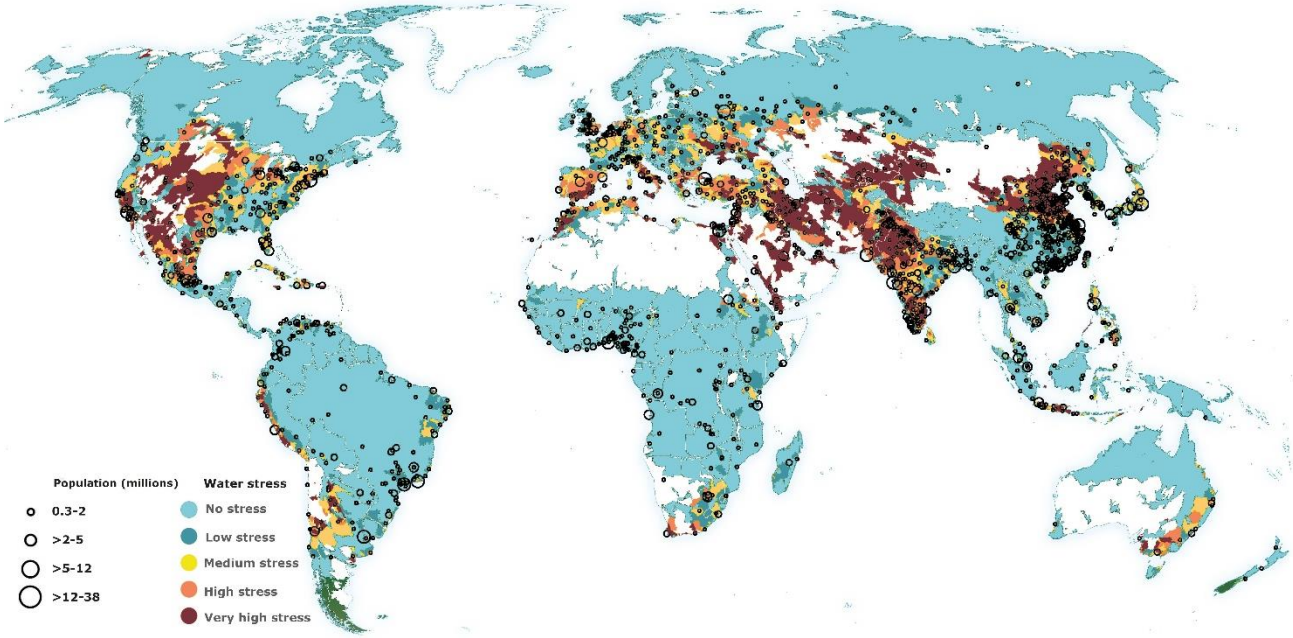

Figure 4.1: Worldwide spatial distribution of the Water Stress Index [179],[180],[181]. WSI measures total annual withdrawals as percentage of the total freshwater resources, at surface and underground level (also called 'blue water'). This map shows the WSI distribution using water withdrawals of 2010, over the mean available blue water in the period of 1950-2008.

Different scientific papers report the total volume of freshwater contained in the atmosphere close to 13,000 km^3. The comparison with other freshwater sources suggests that atmospheric water vapor as the potential to be an alternative freshwater source, at least in terms of global volume: 2120 km^3 flow through rivers, 1650 km^3 are contained in the soil, and 91000 km^3 belong to fresh lakes [143]. More difficult is to state similar conclusions at regional level. The availability of water vapor is enough to replace the lack generated by the absence of conventional sourcesi? And the use of air moisture, can be comparable to other sources in terms of cost and energy intensity?

Responding to these questions is not simple and require a deep knowledge of local dynamics and climate characteristics. The keystone is a deep and detailed knowledge of the spatial distribution of water vapor in the atmosphere. Indeed, despite the spatial distribution of this source is definitely wider than any other conventional sources, vapor concentration over earth surface is inhomogeneous and influenced by seasonal turnover. Sparsity of vapor concentration is always dependent by temperature distribution and strongly linked to atmospheric convective movements and solar radiation distribution. Complexity of the problem makes very hard to make a theoretical estimation, requiring a holistic approach to obtain accurate results. Anyway, extensive measurements have been carried out in the last decades, recurring to extra-terrestrial remote sensing approach to measure atmospheric variability in terms of dynamics and aerosol concentrations, included the moisture distribution. Main research project were: *i)* APO Smithsonian institute[187]; *ii)* ERA-Interim Reanalysis ERA-Interim is the latest global atmospheric reanalysis product produced by the ECMWF[188]; *iii)* Aura Microwave Limb Sounder[189–191]; *iv)* Earth Observation System with the two trains of monitoring called *Afternoon* and *Morning* constellations.

This last program provides very helpful info about the atmospheric distribution of water vapor. EOS is a NASA program of dynamic observation of Earth surface and atmosphere. Among different satellites constituting the observation train, two satellites named Terra (EOS-AM1 launched in 1999) and Aqua (EOS-PM1 launched in 2002) provide specific information for the estimation of water vapor distribution across the world: the column of precipitable water vapor TPW. This value ranges between 0-6 cm, representing the equivalent height of a normalized volume if all the water vapor contained through the normal column would be condensed.

The two satellites are equipped with a scanning spectroradiometer, called MODIS (Moderate Resolution Imaging Spectroradiometer) measuring the radiative response of the atmosphere, within 36 spectral bands: visible; near-infrared (IR), and IR. The combination of a wide wavelength range (0.4-14.4μm), high spatial resolutions (1x1 km at nadir), and a quasi-daily global coverage, makes MODIS suitable for the continuous observation of earth's atmosphere and surface, monitoring the relative changes [192],[193]. Monitored spectrum data are elaborated with different algorithm to retrieve the spatial distribution of typical atmospheric parameters (temperature,

[i] This condition can be generated by multiple factors: no access to fresh rivers or lakes; no access to salt water sources; economic issues creates a barrier for the deployment of water infrastructure or for water trades or to build water treatment plants.

moisture, surface skin, ozone, etc…). In particular, the computing scheme calculate first the radiative transfer, with the algorithm PFAAST (Pressure-Layer Fast Algorithm for Atmospheric Transmittances [192]), then apply a statistical regression, based on field measurements at surface level, to link the observed/modelled radiances with corresponding atmospheric profiles. This leads to the retrieval of different atmospheric physical parameters (temperature, vapor pressure, aerosol, dust, ozone, etc…), in particular the elaboration of radiative response at the band interval 890-965nm and 1.36-7.48μm, gives the specific influence of water vapor on the emitted radiation from earth, that is then aggregated within the TPW index [192],[193]. TPW estimations are provided through product files MOD05_L2 and MOD07_L2 for Terra and MYD05_L2 and MYD07_L2 for Aqua, in which the distinction 05 and 07 refers respectively to the above-mentioned wavelength bands. The accuracy of the algorithm has been validated and improved considering parallel and parasitic phenomena such as aerosol presence, surface emissivity problems and solar reflectance to guarantee reliability of measurements [194],[195]. Further on, the elaborating algorithm relies on observation of water vapor attenuation of reflected solar radiation only in the near-IR MODIS channels, so that the product is produced only over areas where there is a reflective surface in the near IR[192],[193],[195]. These data are public and can be downloaded from the MODIS portal with a daily, weekly and monthly database covering the last 20 years [196],[197]. An example of TPW distribution is elaborated with the map in Figure 4.2, obtained from the average data for the month of August 2019. The map shows up a strong correlation between TPW and geographical position. In particular, the equatorial belt accounts for the higher density of TPW values belonging to the upper band of 3-6 cm. This is the moister area of the planet, where most of the precipitations are indeed occurring, on the contrary, regions of the sub/sup tropical collect more data point in the lower band of 0-3 cm. This distribution result from the combined effect of solar radiation distribution on the earth surface (higher intensity within the tropical area) and tropospheric convective movements. The equatorial area collects winds generated from the backward movement of the Hadley cell, with a convergence in proximity of the equatorial line: this area is called the Intertropical Convergence Zone (ICZ), or the *"climatic equator"* [188]. During the converging movement tropospheric currents collect most of the moisture from water surface evaporation and evapotranspiration from vegetation, concentrating the vapor in the zone of low pressure of the Hadley cell (around the equator), where the ascensional currents move all the vapor up to the tropopause [175],[189],[191]. The *climatic equator* is not fixed during the year, and the ICZ shifts along the latitudinal direction crossing the geographical equator with a seasonal frequency. This movement is visible from the graph on the right of Figure 4.2 where the TPW distribution is scattered along the geographical latitude, for the average day of January and August of 2019. January has the peak of the latitudinal distribution shifted up towards the north, occupying the area between the equator and the tropic of Cancer. On the contrary in August the inversion movement shift down the area with higher TPW intensity, towards the tropic of Capricorn. This variation is much more stressed in the central zone then in the sub-tropical and the temperate area [188], [198], [199]. Figure 4.3 gives a complete overview of the TPW distribution among one year, depicting local TPW

value (monthly average) from January to December of 2019, giving a clear graphic of this typical seasonal movement. With this huge amount of available data, the evaluation of the cumulative value of TPW, and then of the total amount of water contained in the atmosphere, can be estimated integrating elements of the data array (3600x1800), excluding the damaged items, weighted over the global earth surface extension. This operation was computed over the available data between 2010-2019, resulting a range between 8000-12000 km^3 during the year as showed I the right of Figure 4.3. The wave shape is characterized by two peaks (an absolute maximum between July-August, and a relative one between December-January) and two valleys (with similar values and located between February-April and October-November). This analysis gives us an important information about when this resource is more or less abundant around the world. Clearly the focus has to be local, because as highlighted more recently by Chen et al.[188], and in the past by others [187],[189] the fluctuation is mostly imputed to variations within the ICZ, while in the sub/sup tropical area this fluctuation is very flattened.

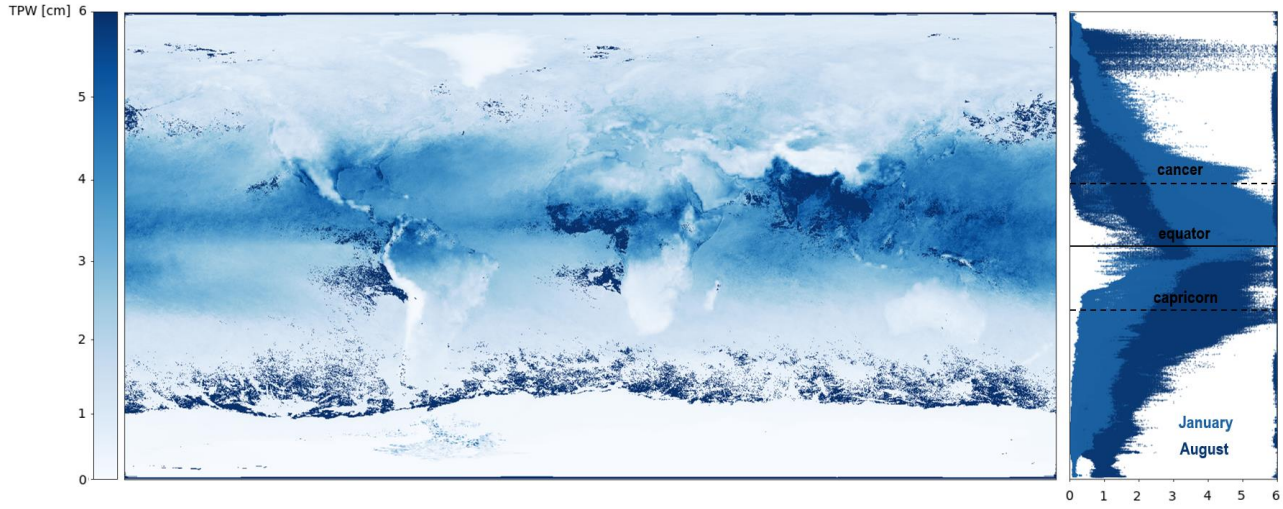

Figure 4.2: TPW distribution from data provided by MODIS instrument onboard of Terra satellite (parameter MOD05_L2). Data depicts the average distribution during August (2019). Water vapor are determined with errors typically in the range between 5 and 10 percent [192][193]. On the right the spectral distribution of the map over the latitude for the average day of January and August 2019. The interesting aspect is the seasonal movement of the *climatic equator*.

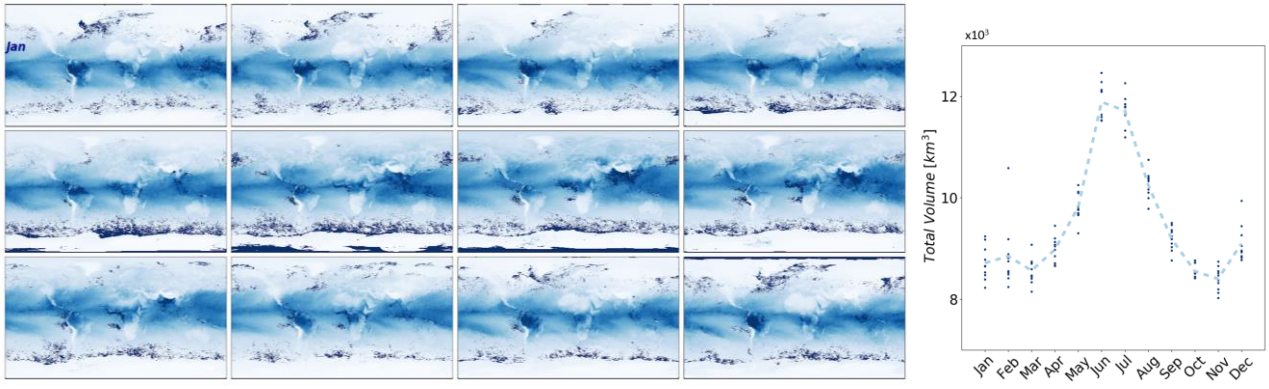

Figure 4.3: On left maps depicting TPW distribution across the Earth, during 2019. On the right the seasonal fluctuation of total volume of water contained in the atmosphere, estimated between 2010-19.

With the purpose to investigate on the purpose of using water vapor as potential source of water for anthropic activities, the regional focus was concentrated only to such regions with considerable high-water stress. This

operation required a Boolean manipulation of data array: first from the map in Figure 4.1 has been created a binary data array where 0 correspond to an area with no water stress, while 1 is for the two categories *"high stress"* and *"very high stress"*. Second, this binary array was intercepted with the monthly TPW data array, resulting in the selection of TPW values specifically for stressed areas. Result of this operation is showed in Figure 4.4. Highlighted regions were regrouped in 5 macro area[i]: the macro area including China and part of India (CH); north America (NA); the region comprehensive of minor Asia, Turkey, Iran and Iraq (AM); North Africa (NAf) and Europe (EU). For each macro area has been evaluated the density distribution of TPW for the average day of January, March, May, July, September and November of 2019. The density function has been realized sampling randomly 1000 items from the available dataset of the macro area. Strong variations are in the for NA, NAf and CH, while EU ad AM are characterized by a flatter variation of the distribution. For all of them, the shift to lower TPW (between 0-1 cm) is within the interval Nov-Jan.

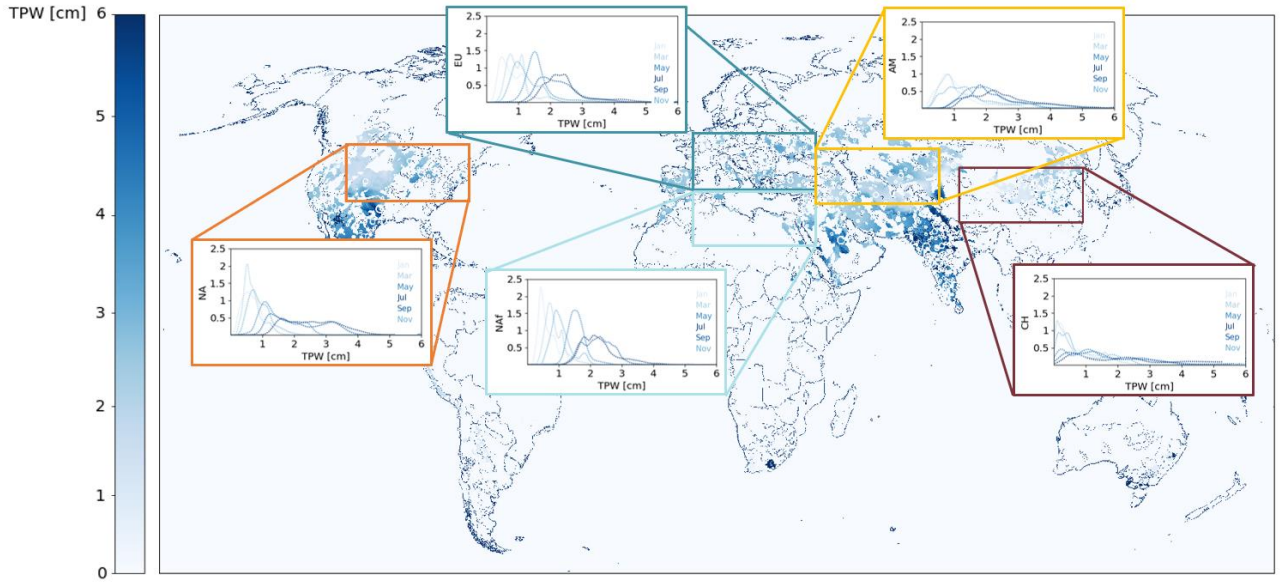

Figure 4.4: Focus of the TPW analysis for the macro areas characterized by water stress. For the 5 macro-areas has been analyzed the density function of the TPW (sampling from 1000 random selected items contained within the macro-area) for the average day of January, March, May, July, September, November.

This is very stressed for NA and NAf. While, the period between Jul-Sept is characterized with considerable higher TPW values. Main reasons behind this behavior is the geographic distribution. All these areas are in the boreal hemisphere, and the Nov-Jan correspond to the winter season while Jul-Sept to the summer period. The higher temperature drives higher TPW values and moisture concentration: the temperature increase of 1K is associated to a RH increase of around 8-13%.

The final part of this analysis deals with the water uptakes of the material, especially for what tested in this application, silica gel. The question is: given this spatial and seasonal distribution of water vapor for water stressed regions, what is expected, at least in potential, from this material?

[i] Each region is a matrix of 400X180 pixel with a specific surface extension per pixel of ~1.22571x10^3 m2. Earth surface is discretized in a data array of 3600x1800 pixel and equivalent to 5.094953216x10^{14} m2 [261].

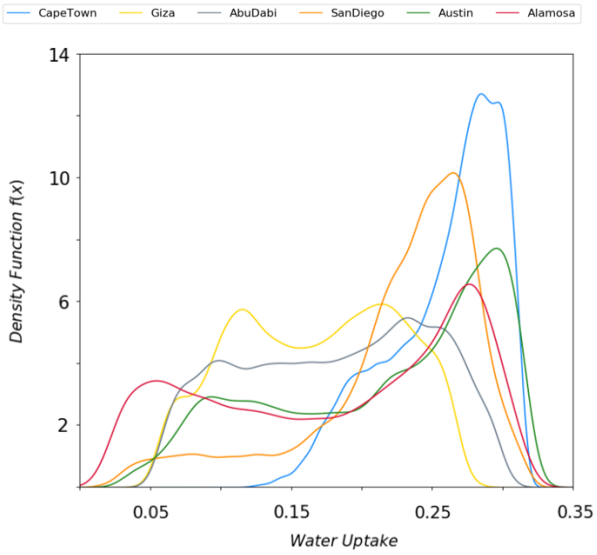

Figure 4.5: Density distribution of potential water uptake of silica gel for selected climatic conditions. Meteorological data obtained from METEONORM database for cities that recently experienced drought events and belonging to the macro areas NA and NAf.

Water uptake values, considered as equilibrium concentrations, are strongly function of the combined values T and RH. A preliminary estimation has been carried out, using meteorological data from METEONORM database[200], and combined with the equation (2.5), describing the isotherm family of tested silica gel. Despite the Figure 4.5 is not an exhaustive representation of the problem at global level, can give an order of magnitude of the numbers involved. Selected cities belong to the macro-areas NA and NAf, and recently experienced drought crisis.

The two pronounced peaks are the result of the situation described before with the TPW. A drier climate, during the days of the winter season, results in equilibrium potentials lower than 0.1 $kg_w\ kg_{SiO2}^{-1}$, while much higher values are for the summer season, with peaks at values higher than 0.25 $kg_w\ kg_{SiO2}^{-1}$.

Some very dry climates, such as the Alamosa case, show actually values much lower than 0.05 $kg_w\ kg_{SiO2}^{-1}$, giving basically few chances to consider silica gel as a feasible solution.

For the rest of the cases the value of 0.1 $kg_w\ kg_{SiO2}^{-1}$ has been considered as a turning point to establish a not extreme dry conditions, and will be used as minimum value for the theoretical definition of an efficient cycle, and its testing in the next paragraphs.

4.3 Method of the Cycle

The working principle of AWH is based on the cycling of adsorption and desorption phases during which water is captured and condensed respectively. This process takes place under the water vapor partial pressure and is driven by the relative pressure difference between the free water molecules and the ones trapped over the solid surface of the adsorbing material, governing the water mass transfer from the vapor state into the porous structure of the adsorbent. If the temperature of the adsorbent increases, the direction of water flow switches,

yielding water vapor desorb from the solid to the gas phase. Indeed, the energy of the adsorbed water molecules inside the porous structure of the sorbent increases due to the absorbed heat flux. As a result, the pressure of water vapor increases generating a positive gradient towards the external air. The energy needed for the process changes with material type and internal porous structure but, as mentioned in the previous chapter, the order of magnitude is comparable with water latent heat. For instance, adsorption heat of Zeolite and MOF ranges between 4000-3000 kJ kg^{-1}, for silica gel is 2300-2500 kJ kg^{-1} [66],[201],[81]. This energy can be a heat supply produced from solar energy, but some limits define the constraints under which a cycle should be built to realize the final objective, condensing water vapor:

- Regeneration temperature must be in the range of 50-70°C to be compatible with heat generation from low temperature solar conversion technologies (flat plate, evacuated tubes).
- Hot and humid flow generated through regeneration needs a dew point higher than the temperature of the external environment. In this way the condensation is driven spontaneously without using any refrigeration system but using directly the ambient for heat rejection.
- A total passive system is hard to be realized, and some power will be required to drive auxiliary components (water circulators, fans, dampers).
- Being driven by solar energy, the temporal slot under which regeneration can be driven corresponds to the daylight duration (6-10 hours). In reality, at the begin and the end of the daylight period, the solar radiation could be too low (<200 w m^{-2}) to generate sufficient amount of heat for regeneration. This reduces the total available time.
- Reducing as much as possible the operative temperature for regeneration will lead to an increase of the thermal efficiency of a solar collector (as the Hottel-Whillier [202] efficiency curve suggests). Further on, lower regeneration temperatures enable the use of a wider potential source, such as the waste heat from industrial processes.

The regeneration phase generates most of the criticalities, and a suitable working cycle satisfying the above bullet points needs to be defined. The working cycle results from the alternation of two sequential phases:

- *Adsorption:* mostly driven in the period of absence of solar radiation. During this phase the system is in an open loop with the goal to charge the sorbent with water vapor, increasing the water uptake as much as possible. The energy cost of this phase is associated to the pressure drops generated with the air stream crossing of the sorbent mean/particles. Limiting factors for this stage are mainly linked to material isotherms and working environmental conditions.
- *Regeneration:* driven in presence of solar radiation. During this phase the air loop is closed, and the air mixture is subjected to transformations operated between two temperature levels, the regeneration temperature and the ambient temperature. Different steps of the transformations are described in psychrometric chart of Figure 4.6.

The working cycle in Figure 4.6 is based on some hypothesis, and in any cases represents equilibrium and ideal points, going cyclically between point 1 and 4. The regeneration temperature has been fixed at 55°C, and ambient temperature at 30°C. In this way at each value of air temperature and humidity is associated the maximum water uptake achievable. Transformation 1-2isoT represents the regeneration of the material throughout an isothermal desorption, operated with an ADS-HX as described in the Chapter 3.

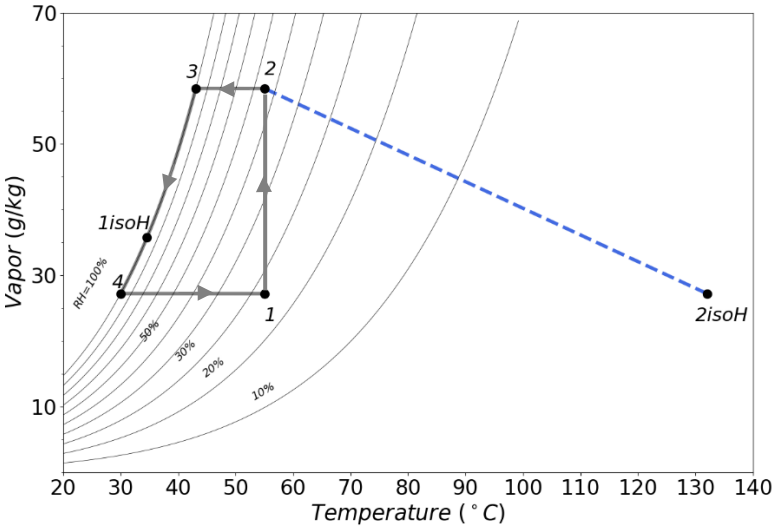

Points	T	x	RH	Enthalpy
-	°C	$g_{H2O}\ g_{dry\ air}^{-1}$	%	kJ kg^{-1}
1	55	27.2	27	126.2
2 isoH	132	27.2	<1.5	207
2	55	58.5	55	207
3	43.1	58.5	100	194.4
1 isoH	34.6	35.8	100	126.2
4	30	27.3	100	100

Table 4.1: Thermodynamic properties of the points depicted in the cycle on the left.

Figure 4.6: Working cycle of regeneration/condensation on the psychrometric chart. The comparison claims to show the differences between an iso-thermal approach (blue path), versus an iso-enthalpic approach (grey path). If from the energy point of view the two cycle are equivalent, the temperature levels are deeply different. The isothermal approach enables the possibility of using very low thermal sources.

Through the step 2-3 the hot and humid air flux resulted from the regeneration of the sorbent is cooled up to the dew point. Condensation of water starts at point 3 and continues along the saturation line (relative humidity ~100%) up to the maximum exploitable potential. The minimum point here is the point 4, with a temperature value in the ideal case equal to the ambient temperature, and RH=100. After that the air stream is re-heated the from 4 to 1, the regeneration can start again, and all the previous steps can be performed again. Corresponding values of T, RH, x and enthalpy of points 1, 2, 3 and for are reported in Table 1.

To realize the isothermal regeneration (1-2) a system is required, that gives the possibility to exchange at the same time heat and mass. Indeed, without a continuous supply of heat, during the regeneration the temperature will easily drop down due to the endothermic nature of the desorption phenomenon.

The point 2 is not an absolute term but a function of the instantaneous value of sorbent water uptake, that for equilibrium consideration as the points in Figure 4.6 are, can be determined with equation (2.5). For this analysis, and for the experimental testing, the sorbent selection has fallen on silica gel for different reasons. One of the most important drivers is the lower cost if compared with more efficient means. Second reason is the aim to demonstrate that despite material properties are very important, the role of the *"way"* in which you regenerate the material and how the harvesting cycle is approached is very fundamental. For these reasons, the experimental results of the performing cycle will be compared in next paragraphs with other experience in literature were the focus was mainly on materials side than cycle.

The isothermal regeneration, driven at a maximum temperature of 55°C, leads to higher dew points if compared with conventional system operating through a typical adiabatic regeneration (iso-enthalpic). We can reach the dew point 3 at 43.1°C with an isothermal desorption, against 34.6°C for an iso-enthalpic one (point 2isoH). As a result, the water uptake required at the end of adsorption to achieve equilibrium points 1-isoH and 2 are 0.318 and 0.125 kg_w/kg_s, respectively. Consequently, higher dew points are achievable even at lower humidity level through this desorption process. This regeneration approach enables the use of silica gel for atmospheric water harvesting in low humidity climates, despites the lower water uptake compared with more innovative means. Evaluating the iso-enthalpic transformation for comparative purposes (h_{2iso-T}=207.6 kJ/kg_a) the required desorption temperature would be as high as 132.5°C to provide the same amount of water as the values approached with 2isoT. An equivalent iso-H would require higher temperature heat source, lowering efficiency from the exergy point of view, and forcing the use of optical concentrators for a feasible exploitation solar energy, loosing points o the global efficiency.

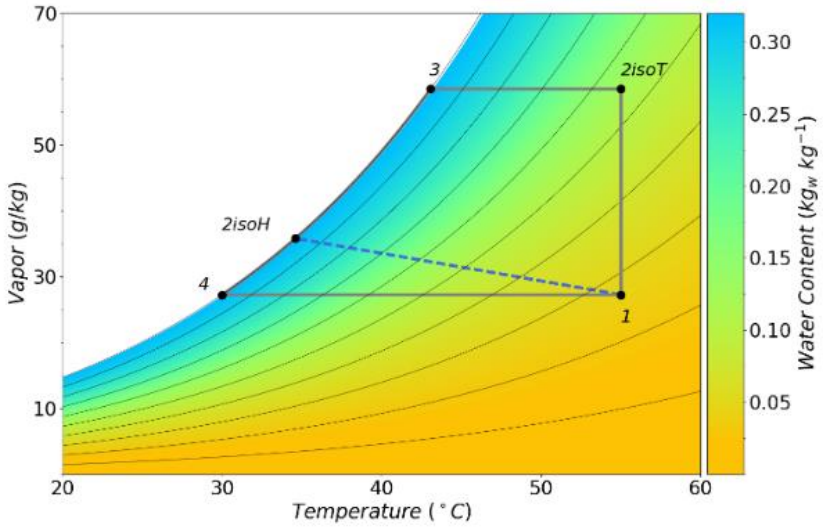

Figure 4.7: Desorption cycle for water harvesting through an isothermal regeneration of silica gel on the psychrometric diagram. The comparison between the iso-thermal regeneration vs. the iso-enthalpic show the increase of achievable maximum dew point and vapor content. The regeneration cycle is obtained combining the thermodynamic properties of humid air (T, P_v, h) and water uptakes of the silica gel in equilibrium with the equation (2.5)

At the maximum temperature of the cycle corresponds the minimum value of water uptake, while at the equilibrium it is close to of 0.045 $kg_w\ kg_{SiO2}^{-1}$, corresponding to equilibrium condition at point 1. Then, for each kg of dry silica gel particle, the net amount of water pulled out from the air is 0.08 kg, and the minimum energy required for the regeneration 4-1-2isoT is 108 kJ/kg_{air}. This is clear from the graph on Figure 4.7, where the cycle previously explained is coupled with a colormap depicting silica water uptakes at equilibrium at each point of the psychrometric chart.

The total energy required for the regeneration step can be reduced using a regenerative heat recovery system: the preheating step 4-1 is achievable with free energy coming from vapor condensation at higher temperature. This method can potentially save up to 24% of the total energy, increasing consistently the efficiency of the cycle. As said, these diagrams are instantaneous picture of equilibrium conditions that, as the water is pulled

out from the sorbent, declines. As consequence, the actual cycle will move along the chart, as the actual water uptake of the material, and operative conditions (regeneration and ambient temperature) changes. Indeed, since our system is being used in batch mode (alternation of adsorption/desorption in a static component), the continuous discharge of water reduces the total water uptake, then the line 2-3 will shift down resulting in a reduction of water production and efficiency over time.

4.4 Experimental Setup

The ADS-HX configuration used for this experimental analysis is similar to the packed bed configuration described in chapter 3.

The AWH device and its components, along with its working principle are summarized in Figure 4.8. The system works on a batch process, switched through the 4-way valve I, alternating adsorption and desorption stages in the adsorption heat exchanger (ADS-HX) A. Water harvesting tests were performed within a day/night cycle, recreating typical environmental condition of a dry climate both in adsorption and desorption. In adsorption mode (ADS) outdoor air (25-35°C, 30-50%, 100 $m^3\ h^{-1}$) is directly blown through A, and the outlet stream is rejected to the ambient. During the tests several air temperature and humidity sensors monitor the stream, and a load cell measures continuously the weight of the A. Switching the valve I to regeneration mode (REG) the air loop is closed, and the same stream flows between the ADS-HX and the condensation unit. The solar thermal facility installed on the roof of the lab produces hot water (H) at 50-60°C for the regeneration of the ADS-HX, delivered with the water pump G (42 Wel max, 60 L min-1). The condensation unit consists in an air to air heat recovery system C and an air to water radiator B. In C, the condensation heat is partially recovered to preheat the air before going back to A, reducing the total energy for regeneration. The condensation heat is dissipated through an external dry cooler F at a constant temperature between 25-35 °C, regulated with a thermostat in order to simulate different climatic conditions. Finally, the condensed water droplets on the radiator B are collected in the basin D and recovered and stocked at the end of each test. During regeneration, the valve I prevents any communication with the external environment, and the air flow driven by a fan E (450 Pa, 100 m^3h^{-1}, 65 W_{el} max) to complete all the regeneration steps. All the actuators have been controlled with a PLC defining continuously the power percentage of continuous variable components, and the state of the on/off ones. Some precautions were needed for the selection of the centrifugal fan E: operational environment with a temperature up to 80°C, RH>70%, metallic impeller and electronics with a 24 IP protection and a variable speed control with a PWM 0-10V signal. The heat recovery unit C is a PET counterflow air-to-air plate heat exchanger (from Klingerburg model GS-K-366), with a channel opening of 3 mm, and a total exchange surface of around 18 m^2. The WAT-AIR lab facility has been assembled with the purpose of verifying the effectiveness of the water harvesting cycle in a Lab environment and to perform the ideal cycle envisaged in Figure 4.6 and 4.7. To pursue the goal of a

cost-effective liter-scale system, the test rig contains around 27 kg of silica gel beads (3 mm average diameter) in the ADS-HX.

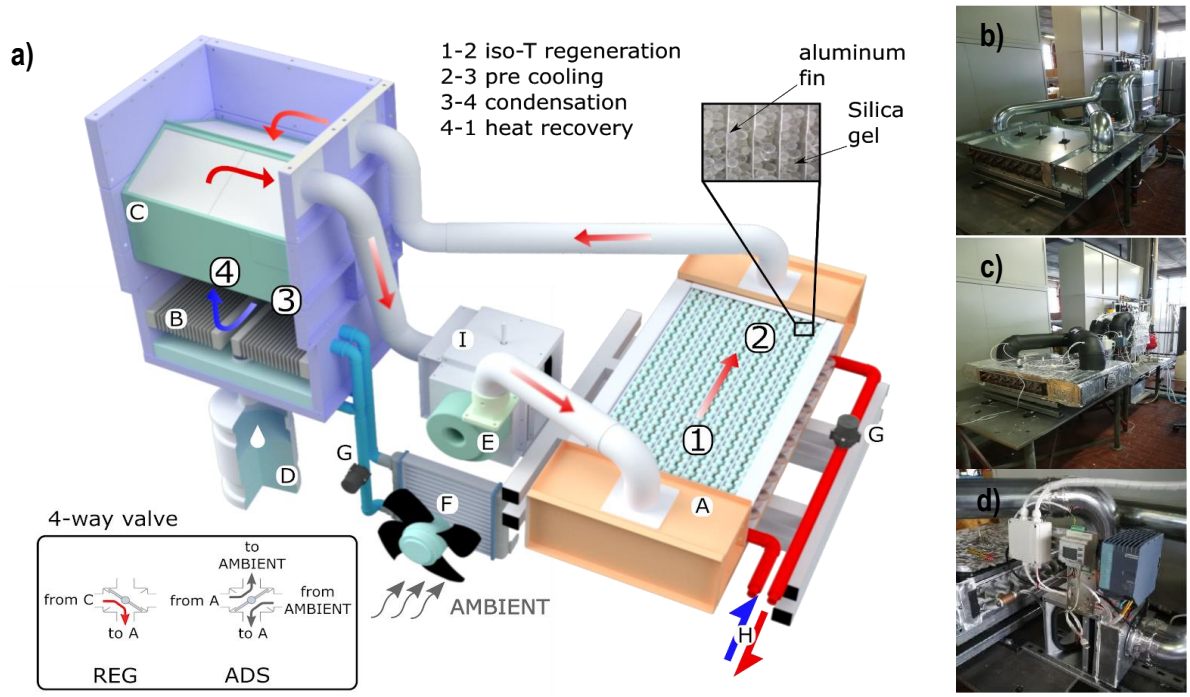

*"**Figure 4.8:** WAT-AIR lab facility to test water harvesting cycle in a controlled environment. a) scheme with the different components, where the symbols indicate respectively: **A** is the ADS-HX, **B** are the condenser radiators, **C** is the regenerative air to air HX within the condensation unit, **D** is the basin for water collection, **E** is the centrifugal fan for the process air, **F** is the dry cooler unit, **G** are water pumps, **H** indicates the inlet/outlet points of the hot water flow through the ADS-HX; b) picture of the setup after the assembling; c) picture of the final setup with sensors and insulation layers; d) detail of the controlling unit consisting of a PLC, a 24VDC power supply of 100W_{max} and the air valve for the switching between the open and closed loop."*

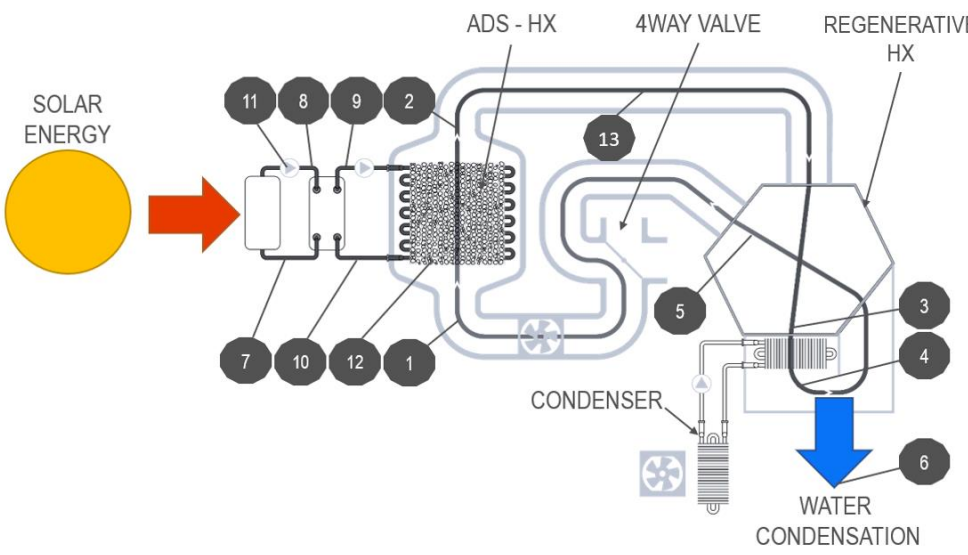

Point	Variable Name	Units
1	RH_{in} ADS-HX	%
2	RH_{out} ADS-HX	%
1	T_{in} ADS-HX	°C of air
2	T_{out} ADS-HX	°C of air
3	T_{in} cond	°C of air
4	T_{out} cond	°C of air
5	T_{out} rec	°C of air
6	T_{in} can	°C of air
6	RH_{amb}	%
1	x_{in}	$g_{H2O}/kg_{dry\ air}$
2	x_{out}	$g_{H2O}/kg_{dry\ air}$
7	$T_{w\ prim\ in}$	°C of water
8	$T_{w\ prim\ out}$	°C of water
9	$T_{w\ sec\ out}$	°C of water
10	$T_{w\ sec\ in}$	°C of water
11	m_w	Liter/min
12	Load cell	Kg
13	v_{air}	m/s

Figure 4.9: Scheme of the experimental setup and positioning of sensor for air temperature and humidity, water temperature and flow rate, weight of sorbent.

This silica gel beads occupy the 5 mm spacings between the fins with a total filling degree of about 58% of the total volume of the exchanger. The silica gel was purchased from Oker-Chemie GmbH and used without any pre-treatment. The silica beads have a bulk density of 0.78 g/cm^3, 99.5% purity, and a surface area about 800 m^2/g. Several auxiliary systems for the automation of all the cycle steps: adsorption/desorption switching; air flows regulations; regeneration heat management. A complete list of the auxiliary equipment is described in the Annex C. All the parameters required for the evaluation of cycle performances are constantly monitored and logged as listed in the scheme of Figure 4.9. The temperature of air (T_a), and water (T_w) were measured using IC temperature sensors (LM35CAZ, ± 0.2°C). The relative humidity (RH) of air was measured with thermoset polymer capacitive sensors (HIH4000-4, ± 3.5%). Electromagnetic flow meter has been used for the measurement of the hot water flow for the silica regeneration, in the range of 0.5-20 L/min (LFE SMC, ± 1.5% FS), and hot wire anemometer for the air velocity (Testo416, ±1.5%+0.2 m/s). At the same time the mass variation of the ADS-HX with silica gel due to the alternating capture and release of water vapor were directly measured through an aluminium alloy IP65 single point load cell (2 ± 0.002 mV/V; ± 0.023 of %F.S.). In this way the direct measurement of the average water uptake of the packed bed configuration is possible, reducing uncertainty of indirect measurements. Finally, the water collected from the basin is stored in bottles and separately weighted at the end of each cycle. This final weight was on the average 90% lower than the mass variation of the load cell. Main reason of this difference was the presence of some undetected leaks among the air loop, and the impossibility to collect all the water droplets that remain on the surface of channel and plates of the recovery heat exchanger.

Analog outputs of different sensors have been continuously logged with a 16bit Analog/Digital converter (Seneca Z8AI) and real time monitored through a LabView VI interface. The architecture is the same of what explained in chapter 3.

4.5 Experimental results and discussion

Testing methodology aims to replicate a day/night cycle in a dry climate environment. Regeneration phase driven at temperatures lower than 60°C and powered with solar thermal collectors. In the ADS stage water final uptakes between 0.1-0.15 are achievable within 15 hours with ambient temperature of 20-25°C and dew points between 2-8°C. These are considered as environmental condition during the night period of a dry climate. Regeneration was carried out instead for less than 10 hours, just after the adsorption stage, and at different condensing temperature in the range of 25-35°C. Control of air moisture content for the simulated environment was not necessary during regeneration because the cycle works in a closed loop without any mass exchange, but only thermal exchange through the external radiator. When the cycle is switched between adsorption and regeneration the air valve sketched in Figure 4.9 rotates modifying the air loop from the *open* to the *close* configuration and vice-versa. This operation is actuated with a typical rotating damper controller, usually applied for HVAC systems, with a max torque of 6 Nm, and a 3 points control. The continuous monitoring of parameter

listed before led to the evaluation of some aggregated indicators, to perform comparisons among different operational conditions.

Dew point of the humid air mixture

$$T_{dew} = C \ln\left(P_{sat}\frac{RH}{A}\right)\left[B - \ln\left(P_{sat}\frac{RH}{A}\right)\right]^{-1} \quad (4.1)$$

where the coefficients A, B, C are respectively 611.85, 17.502, 240.9.

Thermal Efficiency of the cycle

$$\eta_{th} = \frac{M_w\, H_{lat}}{Q_{reg}} = \frac{M_w\, H_{lat}}{\dot{m}_w\, c_{p_w}\left(T_{w_{in}} - T_{w_{out}}\right)} \quad (4.2)$$

Where M_w is condensed water, H_{lat} is the condensation heat and Q_{reg} is the regeneration temperature. If the thermal power terms consider also the source, and the way in which the solar power (Q_{sol}) is converted into heat, this efficiency can be defined in terms of primary energy as following:

$$\eta_{PE} = \frac{M_w\, H_{lat}}{Q_{sol}} = \eta_{th} * \eta_{sol} \quad (4.3)$$

This approach is particularly important when the comparison across the different devices present in literature will be performed.

Another interesting parameter is the charging level of the ADS-HX. This indicator is connecting the average water uptake of the material (directly measured with the load cell) and the potential value obtained through the isotherms. This value is the maximum (or the minimum if we are in the regeneration phase) achievable with the configuration when the equilibrium condition with the inlet air (@ T_{in} and Pv_{in}) will occur:

$$Charge\ level = \frac{W_{istataneous}}{W_{equilibrium}\big|_{T_{in},\ Pv_{in}}} \quad (4.4)$$

The equilibrium value is computed with the fitting polymer of the equation 2.5, while the instantaneous water uptake is estimated as:

$$W_{istataneous} = \frac{Weight - M_{dry\ silica} - M_{metallic\ frame}}{M_{dry\ silica}} \quad (4.5)$$

Where the weight is constantly monitored with the load cell sensor. The dry mass of silica was separately weighted before the ADS-HX assembling, after driving a full regeneration (T>90°) in the climatic chamber. Similarly, the metallic frame was weighted before assembling it. Anyway, at the begin of the testing campaign an offset analysis was carried out through a full one-day regeneration of the assembled ADS-HX, to obtain the minimum weight corresponding to a zero-water mass. Further, a full calibration of the load cell was required during the assembling of the test RIG to correlate the output from the wheatstone bridge with a known tare. In the Annex D is reported the calibration procedure and results of the load cell sensor.

The condensing water rate, defines the instantaneous amount of condensed water in the collecting basin, and is estimated starting from the evaluation of the mass variation of the ADS-HX between two consecutive measurements:

$$Water\ rate = \frac{M_{w\,t2} - M_{w\,t1}}{\Delta t} \quad (4.6)$$

The integral of this parameter over the entire test is the total amount of water produced, that is compared with the amount of water collected during the discharge of the colleting basin, as in the Table 4.2, showing a discrepancy close to 10%, for the reasons explained before.

An inverse indicator, giving information about the energy cost for the process is the Specific Thermal Energy, defining the energy input to the cycle for the production of 1 liter of liquid water.

$$STE = \frac{1}{n}\sum_{i=1}^{n=30}\left(\frac{\dot{m}_w\ cp_w\left(T_{w_{in}} - T_{w_{out}}\right)}{water\ rate}\right)_i \quad (4.7)^{i}$$

More than 40 tests have been realized, here and in the next are reported the performance of the most representative for the purpose of showing the effect of the environmental conditions on testing performances.

TEST	Fan	$T_{in_{ADS}}$	$RH_{in_{ADS}}$	$T_{dew_{ADS}}$	$T_{reg_{prim}}$	$T_{reg_{sec}}$	$T_{codenser}$	Δm_{ADS}	Δm_{REG}	Collected Water
-	%	°C	-	°C	°C	°C	°C	kg	kg	kg
20-21	70%	21.2	0.33	4.11	57.4	56.3	20.8	2.55	2.74	2.5
22-23	30%	22.9	0.29	3.91	57.1	56.2	23.1	2.49	2.00	1.8
24-25	50%	21.3	0.40	7.23	56.1	54.7	20.1	3.33	2.97	2.7
26-27	30%	21.9	0.38	6.90	57.4	56.2	33.0	3.04	3.51	3.2
28-29	50%	22.4	0.40	7.98	55.4	54.1	27.6	2.57	2.76	2.5
30-31	70%	22.4	0.27	2.51	56.1	54.9	29.4	1.86	1.91	1.8
32-33	70%	21.9	0.31	3.98	55.9	54.8	29.6	1.76	1.74	1.6
36-37	30%	22.0	0.37	6.52	56.4	55.3	34.7	2.02	1.90	1.7
38-39	50%	23.8	0.33	6.67	56.4	55.1	35.3	0.94	1.85	1.7

Table 4.2: Summary of testing condition and collected water.

The FAN speed control requires a correlation between the percentage of absorbed power with the air flow rate circulating in both open and closed loop case. This estimation is based on the measurement of the mean velocity of the stream through the circular duct. The measurements were carried out with a hot wire anemometer with the following method:

[i] Time step between each i[th] element has a timestep of 10 seconds, equal to the acquisition time. Total sampling time for the evaluation of STE is 5 minutes.

- the probe position is at 1 metre distance from the elbow connecting the outlet of the ADS-HX with the inlet of the condensing unit. This to respect the general rule of a minimum free path length equals to 7 times the diameter (D_{duct}=12 cm) ;
- the probe measured mean velocity, within a temporal period of 2 minutes of continuous acquisition, at different depth along the radial direction of the duct section (shown in the sketch below), over three different and independent samplings;
- The procedure was repeated at different speed regimes, equivalent to a 20, 40, 60, 80, 100% of the maximum power.

The air velocity measurements are contained in the table of Annex E. The final mean air velocity trough the is reported in Table 4.3 was evaluated as the weighted average on the sectorial area as:

$$v_{avg} = \frac{\sum_{i=1}^{N} v_i A_i}{\sum_{i=1}^{N} A_i} \quad (4.8)$$

Where i is the reference number of the sector, N is 7, v the average velocity over the three different samplings, and A the area of the sector evaluated as reported in the equations below:

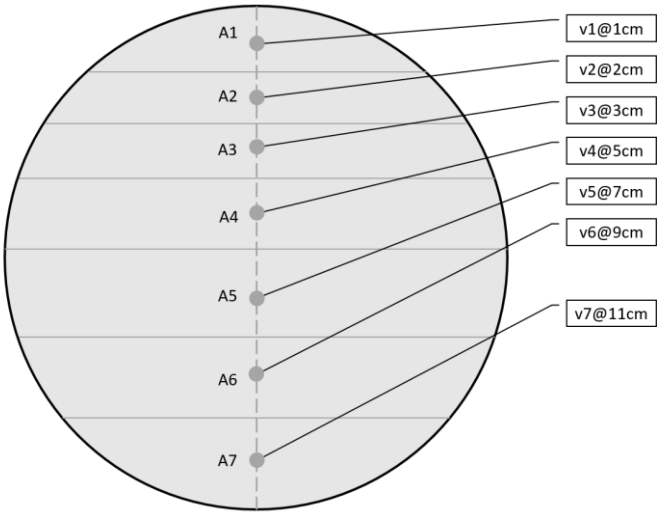

Area of the first sector:

$$A_1 = \frac{\beta_1 R^2}{2} - \frac{X_1(D - h_1)}{2} \quad (4.9)$$

$$X_1 = 2\sqrt{R^2 - (D - h_1)^2} \quad (4.10)$$

Area of the sectors 2 to 7:

$$A_i = \frac{\beta_i R^2}{2} - \frac{X_i(D - h_i)}{2} - \sum_{k=1}^{i-1} A_k \quad (4.11)$$

$$X_i = 2\sqrt{R^2 - (D - h_1)^2} \quad (4.12)$$

Power	Open Loop		Closed Loop	
%	m s^{-1}	m^3 h^{-1}	m s^{-1}	m^3 h^{-1}
20	0,29	11,6	0,26	10,2
40	0,74	29,1	0,64	25,2
60	1,07	42,1	0,97	38,2
80	1,27	50,4	1,11	43,6
100	1,57	62	1,28	50,7

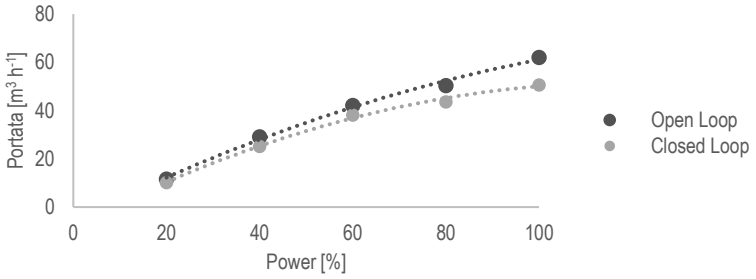

Table 4.3: Characteristic curve of power level/volumetric flow of the FAN 1, with the two different loop configurations, open and closed. On the left the table with values measured with the procedure explained above; on the right the plot of the extrapolated curves from the equations (4.13) and (4.14).

Where R and D are the radius (6 cm) and the diameter of the section, while β is the angle between the radius ad the intercept of the ith chord. Final values and related correlations are reported below with the equations (4.13) and (4.14):

$$\dot{Q}_{a_{ADS}} = -2.9 * 10^{-3}X^2 + 9.621 * 10^{-1}X - 5.806 \quad (4.13)$$

$$\dot{Q}_{a_{RIG}} = -4.2 * 10^{-3}X^2 + 1.002X - 7.996 \quad (4.14)$$

Where X is the percentage of the FAN (equivalent to PWM/10); $\dot{Q}_{ADS}$ is the airflow rate during the adsorption phase through the open loop; while $\dot{Q}_{RIG}$ is during the regeneration phase through the entire closed loop.

4.5.1 Charge Level Dependency

This paragraph investigates on dependencies of cycle performances on the charging level of the ADS, analysing in detail specific results of the adsorption/regeneration test couple #20-21. The following paragraph will report, with the same point of view, residual experiments. The graph on the left of Figure 4.10 shows inlet conditions to the ADS-HX and the mass variation during the 15 hours of testing. During the entire adsorption the fan was at 100% of rotation regime, corresponding to an air flow rate of 61.4 $m^3\,h^{-1}$. The average inlet temperature was in the average 21.2°C with a dew point of 4.1°C, corresponding to a relative humidity of 33%. At the begin of test the load cell measured an adsorbed water mass equal to 0.415 kg_w, corresponding to an initial water uptake of 0.017 $kg_w\,kg_{SiO2}^{-1}$. After 15 hours of adsorption the measured water mass was 3.01 kg_w, equivalent to a water uptake of 0.111 $kg_w\,kg_{SiO2}^{-1}$, as reported in Figure 4.11. The charge level indicator shows that within these operative constraints, the variation was from an initial value of 9.5% to the final 94%, with a curve derivative highly fluctuating as the environmental condition changes over time. The analysis of the outlet dew point from the ADS-HX, shows very high dry conditions for the first hour of adsorption (-3.5°C), reaching a final value close to the inlet at the end of the process (3.6°C inlet dew point versus 3.3°C outlet dew point). The switch to the regeneration phase required two preliminary steps before the begin of water condensation. Firstly, the air valve needs to complete the full rotation to close the air loop, with an elapsed time of 2.5 minutes. Secondly, the ADS-HX is heated up to the regeneration temperature. The pump G is flowing water between the ADS-HX and the plate exchanger H, reaching a final temperature of 55.4°C compared to the inlet temperature on the primary circuit of 58°C (red line of the graph on the right of Figure 5). This heating phase takes at least 15 minutes and is a transient necessary to lift up the temperature of entire sorbent mass (27 kg) from the adsorption value (21°C) to the regeneration (55°). The fan is off during these phases and reactivated only at the end of the preliminary steps, with a partial speed decided a priori, starting eventually the real step of regeneration and condensation of water. For the test #21 fan power level was 70%, corresponding to an air flow rate of 41.5 $m^3\,h^{-1}$. In the meanwhile, the activation of the other pump G and the blower F permits to reject outside the heat for the condensation of water in B maintaining the temperature close to the external environment, maintained constant with the external thermostat. Once the regeneration starts, the outlet dew point from ADS-HX (yellow line on the right graph of Figure 4.10) increases immediately from the value of 3.3°C up to 38.9°C. The rejection of heat permits to maintain the temperature at the condenser from 28°C up to 21°C during the 9 hours of regeneration, reducing as the total heat dissipated reduces. The mass reduction during regeneration is much faster than the

increase during adsorption, this permits to obtain a similar water uptake variation from 0.111 to 0.012 $kg_w\ kg_{SiO2}^{-1}$, then a total difference of 0.099 $kg_w\ kg_{SiO2}^{-1}$. In less than 10 hours this value reduced from 42 to 32°C, as the water contained in the ADS-HX is lower than 0.5 kg. When the outlet dew point and the ambient are equal, water condensation stops and the water harvesting cycle is concluded. The mass difference between the end of ADS and REG is corresponding to condensed water, around 2.4 kg with a water uptake variation within the cycle of 0.089 $kg_w\ kg_{SiO2}^{-1}$. The difference between the outlet dew point and the condensing temperature reduces in time as the progressive discharge of the material. This means also that the potential moisture difference at the condensation step is reducing in time, decreasing the rate of condensation, with drawbacks on energy performances. This is clear from the graph in Figure 4.12, where both the water condensation rate in cL min^{-1} and the STE in kWh L^{-1} are compared. Differently from the previous graphics, where each plotted point is an instantaneous measurement within the monitoring time step Δt~11s, values in Figure 4.12 are evaluated as the arithmetic average over 40 consecutive values.

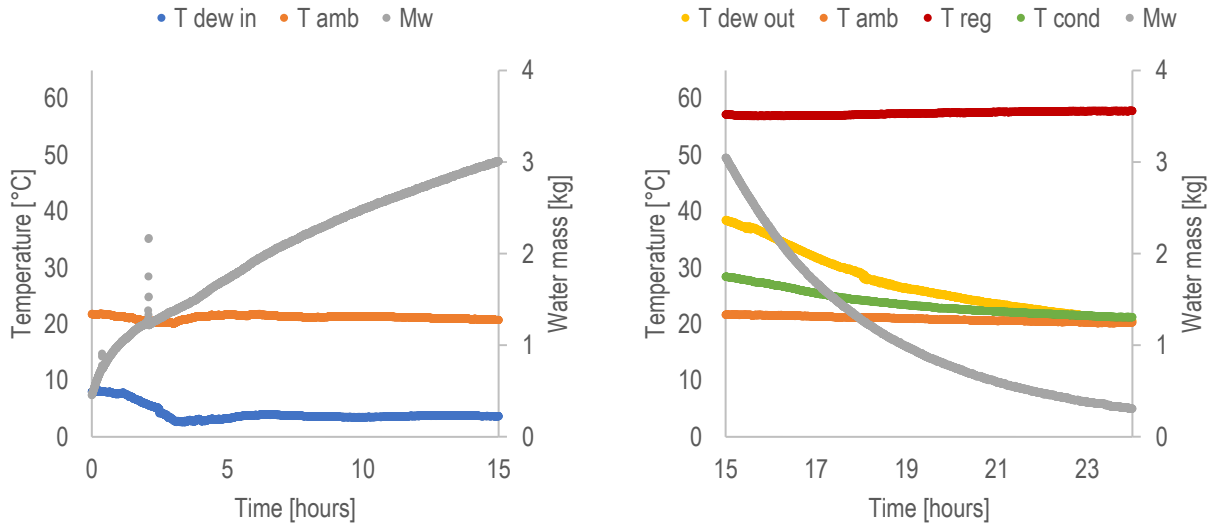

Figure 4.10: On the left the adsorption test #20. Air inlet dew temperature ($T_{dew\ in}$), inlet ambient temperature (T_{amb}), and total adsorbed water mass (M_w) are depicted over the entire adsorption operational time (15 hours). On the right the regeneration/condensation test #21. Air outlet dew point ($T_{dew\ out}$), ambient temperature outside from the closed loop (T_{amb}), inlet water temperature for sorbent regeneration (T_{reg}), air temperature measured at the condensation point (T_{cond}) and total adsorbed water mass (M_w) are depicted over the entire regeneration operational time (9 hours).

The timestep between each point is ~7.5 minutes. The maximum value of condensation rate is 1.41 cL min^{-1} reducing rapidly to 0.35 cL min^{-1} after 5 hours of continuous functioning. After 8 hours values are quite negligible, and the fluctuation due to the increased uncertainty of direct measured values generate a consistent oscillation of the post computed indicators, reducing its reliability on the description of the phenomenon. The STE has an opposite behaviour: the rate of condensation (denominator) is reducing faster than the absorbed thermal power (numerator) by the machine, consequently the relative ratio is an increasing function over time. Tested results showed values close to 1 kWh L^{-1} and quite constant for the first 2 hours of functioning, reaching the value of 2.3 kWh L^{-1} after 5 hours. The consecutive phase is characterized by a faster reduction of the process efficiency,

and the rise of the STE is higher than 5 kWh L^{-1}. As before, after 5 hours of continuous process, data fluctuations are comparable to the data values itself, increasing consistently the uncertainty.

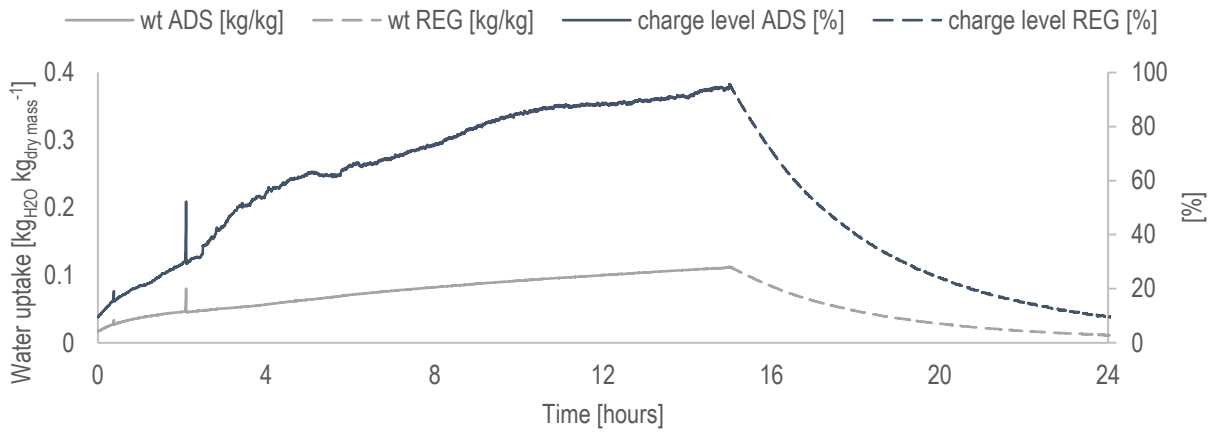

Figure 4.11: Transient behaviour of the silica water uptake and level of charge for both adsorption and regeneration tests #20-21.

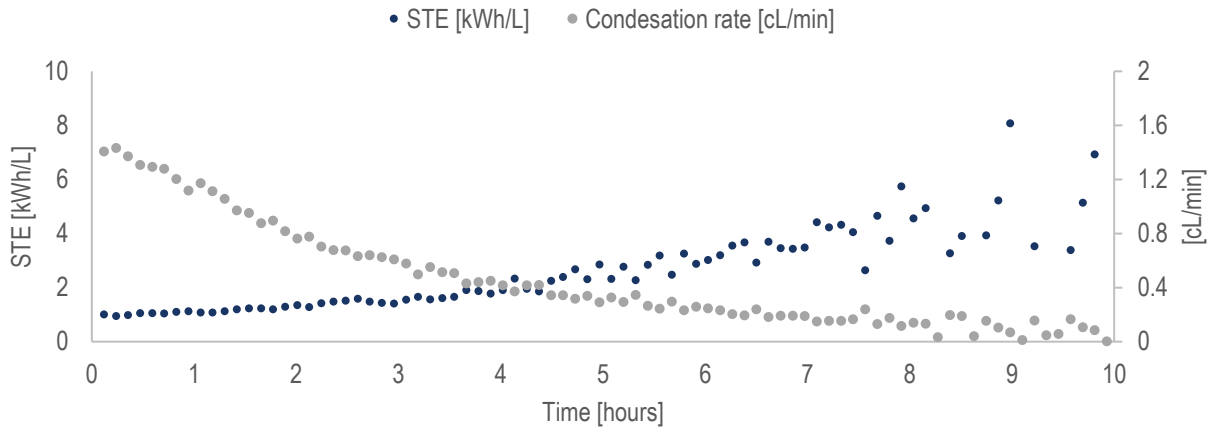

Figure 4.12: Transient behaviour of Specific Thermal Energy (STE) and water condensing rate over the regeneration/condensing test #21. Each point represents the average value of 40 consecutive values.

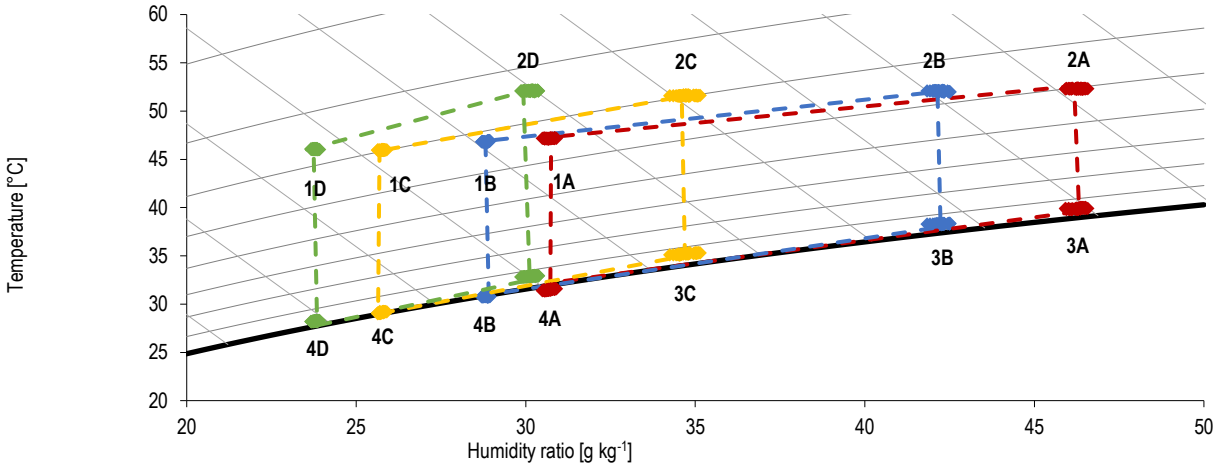

Figure 4.13: Real cycle of regeneration for water condensation with the intermediate heat recovery. Transformation 1-2 is the regeneration of the sorbent, 2-3 is the heat dissipation towards the dew point, 3-4 is the vapor/liquid phase change among the dew line, 4-1 is the preheating step recovering the heat from the entire condensing line 2-3-4. Cycle A depicts the situation @30 minutes from the begin of the regeneration; B @90 minutes; C @190 minutes; D @270 minutes.

Most of the inefficiencies of this cycle are connected to parasitic terms of heat absorption not directly connected to the condensation of water and not recovered in the exchanger C. Indeed, during the transformation, a portion of heat supplied to air causes a sensible rise of temperature instead of a latent transformation that, at the end of the cycle, goes rejected to the environment through the dry cooler unit F and G, without any positive contribution. This situation is graphically depicted in Figure 4.13, where different and measured steps of the cycle (from 1 to 4) are drawn positioned over the psychrometric chart over different moments of the entire test #21. The graph is a picture of the cycle situation collecting consecutive measured points over a 10 minutes window, and at a different time scale from the begin of regeneration, respectively @30 minutes (red), @90 (blue), @180 (yellow), @270 (green). The first aspect is that the real cycle is moving on the (T, x) diagram from the right to the left, due to the lower release of moisture from the sorbent media. Water uptake reduction together with a constant regeneration temperature means a continuous reduction of the equilibrium RH.

Second aspect is the shape variation of the cycle. For example, the regeneration step 1-2 of A is different from D on both the quantitative and qualitative aspects: the total enthalpy variation of the transformation is $h_{1\text{-}2A}$~45 kJ kg^{-1}, of which only 7 kJ kg^{-1} corresponds to a sensible increase and 38 kJ kg-1 are the latent part. At D the weight of sensible part increased because its value is constant at 7 kJ kg^{-1}, while the latent one is reduced to 16 kJ kg^{-1}. This lead an increase of the transformation tilt, going away from the isothermal line. Another shape modification is caused by the ratio between the precooling stage 2-3 and the condensing line 3-4. Because the maximum vapor pressure generated from regeneration is reducing, the distance between 2 and the corresponding dew point increases, consequently the enthalpy difference increases from $h_{3\text{-}2A}$~14 kJ kg^{-1} to $h_{3\text{-}2D}$~20 kJ kg^{-1}, while condensing line reduces consistently from 16 to 6 kJ kg^{-1}.

4.5.2 Condensing Temperature dependency

With similar initial charge level of the ADS-HX, the increase of ambient temperature reduces global performances, both on water production and efficiency. For example, increasing the temperature from 23 to 35°C (as shown with tests #25 and #37 in Figure 4.14) corresponded to a reduction of water production from 3 liters to 1.9, despite the similar initial water content of 0.13 kg_w/kg_{SiO2}. On the contrary there's no effect on the outlet dew point, that had similar maximum value close to 40°C. This indeed is mainly function of the two variables, water uptake and equilibrium temperature, that in both cases is close to the regeneration temperatures respectively 54.7°C and 56.4°C for #25 and #37. It is important to notice that the flow regime between the two tests is slightly different because the different fan level power: 50 against 30%, accounting respectively for 31.6 and 18.3 m^3h^{-1}. In Figure 4.15 is instead shown the behaviour of the 3 performance indicators, STE, thermal efficiency and condensing rate, with a condensing environment of 20, 27 and 35°C. As saw before, the increase of temperature reduces the rate of production of liquid water, but the benefits of a lower condensing temperature became negligible after around 4-5 hours of working. Indeed, if at 20°C the water rate is almost the double than at 35°C (1.2 cL min^{-1}@20°C against 0.55 cL min^{-1} @35°C), after 5 hours the value is similar and equal to 0.42

cL min^{-1} @20°C and 0.31 cL min^{-1} @35°C, finally after 10 hours it reduces again of 55-70%. The STE has the minimum value of 1.1 kWh L^{-1} at 20°C, 1.45 at 27°C and 1.93 at 35°C, increasing of 4-5 times at the end of each test. On the contrary, the maximum of the global thermal efficiency was respectively 62, 47 and 34% for each test, diminishing after 10 hours up to 9-17%. Clearly these evaluations cannot be taken as absolute considerations, but from the qualitative point of view this is useful to identify the criticalities behind this system:

- driving a full adsorption is not always the best approach. For the adsorption stage the goal is to reach the highest level of charge, with the constraints of outside conditions. Very good example are tests #26 and #30 where can be noticed that despite the system is still in adsorbing mode, the level of charge is not changing (even reducing in test #30) after many hours. Inlet air conditions are strongly influencing this aspect;
- if a full regeneration maximizes the total amount of water that can be extracted, at the same way results in a less efficient utilization of the energy if compared to a partial cycle. This is also important when the heat availability is a constraint. In the case of solar energy constraints are the surface availability, and operative time, that reasonably doesn't exceed a duration of 5-8 hours.

These considerations outline an eventual problem of "management" of a system like this. The use of numerical modelling to describe the functioning of the ADS-HX ca be a solution to forecast performances according to variation of environmental conditions. Further, this can be used as tool for a correct design of the component, but eventually also as a decision tool to understand how much long a cycle should be stand. The elaboration of this model is in the paragraphs 4.7.

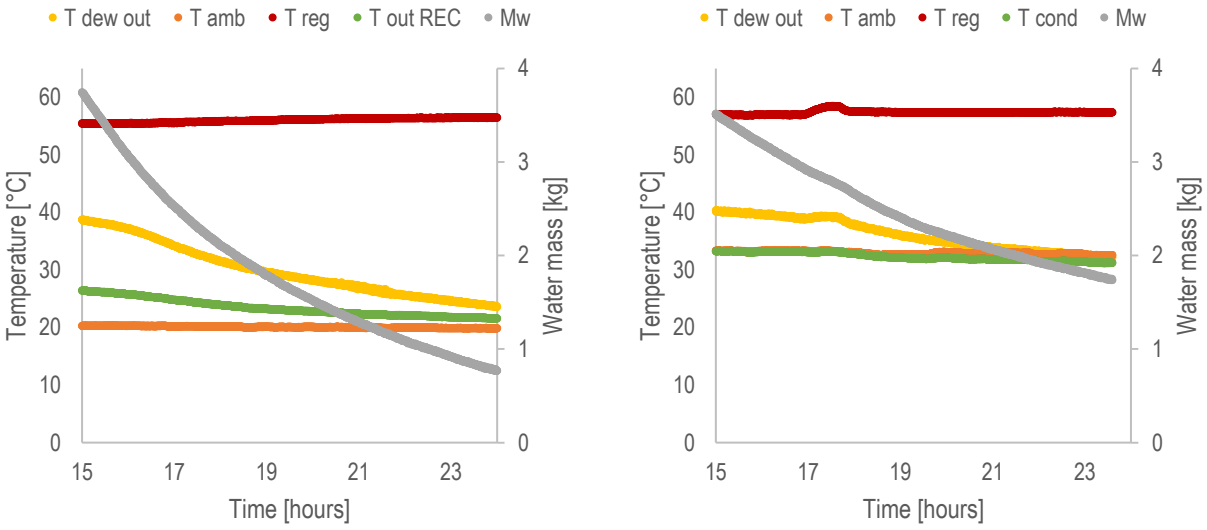

Figure 4.14: Comparison between two different tests. On the left regeneration #25, where the condensing environment was during the 10 hours of functioning 23.2°C in the average. While on the right regeneration test #37 with an average condensation temperature of 34.7°C.

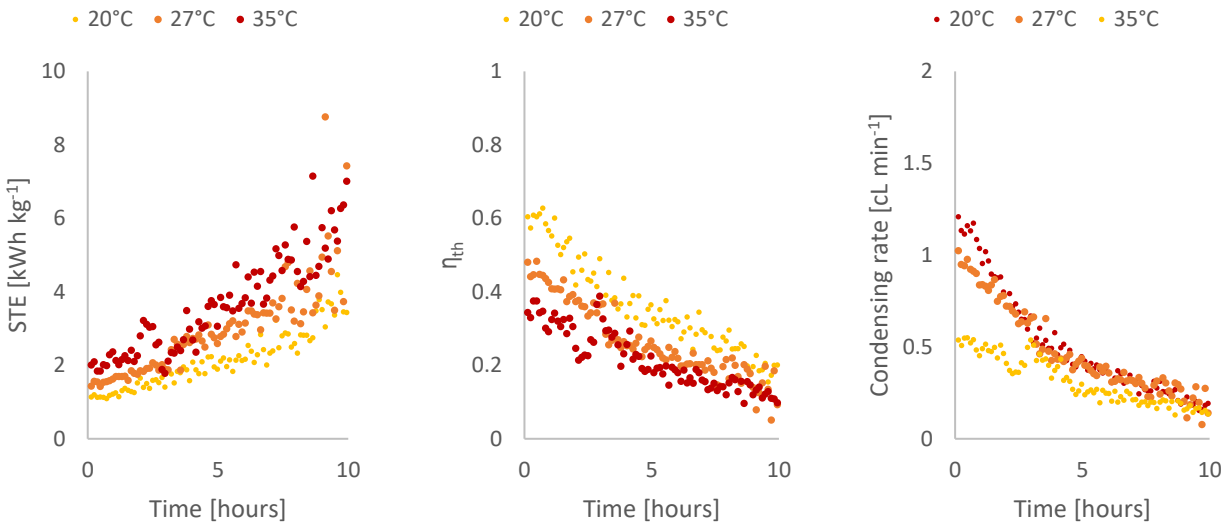

Figure 4.15: Effect of condensation temperature (20-35°C) on STE, thermal Efficiency and rate of water generation.

4.5.3 Entire Test Collection

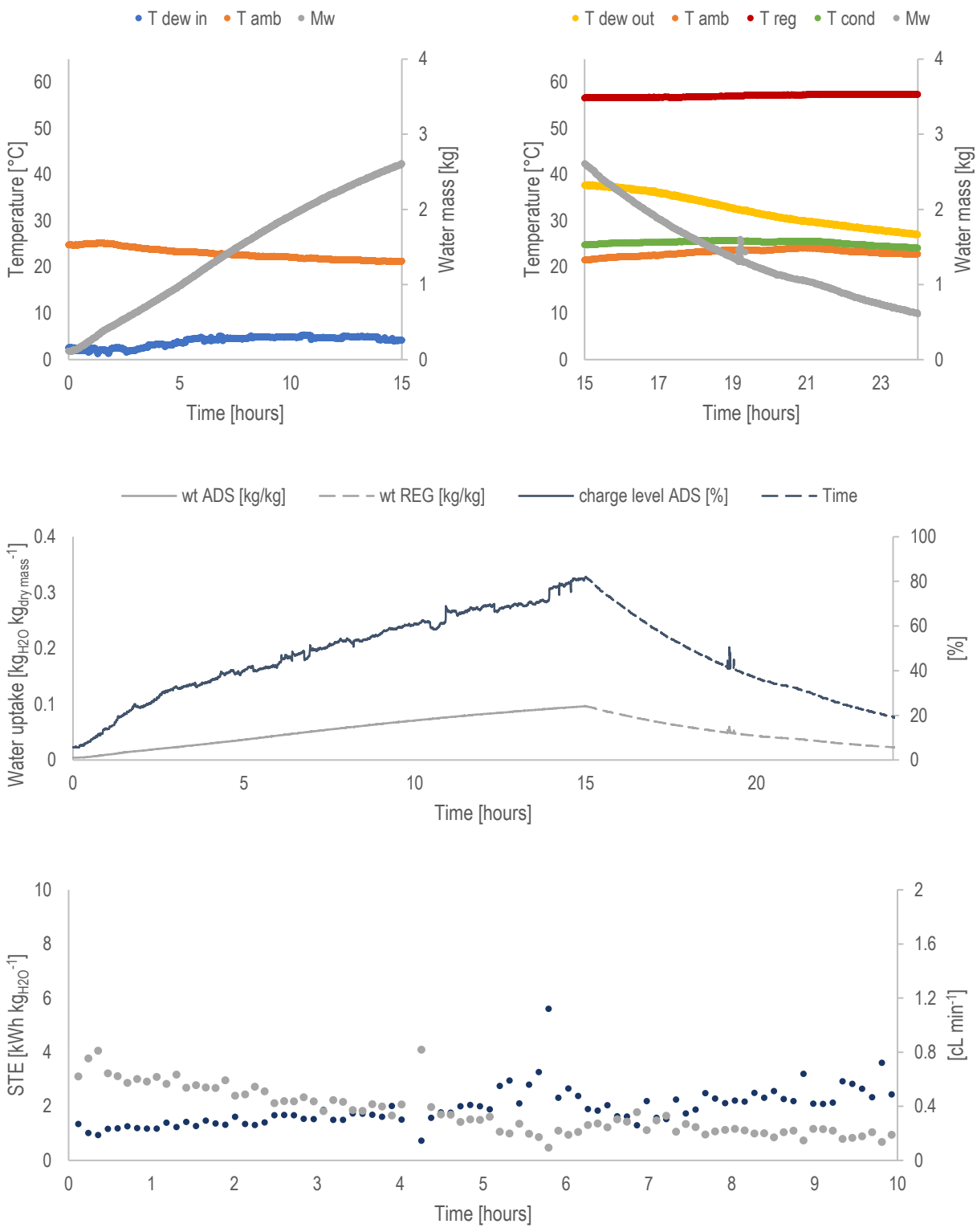

Figure 4.16: Test 22-23

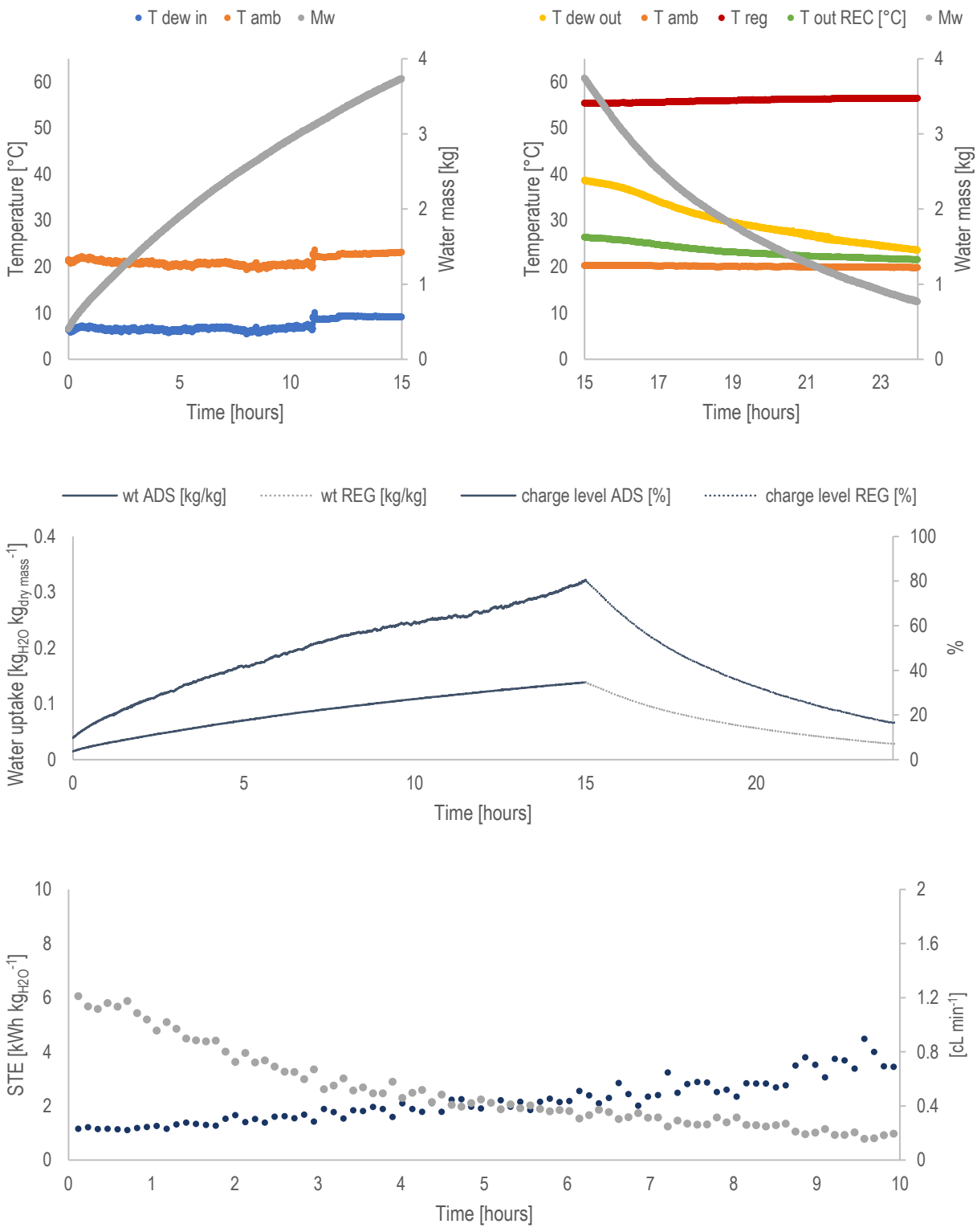

1758 **Figure 4.17:** Test 24-25

1759

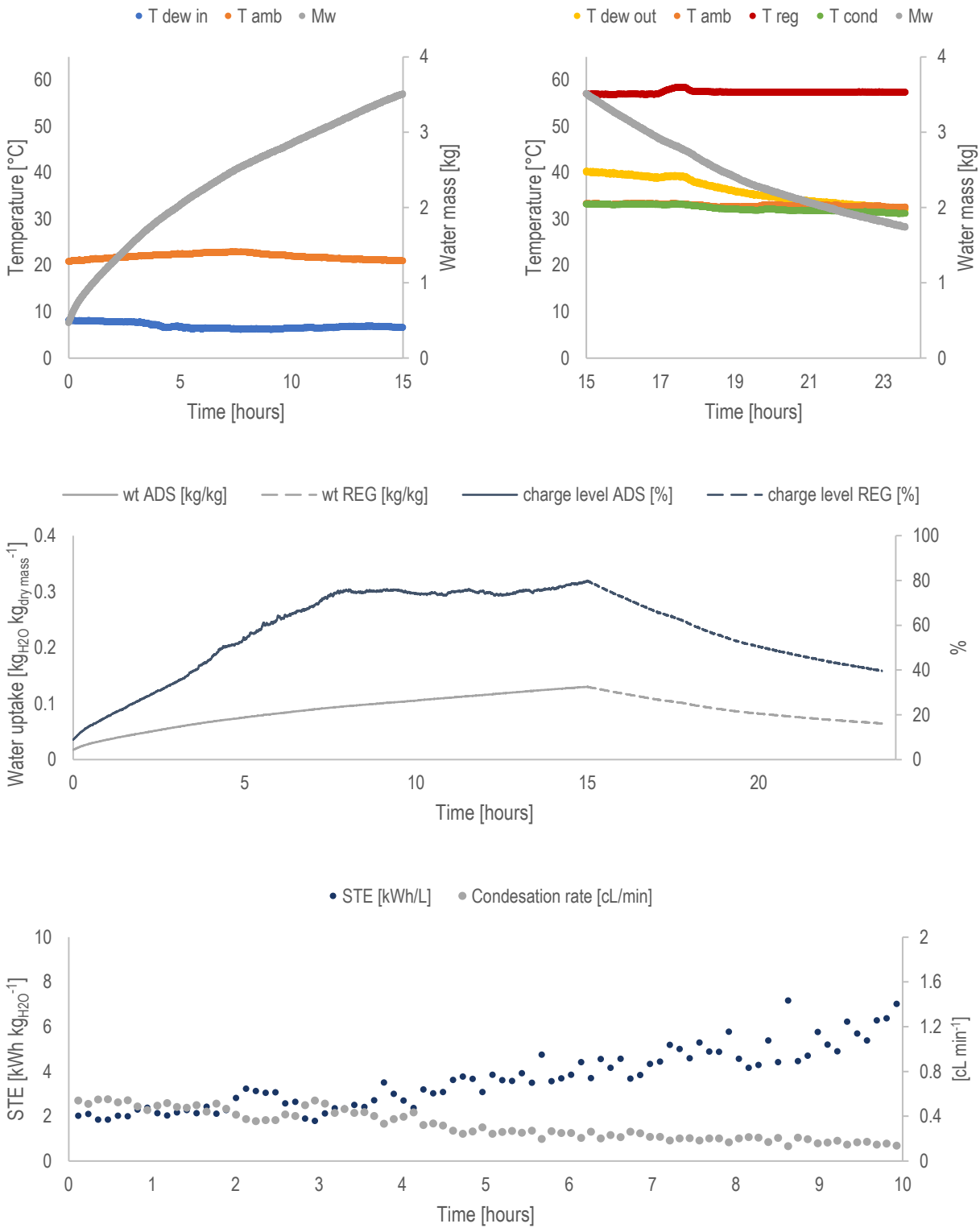

1760 **Figure 4.18:** Test 26-27

1761

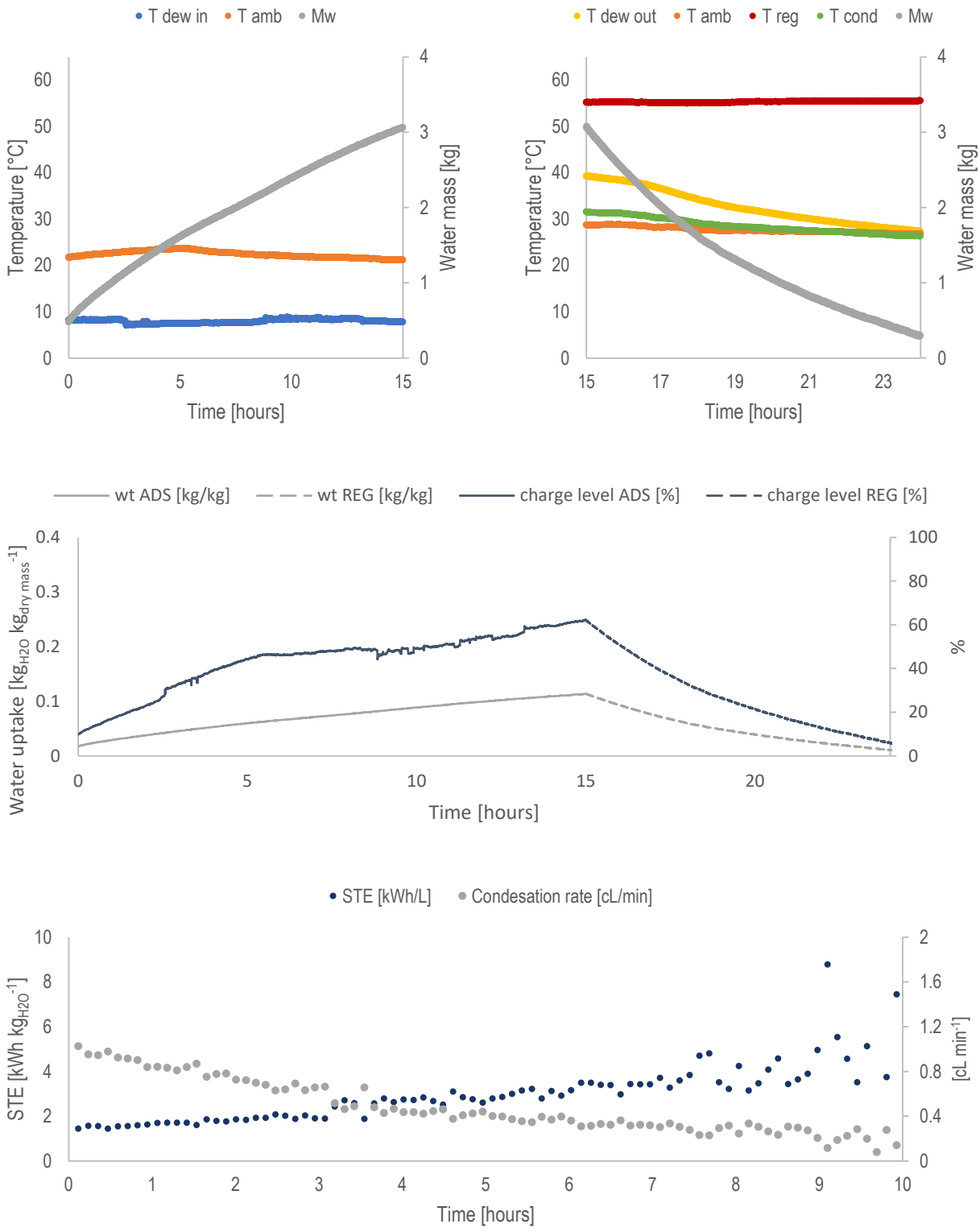

1762 **Figure 4.19:** Test 28-29

1763

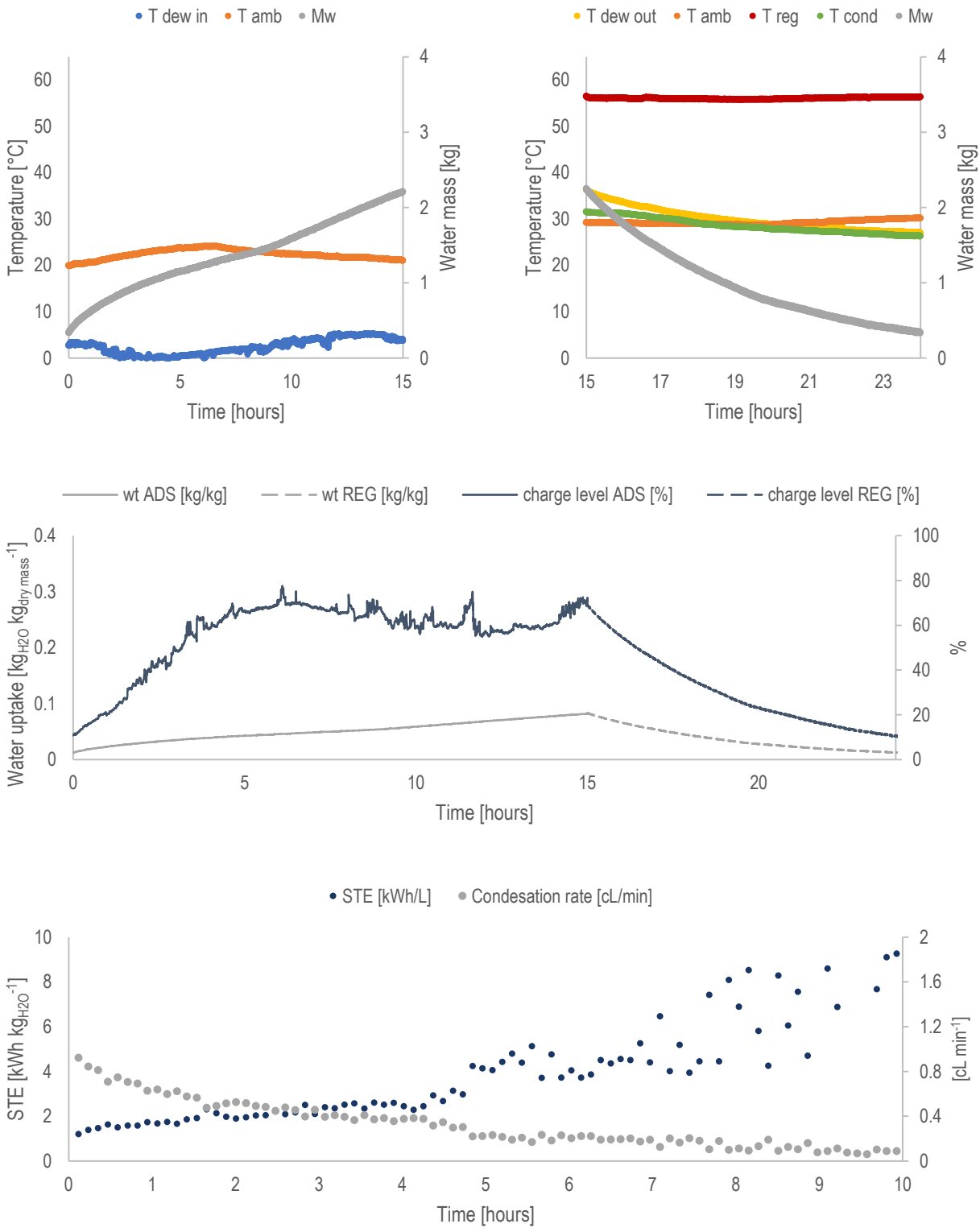

1764 **Figure 4.20:** Test 30-31

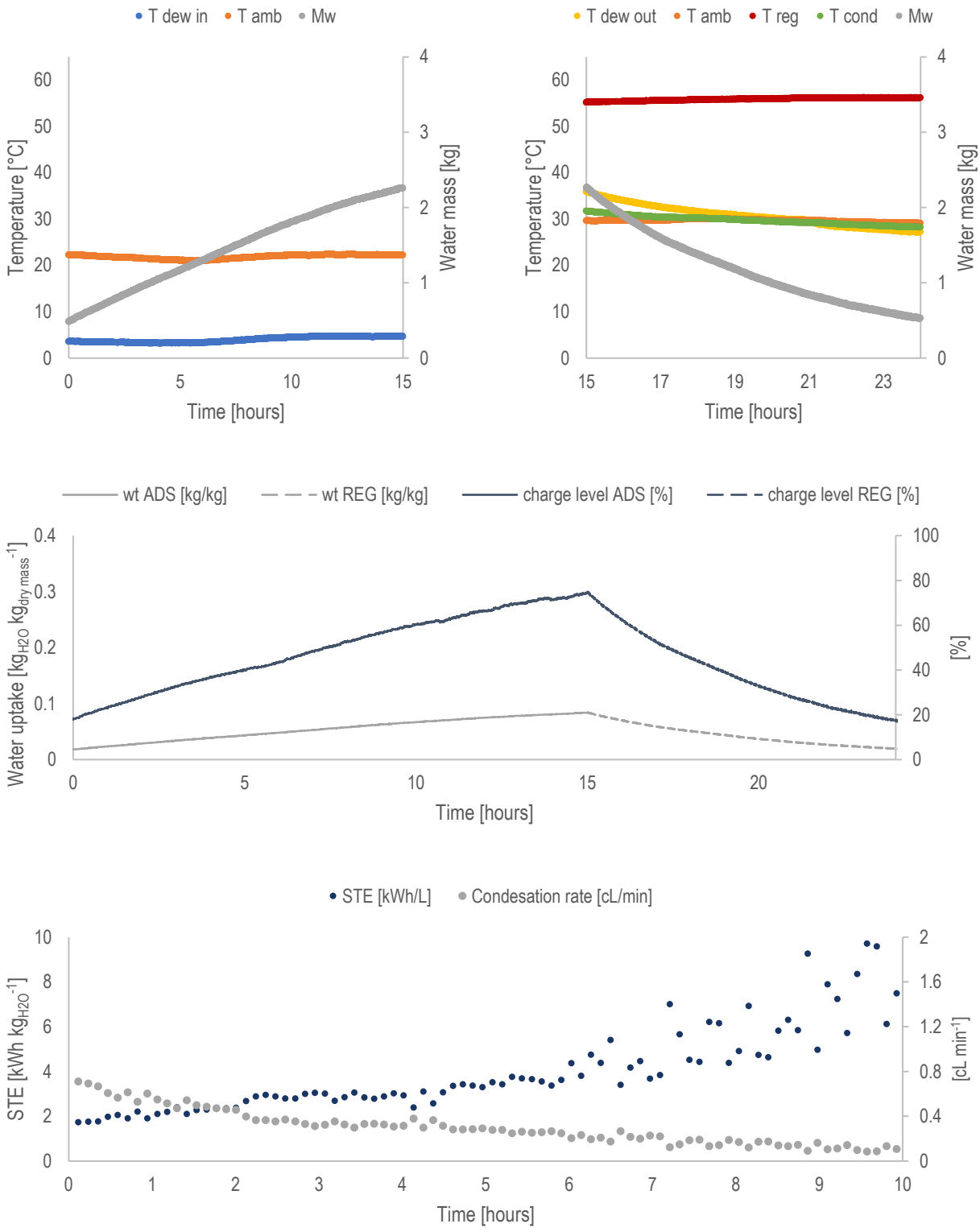

Figure 4.21: Test 32-33

1767

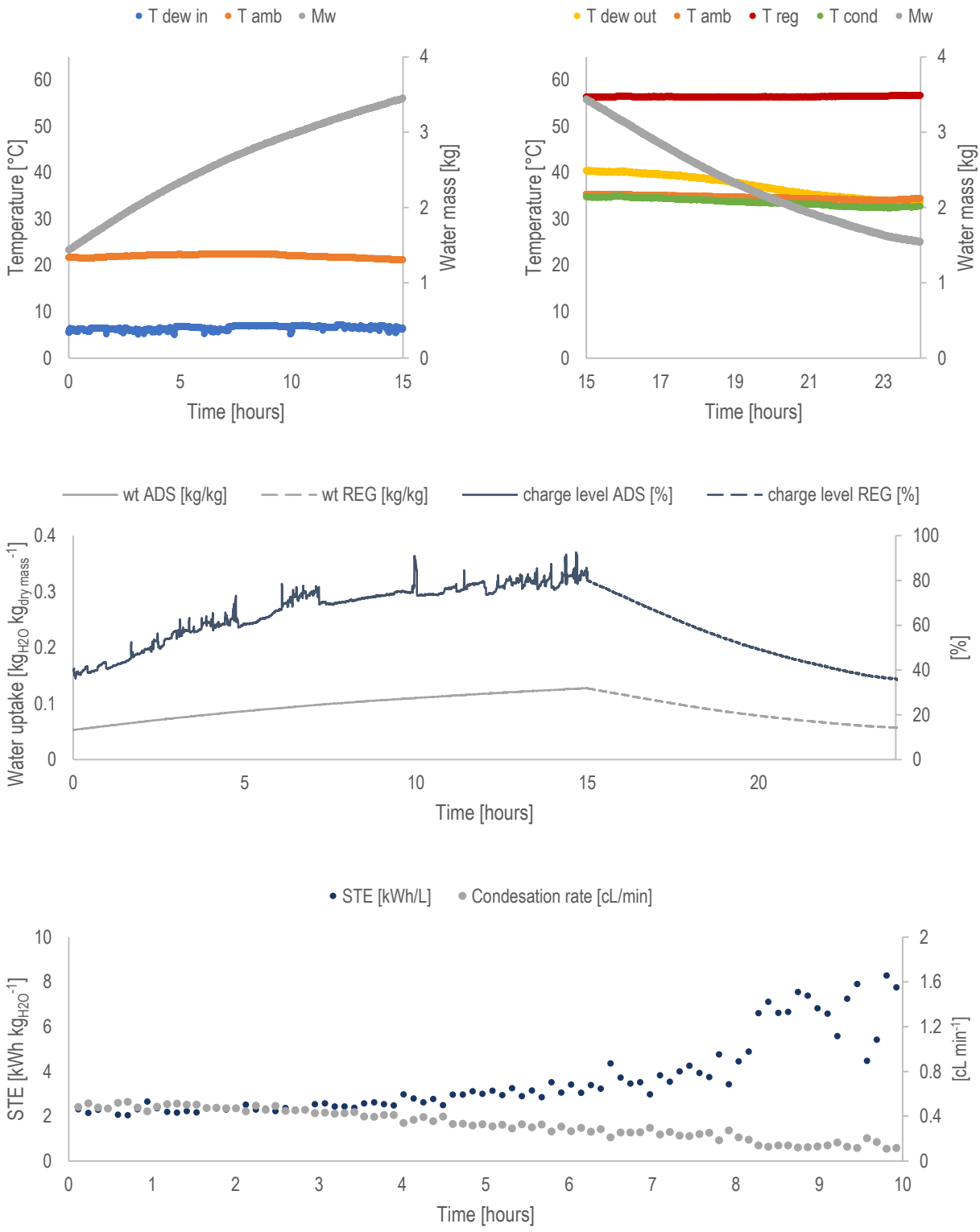

1768 **Figure 4.22:** Test 36-37

1769

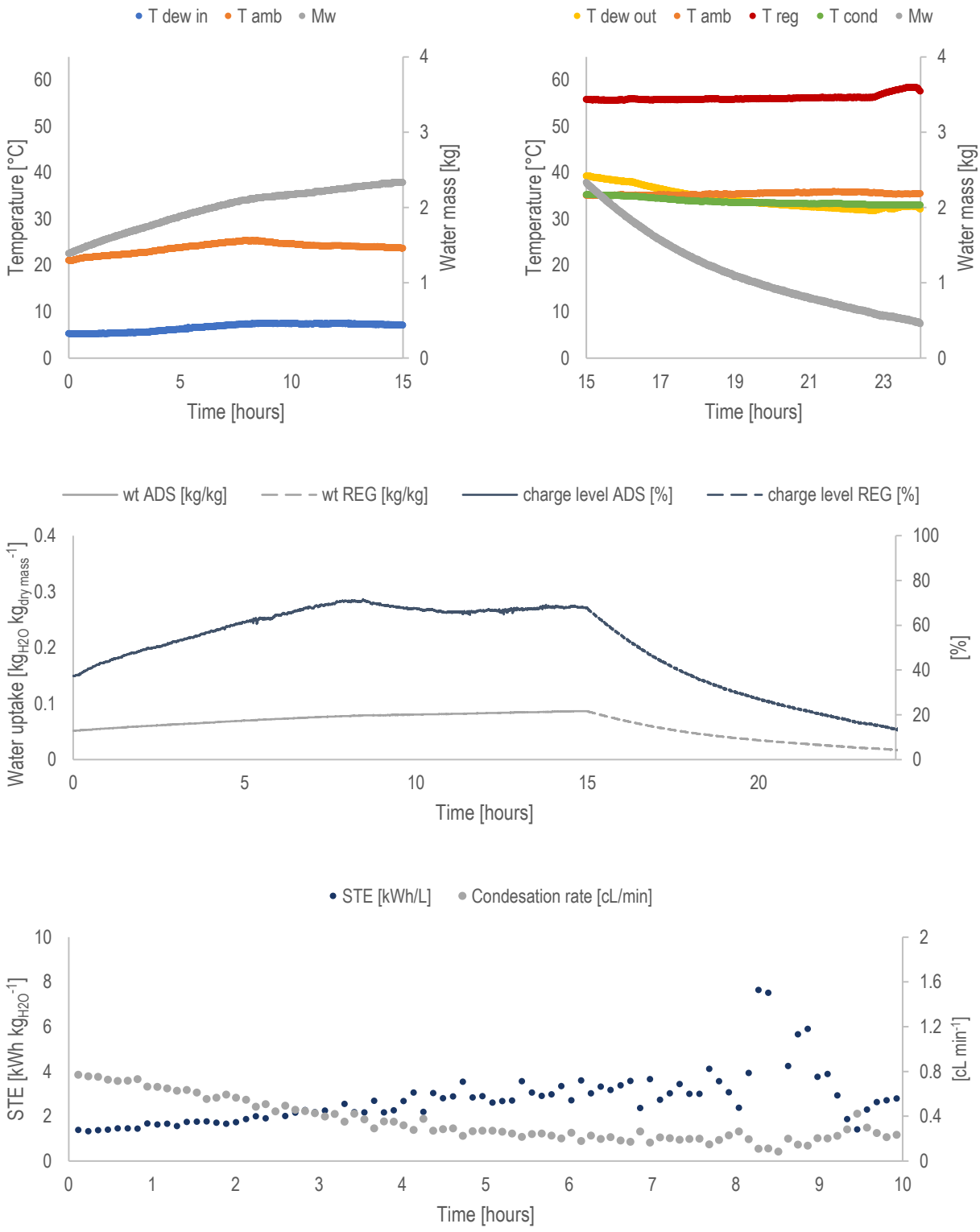

1770 **Figure 4.23:** Test 38-39

1771

4.6 Comparison with other AWG devices

Experimental analysis showed performances of the investigated configuration, emphasizing some important parameters: the total amount of heat used for the transformation, and then the efficiency; the total amount of produced water; the water uptake variation. In this paragraph will be carried out a comparison with other systems under development [160] [163] [165] [166] [170] [203] [204]. In these papers, authors engineered solar driven prototypes, with the goal of producing liquid water out of the humid air using new and innovative sorbent materials and composites. The novelty of these systems mainly consists in the use of sorbent with enhanced water uptakes especially for dry climates (T_{dew}<10°C). However, when the application at component/prototype level is tested in a real/simulated working environment, a general decline of performances from theoretical is experienced. Indeed, the working environment defines different constraints limiting presumed performances: for example, the use of solar energy, without concentration, limits the maximum working temperature in the range of 50-70°C, to guarantee reliable solar fractions all over the daytime [202]. In addition, condensing at ambient temperature, without refrigeration, implies typical minimum values around 20-35°C, according to the local climate. These values defined roughly boundary limits of an adsorption/desorption cycle operated in a real environment.

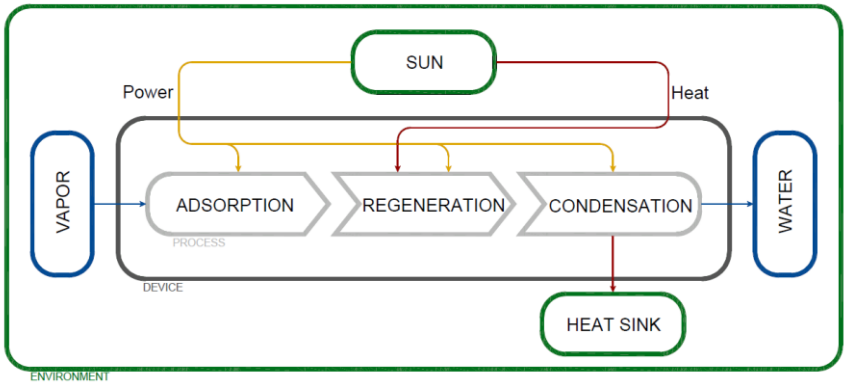

Figure 4.24: Sketch of the boundary for the energetic analysis of Atmospheric Water Generators

Results from reference papers where used as baseline of comparison, applying a common methodology, for the estimation of related performances. Data needed for this comparison, often provided by authors, are the mass of collected/estimated water (M_w, obtained among the day or the experiment) and mass of dry sorbent (M_s) used in the prototype; specific incident solar radiation (G); surface of solar collector aperture (A_C); operational times for adsorption (t_{ADS}) and regeneration (t_{REG}). Among different possibilities for the evaluation of prototypes performances, following parameters have been chosen for their relevance:

- the Specific Solar Energy (SSE) defines the total amount of solar radiation, incident over the collector aperture, necessary to produce 1 liter of liquid water, and is evaluated as the ratio between incident total radiation ($A_C \sum_i^{t_{REG}} \Delta t_i \, G_i$) and M_w. The only difference with the STE is the limit boundary for the

analysis (Figure 4.24): for the STE is only limited to the device, while for the SSE includes also the efficiency of the technology converting solar energy into heat.

- The water uptake variation of the sorbent (Δ_w), between the adsorption phase and regeneration phase, evaluated as the ratio M_w/M_s;
- the global efficiency (η) of the process, defined as the ratio between the energy content of produced water (the latent heat content of condensed water, at the specific condensing temperature $H_w|_{T_{cond}}$), as the ratio $A_C \sum_i^{t_{REG}} \Delta t_i \, G_i * \left(M_{w_i} H_{w_i}|_{T_{cond}}\right)^{-1}$.

Experiment			Material			
Ref#	Year	Descritption	Type	Mass	Volume	H_{ADS}
				kg	m^3	kJ mol^{-1}
1[205]	2017	RH controlled environmental chamber with solar simulator	MOF-801	$1.79x10^{-3}$	$1.03x10^{-5}$	45
		Outdoor with solar radiation	MOF-801	$1.34x10^{-3}$	$7.75\ x10^{-6}$	45
2[170]	2018	Outdoor with solar radiation 0.8-1 kW/m2	MOF-801	$2.98\ x10^{-3}$	$1.08\ x10^{-5}$	45
		Outdoor with solar radiation 0.8-1 kW/m2	MOF-801	$2.98\ x10^{-3}$	$1.08\ x10^{-5}$	45
		Outdoor with concentrated (X1.8) solar radiation	MOF-801	$2.98\ x10^{-3}$	$1.08\ x10^{-5}$	45
3[160]	2019	Indoor water harvesting	MOF-303	4.33E-01	0.21	52
		Outdoor and solar electricity	MOF-303	4.33E-01	0.21	52
4[166]	2007	Controlled regeneration environment	MCM-41/CaCl2 30÷60%	0.1	-	50
		Outdoor, total passive solar device	MCM-41/CaCl2 53%	0.4	-	50
5[165]	2017	Outdoor, regeneration driven with air evacuated tube	ACF/CaCl2	2.25	-	-
		Outdoor, regeneration driven with air evacuated tube	ACF/LiCl	40.8	-	-
6[206]	2018	Evaluation of weight reduction after sun exposure, from complete saturated state	CuCl2	-	-	-
			CuSO4	-	-	-
			MgSO4	-	-	-
7[163]	2018	Proof of concept of sunlight regeneration. 0.8÷1.2 kW/m2	PAM-CNT-CaCl2	35	$7.88\ x10^{-3}$	-
8[169]	2020	Rotating cylinder, 25% surface exposed to simulated sunlight	HCS-LiCl nanoparticle	$2.93\ x10^{-3}$	6.92E-04	-
9[207]	2019	Thermal switching between hydrophilic/hydrophobic	PPy-Cl/poly-NIPAM	-	-	-

Table 4.4: Summary table with the characteristics of the experiments for the reference papers.

Data from reference papers needed for the evaluation of comparison parameters are collected in the Table 4.4 and 4.5. In this study parameters needed to perform energetic analysis are directly sampled: inlet and outlet

temperature of water stream (T_w) during regeneration; the related mass flow rate ($\dot{m}_w$). The solar energy is then evaluated as the ratio between the heat absorbed by the adsorption heat exchanger $\sum_i^{t_{REG}}(cp_w \dot{m}_w \Delta T_w)_i dt_i$ and the solar thermal collector efficiency η_{SOL}. This value, defined by the power curve equation as in the standard EN12975, is equal to:

$$\eta_{SOL} = a_0 + a_1 * \frac{T_m - T_{amb}}{G} + a_2 * \frac{(T_m - T_{amb})^2}{G} \quad (4.14a)$$

Where T_m is the medium temperature of the heat transfer fluid flowing through the plat plate collector; T_{amb} is the external ambient temperature; G is conventionally a normal radiation equal to 1000 W m^{-2}; $a_0(0.82)$ considers the optical losses reducing the total amount of absorbed sunlight on the surface of collector; $a_1(3.82)$ and $a_2(0.01)$ are related to the thermal loss (radiative, convective and diffusive) in the conversion of the absorbed sunlight in to heat.

Results of this comparison analysis are reported in Table 4.5 and Figure 4.25.

Three graphs in Figure 4.25 depict a sort of rank among the different configurations and experiments. Lower regeneration temperature led in general to lower SSE. But this is not sufficient. For example, on the left of Figure 4.25 is evident how the case of MOF-801 represent a sort of outlier from the rest of points. Main reason in this case was a not high enough temperature for regeneration (without concentration lens) that basically resulted in a failure test. Experiment carried out in this research showed lowest values of SSE at the lowest regeneration temperature. Similar conclusion, but with opposite behaviour, comes from the graph on the right. In particular, in this case it is interesting to see how, despite improved properties of adsorption material, resulting operation is not necessarily associated with an improved performance of the system. Anyway, in the range of dew point equal to 3-10°C silica gel showed comparable water uptake variation compared to one of the best materials available today, MOF-801. Main merits for this equivalence are the reduced regeneration temperatures obtained with an isothermal process. Despite these considerations, must be clarified that silica gel is not suitable for all the climates. In very dry environments with dew points lower than 0°C, silica gel cannot exhibit any sufficient Δw to be applied in a cycle to produce water.

	Adsorption							Regeneration					Condensation			
#Ref	T_{amb} [°C]	T_{ADS} [°C]	RH_{ADS} [%]	Pv [kPa]	T_{dew} [°C]	W_{ads} [g g-1]	Time [hours]	How [-]	T_{REG} [°C]	W_{REG} [g g-1]	Time [hours]	Δw [g g-1]	How [-]	T_{cond} [°C]	T_{amb} [°C]	M_w [kg]
1[205]	35	35	20	1.2	10	0.25	1.17	F/D	80	0.02	0.5	0.23	e	10	35	$4.12*10^{-4}$
2[170]	25	25	65	2	18	0.35	all night	A	66	0.05	8	0.3	e	23	32	$4.02*10^{-4}$
	20	17	40	0.94	6	0.28	8 ÷ 11	A	74	0.16	3.67	0.12	a	28 ÷ 33	28 ÷ 33	$3.58*10^{-4}$
3[160]	23	20	50	1.4	12	0.31	8 ÷ 11	A	74	0.175	4	0.135	a	30 ÷ 35	30 ÷ 35	$4.02*10^{-4}$
	20	17	40	0.94	6	0.28	8 ÷ 11	B	100	0.01	2	0.27	a	28 ÷ 33	28 ÷ 33	$8.05*10^{-4}$
	27	-	32	1.1	9	-	14[1]	F/D	120	-	9[1]	0.13 ÷ 0.16	d	0	27	1.3
4[166]	15 ÷ 25	-	10 ÷ 70	0.3 ÷ 1.2	-9 ÷ 9	-	12 ÷ 15[2]	F/D	120	-	8÷10[2]	0.03 ÷ 0.12	d	0	15 ÷ 25	0.55 ÷ 0.75
	10 ÷ 15	-	80 ÷ 90	1 ÷ 1.5	6.7 ÷ 13.4	0.8 ÷ 1.4	24	F/D	80	<0.1	2.5	-	-	-	-	0.24 ÷ 0.29
5[165]	10 ÷ 15	-	80 ÷ 90	1 ÷ 1.5	6.7 ÷ 13.4	0.87	all night	A	80	0.26	all day	0.61	c	-	-	0.223
	25	-	70	2.2	19.2	0.53	8	D	85	0.14	5	0.39	b	40	30	0.32
6[206]	30 ÷ 33	-	70 ÷ 85	3 ÷ 3.7	30	0.27	11	D	80	0.02	7.5	0.25	b	40	30	9
	22	-	60	1.6	13.9	-	>24	C	80	-	1.5	0.17	c	22	22	-
7[163]	22	-	60	1.6	13.9	-	>24	C	80	-	1.5	0.21	c	22	22	-
	22	-	60	1.6	13.9	-	>24	C	80	-	1.5	0.16	c	22	22	-
	26	-	60 ÷ 70	2 ÷ 2.4	17.6 ÷ 20	1.06	15	A	75	0.49	2.5	0.57	c	-	28 ÷ 32	20
8[169]	22	22	60	1.4	12	-	3[3]	C	47 ÷ 50	-	1[3]	0.1	c	22	22	$1.25*10^{-3}$
9[207]	25 ÷ 27	25	60 ÷ 90	2.1÷2.7	18÷22	5	4	A	42 ÷ 65	0.2	3.5	4.8	f	25	25	-

Table 4.5: Summary of al the information recovered from reference paper for the evaluation of performance indicators as mentioned above. The column "How" indicates the approach used to drive regeneration and condensation. For regeneration: A=direct sun exposition; B=concentration of solar radiation; C=simulated solar radiation @1kW m^{-2}; D=hot air; E=hot water; F=electric resistance heater. For condensation: a=passive heat sink; b=dry cooler; c=passive surface condensation; d=vapor compression unit; e=thermoelectric cooler; f=direct liquid recovery. [1]9 cycles in 24 hours of around 1.5-2 hours of adsorption and 1 hour of regeneration; [2] 8-10 cycles in 24 h of around 1.5-2 hours of adsorption and 1 hour of regeneration; [3] continuous regeneration operating 3 cycles in 4 hours of which 25% of time is regeneration and 75% adsorption

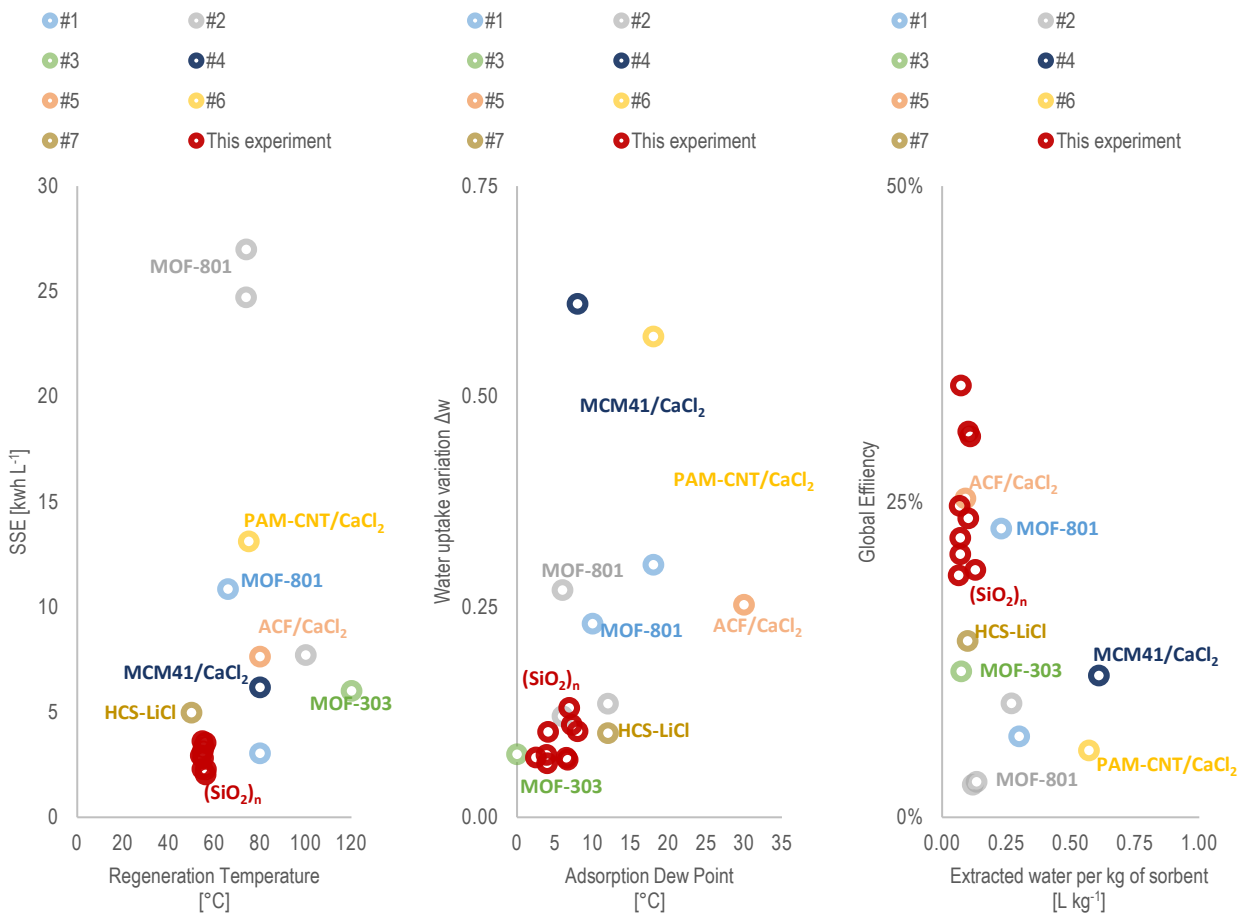

Figure 4.25: Comparison charts between reference paper [160]·[163]·[165]·[166]·[170]·[203]· [204] and this experiments. On the left the SSE is ordered over the specific regeneration temperature of those experiments. In the middle the total water uptake variation is compared using as reference the dew point during the respective adsorption phases. On the right the global system efficiency is ordered over the extracted liters of water per unit of dry sorbent mass.

Thermal energy is not the only requirement to perform all the steps of a complete water production cycle (adsorption, regeneration, condensation). Indeed, the three process may need in general power to drive auxiliaries (fans, pumps, valves, etc…), as our case. Further on, some of the experiments analysed used active refrigeration [171] as a trick to assist the condensation step. This increase obviously the need of electric energy, and from the global point of view, may result in a reduction of efficiencies. The evaluation of the total electric energy requires than the average power for each step of the process ($P_{el_{STEP}}$) and related time (t_{STEP}).

$$E_{el} = P_{el_{ADS}} * t_{ADS} + P_{el_{REG}} * t_{ADS} + P_{el_{COND}} * t_{REG} \quad (4.14b)$$

Where the term $P_{el_{ADS}}$ typically takes into account power required to drive air fans, moving the air through the sorption material, t_{ADS} the duration of the adsorption phase; $P_{el_{REG}}$ the power during regeneration, to heat up the sorbent and to drive all the required auxiliaries (air fan, pumps, valve). If liquid water is obtained condensing the air stream from regeneration with a pure passive method (dissipation through metallic heat sink exposed to ambient temperature and natural convection), then the term $P_{el_{COND}}$ is null. Instead, when a dry cooler is driving condensation (temperatures higher than external ambient) $P_{el_{COND}}$ is small but not null (auxiliaries of the dry

cooler). Instead, $P_{el_{COND}}$ is considerably high when active refrigeration is involved (temperatures lower than external ambient). Total electric consumptions are reported in Annex E.

For a feasible system is mandatory to reduce as much as possible this component, improving the design of the system. In particular, reducing the power consumed by the fan to move the air through the ADS-HX. For this purpose, much smarter configurations are needed in substitution of the packed bed configuration, as will be showed in the conclusive chapter of this research.

4.7 Numerical model of the packed ADS-HX

4.7.1 Hypothesis and equations

The theoretical model results in a set of energy and mass balances between the energy source (hot water), solid mass of silica gel, and the gas phases (air and water vapor). The hypotheses necessary to define the final set of equations are listed below:

1. Adsorption/Desorption processes involve only water vapor and the sorbent. The presence of other non-condensable gases is neglected
2. Adsorption heat is generated inside the pores of the sorbent. The heat generation is function of the water uptake of the material.
3. Adsorption/Desorption processes are much faster than other phenomena (intraparticle diffusion; heat exchange)[2],[56]. This lead to the assumption that near the sorbent surface, the local vapor/sorbent equilibrium can be approximated with water-SiO_2-$_n$(H_2O) adsorption equilibrium curves. With this approach, the vapor mass transfer between air and SiO_2-$_n$(H_2O) is a function of equilibrium conditions, approximated with the Linear Driving Force (LDF) method [56],[208]. Anyway, due to the long duration of experiments, the vapor diffusion inside a particle plays a significant role on global resistance to the mass transfer.
4. The phenomena are mostly mono-dimensional and coherent with the air flow direction.
5. The significant heat transfer mechanism is convection between air and the solid surface of the sorbent and the metal heat exchanger. Conduction and radiative exchange are neglected.
6. The role of thermal losses towards external environment is minimized by the abundant use of thermal insulation and are not considered in the energy balance.

Based on this hypothesis the following set of heat and mass transfer differential equations are built to describe: the heat and mass transfer between water vapor/ SiO_2-$_n$(H_2O)/HX/water.

The time dependency of water uptake is correlated to a mass transfer rate, defined with the LDF approach as follow:

$$\rho_b \frac{\vartheta W}{\vartheta t} = \rho_a K_G a_s (x_a - x^*) = \dot{G} \quad \left[\frac{kg}{m^3\ s}\right] (4.15)$$

where ρ_b is the bulk density of silica gel; W is the silica moisture content; K_G is the global water mass transfer; a_s the surface area; x_a the actual moisture of air measured at the bulk; x^* is the equilibrium value between the air and the solid sorbent. The equilibrium value is computed using the polymeric correlation of equation 2.5, as a function like RH*=f(w,T). The conversion from RH to moisture content is done using typical psychrometric equations as reported in chapter 3. The differential equations in space and time for the energy and mass balance are reported as following:

$$\varepsilon_b \rho_a \frac{\vartheta x_a}{\vartheta t} d_V = -\dot{m}_a \frac{\vartheta x_a}{\vartheta z} d_z - \dot{G}\, d_V \quad \left[\frac{kg}{s}\right] \quad (4.16)$$

$$\varepsilon_b \rho_a c_{p_a} \frac{\vartheta T_a}{\vartheta t} d_V = -\dot{m}_a c_{p_a} \frac{\vartheta T_a}{\vartheta t} d_z + h_t(T_s - T_a) d_V - U_L a_L (T_a - T_{amb}) d_V + U a_F (T_a - T_w) d_V \quad [W] (4.17)$$

$$c_{p_b} \rho_s (1 - \varepsilon_b) \frac{\vartheta T_s}{\vartheta t} d_V = H_a \dot{G} - h_t (T_s - T_a) \quad [W] (4.18)$$

$$\rho_w c_{p_w} \frac{\vartheta T_w}{\vartheta t} d_v = -\dot{m}_w c_{p_w} \frac{\vartheta T}{\vartheta z} d_z - U a_F (T_w - T_a) d_V \quad [W] (4.19)$$

Where (4.16) is the equation for the mass balance between the air and water vapor, (4.17) is the air thermal balance; (4.18) is the thermal balance of the sorbent mean; (4.19) is thermal balance of the water/heat exchanger complex. ε_b is the bed porosity of the tested ADS-HX configuration and equal to 0.427 and z is the axial direction of the air stream.

4.6.2 Auxiliary model equations

Additional auxiliary equations are needed, together with the numerical algorithm, to solve the set of equations from (4.15) to (4.19).

Air physical conditions are evaluate using equation (3.2) for the moisture content, (3.3) for the saturation pressure of water vapor, (3.11) for dependency of air density from temperature. The dynamic viscosity of air, specific heat and molecular diffusivity with the equations (4.20), (4.21), (4.22)[209]

$$\mu_a = \frac{(T_a + 300)}{50} \times 23.6 \times 10^{-7} + 184.6 \times 10^{-7} \; [Pa\, s] \quad (4.20)$$

$$cp_a = 1884\, x_a + 1004\, (1 - x_a) \left[\frac{J}{kg\ K}\right] \quad (4.21)$$

$$Dm_{H_2O-air} = 1.735 \times 10^{-9} \frac{(T_a + 273.15)^{1.685}}{P_{atm}} \left[\frac{m^2}{s}\right] \quad (4.22)$$

Silica gel properties dependent from temperature (T) and water uptake (W) are the specific heat (4.23) and the heat of adsorption (4.24) and (4.25).

$$cp_s = 4186\, W + 921 \left[\frac{J}{kg\ K}\right] \quad (4.23)$$

$$H_{ads|W \le 0.05} = 3500 - 13400\, W \left[\frac{J}{kg}\right] \quad (4.24)$$

$$H_{ads|W > 0.05} = 2950 - 1400\, W \left[\frac{J}{kg}\right] \quad (4.25)$$

In addition to physical properties, other auxiliary equations are needed for the estimation of the heat and mass transfer coefficients, necessary to solve the thermal and mass balance between air, silica gel, and the heat exchanger.

The global coefficient for the heat exchange between humid air and the heating/cooling water ($\underline{U}$) [209],[210] of the equations (4.17) and (4.19) is evaluated with the equation:

$$\frac{1}{\underline{U}A} = \frac{1}{\eta_0 h_a A} + \frac{ln(D_o/D_i)}{2\pi L k_{cu}} + R_i \quad (4.26)$$

where A is the surface of thermal transfer media constituted by fin and tubes. The additional terms accounts for the different resistance mechanism for the thermal transfer respectively: convective resistance, conductive resistance of copper pipes, and internal resistance of water. These last term changes depending by the type of operation, adsorption or regeneration. Indeed, during adsorption the water is static and not flowing. For this case the value can be computed using the equation of conductive resistance through a pipe of cylindrical geometry.

$$R_i = \frac{\ln\left(\frac{D_i}{D_c}\right)}{2\,\pi L k_w} \quad (4.27)$$

In this case was used the trick of considering a fictitious water pipe with a very small internal diameter, but not null. In the case of regeneration, due to the water flow, the resistance is purely convective, and the heat transfer coefficient h_i was estimated computing the Nusselt number with the Dittus-Boelter relation[209]:

$$Nu = 0.023 Pr^{0.4}\, Re^{0.8} \quad (4.28)$$

Heat transfer on the air side is mainly convective, and the related transfer coefficient h_a has been estimated as function of the Nusselt number with the following equation [211],[212],[213].

$$h_t = \frac{k_a}{2\,R_p}\left(2 + 0.6 Re^{0.5} Pr^{0.33}\right) \quad (4.29)$$

The estimation of global mass transfer coefficient K_G in equation 4.15, requires the computation of the global mass transfer resistance, according to the LDF method. Through this approach only two main mechanisms contribute to the global resistance. First, the convective mass transfer resistance between the bulk of the air stream and the boundary layer (defining the transition from convection to diffusion mechanism) surrounding sorbent surface. Second, the intraparticle vapor diffusion, function of the temperature and water uptake.

According to the assumption three the adsorption reaction, being much faster than other mechanisms, is not a determining step for the transfer resistance, defining an equilibrium condition on the adsorption sites. These are located over the internal porosity of the material, that generate the intraparticle resistance.

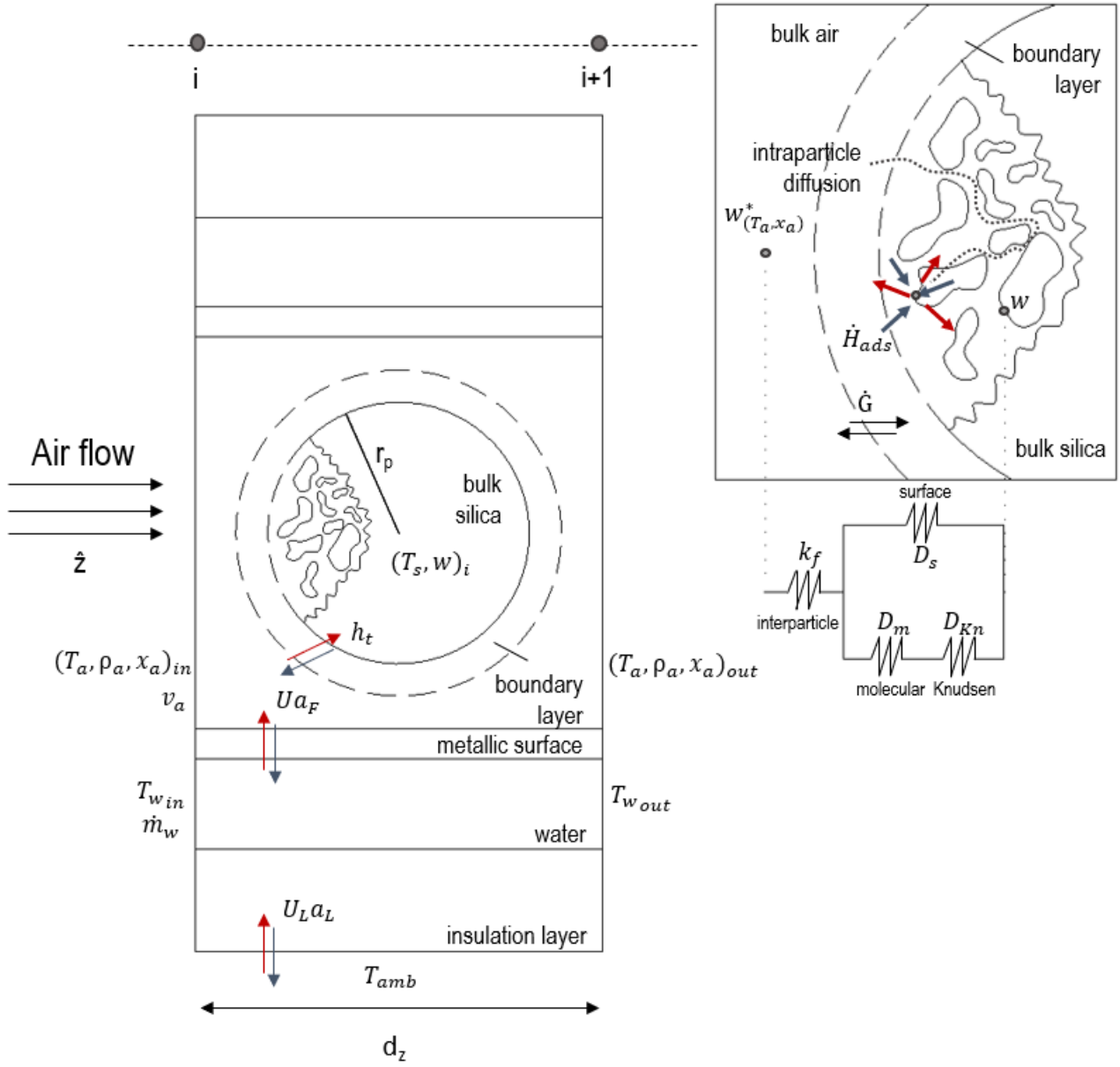

Figure 4.23a: On the left schematic diagram of the heat transfer mechanisms considered for modelling the elemental cell of the ADS-HX. On the right a similar arrangement highlights the mass transfer resistances, and the generation/sorption of the adsorption heat.

Here indeed, the diffusion mechanism is governed by two molecular interaction: the molecular collision regulates the diffusion through pores with a diameter sufficiently larger than the mean free path. The second interaction named Knudsen diffusion, between gas molecules and the solid surface, becomes more probable at smaller pore diameter, especially when this is comparable to the mean free path of the gas molecules. They both contribute in series for the diffusion of the gas from the bulk to the adsorption site. In parallel to this mechanism, there's the diffusion of the adsorbate phase over the solid surface that, driven by a gradient of the adsorbate phase, along the particle diameter, permeates through the internal part of particles. This mechanism is usually identified as surface diffusion.

In definitive, the convective and diffusive resistances work in serious, while the gas phase diffusion (series of molecular and Knudsen diffusion) is in parallel with the adsorbate diffusion, the surface diffusion. This approach grounds on the electrical resistance analogy as applied in [214] for thermal and mass exchanges. The global mass transfer coefficient between water vapor and silica gel K_G can be estimated with the equation (4.30) [214].

$$\frac{1}{K_G a_s} = \frac{1}{\frac{h_m}{\rho_a} a_s} + \frac{1}{(1-\varepsilon_b) K_p K_0} \quad (4.30)$$

Where h_m is the convective mass transfer, function of air properties and the flow regime[211], and a_s the surface area generated by the random distribution of the beads on the confined volume of the heat exchanger. Evaluation of this number requires the knowledge of the molecular diffusivity of water vapor in air (Dm_{H_2O-air}), and the Reynolds and Schimdt numbers:

$$h_m = k_f \, \rho_a = \frac{Dm_{H_2O-air}}{2 \, R_p} \left(2 + 0.6 Re^{0.5} Sc^{0.33}\right) \quad (4.31)$$

The second term of the equation (4.30) is instead the cumulative resistance generated by multiple mass transport mechanisms within the porous structure of the sorbent, and mainly related to intraparticle diffusion[211]. This is the cumulative result of three sub-mechanisms, generating the global effective diffusion coefficient D_{eff}. Molecular and Knudsen diffusion are the resistance to the mass transport operating together at the pore scale while in parallel, the adsorbate diffusion at the surface level, that for this reason is typically called Surface diffusion. The global diffusion results from the parallel composition of the pore and surface resistances, and can be estimated through the (4.32):

$$D_{eff} = \frac{1}{R_{Surface}} + \frac{1}{R_{Pore}} = \frac{1-\varepsilon_p}{\varepsilon_p} \frac{K_0 D_S}{\tau_p} + \frac{1}{\frac{\tau_p}{D_m} + \frac{\tau_p}{D_{Kn}}} \left[\frac{m^2}{s}\right] \quad (4.32)$$

Where K_0 is the equilibrium constant equal to function of the silica water content and of air properties $(\rho_s \, w)/(\rho_a \, x_a)$; ε_p is the mean particle porosity equal to 0.35 for silica and τ_p the tortuosity factor equal to 1. The estimation of D_{eff} requires also the computation of separately of D_m with the (4.22) and D_{Kn}, D_S respectively with the equations (4.33) and (4.34). Finally the mass transfer coefficient due to the porous internal resistance K_p can be computed with the (4.35) [215] and used to solve the equation (4.30) for the estimation of the global mass transfer coefficient K_G.

$$D_{Kn} = \overline{r_p} \; 22.86 \; (T + 273.15)^{0.5} \left[\frac{m^2}{s}\right] \quad (4.33)$$

$$D_S = \frac{D_0}{\tau_s} e^{-0.947 \frac{H_{ads}}{T+273.15}} \left[\frac{m^2}{s}\right] \quad (4.34)$$

$$K_p = \frac{60\varepsilon_p D_{eff}}{D_p^2 K_0}\left[\frac{m}{s}\right] \quad (4.35)$$

Having all the equations for the calculation of transfer coefficients, the solution of the differential equations set (4.15) (4.16) (4.17) (4.18) (4.19) requires a numerical method. All of them have been discretized in space, dividing the z continuous direction in finite elements of discrete Δz of 3 mm, and in time considering a finite timestep Δt of 1 second. The space derivative has been approximated using a backward finite difference method $\partial x/\partial z \simeq (x_i - x_{i-1})/\Delta z$ where x is the generic variable to be discretized and i is the generic element of the discrete space vector. The time derivative has been discretized with a backward Euler method, avoiding problems of solution instability, $\partial x/\partial t \simeq (x_i^{t+\Delta t} - x_i^t)/\Delta t$.

4.6.3 Numerical solution

The following part will resume the numerical solution of differential equation set, and the different boundary conditions (BC) for the space vector, and the initial values (IV) for the time.

Numerical solution of (4.15): silica gel water content

$$\rho_b \frac{W_i^{t+\Delta t} - W_i^t}{\Delta t} = K_G a_s \left(x_{a_i}{}^t - \bar{x}_i^t\right) \quad (4.36)$$

$$IV: \quad W(z, t=0) = W_0 \quad (4.37)$$

Numerical solution of (4.16): Air-water mass balance

$$\varepsilon_b \rho_a \frac{x_{a_i}^{t+\Delta t} - x_{a_i}^t}{\Delta t} d_z = -\dot{m}_a \frac{x_{a_i}^{t+\Delta t} - x_{a_{i-1}}^{t+\Delta t}}{\Delta z}\, d_z - K_G\left(x_{a_i}^{t+\Delta t} - \bar{x}_i^t\right) d_v \quad (4.38)$$

$$x_a^{t+\Delta t} M_A = Q_A = (x_a^t + \Delta t\, A_2\, \bar{x}_t) \quad (4.39)$$

$$M_A = \begin{bmatrix} 1+\Delta t(A_1+A_2) & \dots & \dots \\ -\Delta t\, A_1 & 1+\Delta t(A_1+A_2) & \dots \\ \dots & -\Delta t\, A_1 & 1+\Delta t(A_1+A_2) \end{bmatrix} \quad (4.40)$$

$$A_1 = \frac{v_a}{\varepsilon_b \Delta t};\ A_2 = \frac{K_G\, a_s}{\varepsilon_b\, \rho_a}; \quad (4.41)$$

$$IV: \quad x_a(z, t=0) = x_a(z=0, t) = x_{a\ inlet} \quad (4.42)$$

$$BC: \quad M_A(1,1) = 1;\ M_A(1,2) = 0;\ Q_A(1) = x_{a\ inlet} \quad (4.43)$$

Numerical solution of (4.17): Air thermal balance

$$\varepsilon_b \rho_a cp_a \frac{T_{a_i}^{t+\Delta t} - T_{a_i}^t}{\Delta t}\,\mathrm{dV} =$$

$$-\dot{m}_a cp_a \frac{T_{a_i}^{t+\Delta t} - T_{a_i}^t}{\Delta t} d_z + h_t\left(T_{s_i}^t - T_{a_{i-1}}^{t+\Delta t}\right)\mathrm{dV} - U_L a_L \left(T_{a_i}^{t+\Delta t} - T_{amb}^t\right)\mathrm{dV}$$

$$+U a_F \left(T_{a_i}^{t+\Delta t} - T_w^t\right) dV + Q_f dV \quad (4.44)$$

$$T_a^{t+\Delta t}\, M_B = Q_B = T_a^t + \Delta t\, B_2\, T_s^t + B_3 T_w^t + \Delta t\, B_4\, T_{amb} + \Delta t\, Q_f \quad (4.45)$$

$$M_B = \begin{bmatrix} 1+\Delta t(B_1+B_2+B_3+B_4) & \dots & \dots \\ -\Delta t\, B_1 & 1+\Delta t(B_1+B_2+B_3+B_4) & \dots \\ \dots & -\Delta t\, B_1 & 1+\Delta t(B_1+B_2+B_3+B_4) \end{bmatrix} \quad (4.46)$$

$$B_1 = \frac{v_a}{\varepsilon_b \Delta z};\ B_2 = \frac{h_t\, a_s}{\varepsilon_b\, \rho_a\, c_{p_a}};\ B_3 = \frac{U\, a_s}{\varepsilon_b\, \rho_a\, c_{p_a}};\ B_4 = \frac{U_L\, a_L}{\varepsilon_b\, \rho_a\, c_{p_a}}; \quad (4.47)$$

$$Q_f = \frac{\dot{m}_a}{2}\left(\frac{\dot{m}_a}{\varepsilon_b\, \rho_a\, A_b}\right)^2 \left(\frac{a_s\, \xi}{\varepsilon_b\, A_b}\right); \quad (4.48)$$

$$IV: \quad T_a(z, t=0) = T_a(z=0, t) = T_{a\ inlet} \quad (4.49)$$

$$BC: \quad M_B(1,1) = 1;\ M_B(1,2) = 0;\ Q_B(1) = T_{a\ inlet} \quad (4.50)$$

Numerical solution of (4.18): SiO_2 thermal balance

$$c_{p_b}\rho_s(1-\varepsilon_b)\frac{T_{s_i}^{\,t+\Delta t} - T_{s_i}^{\,t}}{\Delta t} = H_A K_G a_s\left(x_{a_i}^{\,t} - \bar{x}_i^{\,t}\right) - h\, a_s\left(T_{s_i}^{\,t+\Delta t} - T_{a_i}^{\,t}\right) \quad (4.51)$$

$$T_{s_i}^{t+\Delta t} = \frac{T_{s_i}^{\,t} + \Delta t C_1\left(x_{a_i}^{t} - \bar{x}_i^{t}\right) + \Delta t C_2 T_a^t}{1 + \Delta \mathrm{t}\, \mathrm{C}_2} \quad (4.52)$$

$$C_1 = \frac{H_A K_G a_s}{\rho_s(1-\varepsilon_b)\, c_{p_s}};\ C_2 = \frac{h\, a_s}{\rho_s(1-\varepsilon_b)\, c_{p_s}}; \quad (4.53)$$

Numerical solution of (4.19): Water loop thermal balance

$$c_{p_w}\rho_w \frac{T_{w_i}^{\,t+\Delta t} - T_{w_i}^{\,t}}{\Delta t} dV = -c_{p_w}\, \dot{m}_w \frac{\left(T_{w_i}^{\,t+\Delta t} - T_{w_{i-1}}^{\,t+\Delta t}\right)}{\Delta z} d_z + U\, a_f\left(T_{w_i}^{\,t+\Delta t} - T_{a_i}^{\,t}\right) dV \quad (4.54)$$

$$T_w^{t+\Delta t}\, M_D = Q_D = T_w^t + \Delta t\, D_2\, T_a^t \quad (4.55)$$

$$M_B = \begin{bmatrix} 1+\Delta t(D_1+D_2) & \dots & \dots \\ -\Delta t\, D_1 & 1+\Delta t(D_1+D_2) & \dots \\ \dots & -\Delta t\, D_1 & 1+\Delta t(D_1+D_2) \end{bmatrix} \quad (4.56)$$

$$D_1 = \frac{\dot{m}_w}{\rho_w\, A_b\, \Delta \mathrm{z}};\ D_2 = \frac{U\, a_s}{\rho_w\, c_{p_w}}; \quad (4.57)$$

$$IV: \quad T_w(z, t=0) = T_w(z=0, t) = T_{w\ inlet} \quad (4.58)$$

$$BC: \quad M_D(1,1) = 1;\ M_D(1,2) = 0;\ Q_D(1) = T_{w\ inlet} \quad (4.59)$$

4.6.4 Comparison with experimental results

To verify the validity of the model and numerical solution, a cross comparison of the model outputs against experimental results has been carried out for all the adsorption and regeneration tests mentioned in the previous paragraph. The diagram of the procedural algorithm is depicted in Figure 4.25.

The numerical model requires first an initial configuration with the geometrical parameters of the ADS-HX, thermophysical intrinsic properties of air, silica and heat exchanger media. Experimental data such as air flow rate, water flow rate, inlet air conditions and inlet water conditions are used also as a dynamic input for the numerical model. The response of the model is compared with the corresponding outlet of the experiments, such as air temperature and moisture content, adsorbed water mass. Finally, the relative and absolute errors are evaluated to establish the quality of the model in both operational phases.

Because the different time discretization of the data array and numerical results (~11 seconds against 1), the first operation is the homogenization of inputs, repeating the experimental value as much times as required to have coherent input vectors. After the computation of IV (initial values) and BC (boundary conditions), input values are used to estimate first the equilibrium values from the isotherms in each node of the z direction, second the thermophysical properties function of temperature and humidity, third the heat and mass transfer coefficients. All these parameters become the input for the heat and mass balances (4.36), (4.38), (4.44), (4.51), (4.54). The output of this process update then the IV, BC, for the second round of the iteration, and are compared with the experimental data. This process continues for the entire duration of the adsorption and regeneration tests.

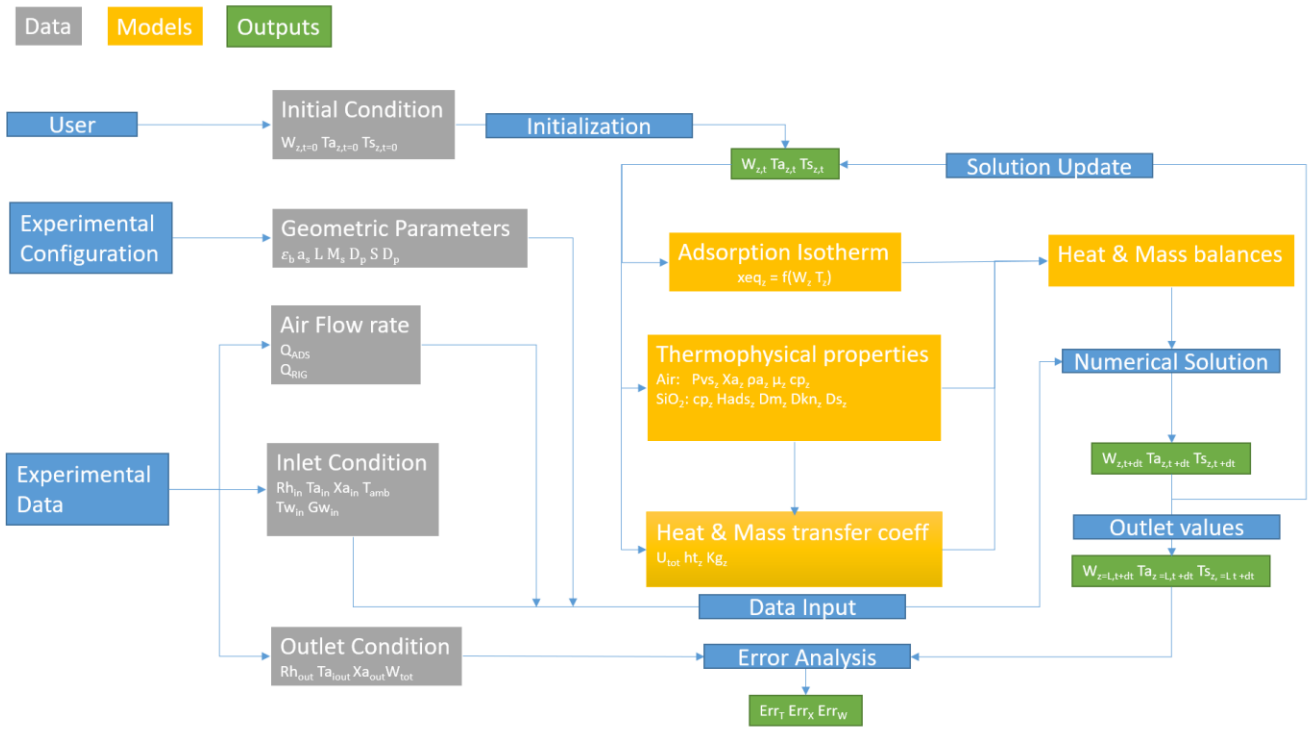

Figure 4.25: Diagram of the resolution algorithm of the numerical model for the silica packed bed ADS-HX. Grey box are the input data taken from the experiments, Yellow box identify the different passage of the numerical model for the estimation of equilibrium values, heat and mass transfer coefficients, and resolution of equations (4.36), (4.38), (4.44), (4.51), (4.54).

An example of comparison is reported in Figure 4.26 and 4.27, where outlet moisture x_{out}, the outlet air temperature T_{out} and water mass M_w are compared for tests #24, #25, #36, #37. Instead in Tables 4.6 and 4.7 are reported the comparison graph Experimental/Numerical with the bands of uncertainty.

In both adsorption and desorption tests, the T_{out} showed the lowest discrepancy between model and experimental data. On the contrary, the error analysis on both moisture content and water mass shows a deviation in the last part of regeneration tests. Indeed, despite in the first part of the transient (5 hours), there is good accordance between theory and experiments. After five hours, the error range increases due to the overestimation of the desorbed water rate. In general, the model simulates much better the adsorption test than the desorption, with a lower absolute and relative mean errors and less statistical dispersion during the 10 hours transient. An explanation behind this difference can be the introduction of the uncertainty for the evaluation of transfer coefficients. Indeed, solving equations (4.30) and (4.35) implies multiple numerical passages function of air/sorbent equilibrium temperature and different hypothesis about material properties that most of the time were done using data from literature. The adsorption process, differently from the regeneration, is less dependent by the heat transfer. Indeed, water circulation was stopped during adsorption tests, and except for the parasitic heat dispersions through the coil, the transformation can be considered as an iso-enthalpic. Regeneration is on the contrary totally dependent by the heat transfer mechanisms, and their uncertainty can amplify errors on the estimation of mass transfer coefficients.

A second source of potential errors is the simplification operated through the LDF theory. This approach has been used by many authors in literature, especially when applied for silica gel. This theory provides a good compromise between the validity of the model outputs, and the computational efforts for their elaboration. Anyway other study cases showed a characteristic behaviour that also this comparison highlighted: underestimation of water uptake in the first transient and overestimation in the long period are typical of algorithms based on the LDF method [211],[216],[217]. Most of the mismatch between experimental and numerical values are within the first hour of functioning, especially for the regeneration cases, while in general over the operational time the tendency is the alignment of curves. However, for the entire tests duration this technique yields in the average errors in the range of ±10% for the air properties during the adsorption tests. The analysis of water mass error showed more accordance between numerical and experimental values, with an average error within the interval of ±5%.

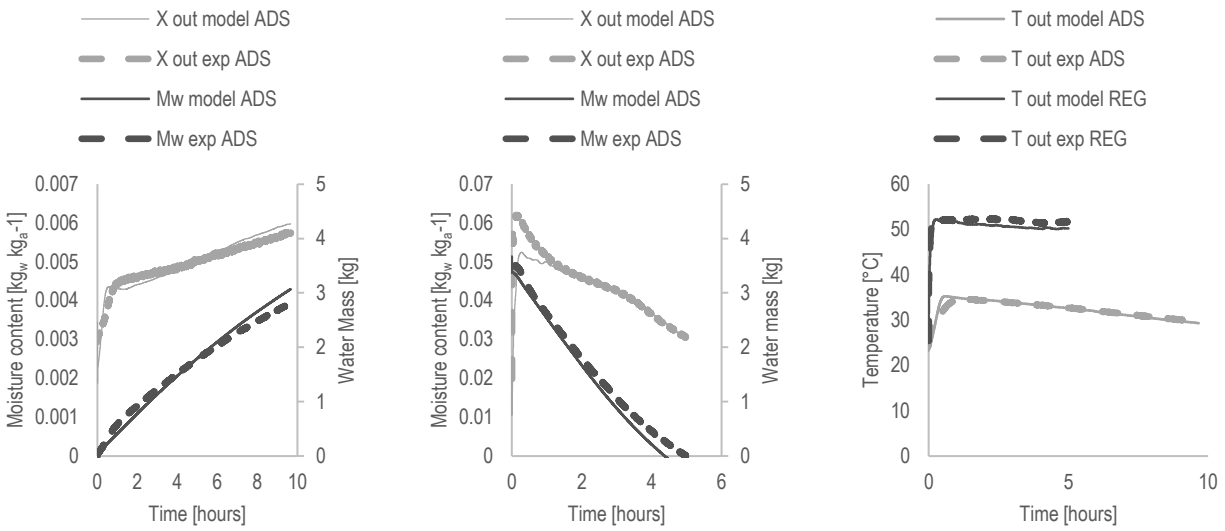

Figure 4.26: Comparison between experimental data and model results of moisture content of outlet ai (x_{out}) from ADS-HX, outlet air (T_{out}) and water mass contained adsorbed by the sorbent beads (M_w). On the left the comparison on x_{out}t and M_w carried out for the adsorption test #24; in the middle the comparison on the comparison on x_{out}t and M_w for both regeneration test #25; on the right the comparison on T_{out} for both adsorption and regeneration tests #24-25.

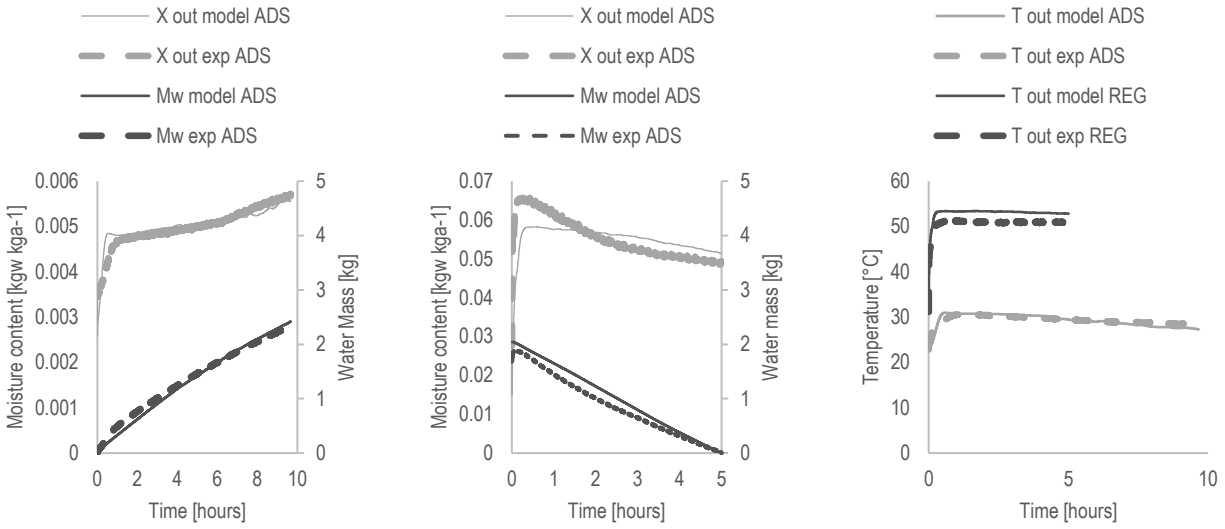

Figure 4.27: Comparison between experimental data and model results of moisture content of outlet ai (x_{out}) from ADS-HX, outlet air (T_{out}) and water mass contained adsorbed by the sorbent beads (M_w). On the left the comparison on x_{out}t and M_w carried out for the adsorption test #36; in the middle the comparison on the comparison on x_{out}t and M_w for both regeneration test #37; on the right the comparison on T_{out} for both adsorption and regeneration tests #36-37.

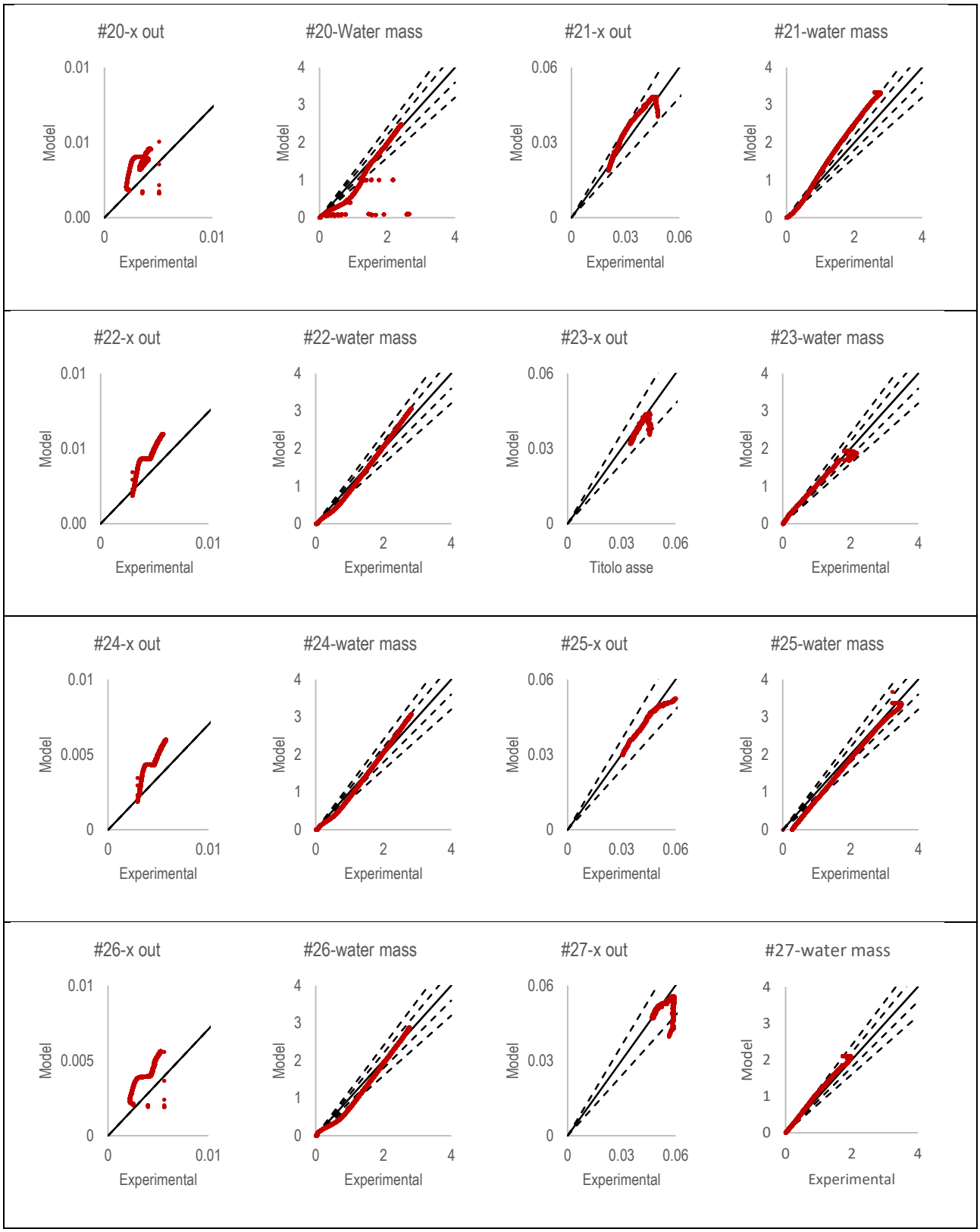

Table 4.6: Comparison of experimental data against numerical, for each timestep of simulated experiments #20, #21, #23, #24, #25, #26, #27. The comparison is done on the two most interesting values: outlet moisture x_{out} ad water mass balance M_w. For the x_{out} graph dashed lines defines the uncertainty interval of ±20%. For M_w graph the uncertainty interval is double, the first at ±10%, the second at ±20%.

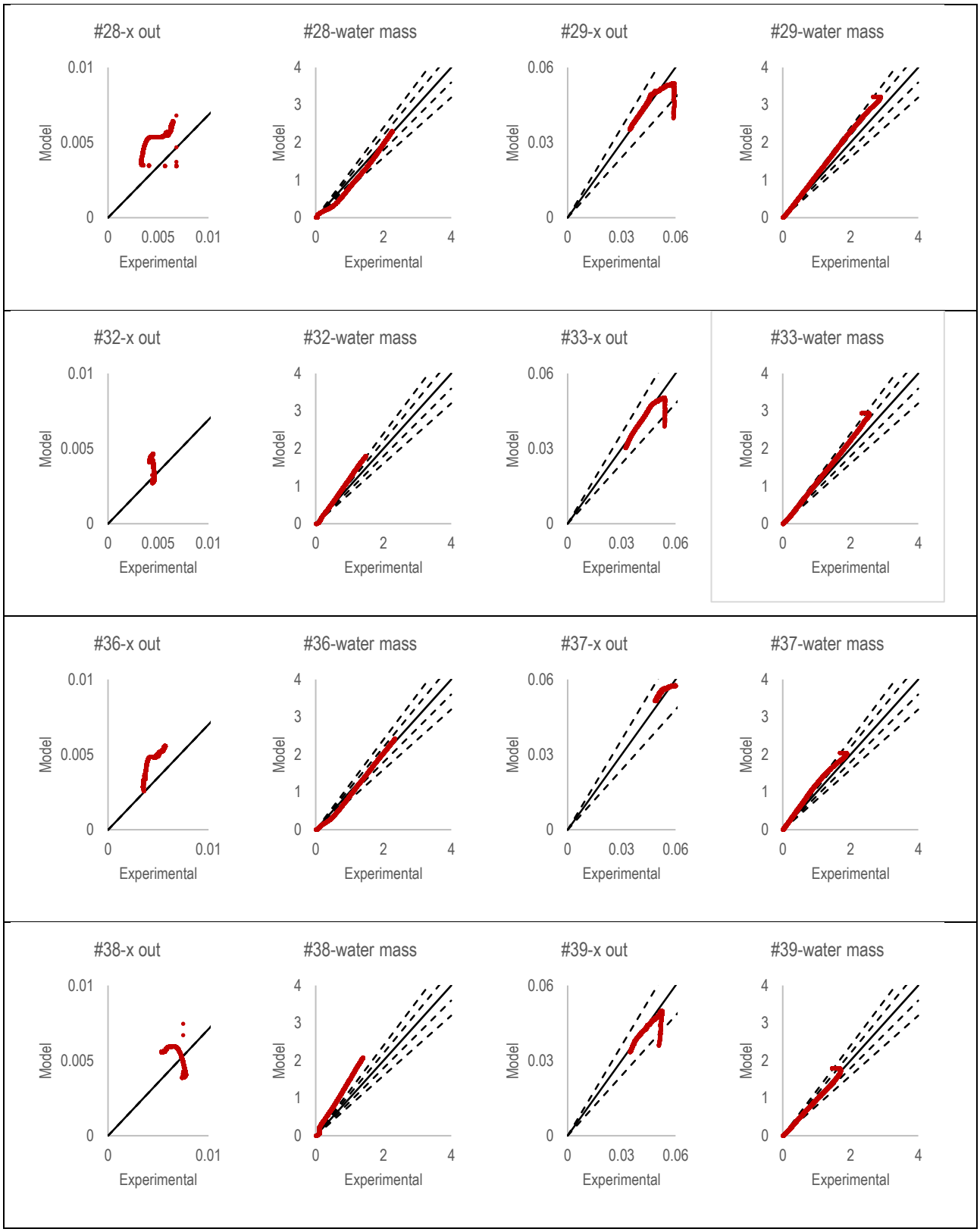

Table 4.7: Comparison of experimental data against numerical, for each timestep of simulated experiments #28, #29, #32, #33, #34, #35, #36, #37, #38, #39. The comparison is done on the two most interesting values: outlet moisture x_{out} ad water mass balance M_w. For the x_{out} graph dashed lines defines the uncertainty interval of ±20%. For M_w graph the uncertainty interval is double, the first at ±10%, the second at ±20%.

Conclusions

Global water vapor availability varies during the year, reaching higher values during the period of July-September, and a total volume higher than 12000 km^3. Most of the water is concentrated within the ICZ, but a discrete availability can be found in zones that recently have experiencing a water stress situation with occasional drought events: in north America, south Europe, the Asiatic and the MENA region. The definition of a good performing cycle, as what studied in this research, enable the use of poor performing materials such as silica gel, with water uptake as much as lower of 0.1 $kg_w\ kg_{SiO2}^{-1}$, and compatible with most of the conditions of water stressed regions. The realized prototype produced between 3.3 and 1.5 L of water, with low initial water content of silica (<0.1 $kg_w\ kg^{-1}_{SiO2}$ typical of dry environments), regeneration temperature of 57°C, over an operational time of ten hours. Compared to existent prototype in literature, this configuration is one of the most efficient at the liter-scale dimension. Despite these evidences, it is clear that silica gel, given its intrinsic properties, is not suitable for all the climates. In very dry environments, with dew points lower then 0°C, silica gel cannot exhibit any sufficient Δw to be applied in a cycle to produce water. At the same time, very dry climates are not necessary connected to a water stress condition. Further development will be carried out to apply this cycle with more performing material, without increasing the regeneration temperature. The theoretical model, based on the LDF theory, is in good agreement with experimental, in both adsorption and regeneration. The estimated average errors on air temperature, air moisture and silica water content are below 10%. Depending on weather condition (temperature and humidity), regeneration time with a minimum thermal efficiency of 50% should not overcome 3-5 hours of functioning with initial water uptake between 0.1-0.2 $kg_w\ kg_{SiO2}^{-1}$. The developed model is a suitable tool for the design optimization of an engineered system according to the climatic condition of a location. Further on, with a tuned calibration to overcome the errors generated with the LDF, thanks to the very low computational costs (10 hours of real process simulated in less than 1 minute) this model will be implemented on a new prototype version (Figure 4.28). This has been implemented to have an all in one configuration, with all the components below two solar thermal panels. This model will be used as management tool to establish control logic for the switch between to ADS-HX, according to the variation of climatic conditions.

Figure 4.28: The autonomous Solar Atmospheric Water Generator (SAWG) presented at Polito at the Italian Techweek in 2019)

5. Application of New Sorbent Polymers

Abstract

In this section physical and chemical properties of various types of polymeric materials, possessing hydrophilic characteristics, have been investigated with the purpose of developing alternative configurations of a heat and mass exchanger to capture moisture from ambient air and convert it into fresh water. In the following sections, the different types of organic materials studied will be described, analyzing in detail the adsorption properties of the materials under well-defined atmospheric conditions, defined by the couple of T and RH. In the end, it will be described prototypes of ADS-HX that can be used to produce fresh water by exploiting the performance of various organics materials. Two materials have been studied: different type of liquid polymers, and a novel bio-hydrogels. Most of the research was carried out in the framework of the PrinceTo project, an exchange project with Princeton University. Promising results from the application of liquid polymers and biological hydrogels in the water harvesting sector. This step of the research, driven by the need for more performing materials in condition of drought, aims to overcome the low capacity resulted from the WAT-AIR Lab, identified as the main limiting factor for the increase of the water density of the SAWG prototypes.

5.1 Liquid Polymers

The advantages of using liquid desiccant from the systemic point of view are multiple. The possibility to pump a fluid from the absorber to the regenerator has different implications on a final system. Indeed, if in a solid configuration the switching time and water uptake capacity, define most of the constraints about prototype capacity, in liquid configurations dynamic properties are definitively more relevant.

Decoupling the total mass of the desiccant of a system from the total water capacity, is the main implication of liquid systems, that may potentially generate positive consequences: a reduction of weight and the increase of miniaturization and transportability. This direction of the research aims to open new possibility for the exploitation of sorbents in the sectors of water harvesting.

One of the oldest studied liquid desiccant are water solution of calcium chloride and lithium chloride [89]. Typical problems that have characterized this solution are the typical corrosion with metallic surface; higher regeneration temperature if compared with silica gel, reducing the exploitability of solar energy; being irritating for human mucous, the carry over problems are a crucial aspect for system dimensioning.

The main driver for this research was always the necessity of dealing with materials offering an easy switch between the phase of water capture and regeneration, applying a thermal lift of the order of 30°C, and with maximum regeneration temperature defined by the constraints of efficient solar energy exploitation, as extensively defined in the Chapter 4.

The analysis of typical sorbent properties in the Chapter 2 highlighted the importance of functional groups over the structure, activating, modifying and improving the affinity with water. In this sense the role of silanols and hydroxyls are relevant on the definition of water uptakes.

Over different alternative materials, a particular effort was carried out on the study of dimethylpolysiloxane (PDMS) properties. This organosilicon polymer in its basic form is hydrophobic. This characteristic, together with the thermal stability and solvent resistance has been widely exploited in many industrial applications[218], such as water-repellent for textiles. There's a rising sector, namely microfluidics for biomedical applications, that is actually looking to the exactly opposite properties[219–224]. The modification of PDMS, to improve its properties for specific applications was investigated under three different approaches: bulk, surface and functionalization. If the first two resulted in less stable modification, the third has a very important effect on the long term properties modifications.

Functionalization of the polymeric chain implies the substitution of some of the methyl groups with alternative functional groups. In Figure 5.1 are presented three different PDMS types analysed and tested in this research, and provided by Gelest [225–228]. The first, a typical standard PDMS-CH3 with methyl terminations, is presenting as an optically clear oil, inert and non-dangerous material (non-toxic and non-flammable)[229].

The second is a PDMS in which terminal methyl groups are substituted with hydroxyl groups. Investigating this configuration of the material has the role to verify the effect on the interfacial surface tension of the chain[230][231], especially when highly hydrophilic groups are attached. This configuration will be named for the rest of the text PDMS-OH

The third configuration is a substantial modification of material properties, caused by the functionalization of the chain with the insertion of a poly-ethylene-oxide chain, deeply changing the properties of this material. This block-copolymer configuration is defined as PDMS-b-PEO [232–234]. Presence of –PEO chain may change the distribution of the electronic cloud around the polymeric molecule, creating a periodic induced dipole that gives stable hygroscopic properties[235].

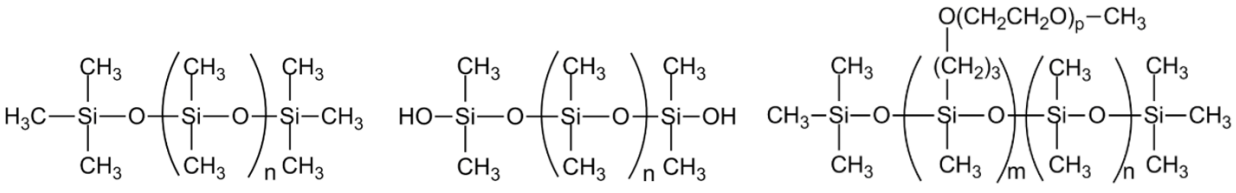

Figure 5.1: Different functionalized PDMS types. A is a pristine PDMS polymeric chain -methyl terminated (PDMS-CH3). B is a PDMS polymeric chain -hydroxyl terminated (PDMS-OH); C is a PDMS polymeric chain functionalized with poly-ethylene-oxide groups (PDMS-b-EO)

Two different configurations of this last polymer have been analysed, PDMS-b-PEO 60% and PDMS-b-PEO 80% where the percentage represent the concentration of the ethylene oxide over the entire structure. Higher concentrations result in higher water solubility. For example, materials with ethylene oxide contents higher of

75% are freely soluble in water. Differently from the others, this presents some health risks, classified with an hazard label similar to calcium chloride (GHS07).

In addition to this list a further polymer has been investigated, a tri-ethylene-glycol, widely known in literature for its hydrophilic properties [236–240].

5.1.1 Equilibrium tests

The measurements of the vapor pressure and moisture content of water-air in equilibrium with the liquid polymer at different water content and temperature was realized with the setup sketched as in Figure 5.2.

The concept behind the experiment is very simple: within a sealed volume is poured a fixed and known amount of liquid material. If the liquid has some desiccant properties, the water vapor contained in the air volume will be absorbed, until an equilibrium condition will occur. The equilibrium, dependent by the temperature of both the liquid and the air volume, is reached when the vapor pressure dispersed in the air is equal to the pressure of water absorbed in the liquid substances.

The possibility to change the vapor pressure are two: i) adding water mass to the volume; ii) changing the temperature of the volume.

The volume is realized with a cylindrical borosilicate glass beaker of 450 mL capacity. To confine and seal this air volume was realized a specific lead, with a lateral Teflon tape, guarantying as much as possible the air sealing. The lead is provided with specific supports to sustain a 4x4cm axial fan, and two small apertures. One for the cables powering the fan and the sensors (5 mm diameter), the other is allowing the passage of a syringe needle (0.5 mm). Once the electrical connections were assembled, the cable passage through the lead was sealed with an impermeable glue, while the small hole for the syringe was not sealed. The lead was realized with a stereolithographic printer with high resolution (Form2), guarantying a very small tolerance between the needle and the 0.5 mm hole, to reduce eventual vapor leaks.

The lead is equipped with the 5 volts DX axial fan, to create a continuous air mixing in the beaker, reducing as much as possible the diffusive resistances on the air side. Further, an integrated circuit temperature sensor (LM35CAZ, ± 0.2°C) measures the temperature of the air, while a thermoset polymer capacitive sensor (HIH4000-4, ± 3.5%) measures the relative humidity. A DS18B20 digital sensor provide instead the temperature of the liquid desiccant contained in the bottom of the beaker. Resulting of the setup is showed in picture of Figure 5.2.

The beaker was inserted within an insulating foam to guarantee an adiabatic condition all over the lateral surface, reducing as much as possible heat dispersions. The bottom of the beaker is in direct contact with the hot plate of the magnetic stirrer (the stir bar is inside the beaker, and activated @200 rpm, to guarantying the continuous homogeneity of the desiccant reducing as much as possible the relevance of the liquid diffusive resistances). The system is regulated with the thermostat of the stirrer, to maintain a constant temperature over the surface

of the hot plate, and then of the air/liquid mixture in the beaker. All the sensors were connected to Particle Photon shield, equipped with an ARM Cortex M3 processor, and 8 DAC channels @12bit and maximum input of 5V. Elaborated digital data were then communicated to a central server, through WiFi communication protocols.

Testing methodology is elaborated trough the following passages:

- desiccant samples of PDMS-CH3, PDMS-OH, PDMS-b-PEO, TEG were constantly stored in a ventilated oven, at constant temperature of 80°C. This temperature provides a very dry environment, without deteriorating the materials;
- 20 grams of liquid polymer are poured inside the beaker and weighted with a 5 digits analytical balance. The beaker was previously cleaned with isopropyl alcohol, and dried with compressed air;
- once the mass of the sample is reached the beaker is closed with the sealed lead and stirred @200rpm. With the thermostat is fixed the desired testing temperature. The air fan is always activated;
- for tests at ambient temperature around 5 minutes are necessary for the desiccant to reach the local temperature (20-22°C). While for higher temperatures (up to 50°C) the elapsed time for equilibrium was higher;
- air temperature, relative humidity and liquid temperature are constantly monitored and logged with a timestep of ~ 5 seconds;
- the first point of equilibrium is between the air (at initial condition as the Lab T and RH) and the dry liquid sorbent, with a water uptake ~0%;
- through the syringe is injected a known volume of water, equal to 0.2 mL, that corresponds to 1% of the mass of the initial dry desiccant. Some parallax errors can occur during this phase. To minimize as much as possible this source of error, was used a calibrated syringe with 0.5 mL of capacity, and a graduated scale of 0.005mL;
- after a while a new equilibrium condition is reached. The second injection of 0.2mL will establish a new equilibrium. In this way a step increase of 1% water uptake is realized and progressively performed until the RH of the air in equilibrium with the desiccant reached values lose to 90%, meaning that the sorbent is saturated, at the temperature T.

Moreover, to verify the validity of the testing methodology, a cross check with Calcium Chloride was performed. Indeed, $CaCl_2$ is a very well-known deliquescent salt, deeply studied, with a lot of available data from literature. One of the most known work is the experimental activity of Conde[89]. RH equilibrium measurements with aqueous solution of $CaCl_2$ at three different concentrations, ζ_1=0.5, ζ_2=0.4 within a temperature range of 22-80°C, as shown on the left f Figure 5.3. Most of collected point belongs to the uncertainty range of ±10%. This range was considered acceptable if considered the very simplicity behind the manufacturing of the setup and used methodology. Further, if used to compare performances of different materials within the same setup (such as on the right of Figure 5.3.), the errors generated from the comparison on the CaCl2 are less relevant.

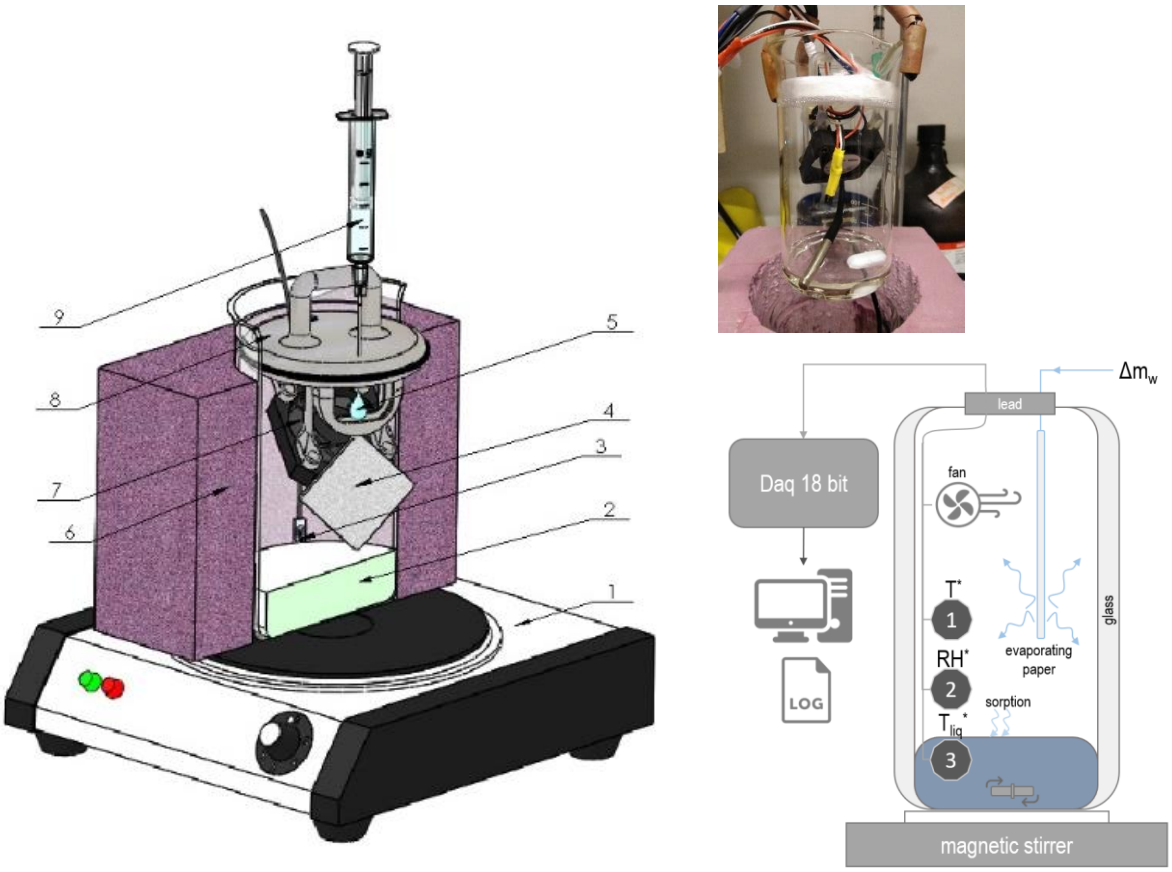

Figure5.2: On the left the schematic of the setup assembled to evaluate the equilibrium condition between air and the liquid polymer. 1) magnetic stirrer with hot plate for temperature regulation; 2) liquid desiccant to be tested; 3) air temperature and humidity sensors; 4) paper support for water evaporation; 5) water droplet; 6) thermal insulation; 7) air fan; 8) lead; 9) calibrated syringe for water injection. On the top right, a picture of the assembled beaker. To be sure of the thermal equilibrium between air and desiccant, an additional temperature sensor measures constantly polymer temperature. On the bottom right the schematic of the experimental setup.

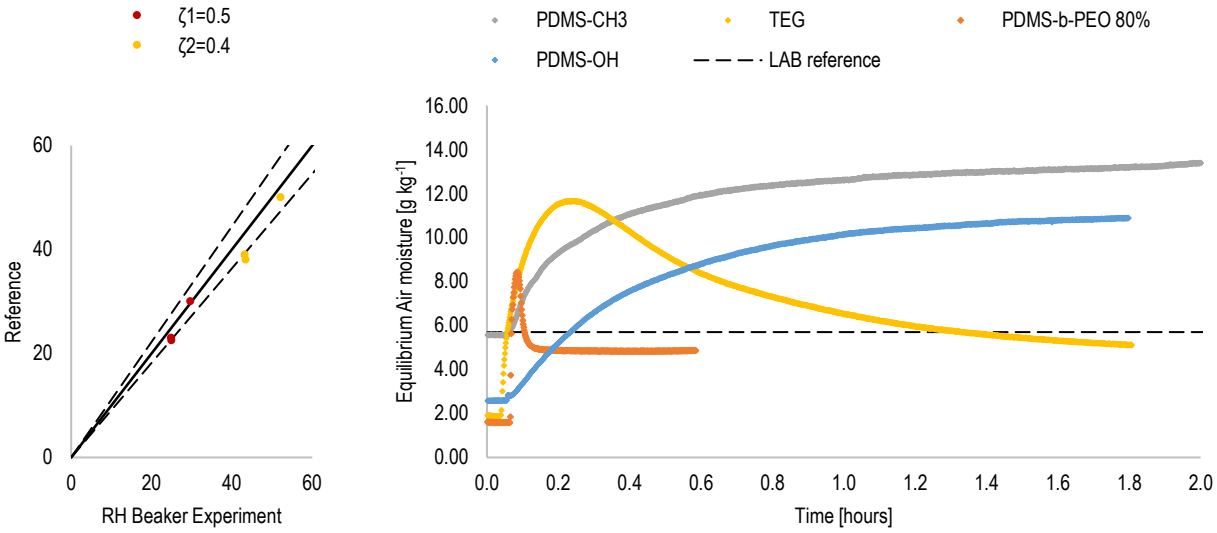

Figure 5.3: The graph showes on the left the comparison between RH measurements obtained with this setup, against reference [89]. On the right the dynamic of the air in equilibrium with the different tested liquid desiccants. At the time zero all the polymers started with an initial water uptake close to 0%. The injection, after 5 minutes from the begin of data monitoring, increase the RH activating the absorption of water vapor from initial value, in equilibrium with the liquid polymer at 0%, up to final point in equilibrium with 1%.

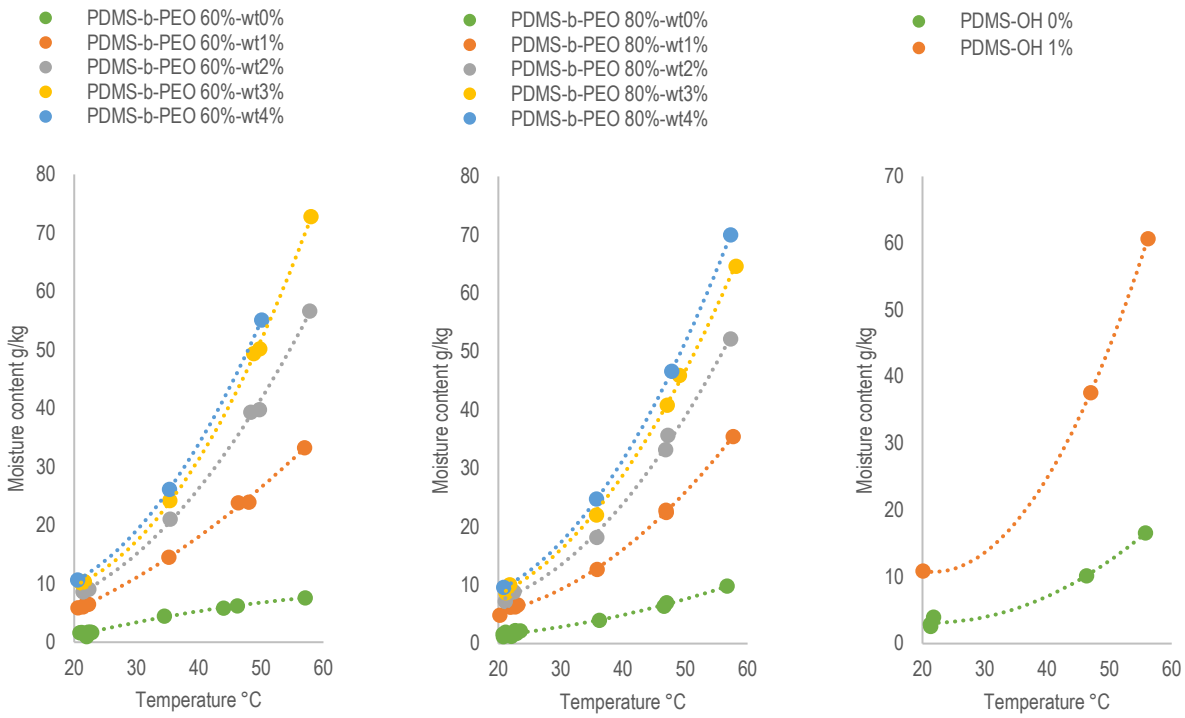

Figure 5.4: Equilibrium curves for the three different types of functionalized PDMS. Being the system thought to work in open environment, equilibrium lines are expressed as moisture content function of temperature and water uptake.

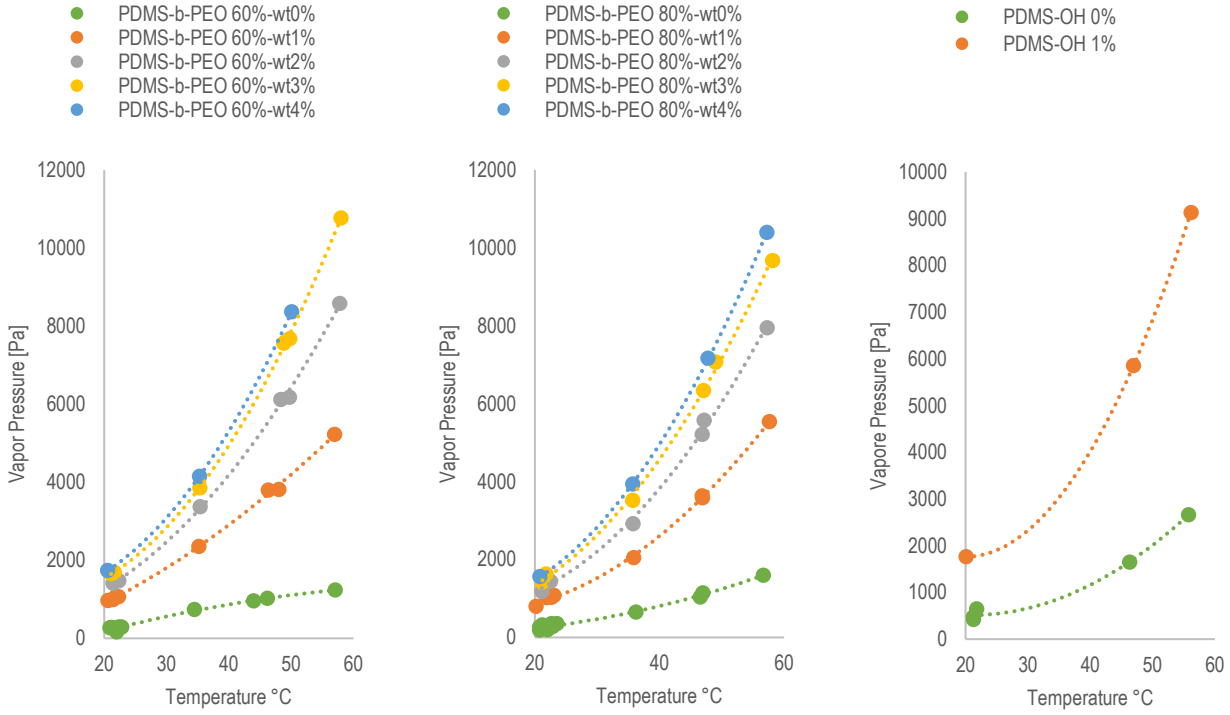

Figure 5.5: Equilibrium curves for the three different types of functionalized PDMS. Equilibrium lines are this time expressed as absolute vapor pressure function of temperature and water uptake.

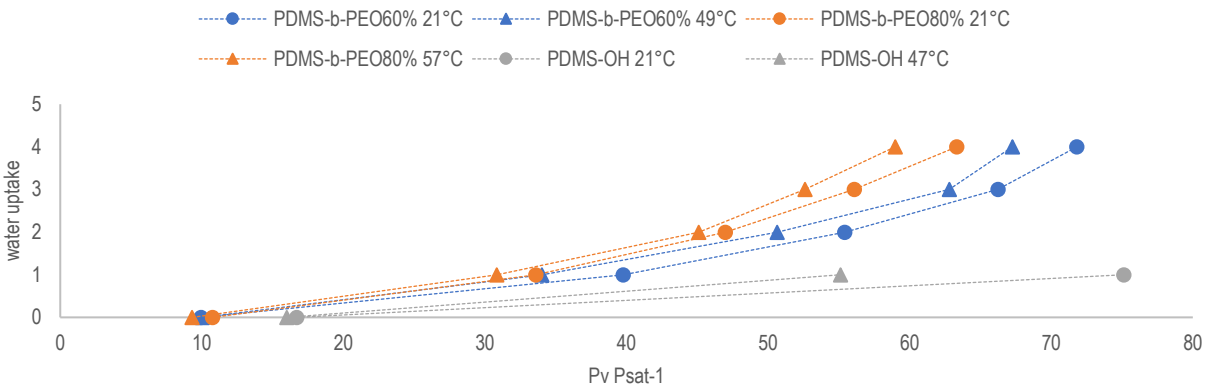

Figure 5.5a: Equilibrium curves for the three different PDMS.

As suggested from the literature review, PDMS-CH3 is hydrophobic also in its free and not-cross linked structure. Indeed, the 0% water uptake measurement (first 5 minutes of data acquisition) shows a moisture content equal to what measured in the LAB environment (a centralized air conditioning system maintained average indoor condition at constant level of 19.5°C and 41%, corresponding to a vapor pressure 930Pa. After the first injection of 0.2mL of water, the continuous rise of x, up to values close to RH=100% @20°C, is a confirmation that what measured inside the beaker is the gradual saturation of the internal volume, following the dynamics of evaporation rate over the paper media. For the other polymers, the 0% measurements gave a consistent reduction of the moisture content inside the beaker. With 0% of water uptake equilibrium vapor pressure was 265Pa for TEG@26.6°C, 266Pa for PDMS-b-PEO@20.8°C and 424Pa for PDMS-OH@21.3°C. The injection of 1% of the dry mass in water, shifted the equilibria at 600Pa for TEG@26.6°C, 798Pa for PDS-b-PEO@20.3°C and 1849Pa for PDMS-OH@20.8°C. PDMS-OH, despite showed hydrophilic properties when is dry, it reached a quasi-saturation with just one step of percentual increase. On the contrary TEG and PDMS-b-PEO have similar equilibrium values, but totally different dynamics. PDMS showed a much faster rate of uptake respect to TEG: equilibrium was reached in less than 15 minutes, while TEG requires at least 1.5 hours.

PDMS-PEO is resulting more interesting for its improved dynamics, indeed for a liquid desiccant the diffusivity and vapor permeability are much more important than total capacity properties.

In Figure 5.4 are collected the equilibrium conditions of the two different type of analysed PDMS-b-PEO, the 60% and the 80%. For comparison purpose is also shown the PDMS-OH and its incapability of taking up much more than 1% of water.

Range of operability of the polymer is in between of 0-4%, depending on environmental conditions. @20◦C the water content variation within the 0-3% interval the moisture content of the air in equilibrium with the liquid polymer increases from ≈ 1.5 -> 10 g /kg. These values are compatible with most of the applications requiring dehumidification of the indoor environment: a thermal swing from 20 to 50°C with a water content of 1% moves the equilibrium point from 6.5 to 24.5 g/kg. These 2 points can be considered interesting for applications of direct cooling and dehumidification.

Considering higher water uptakes, such the upper limit of 3% and a thermal swing between 20-50°C, the equilibrium movement is between 10-50 g/kg. Dew points with moisture contents higher than 50 g/kg are very interesting for application with the water harvesting cycle as presented in the Chapter 4.

5.1.2 Dynamic regeneration test

A similar scheme as in Figure 4.8 and 4.9 can be rearranged to exploit now the characteristics of the liquid PDMS-b-PEO. For this analysis was used the copolymer version with a concentration the -PEO blocks concentration of 80%. This is because considering an equal temperature swing between a hypothetical absorption phase (20-30°C) and the regeneration stage, the moisture difference (or the vapor pressure difference) is slightly higher, resulting in higher amount of extracted water.

The reference scheme is reported as in Figure 5.6. Main difference is on the batch process. Indeed, the desiccant is a liquid this can be pumped continuously between the regenerator (red) and the absorber (blue). The absorber absolves the function of continuously capturing the water vapor realizing the intimate contact between the air stream and the free surface of the desiccant. As consequence, this part of the circuit will be always as an *open loop*.

The regenerator, in the meanwhile, ensures for the heat supply for desiccant regeneration, realizing a tri-functional contact as needed for the realization of conjugated heat and mass transfer. The air stream will follow the closed loop approach, as described in the Chapter 4.

Despite the condensation unit does not require modification, the rest of the circuit requires additional components: *i*) two distinct fans works independently and in parallel. A third fan will be needed for the heat rejection through the dry cooler. *ii*) two pumps are needed to manage the desiccant circulation between the absorbed and the regenerator; iii) a specific design for the regenerator is needed to realize the conjugated heat and mass transfer.

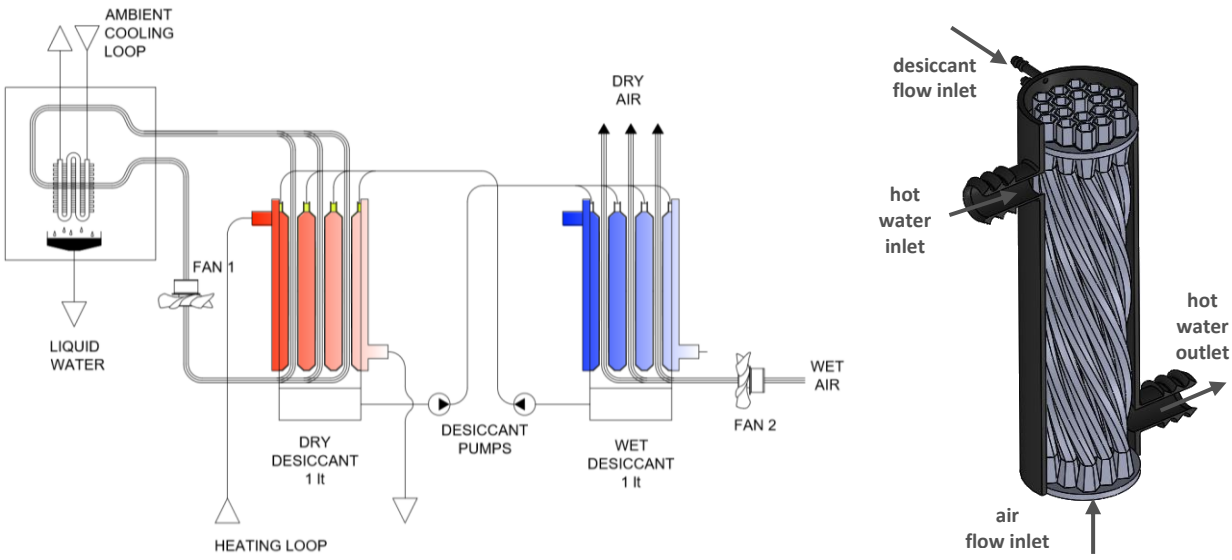

Figure 5.6: On the left the scheme for the implementation of the water harvesting cycle as in the chapter 4, with the liquid desiccant. On the right the configuration of the regenerator.

A prototype of the regenerator is realized as depicted on the right of the figure above, to proof the concept of the dynamic regeneration of the polymer.

The basic configuration is similar to typical shell and tubes geometry, widely spread in different industrial applications. The hot water flows from the top inlet, towards the outlet below. During this path, the hot stream licks the external surface of the tubes, delivering the heat to the internal part. The desiccant is pumped to the top of the regenerator. This fills up the small basin until the upper limit of the honeycomb structure, as in the picture. Once the desiccant level is higher than the channel height, this will fall through the channels for the gravitational action, wetting the internal surface of the tubes and absorbing the heat conducted through the tubes thickness. In the meanwhile, the air is flowing in the opposite direction of the desiccant flow, pushed with the fan through the tube channels. During this path, the water vapor released from the regeneration of the desiccant is mechanically transported to the condensing unit.

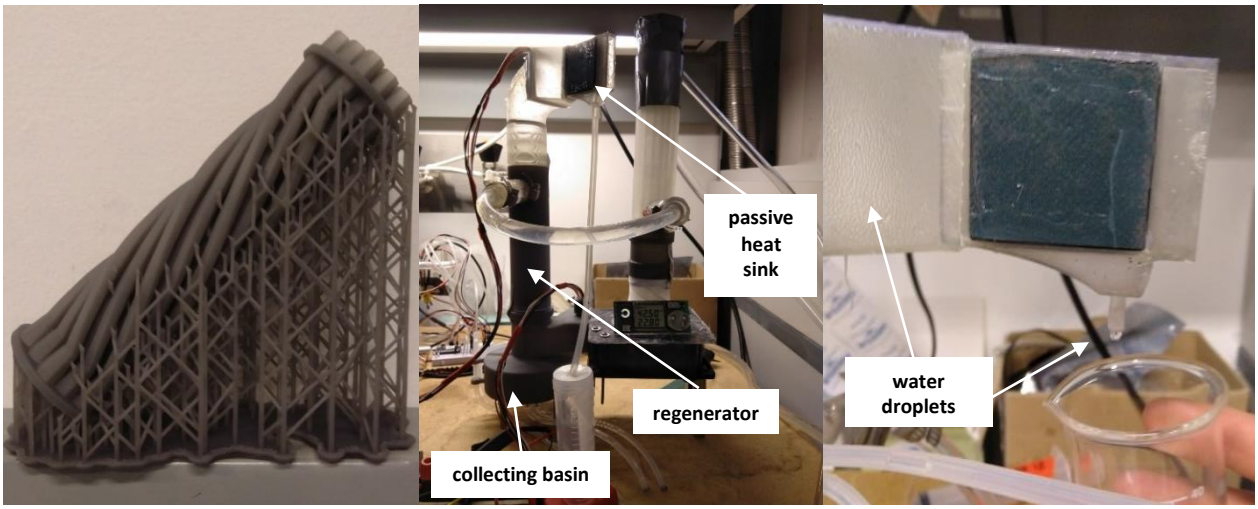

Figure 5.7: On the left the helicoidal tubes used for the regenerator configuration. In the middle the setup used for the testing of the proof of concept. On the right the magnification of the condensing unit, with just some drops of water collection.

This configuration has been realized as showed in Figure 5.7 through additive manufacturing (Form2 stereolithography printer). The helicoidal shape increases the length of the path per unit volume of the shell and tube, giving more contact time between the desiccant and the tube. This can increase the heat absorption and the release of water vapor. Instead of testing the entire cycle, a simple proof of concept test was realized with the setup as showed in the central picture, to demonstrate the feasibility of a dynamic regeneration, producing sufficiently high dew points for the spontaneous condensation. The outlet of the regenerator was connected to a square pin metallic heat sink, typically used in the electronics industry for the dissipation of heat. The picture on the right shows the heat sink, and the formation of water droplets all over the shell of the plastic channels, for the condensation of the hot and humid flow generated through the regeneration.

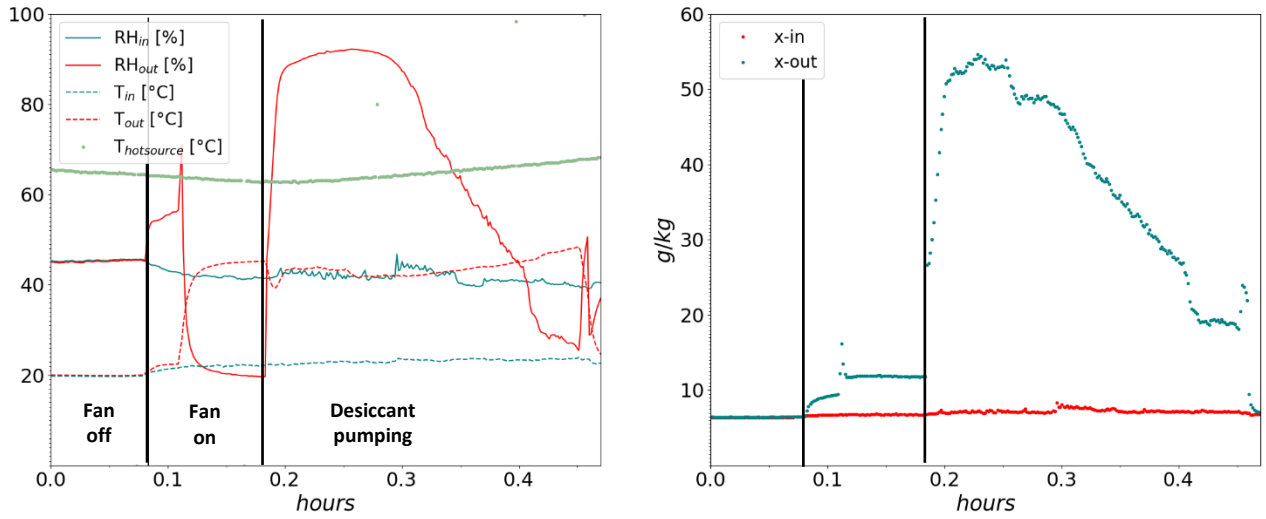

Figure 5.8: Regeneration test. In the graph of the left are reported the inlet/outlet temperature and relative humidity of the air through the tubes of the regenerator, together with the inlet temperature of the hot source. On the right the moisture difference.

Data of this test are reported in Figure 5.8. The graph on the left reports the inlet/outlet temperature with relative humidity and the inlet temperature of the hot water. Before starting the test, the basin for the collection of the desiccant was filled with 51.42 grams of dry PDMS-b-PEO @80% concentration, previously mixed with 1.03 grams of water, in order to have a desiccant with a water concentration equivalent to 2% in mass. At the time zero of the graph only hot water is circulating through the heat exchanger, while the fan in off. After few minutes the fan is powered flowing the air directly from the Lab environment (23.4°C and 43.9%), and heated up through the regenerator. This air movement generates a small increase of outlet moisture content due to two main factors: the presence of previous residual of desiccant over the regenerator surface. Second, before entering the tube channels the air stream flows over the free PDMS surface inside the collecting basin, removing some of the vapor released from the desiccant.

After the stabilization of this phase (around 6 minutes), the desiccant was pumped from the collecting basin, to the top of the regenerator, and continuously recirculated for the entire duration of the test. A 12VDC peristaltic pump was used for the desiccant recirculation.

The effect of the introduction of the desiccant is instantaneously evident. Relative humidity rises up to values close to 90%, with an air temperature that in the average was around 45°C. This condition activates in few minutes the condensation over the heat sink. Indeed, for around 6 minutes the outlet dew point from the regenerator was between 38-43°C. After the 6th minute the reduction of liquid water uptake lead to the reduction of the outlet conditions, meaning that the regeneration is going towards the final equilibrium point. The regeneration was considered concluded in approximately 15 minutes, and for half of this time the dew point generated was higher than 38°C.

A continuous supply of wet desiccant, generated from an equivalent absorber, will be necessary to guarantee a constant water uptake in the recirculation basin, necessary to sustain the generation of dew points higher than external temperature.

5.2 Composite Alginate Hydrogel

Previous experience showed that an alternative solution, to improve the performances of the water harvesting cycle analysed in the Chapter 4, can be the use of polymeric liquid desiccants. In this way, the increase of the daily productivity is disjointed from the total amount of used sorbent, eliminating the problem of encumbrance and total weight.

Indeed, one of the problems related to the use of silica gel, was the very low water uptake difference exploitable in the water harvesting cycle. For dry climates this value was between 0.1-0.06 $kg_w\ kg_{SiO2}^{-1}$, meaning that for the production of 15L of water per person per day (minimum requirements defined by WASH UNICEF for drinking, cooking and hygiene, in the context of the Sustainable Development Goal 6 [241]), will be required an equivalent dry mass of silica gel between 150-250kg. This is clearly a relevant limiting factor.

Anyway, the general approach used from material science on very innovative materials is not always towards the simultaneous fulfilment of all the requirements for a real, feasible, economic and safe application.

The exploration of hygroscopic polymers, derived from organic matter, is instead an interesting path respecting different constraints.

Other Authors already investigated on other different hydrogel types, that in most of the cases fail the main purposes: safe and healthy water quality, and durability or the material[163][164][242]. In this optic a special effort has been done with this research in order to develop a technological solution of ADS-HX based on the use of composite alginate hydrogels[162][243]. A composite hydrogel was realized starting from Bentonite, Calcium chloride and Sodium Alginate, a polysaccharide derived from brown algae and heavily distributed in their cell walls[244].

Thanks to its high biocompatibility, low cost, and the facility of manufacturing, a new high performing ADS-HX was realized throughout ionotropic gelation process [245–248]. The sodium alginate, polymer constituted of repeating blocks of guluronate and mannuronate monomers, is the starter of a cross linking process that, in the presence of an ionic solution with water and divalent cations (Ca^{+2}, Mg^{+2}, etc...), leads to the jellification of the viscous fluid into a solid hydrogel [248–255]

The crosslinking process, transforming the viscous gel in a solid hydrogel, is realized with ionotropic gelation technique in which the Na^{+}, contained as functional group in the alginate, that is exchanged with Ca^{+2} (or one of the others mentioned before) cation dissolved in a water solution. Having the calcium a higher valence number, this activated a cross linking among the different polymeric chains of the alginate, realizing the so called egg-box geometry (sketched in the scheme of Figure 5.9).

During this process, the bentonite fills the space between the polymeric chains and, being a hygroscopic clay with a very high level of porosity, increases the water capture capacity of the composite polymer material.

The use of the alginate is already experienced in different sectors of biological science, being a material extremely compatible with human health. Some of main biomedical applications are drug delivery and scaffold for cell cultivation.

5.2.1 Equilibrium tests

Isotherms of the material have been measured at different solution concentration. The setup used for testing equilibrium properties was similar to what explained in the paragraph 5.1.1. The calcium bentonite powder was dissolved in 1 Liter of deionized water (DIW) (wt 1-20%) and stirred at high rotation speed for 1 hour (>700 rpm). The solution is filtered multiple times (final mesh < 5μm), to remove impurities and not dissolved particles from water/bentonite liquid solution. Each filtering is alternated with an intermediate stirring phases of reduced time (10 mins and rotational speed >700rpm). In the Bent/DIW solution is added the gelling agent, the sodium salt from the alginic acid, within 0.5-4% of concentration, and rapidly mixed until the complete homogeneity of the solution. The obtained very viscous gel is degassed, under vacuum at relative pressure between 200-500 mbar for at least 20 mins, until a final use. The same procedure is realized to produce also a reference case without bentonite. In this case the initial mixing of DIW with the bentonite power is skipped.
In parallel, a DIW/CaCl2 solution is prepared (5-40% of CaCl2), with a continuous stirring of the water and salt until the use and temperature of the solution reduces to ambient temperature (hydration of the salt is a very exothermic reaction). Once the calcium chloride solution reached ambient temperature the alginate hydrogel (or the composite formulation when bentonite is added) was pumped with a peristaltic device and forced to drop in the setup realized in Figure 5.9. This consists of a square dripper, with matrix of 9x9 apertures of 6 mm. Once the alginate drops over each aperture of the dripper reaches a sufficient dimension and weight to overcome the internal viscous tension, they fall down in a basing full of calcium chloride at the desired concentration. An external pump continuously recirculates the divalent calcium solution, removing the beads formed over its surface, guarantying always free space for new forming drops. Once the desired amount of material is formed, 12 hours resting time is given to complete the entire ionotropic jellification, allowing to calcium chloride and Ca^{2+} ions to diffuse and permeate through the alginate wall towards the inner volume, completing the cross-linking operations.

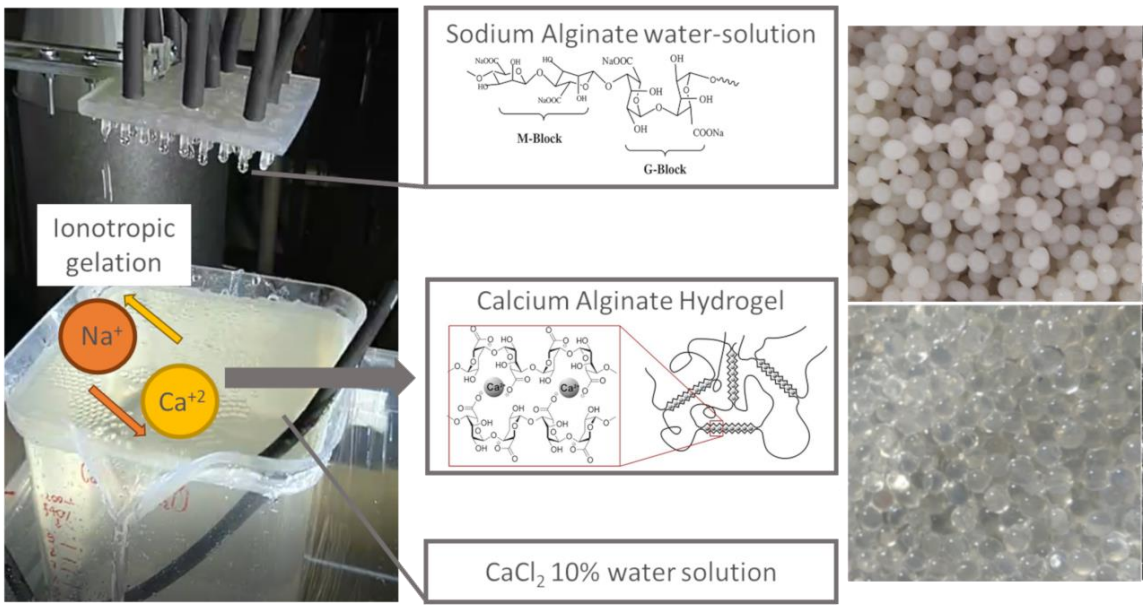

Figure 5.9: Cross-linking process of a Sodium Alginate (2%) with CaCl2 (10%) water solution (left), through the egg-box model. The beads, with an average diameter of 3 mm, manufactured with this process have been tested to evaluate the water uptake dependency with water vapor and temperature of the equilibrium. On the top right the composite hydrogel with bentonite, on the bottom the pristine hydrogel.

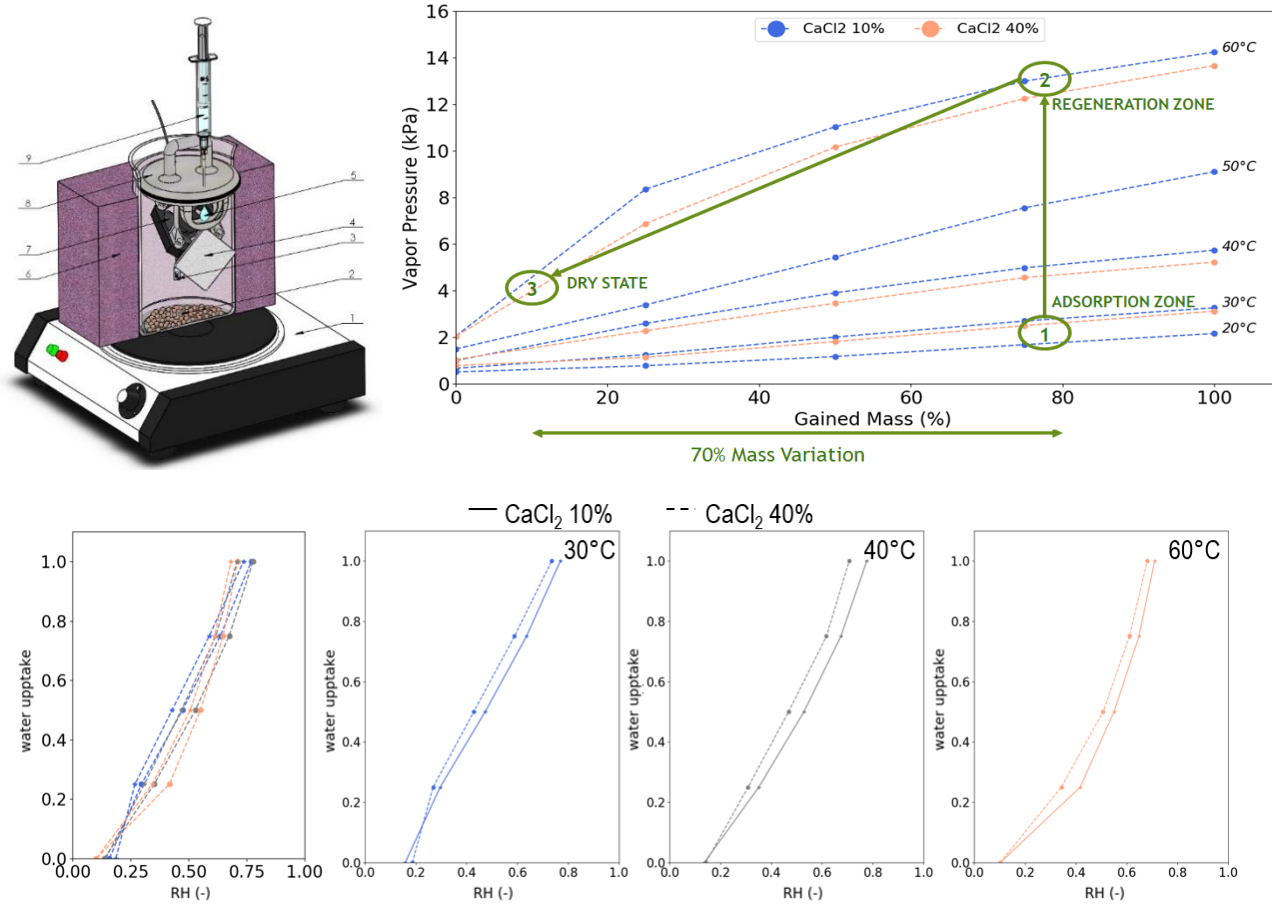

Figure 5.10: On the top left the schematic of the setup assembled to evaluate the equilibrium condition between air and the alginate beads. 1) magnetic stirrer with hot plate for temperature regulation; 2) alginate beads; 3) air temperature humidity sensor; 4) paper absorbing water; 5) water droplet; 6) thermal insulation; 7) air fan; 8) lead; 9) calibrated syringe for water injection. On the right picture of the setup. On the top right the Isothermal Adsorption curves of the hygroscopic polymer. This graph shows the relation between the water trapped in the pores of the material and the pressure and temperature of the water vapor in contact. Equilibrium isotherms at 25

and 65 ˚C, compare with the vapor pressure in dry climates and the condensing pressure at 35˚C (right). On the bottom of the figure the equilibrium points of different uptakes @30, 40 and 60°C and for two different salt concentration, 10% and 40%.

Finally, beads are removed from the salt bath, and thoroughly washed with DIW to remove the excess of $CaCl_2$ over the external surface. Completed this phase the material is cured in a ventilated oven at a temperature between 70°C.

Obtained material was tested with the same methodology as explained in the paragraph 5.1.1, the only differences are the sampled masses: 2 grams dry samples are used inside the beaker, and each injecting volume of water is equal to 0.25 mL, corresponding to a step increase of 25%. Final curves are showed in the graph on the top right of Figure 5.10.

With the final formulation the composite hydrogel reaches more than 40% of water uptake with a vapor pressure of 500 Pa (~35°C; 10%RH). With the hypothesis of applying a thermal swing between the operative adsorption temperature and a regeneration at 65°C, dew points higher than the environment can be easily reached (point 3 in the graph). This is a considerable improvement respect to silica gel, that in the same operative range (35°C, 10%) was not practicable. With this material, a minimum water uptake variation of 30% is easily achievable in very dry context. Anyway, extending the operational environment to wetter climates, water uptakes close to 100% are presumable. In the case of a similar ambient temperature, 35 ˚C, and relative humidity less than 20 %, regenerating the material at 65 ˚C, the water content changes of around 60%.

With an average estimation, can be said that for 1 kg of dry composite hydrogel, 600 ml of liquid water can be condensed at 35 ˚C, without the need of any external cooling source and with a similar cycle as in chapter 4.

5.2.2 Shrinking

Performing tests to evaluate other physical properties were essential to analyse behaviour of the material, especially the shrinking due to the curing stage. This last point is crucial for an effective manufacturing of the ADS-HX, and to have a stable component among the cycles.

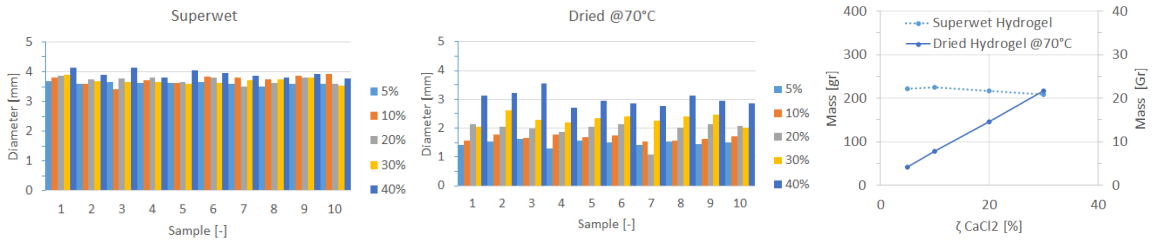

Figure 5.11: Diameter distribution of hydrogel sample with different initial Calcium Chloride concentration. On the left the distribution just after the crosslinking operation with the ionotropic gelation. In the middle the final distribution after the drying operation at 70°C. On the right the mass variation measured before and later the drying process.

Indeed, during the drying process from the initial super-wet condition up to a super-dry, the volumetric shrinking was consistent observing the diameter reduction before and after the drying. In Figure 5.11 is highlighted this aspect comparing the first two column diagrams, at different $CaCl_2$ concentration, from 40-5% (Figure 5.11).

This huge variation leads to the possibility of creep formation, due to the deformation and internal stresses. This huge volumetric variation is mainly due to water evaporation.

5.2.3 Alginate Honeycomb fabrication and Molding

As in the configuration of Chapter 3 and 4, the component to be developed is similarly working in a batch process. The contact area between the sorbent and the heat exchange medium is increased using a honeycomb channel geometry, minimizing the pressure drops generated during the flow of air through the sorbent channels. The schematic concept of ADS-HX is in Figure 5.15. The ADS-HX is realized combining an air/liquid heat exchanger, typically used as radiator in the automotive sector, with the hygroscopic polymer, such that the high contact area between air/sorbent/heat exchanger allowing the enhanced transfer rate of water vapor and energy typical of coated configurations and with low pressure drops on the air side.

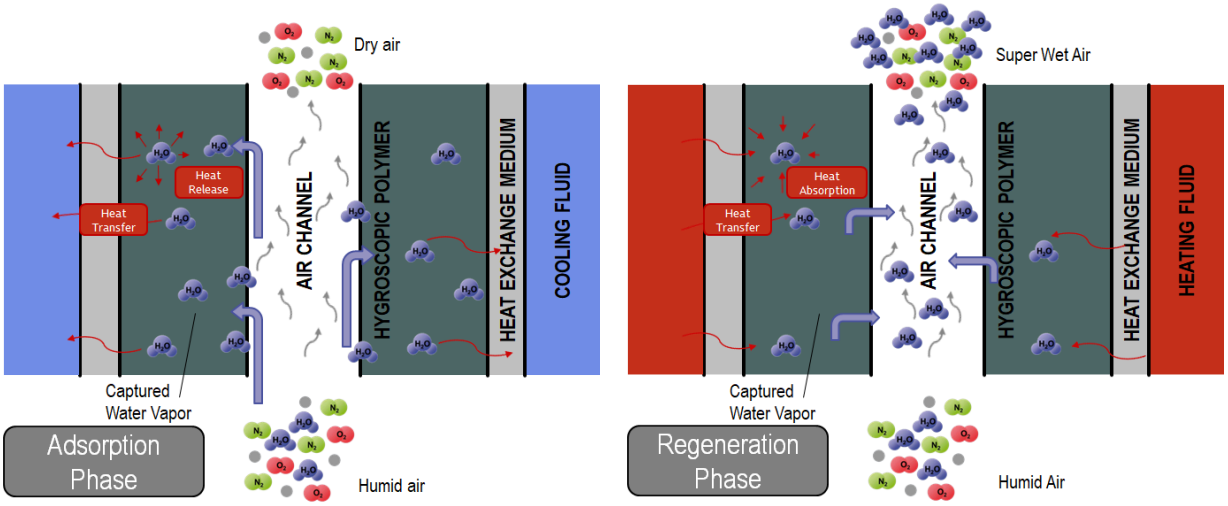

Figure 5.15: Schematic representation of the batch functioning of the ADS-HX with the hygroscopic polymer.

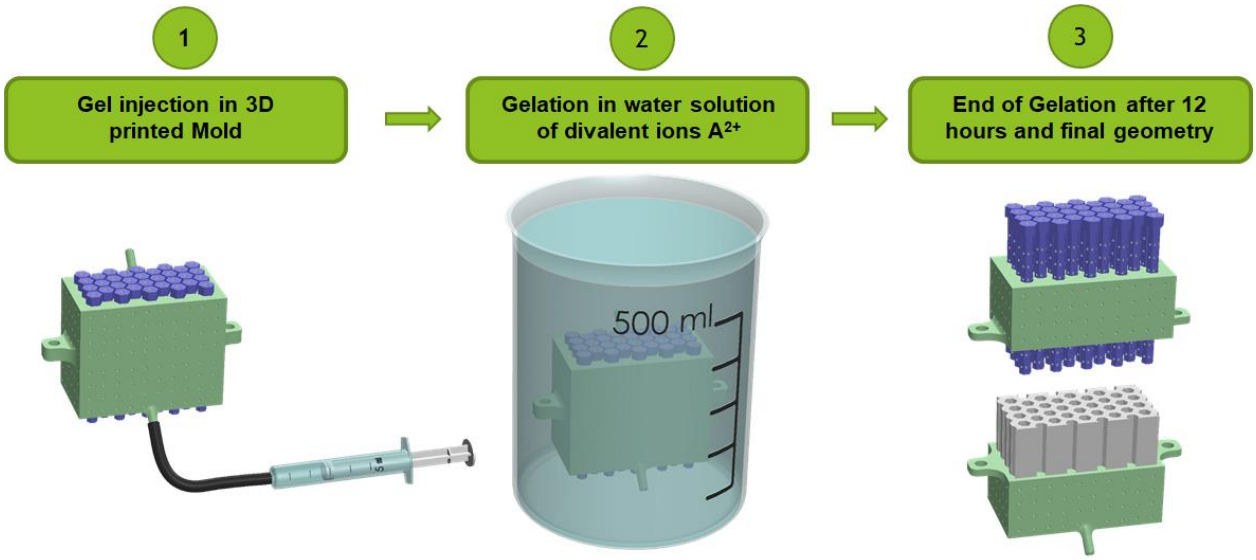

Figure 5.16: Schematic flow diagram of the required steps to shape a honeycomb geometry through the ionotropic gelation of sodium alginate in a ionic solution of water and divalent cations, with a molding technique.

Figure 5.17: Sample of Calcium-Bentonite-Alginate manufactured with a honeycomb structure and applied with a dip molding technique on a conventional packed heat exchanger.

The ionotropic gelation method of sodium alginate was adapted to a molding fabrication, to realize the honeycomb geometry. After the preliminary preparation of the viscous gel containing the main components of the hygroscopic polymer (sodium alginate, calcium bentonite, water), this is injected in a prefabricated mould, to shape the hydrogel in a desired geometry, as shown in the first step of the procedure showed in Figure 5.16. Once the mould is totally filled and degassed, this is deeply immersed in the divalent ionic solution, driving the cross linking for 12 hours. After that time the mould is disassembled, and the final sample removed. The preparation of the gel was similar to what explained before, requiring 13.35 grams of bentonite powder dissolved in 150 ml of deionized water, and stirred at high rotation speed @1000rpm for 1 hour. A total mass of 3.35 grams of sodium alginate was rapidly mixed, until the complete homogeneity. The obtained viscous solution was degassed under strong vacuum, due to the very high viscosity. Around 50 ml of the viscous Na-Alg/Bent/water solutions was manually injected in the 3d printed honeycomb mould, that once totally loaded were immersed in the CaCl2 solution for 12 hours.

The same approach can be used to create the honeycomb geometry directly over a heat exchanger geometry, as showed in Figure 5.18. The mould, with the honeycomb sticks, is directly assembled over a radiator heat exchanger. Once injected the gel, this will fill all the empty part surrounding and enveloping all the metallic structure of the heat exchanger. Final result of the ionotropic jellification is reported in the right of Figure 5.18. A final stable configuration is obtained after the curing of the sample as showed in Figure 5.19. This adherent structure, similar to a coated geometry over the surface of the heat exchanger, is realized more through a mechanical effect than a chemical link between the material of the HX and the polymer.

This is obtained thanks to the tensioning effect generated by the thermal shrinking of the polymer during the curing stage, completing the manufacturing process of the heat exchanger. Just after the ionotropic gelation the polymer is in a super hydrated state, that ends once the material is cured at temperature between 70-90°C for 12 hours. During the curing, the polymer exhibits a consistent volumetric shrinking, as highlighted in the graph of Figure 5.19, that depends by the concentration of the CaCl2, with values close to 90% of the initial volume for CaCl2 concentrations lower than 10%. This volume reduction creates a permanent stress in the material, leading to the cohesion on the surface of the HX. This type of adhesion is considered as an improved solution of typical chemical coatings, because should not suffer of the degradation problems typical of coating methods done with chemical linkers. This consideration is just a hypothesis that is not verified in the context of this research project.

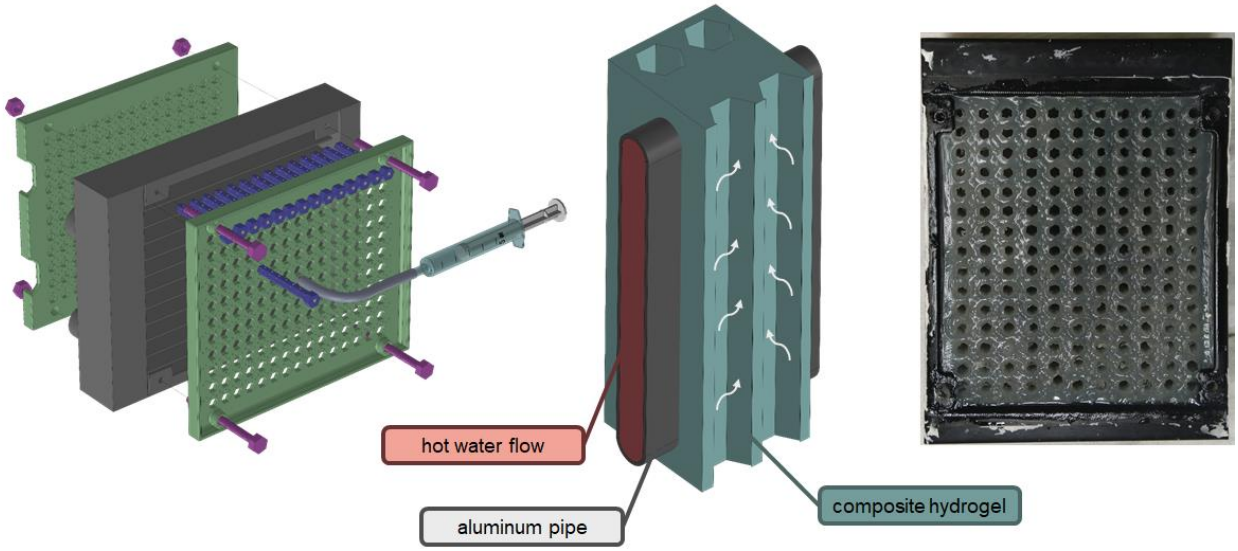

Figure 5.18: On the left a schematic representation of the direct molding approach over the heat exchanger structure. In the middle a simple piece of repeated element that constitute the composite ADS-HX. On the right a picture with a final result of the process.

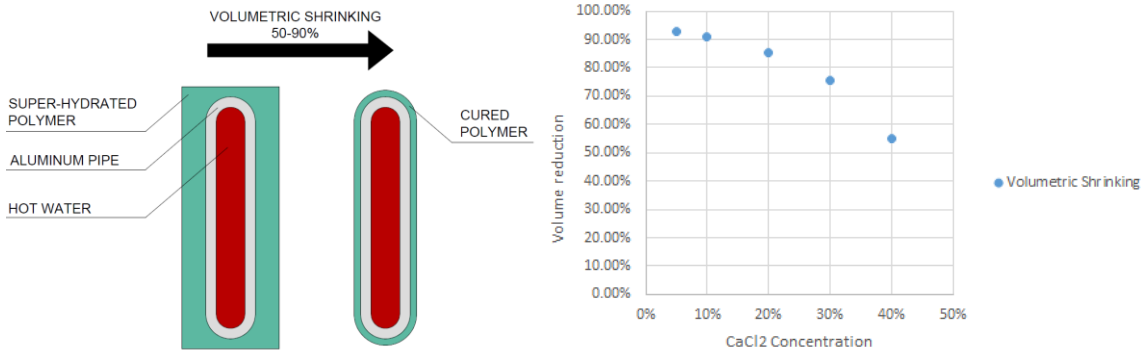

Figure 5.19: On the left the schematic representation of the shrinking effect on the geometry of the coating, during the preliminar curing stage. The volume reduction, due to water evaporation from the superwet configuration up to the final dry state of the polymer, is function of the Calcium Chloride concentration of the water solution during the ionotropic gelation. The graph in the middle shows the behaviour within a concentration range of 5-40%.

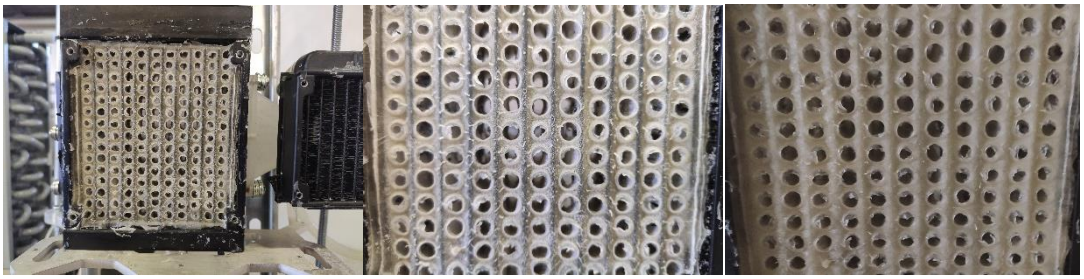

Figure 5.20: The picture in the left and in the middle are showing the deformation resulting from the curing operation at 85°C for 12 hours. The initial honeycomb geometry of the air channels is definitively lost. On the right the different appearance once exposed to air, the material absorb moisture.

As expected from the volumetric shrinking observed in the beads of different diameter and concentration, also in the final configuration of the ADS-HX in Figure 5.20 there's a consistent action of contraction that modify the original shape. Most of the initial shape of the holes (as in Figure 5.18) is lost, with an increased aperture in all the air channels.

The volume reduction observed in the graph of Figure 5.19 is due to the water evaporation from the hydrogel, that at the begin of its life is in an oversaturated condition because the production process. The aluminum

structure works as skeleton for the hydrogel channels, giving static points that interrupted the volumetric deformation between each channel line, along the horizontal of the section. Along the vertical line the presence of channel apertures offers the opportunity to discharge the contraction tension generated by the consistent lost of water during the curing. Most of the structure remained entire with the original geometry.

5.2.4 Internal Structure Imaging

Figures of this section show the external surface magnification, and internal geometry, with a FEI Quanta Scanning Electron Microscope (SEM) of the surface of 3mm beads of Calcium-Alginate (top left) and Calcium-Bentonite-Alginate (top right). Main feature is a more uniform pores distribution with a regular geometric shape coming from the crystalline nature of the aluminium phyllosilicate absorbent.

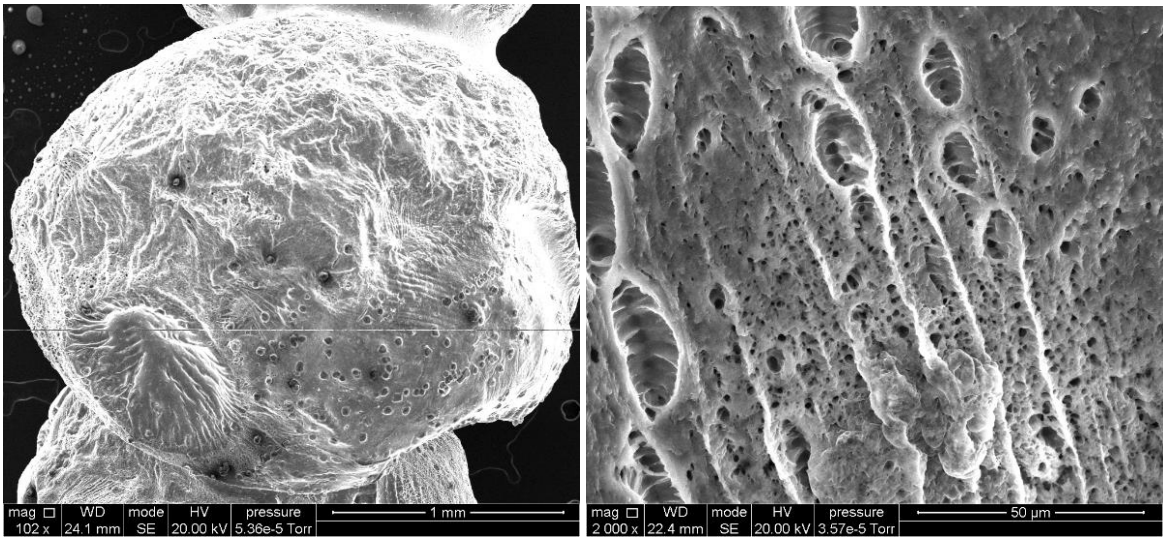

Figure 5.20: On the left the overall geometry of a Calcium-Alginate bead with a solution concentration @40%. On the right the magnification (2000x) of a spot over the bead surface

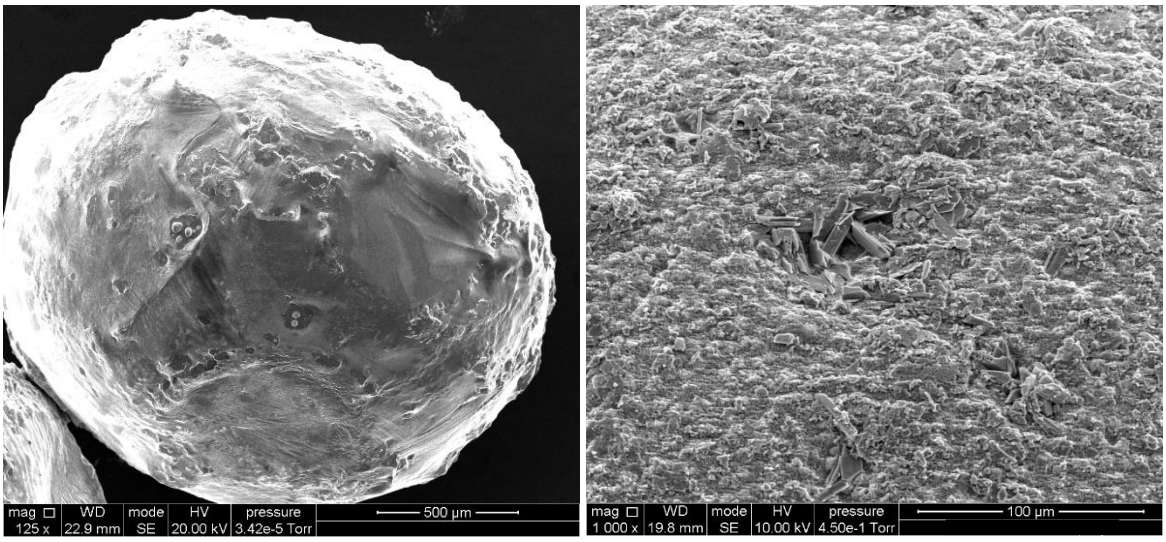

Figure 5.21: On the left the overall geometry of a Bentonite-Calcium-Alginate bead with a solution concentration @40%. On the right the magnification (1000x) over the external surface of the bead.

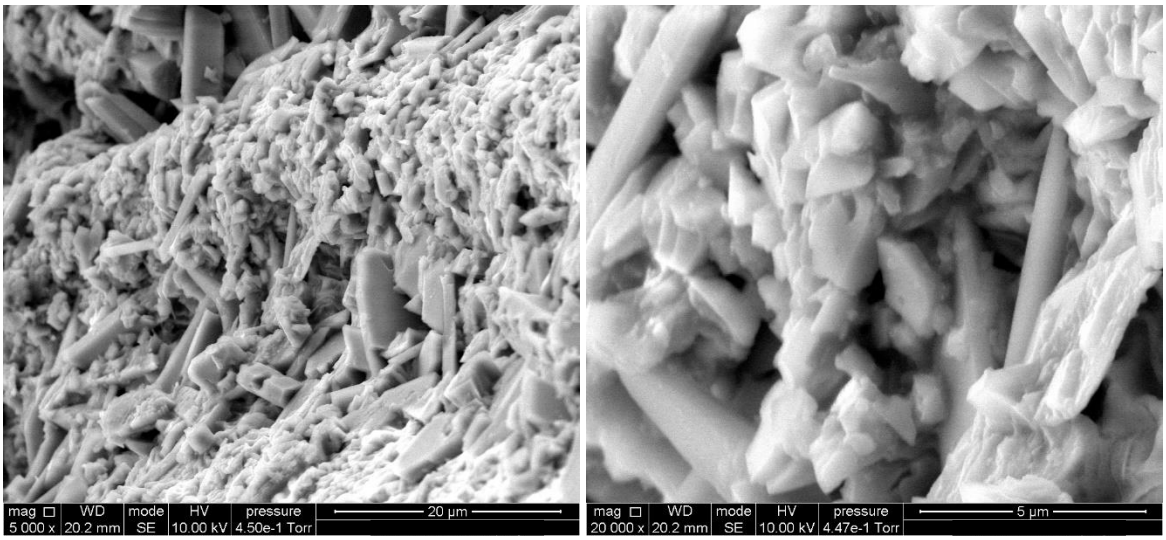

Figure 5.22: On the left magnification (5000x) of exernal surface of a Bentonite-Calcium-Alginate bead with a solution concentration @40%. On the right the magnification (20000x).

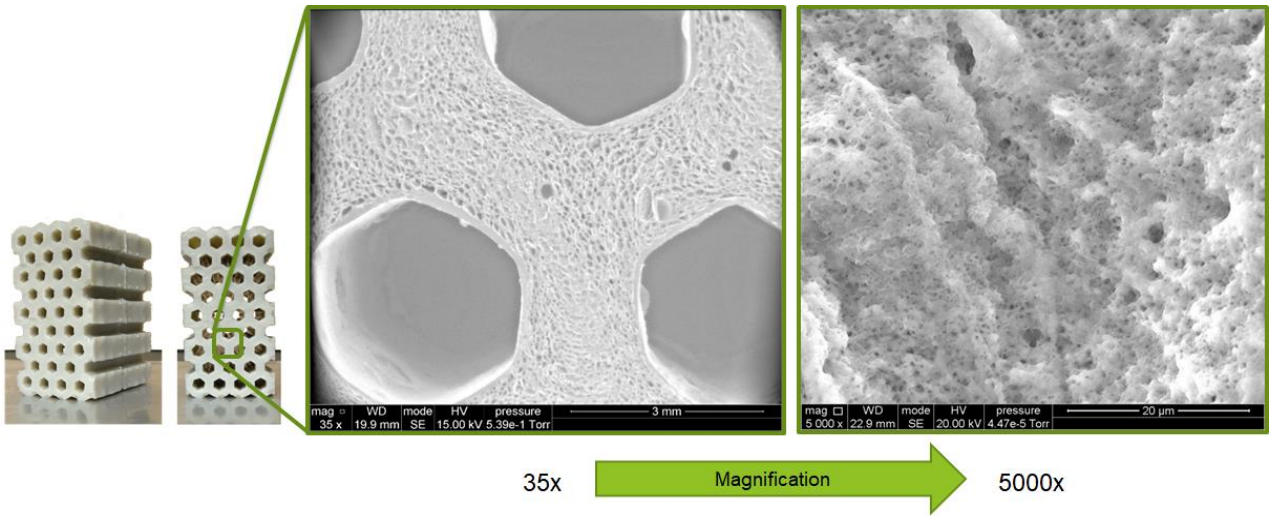

Figure 5.23: On the left magnification 35x magnification of an internal section of the honeyomb structure. On the right a spot magnification of 5000x

The last picture is very interesting, showing the internal structure of the material once the deep molding technique is applied. The most evident aspect is the density difference between the perimetral area surrounding the hexagonal cell and the rest of the bulk, which appears with a much higher level of macro porosity. This characteristic can be explained as result of the different linking process constituting the egg-box model. The presence of a divalent cation is the promoter for the association of different polymeric chains. Two different pairs of two consecutive G-blocks of sodium alginic acid (Figure 5.9) are connected creating the junction zone, coordinated by a Ca^{2+} ion[252]. This cross-linking process have the tendency to propagate towards the polymeric chain, increasing the length of the cross-linked chain. This ability is influenced by the concentration of $CaCl_2$, the number of G-G and M-G consecutive monomers in the alginic chain, and the time for reaction [248] [252] [253] [256–258]. Further one the type of divalent ions is influencing the preferential binding towards G rather than M monomer, that in increasing order of affinity it has been found as Mg<Ca<Sr<Ba[253]. In the case of calcium chloride solutions (as our case), the increase of Ca^{2+} concentrations promote chain formations in the

following order: coordination of the junction zone by the Ca^{2+} cation; egg box propagation through the chain; lateral association between parallel chains through the binding of MG groups with the Ca^{2+}, especially at higher concentrations. Higher concentration of Ca^{2+} positively influences the parallel connection increasing the Young modulus of the compound[259]. The inhomogeneity encountered over the honeycomb section between the cell walls and the inner volume, among different factors, can be imputed to an inhomogeneous distribution of the reactants concentration ($CaCl_2$ and G-G M-G groups) during the diffusion Ca^{2+}cations from the bulk of the bath though the inner part of the mold volume. According to the different steps defining the global process of ionotropic gelation of the alginate, formation of eggbox structures start over the external surface of the mold, where happens the first contact between the polysaccharide and Ca^{2+} cations. The excess of DIW water in the alginic solution leads to the diffusion of calcium chloride towards the inner part, activating the linking process also in the successive layers. In this phase both the eggbox formation and parallel linking create dense layers that propagates toward the inner part. More the chain connections are realized less is the residual free alginic present in the internal solution, and less frequently interchain connection are achievable. The faster formation of a ticker layer over the external surface might also have contributed to reduce the diffusion rate of Ca^{2+} to the inner volume, further reducing the interchain parallel connections. This density difference seems to be the main reason for the contraction of the structure after the drying process.

The modification of the structure has some influences on the hygroscopic properties of the material, as shown in the isotherms of Figure 5.10, but the entity of the increment seems not coherent with the 4 time variation on the salt concentration, showing the non-linearity correlation between the two parameters. As suggested in the paragraph 2.2.3, the effect on hygroscopic properties is more the result of the mutual interaction of sorbent/structure rather than the linear superposition of them. In this case, as for the mentioned composite sorbents, the mechanism of water sorption is more oriented towards the process of filling the pore volume and capillary condensation. The interchain parallel connections, process that have shown not linearly the effects on the volume variation, can be the major responsible for the variation of the pore volume and then of the water uptake at the different salt concentrations.

5.2.5 Conductivity

A different sample was prepared to measure thermal conductivity of the material. The production methodology was similar from the chemistry point of view, but the final manufacturing different. Indeed, the gel was first injected inside a mould replicating the shape of the flux meter Huksefluxe HFP01 (measurement range ±2000W m^{-2}; sensitivity $60x10^{-6}V\ W^{-1}m^2$; uncertainty ±3%). Then, once the mould was totally full, was immersed in the calcium chloride solution for jellification in the final form as in Figure 5.12. The sample was tested in the hot plate chamber Lasercomp Fox 600, imposing a fixed and known temperature difference (monitored with two thermocouple type E) across the two planar surfaces. The flux meter measured the heat flux across a thickness

of material equal to 10, 9 and 8 mm. Results of the monitoring and average values are reported respectively in figure 5.25 and 5.26.

Detected values of thermal conductivity ranged between 0.17 and 0.25 W $m^{-1}K^{-1}$, values that are not much far from the silica references of 0.12-0.2 $Wm^{-1}k^{-1}$ as reported in Table 2.2, or from $CaCl_2$ values (<0.2 W $m^{-1}k^{-1}$). This is evidently a not evident improvement respect to what is present in literature. Anyway, an encouraging way of development to achieve improved thermal properties might be the addition of conductive powders during the mixing stage of alginate/DIW water, to operate improvements on the thermal properties. Higher conductive materials may lead indeed to a massive presence of sorbent material in an ADS-HX configuration, as approached in the previous paragraph.

Figure 5.24: Assembled sample (@11 mm thickness) for the measurement of the heat flux.

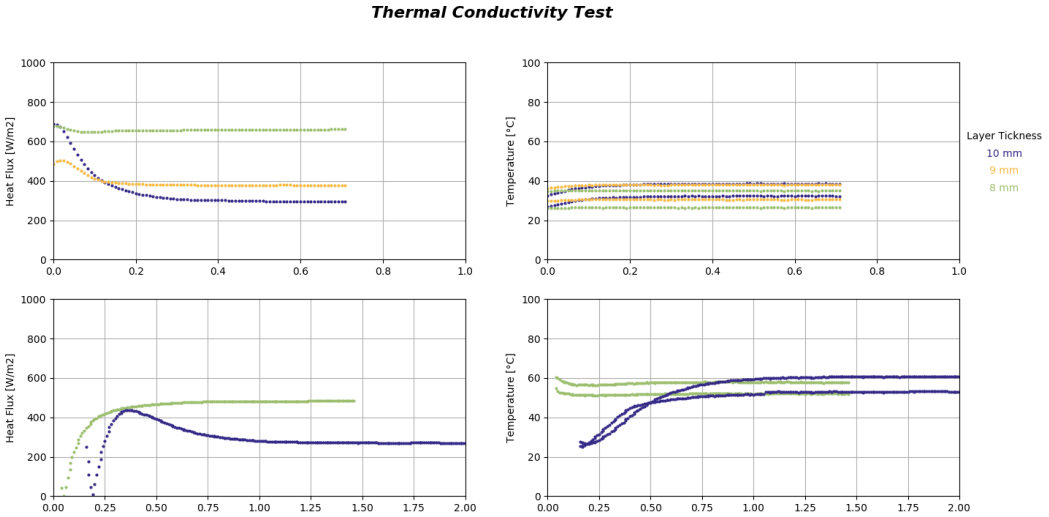

Figure 5.25: Transient of the thermal conductivity tests, operated on the samples @11, 9 and 8 mm of wall thickness.

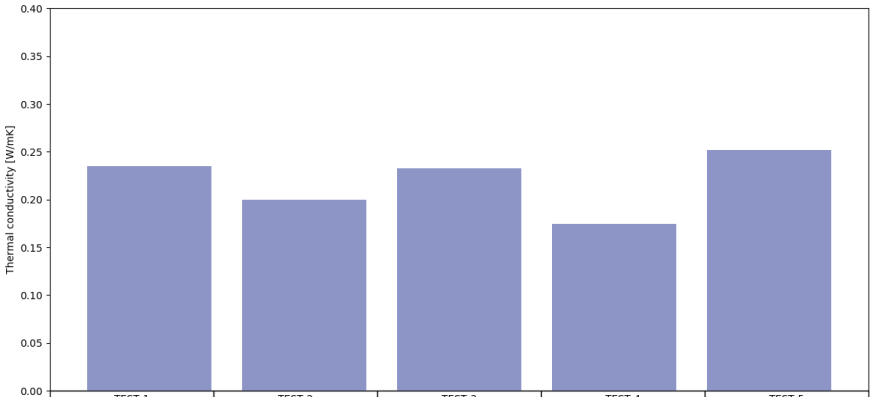

	TEST-1	TEST-2	TEST-3	TEST-4	TEST-5
Heat flux [W/m2K]	295.4	378.2	660.7	267.1	483.5
T up [°C]	32.3	30.5	26.4	53.0	52.0
T bot[°C]	38.6	38.1	34.9	60.7	57.8
L[mm]	5.0	4.0	3.0	5.0	3.0

Figure 5.26: Average value of thermal conductivity measured among different tests and configurations.

Conclusion

In this section solutions alternative to the configuration explored in Chapters 3 and 4 have been explored.

The liquid polymers are interesting for the miniaturization possibility on the global system, intrinsic of non-static desiccant. The copolymer PDMS-b-PEO showed very interesting performances, especially for its very rapid dynamics on absorbing and releasing water vapor. A small prototype has been tested to verify the possibility of regenerating, with dynamic conditions, at temperature between55-65°C. Results are very promising, and push further research interests on that direction.

Improvement of performances is also achievable on the static configuration, with using smarter and biocompatible material giving the possibility of realizing ADS-HX configurations with hybrid geometry respect to classical the coating or the packed bed solutions as in the chapter 3. The use of a composite hydrogel, based on calcium bentonite clay and alginate biopolymer, give the possibility to print configurations combining molding techniques and ionotropic gelation.

The composite hydrogel resulted in very high performances in terms of water uptakes. Figure 4 shows the water absorption capacity of the polymer at different temperatures and pressures of the water vapor in equilibrium. During the adsorption phase (operated at temperature between 20-35°C and pressure of water vapor between 0.8-1 kPa, typical of a dry environment) the water uptake can reach values as much as 80% of the dry basis (the water uptake of silica gel, the most common hygroscopic material, at the same operative condition is 10-15%). The regeneration can be carried out at temperature as low as 60°C, that can reduce the water content up to 10%. The total amount of water released (mass variation of 70%). This, combined with a good density of the polymer (650 kg m^{-3}), increases the total specific density of a machine based on this component, extracting up to 480 liters of water per cubic meter of composite.

BIBLIOGRAPHY

[1] OECD/IEA. The Future of Cooling Opportunities for energy-efficient air conditioning Together Secure Sustainable 2018:92.

[2] Ruthven DM (Douglas M. Principles of adsorption and adsorption processes. Wiley; 1984.

[3] Hirschler AE, Mertes TS. Liquid Phase Adsorption Studies Related to the Arosorb Process. Ind Eng Chem 1955;47:193–202. doi:10.1021/ie50542a019.

[4] Davis W.H., Harper J.I. WER. The Arosorb Process - A new refining tool. Oil Gas J 1952;51:112–6.

[5] Davis W.H., Harper J.I. WER. The arosorb process in Refinery operations. Pet Refin 1952;31:109–13.

[6] Kaneko K. Determination of pore size and pore size distribution. 1. Adsorbents and catalysts. J Memb Sci 1994;96:59–89. doi:10.1016/0376-7388(94)00126-X.

[7] Zdravkov BD, Čermák JJ, Šefara M, Janků J. Pore classification in the characterization of porous materials: A perspective. Cent Eur J Chem 2007;5:385–95. doi:10.2478/s11532-007-0017-9.

[8] Weitkamp J. Zeolites ad catalysis. Solid State Ionics 2000;13:175–88. doi:10.1177/2324709614545225.

[9] Mie G. Zur kinetischen Theorie der einatomigen Körper. Ann Phys 1903;316:657–97. doi:10.1002/andp.19033160802.

[10] Aristov YI, Tokarev MM, Freni A, Glaznev IS, Restuccia G. Kinetics of water adsorption on silica Fuji Davison RD. Microporous Mesoporous Mater 2006;96:65–71. doi:10.1016/J.MICROMESO.2006.06.008.

[11] Israelachvili JN. Intermolecular and Surface Forces: Third Edition. Intermol Surf Forces Third Ed 2011:1–676. doi:10.1016/C2011-0-05119-0.

[12] Hagymassy J, Brunauer S. Pore structure analysis by water vapor adsorption. II. Analysis of five silica gels. J Colloid Interface Sci 1970;33:317–27. doi:10.1016/0021-9797(70)90035-4.

[13] Stephen Brunauer. Contributions to Pore Structure Analysis. Inst Colloid Surf Sci Dep Chem Clarkson Coll Technol n.d.

[14] Polanyi M. The Potential Theory of Adsorption - Authority in science has its uses and its dangers. Science (80-) 1963;141:1010–3.

[15] E. Teller, S. Brunauer PHE. Adsorption of Gases in Multimolecular Layers. J Am Chem Soiety 1938;60:309–19. doi:10.1021/ja01269a023.

[16] Ng EP, Mintova S. Nanoporous materials with enhanced hydrophilicity and high water sorption capacity. Microporous Mesoporous Mater 2008;114:1–26. doi:10.1016/j.micromeso.2007.12.022.

[17] Ahn H, Lee CH. Effects of capillary condensation on adsorption and thermal desorption dynamics of water in zeolite 13X and layered beds. Chem Eng Sci 2004;59:2727–43. doi:10.1016/j.ces.2004.04.011.

[18] Ceratti DR, Faustini M, Sinturel C, Vayer M, Dahirel V, Jardat M, et al. Critical effect of pore characteristics on capillary infiltration in mesoporous films. Nanoscale 2015;7:5371–82. doi:10.1039/c4nr03021d.

[19] Boissiere C, Grosso D, Lepoutre S, Nicole L, Bruneau AB, Sanchez C. Porosity and mechanical properties of mesoporous thin films assessed by environmental ellipsometric porosimetry. Langmuir 2005;21:12362–71. doi:10.1021/la050981z.

[20] Hagymassy J, Brunauer S. Pore structure analysis by water vapor adsorption. II. Analysis of five silica gels. J Colloid Interface Sci 1970;33:317–27. doi:10.1016/0021-9797(70)90035-4.

[21] Ramsay JDF, Wing G. Small angle neutron scatteirng investigations of water sorption in porous silica and ceria gels. J Colloid Interface Sci 1991;141:475–85. doi:10.1016/0021-9797(91)90345-9.

[22] Ramsay JDF. Surface and pore structure characterisation by neutron scattering techniques. Adv Colloid Interface Sci 1998;76–77:13–37. doi:10.1016/S0001-8686(98)00039-6.

[23] Gil A, Grange P. Application of the Dubinin-Radushkevich and Dubinin-Astakhov equations in the characterization of microporous solids. Colloids Surfaces A Physicochem Eng Asp 1996;113:39–50. doi:10.1016/0927-7757(96)81455-5.

[24] Dubinin MM. The potential theory of adsorption of gases and vapors for adsorbents with energetically nonuniform surfaces. Theory Adsorpt Gases Vap 1969.

[25] Dubinin MM, Astakhov VA. Development of the concepts of volume filling of micropores in the adsorption of gases and vapors by microporous adsorbents - Communication 1. Carbon adsorbents. Bull Acad Sci USSR Div Chem Sci 1971;20:3–7.

doi:10.1007/BF00849307.

[26] Hu Q, Zhang Z. Application of Dubinin–Radushkevich isotherm model at the solid/solution interface: A theoretical analysis. J Mol Liq 2019;277:646–8. doi:10.1016/j.molliq.2019.01.005.

[27] Hair ML, Hertl W. Adsorption on hydroxylated silica surfaces. J Phys Chem 1969;73:4269–76. doi:10.1021/j100846a039.

[28] Hontoria, Peinado, Gonzalez, Cervates A. Study of the oxygen-ontaining groups in a series of graphite oxides: physical and chemical characterization. 1Carbon 1995;33:1585–92. doi:10.1016/0008-6223(95)00120-3.

[29] Khraisheh MAM, Al-Ghouti MA, Allen SJ, Ahmad MN. Effect of OH and silanol groups in the removal of dyes from aqueous solution using diatomite. Water Res 2005;39:922–32. doi:10.1016/j.watres.2004.12.008.

[30] Cohen-Tanugi D, Grossman JC. Water desalination across nanoporous graphene. Nano Lett 2012;12:3602–8. doi:10.1021/nl3012853.

[31] Zhuravlev LT. The surface chemistry of amorphous silica. Zhuravlev model. Colloids Surfaces A Physicochem Eng Asp 2000;173:1–38. doi:10.1016/S0927-7757(00)00556-2.

[32] Hofmann U, Endell K, Wilm D. Röntgenographische und kolloidchemische Untersuchungen über Ton. Angew Chemie 1934;47:539–47. doi:10.1002/ange.19340473002.

[33] E.K. R. No Title. Trans Faraday Soc 1936;32:4.

[34] A.V. K. The structure of silicic acid gels. KolloidnZh 1936;2:17.

[35] Annenkov V V, Danilovtseva EN, Pal'shin, A Ol'ga VA, Verkhozina N, Zelinskiy SN, Krishnan UM. Silicic acid condensation under the influence of water-soluble polymers: from biology to new materials 2017. doi:10.1039/c7ra01310h.

[36] Stöber W, Fink A, Bohn E. Controlled growth of monodisperse silica spheres in the micron size range. J Colloid Interface Sci 1968. doi:10.1016/0021-9797(68)90272-5.

[37] Saliba S, Ruch P, Volksen W, Magbitang TP, Dubois G, Michel B. Combined influence of pore size distribution and surface hydrophilicity on the water adsorption characteristics of micro- and mesoporous silica. Microporous Mesoporous Mater 2016;226:221–8. doi:10.1016/j.micromeso.2015.12.029.

[38] N.G. Yaroslavsky. No Title. Zhurnal Fiz Khimii 1950:68.

[39] N.G. Yaroslavsky ANT. No Title. Dokl Akad Nauk SSSR 1949;66:885.

[40] Kurbatov L.N. NGG. No Title. Dokl Akad Nauk SSSR 1949;68:99.

[41] Ng KC, Chua HT, Chung CY, Loke CH, Kashiwagi T, Akisawa A, et al. Experimental investigation of the silica gel±water adsorption isotherm characteristics. n.d.

[42] Razouk RI, Salem AS. The adsorption of water vapor on glass surfaces. J Phys Colloid Chem 1948;52:1208–27. doi:10.1021/j150463a013.

[43] Ding Z, Hu X, Lu GQ, Yue PL, Greenfield PF. Novel silica gel supported TiO2 photocatalyst synthesized by CVD method. Langmuir 2000;16:6216–22. doi:10.1021/la000119l.

[44] Alnaief M, Antonyuk S, Hentzschel CM, Leopold CS, Heinrich S, Smirnova I. A novel process for coating of silica aerogel microspheres for controlled drug release applications. Microporous Mesoporous Mater 2012;160:167–73. doi:10.1016/j.micromeso.2012.02.009.

[45] Mitra S, Aswin N, Dutta P. Scaling analysis and numerical studies on water vapour adsorption in a columnar porous silica gel bed. Int J Heat Mass Transf 2016;95:853–64. doi:10.1016/j.ijheatmasstransfer.2015.12.011.

[46] Sapienza A, Velte A, Girnik I, Frazzica A, Füldner G, Schnabel L, et al. "Water - Silica Siogel" working pair for adsorption chillers: Adsorption equilibrium and dynamics. Renew Energy 2017;110:40–6. doi:10.1016/j.renene.2016.09.065.

[47] Rao RGS, Singh PM, Rai M. Storability of onion seeds and effects of packaging and storage conditions on viability and vigour. Sci Hortic (Amsterdam) 2006;110:1–6. doi:10.1016/j.scienta.2006.06.002.

[48] Sircar S, Golden TC. Purification of hydrogen by pressure swing adsorption. Sep Sci Technol 2000;35:667–87. doi:10.1081/SS-100100183.

[49] Mohammad A, Jabeen N. TLC studies and separation of heavy metal cations on soil amended silica gel layers developed with surfactant-mediated solvent systems. Indian J Chem Technol 2003;10:79–86.

[50] Luckham PF, Rossi S. Colloidal and rheological properties of bentonite suspensions. Adv Colloid Interface Sci 1999;82:43–92. doi:10.1016/S0001-8686(99)00005-6.

[51] Sen Gupta S, Bhattacharyya KG. Kinetics of adsorption of metal ions on inorganic materials: A review. Adv Colloid Interface Sci 2011;162:39–58. doi:10.1016/j.cis.2010.12.004.

[52] Chua HT, Ng KC, Chakraborty A, Oo NM, Othman MA. Adsorption characteristics of silica gel + water systems. J Chem Eng Data 2002;47:1177–81. doi:10.1021/je0255067.

[53] Thu K, Kim YD, Amy G, Chun WG, Ng KC. A hybrid multi-effect distillation and adsorption cycle. Appl Energy 2013;104:810–21. doi:10.1016/j.apenergy.2012.12.007.

[54] Ng KC, Thu K, Kim Y, Chakraborty A, Amy G. Adsorption desalination: An emerging low-cost thermal desalination method. Desalination 2013;308:161–79. doi:10.1016/j.desal.2012.07.030.

[55] Sharma CS. Thermal Conductivity of Catalyst Pellets and other Porous Particles 1975;10:73–80.

[56] Sharafian A, Fayazmanesh K, McCague C, Bahrami M. Thermal conductivity and contact resistance of mesoporous silica gel adsorbents bound with polyvinylpyrrolidone in contact with a metallic substrate for adsorption cooling system applications. Int J Heat Mass Transf 2014;79:64–71. doi:10.1016/j.ijheatmasstransfer.2014.07.086.

[57] Ramzy K A, Kadoli R, Ashok Babu TP. Performance studies on the desiccant packed bed with varying particle size distribution along the bed. Int J Refrig 2012;35:663–75. doi:10.1016/j.ijrefrig.2011.11.016.

[58] Ahamat MA, Tierney MJ. Calorimetric assessment of adsorbents bonded to metal surfaces: Application to type A silica gel bonded to aluminium. Appl Therm Eng 2012;40:258–66. doi:10.1016/j.applthermaleng.2012.02.021.

[59] Ostrovskii NM, Chumakova NA, Bukhavtsova NM, Vernikovskaya N V., Aristov YI. Effect of capillary condensation on water sorption by composite calcium chloride in a porous matrix sorbents. Theor Found Chem Eng 2007;41:200–4. doi:10.1134/s0040579507020145.

[60] Wu JW, Biggs MJ, Pendleton P, Badalyan A, Hu EJ. Experimental implementation and validation of thermodynamic cycles of adsorption-based desalination. Appl Energy 2012;98:190–7. doi:10.1016/j.apenergy.2012.03.022.

[61] Robens E, Wang X. Investigation on the isotherm of silica gel+water systems. J Therm Anal Calorim 2004;76:659–69. doi:10.1023/b:jtan.0000028045.96239.7e.

[62] Freni A, Maggio G, Cipitì F, Aristov YI. Simulation of water sorption dynamics in adsorption chillers: One, two and four layers of loose silica grains. Appl Therm Eng 2012;44:69–77. doi:10.1016/j.applthermaleng.2012.03.038.

[63] Chang SC, Chien SY, Chen CL, Chen CK. Analyzing adsorption characteristics of CO 2 , N 2 and H 2 O in MCM-41 silica by molecular simulation. Appl Surf Sci 2015;331:225–33. doi:10.1016/j.apsusc.2015.01.084.

[64] CFR - Code of Federal Regulations Title 21 n.d. https://www.accessdata.fda.gov/scripts/cdrh/cfdocs/cfCFR/CFRSearch.cfm?fr=172.480 (accessed March 25, 2020).

[65] Taylor JP, Jacob F, Arendt EK. Fundamental study on the impact of silica gel and tannic acid on hordein levels in beer. Innov Food Sci Emerg Technol 2015;31:177–84. doi:10.1016/j.ifset.2015.07.007.

[66] Ng KC, Chua HT, Chung CY, Loke CH, Kashiwagi T, Akisawa A, et al. Experimental investigation of the silica gel-water adsorption isotherm characteristics. Appl Therm Eng 2001;21:1631–42. doi:10.1016/S1359-4311(01)00039-4.

[67] Multivariate Polynomial Regression - File Exchange - MATLAB Central n.d. https://www.mathworks.com/matlabcentral/fileexchange/34918-multivariate-polynomial-regression (accessed April 25, 2020).

[68] Agrawal A, Deshpande PD, Cecen A, Basavarsu GP, Choudhary AN, Kalidindi SR. Exploration of data science techniques to predict fatigue strength of steel from composition and processing parameters. Integr Mater Manuf Innov 2014;3:90–108. doi:10.1186/2193-9772-3-8.

[69] Colella C, Gualtieri AF. Cronstedt's zeolite. Microporous Mesoporous Mater 2007;105:213–21. doi:10.1016/j.micromeso.2007.04.056.

[70] Natural Zeolites Market Size, Share | Industry Trends Report, 2018-2025 n.d. https://www.grandviewresearch.com/industry-analysis/natural-zeolites-market (accessed March 29, 2020).

[71] McCusker LB, Olson DH, Baerlocher C. Atlas of Zeolite Framework Types. Elsevier; 2007. doi:10.1016/B978-0-444-53064-6.X5186-X.

[72] Trckova M, Matlova L, Dvorska L, Pavlik I. Kaolin, bentonite, and zeolites as feed supplements for animals: Health advantages and risks. Vet Med (Praha) 2004;49:389–99. doi:10.17221/5728-VETMED.

[73] Daković A, Tomašević-Čanović M, Dondur V, Rottinghaus GE, Medaković V, Zarić S. Adsorption of mycotoxins by organozeolites. Colloids Surfaces B Biointerfaces 2005;46:20–5. doi:10.1016/j.colsurfb.2005.08.013.

[74] Kabak B, Dobson ADW, Var I. Strategies to prevent mycotoxin contamination of food and animal feed: A review. Crit Rev Food Sci Nutr 2006;46:593–619. doi:10.1080/10408390500436185.

[75] Reháková M, Čuvanová S, Dzivák M, Rimár J, Gaval'Ová Z. Agricultural and agrochemical uses of natural zeolite of the clinoptilolite type. Curr Opin Solid State Mater Sci 2004;8:397–404. doi:10.1016/j.cossms.2005.04.004.

[76] Wang S, Peng Y. Natural zeolites as effective adsorbents in water and wastewater treatment. Chem Eng J 2010;156:11–24. doi:10.1016/j.cej.2009.10.029.

[77] Jiang N, Shang R, Heijman SGJ, Rietveld LC. High-silica zeolites for adsorption of organic micro-pollutants in water treatment: A review. Water Res 2018;144:145–61. doi:10.1016/j.watres.2018.07.017.

[78] Caro J, Noack M, Kölsch P, Schäfer R. Zeolite membranes - state of their development and perspective. Microporous Mesoporous Mater 2000;38:3–24. doi:10.1016/S1387-1811(99)00295-4.

[79] Aristov YI. Challenging offers of material science for adsorption heat transformation: A review. Appl Therm Eng 2013;50:1610–8. doi:10.1016/j.applthermaleng.2011.09.003.

[80] Henninger SK, Schmidt FP, Henning HM. Water adsorption characteristics of novel materials for heat transformation applications. Appl Therm Eng 2010;30:1692–702. doi:10.1016/j.applthermaleng.2010.03.028.

[81] Kim H, Cho HJ, Narayanan S, Yang S, Furukawa H, Schiffres S, et al. Characterization of Adsorption Enthalpy of Novel Water-Stable Zeolites and Metal-Organic Frameworks. Sci Rep 2016;6. doi:10.1038/srep19097.

[82] Chan KC, Chao CYH, Sze-To GN, Hui KS. Performance predictions for a new zeolite 13X/CaCl 2 composite adsorbent for adsorption cooling systems. Int J Heat Mass Transf 2012;55:3214–24. doi:10.1016/j.ijheatmasstransfer.2012.02.054.

[83] Simonetti M, Gentile V, Fracastoro GV, Freni A, Calabrese L, Chiesa G. Experimental testing of the buoyant functioning of a coil coated with SAPO34 zeolite, designed for solar DEC (Desiccant Evaporative Cooling) systems of buildings with natural ventilation. Appl Therm Eng 2016;103. doi:10.1016/j.applthermaleng.2016.02.072.

[84] Harriman LG. The dehumidification handbook. 2002.

[85] Eicker U, Schürger U, Köhler M, Ge T, Dai Y, Li H, et al. Experimental investigations on desiccant wheels. Appl Therm Eng 2012;42:71–80. doi:10.1016/j.applthermaleng.2012.03.005.

[86] Jia CX, Dai YJ, Wu JY, Wang RZ. Use of compound desiccant to develop high performance desiccant cooling system. Int J Refrig 2007;30:345–53. doi:10.1016/j.ijrefrig.2006.04.001.

[87] Aristov YI, Glaznev IS, Freni A, Restuccia G. Kinetics of water sorption on SWS-1L (calcium chloride confined to mesoporous silica gel): Influence of grain size and temperature. Chem Eng Sci 2006;61:1453–8. doi:10.1016/j.ces.2005.08.033.

[88] Aristov YI. New family of solid sorbents for adsorptive cooling: Material scientist approach. J Eng Thermophys 2007;16:63–72. doi:10.1134/S1810232807020026.

[89] Conde MR. Properties of aqueous solutions of lithium and calcium chlorides: formulations for use in air conditioning equipment design. Int J Therm Sci 2004;43:367–82. doi:10.1016/j.ijthermalsci.2003.09.003.

[90] Aristov YI, Tokarev MM, Cacciola G, Restuccia G. Selective water sorbents for multiple applications, 1. CaCl2 confined in mesopores of silica gel: Sorption properties. React Kinet Catal Lett 1996;59:325–33. doi:10.1007/BF02068130.

[91] Gordeeva LG, Aristov YI. Composites "salt inside porous matrix" for adsorption heat transformation: A current state-of-the-art and new trends. Int J Low-Carbon Technol 2012;7:288–302. doi:10.1093/ijlct/cts050.

[92] Breitbach M, Bathen D. Influence of ultrasound on adsorption processes. Ultrason Sonochem 2001;8:277–83. doi:10.1016/S1350-4177(01)00089-X.

[93] Hamdaoui O, Naffrechoux E, Tifouti L, Pétrier C. Effects of ultrasound on adsorption-desorption of p-chlorophenol on granular activated carbon. Ultrason Sonochem 2003;10:109–14. doi:10.1016/S1350-4177(02)00137-2.

[94] Yao Y. Enhancement of mass transfer by ultrasound: Application to adsorbent regeneration and food drying/dehydration. Ultrason Sonochem 2016;31:512–31. doi:10.1016/j.ultsonch.2016.01.039.

[95] Yao Y, Zhang W, Liu S. Feasibility study on power ultrasound for regeneration of silica gel-A potential desiccant used in air-conditioning system. Appl Energy 2009;86:2394–400. doi:10.1016/j.apenergy.2009.04.001.

[96] Pérez-Lombard L, Ortiz J, Pout C. A review on buildings energy consumption information. Energy Build 2008;40:394–8. doi:10.1016/j.enbuild.2007.03.007.

[97] Chappells † H, Shove ‡ E. Debating the future of comfort: environmental sustainability, energy consumption and the indoor environment. Build Res Inf 2005;33:32–40. doi:10.1080/0961321042000322762.

[98] Davis LW, Gertler PJ. Contribution of air conditioning adoption to future energy use under global warming. Proc Natl Acad Sci U S A 2015;112:5962–7. doi:10.1073/pnas.1423558112.

[99] Chenari B, Dias Carrilho J, Gameiro Da Silva M. Towards sustainable, energy-efficient and healthy ventilation strategies in buildings: A review. Renew Sustain Energy Rev 2016;59:1426–47. doi:10.1016/j.rser.2016.01.074.

[100] Sah RP, Choudhury B, Das RK. A review on adsorption cooling systems with silica gel and carbon as adsorbents. Renew Sustain Energy Rev 2015;45:123–34. doi:10.1016/j.rser.2015.01.039.

[101] Hassan HZ, Mohamad AA, Alyousef Y, Al-Ansary HA. A review on the equations of state for the working pairs used in adsorption cooling systems. Renew Sustain Energy Rev 2015;45:600–9. doi:10.1016/j.rser.2015.02.008.

[102] Shmroukh AN, Ali AHH, Ookawara S. Adsorption working pairs for adsorption cooling chillers: A review based on adsorption capacity and environmental impact. Renew Sustain Energy Rev 2015;50:445–56. doi:10.1016/j.rser.2015.05.035.

[103] Li XH, Hou XH, Zhang X, Yuan ZX. A review on development of adsorption cooling - Novel beds and advanced cycles. Energy Convers Manag 2015;94:221–32. doi:10.1016/j.enconman.2015.01.076.

[104] Sah RP, Choudhury B, Das RK. A review on low grade heat powered adsorption cooling systems for ice production. Renew Sustain Energy Rev 2016;62:109–20. doi:10.1016/j.rser.2016.04.036.

[105] Mat Wajid N, Mompuouo B, Omer S, Riffat SB. Review of Heat and Mass Transfer Enhancement Techniques and Current Advancement for Adsorption Heating/Cooling Systems. Int J Low-Carbon Technol 2019;14:461–7. doi:10.1093/ijlct/ctw010.

[106] Pennington NA. Humidity Changer For Air Conditioning 1955:9.

[107] Pennington NA. Air-Conditioner, including furnace. ACM SIGGRAPH Comput Graph 1994;28:131–4. doi:10.1145/178951.178972.

[108] Collier RK, Cohen BM. An analytical examination of methods for improving the performance of desiccant cooling systems. J Sol Energy Eng Trans ASME 1991;113:157–63. doi:10.1115/1.2930487.

[109] Global Desiccant Wheel Market Size, Market Share, Application Analysis, Regional Outlook, Growth Trends, Key Players, Competitive Strategies and Forecasts, 2017 to 2025 n.d. https://www.researchandmarkets.com/reports/4431589/global-desiccant-wheel-market-size-market-share (accessed April 9, 2020).

[110] Global Dehumidifier Market By Type (Desiccant, Refrigerant, Thermoelectric & Others), By End User (Industrial, Residential & Commercial), By Region (APAC, North America, MEA, South America & Others), Competition, Forecast & Opportunities, 2024 n.d. https://www.researchandmarkets.com/reports/4773072/global-dehumidifier-market-by-type-desiccant#rela1-4431589 (accessed April 9, 2020).

[111] Zhang H. NJ. A two-stage desicant cooling system using low-temperature heat. Build Serice Eng Researh Technol 1999;29:51–5.

[112] Finocchiaro P, Beccali M, Nocke B. Advanced solar assisted desiccant and evaporative cooling system equipped with wet heat exchangers. Sol Energy 2012;86:608–18. doi:10.1016/j.solener.2011.11.003.

[113] Beccali M, Finocchiaro P, Nocke B. Energy performance evaluation of a demo solar desiccant cooling system with heat recovery for the regeneration of the adsorption material. Renew Energy 2012;44:40–52. doi:10.1016/j.renene.2011.12.021.

[114] Sultan M, El-Sharkawy II, Miyazaki T, Saha BB, Koyama S. An overview of solid desiccant dehumidification and air conditioning systems. Renew Sustain Energy Rev 2015;46:16–29. doi:10.1016/j.rser.2015.02.038.

[115] La D, Dai YJ, Li Y, Wang RZ, Ge TS. Technical development of rotary desiccant dehumidification and air conditioning: A review. Renew Sustain Energy Rev 2010;14:130–47. doi:10.1016/j.rser.2009.07.016.

[116] Daou K, Wang RZ, Xia ZZ. Desiccant cooling air conditioning: A review. Renew Sustain Energy Rev 2006;10:55–77. doi:10.1016/j.rser.2004.09.010.

[117] Kodama A, Watanabe N, Hirose T, Goto M, Okano H. Performance of a multipass honeycomb adsorber regenerated by a direct hot water heating. Adsorption, vol. 11, Springer; 2005, p. 603–8. doi:10.1007/s10450-005-5992-6.

[118] Meckler G. Two-stage desiccant dehumidification in commercial building HVAC systems. ASHRAE Trans 1989;95:1116–1123.

[119] La D, Dai YJ, Li Y, Tang ZY, Ge TS, Wang RZ. An experimental investigation on the integration of two-stage dehumidification and regenerative evaporative cooling. Appl Energy 2013;102:1218–28. doi:10.1016/J.APENERGY.2012.06.053.

[120] Bongs C, Morgenstern A, Henning HM. Advanced performance of an open desiccant cycle with internal evaporative cooling. Energy Procedia 2012;30:524–33. doi:10.1016/j.egypro.2012.11.062.

[121] Bongs C, Morgenstern A, Lukito Y, Henning HM. Advanced performance of an open desiccant cycle with internal evaporative cooling. Sol

Energy 2014;104:103–14. doi:10.1016/j.solener.2013.07.022.

[122] L. P. Development of a Fixed-Bed Quasi-Isothermal Adsorption Dehumidifier : from Concept to Optimization , through Experimental and Theoretical Investigation. Phd Thesis 2015.

[123] Hales TC, Ferguson SP. A formulation of the Kepler conjecture. vol. 36. 2006. doi:10.1007/s00454-005-1211-1.

[124] Hales TC, Harrison J, McLaughlin S, Nipkow T, Obua S, Zumkeller R. A revision of the proof of the Kepler conjecture. Discret Comput Geom 2010;44:1–34. doi:10.1007/s00454-009-9148-4.

[125] Hales T, Adams M, Bauer G, Dang TD, Harrison J, Hoang LT, et al. A FORMAL PROOF of the KEPLER CONJECTURE. Forum Math Pi 2017;5:1–29. doi:10.1017/fmp.2017.1.

[126] Pistocchini L, Garone S, Motta M. Porosity and pressure drop in packed beds of spheres between narrow parallel walls. Chem Eng J 2016;284:802–11. doi:10.1016/j.cej.2015.08.047.

[127] Finocchiaro P, Beccali M, Gentile V. Experimental results on adsorption beds for air dehumidification. Int J Refrig 2016;63:100–12. doi:10.1016/j.ijrefrig.2015.10.022.

[128] Ergun S, Orning AA. Fluid Flow through Randomly Packed Columns and Fluidized Beds. Ind Eng Chem 1949;41:1179–84. doi:10.1021/ie50474a011.

[129] Hoekstra AY, Chapagain AK. Water footprints of nations : Water use by people as a 2007:35–48. doi:10.1007/s11269-006-9039-x.

[130] Database - Eurostat n.d. https://ec.europa.eu/eurostat/web/environment/water/database (accessed October 14, 2019).

[131] Mekonnen MM, Hoekstra AY. Sustainability: Four billion people facing severe water scarcity. Sci Adv 2016;2. doi:10.1126/sciadv.1500323.

[132] Alcamo J, Henrichs T. Critical regions: A model-based estimation of world water resources sensitive to global changes. Aquat. Sci., vol. 64, Birkhauser Verlag AG; 2002, p. 352–62. doi:10.1007/PL00012591.

[133] UNESCO-WWAP. The United Nations World Development Report 2019. Leaving no one behind. Executive Summary 2019:12. doi:.1037//0033-2909.I26.1.78.

[134] Gleick PH. Water, drought, climate change, and conflict in Syria. Weather Clim Soc 2014;6:331–40. doi:10.1175/WCAS-D-13-00059.1.

[135] Diffenbaugh NS, Swain DL, Touma D, Lubchenco J. Anthropogenic warming has increased drought risk in California. Proc Natl Acad Sci U S A 2015;112:3931–6. doi:10.1073/pnas.1422385112.

[136] Alkhudhiri A, Darwish N, Hilal N. Membrane distillation: A comprehensive review. Desalination 2012;287:2–18. doi:10.1016/j.desal.2011.08.027.

[137] Cath TY, Childress AE, Elimelech M. Forward osmosis: Principles, applications, and recent developments. J Memb Sci 2006;281:70–87. doi:10.1016/j.memsci.2006.05.048.

[138] UNESCO. World Water Development Report 2019. 2019.

[139] Lattemann S, Höpner T. Environmental impact and impact assessment of seawater desalination. Desalination 2008;220:1–15. doi:10.1016/j.desal.2007.03.009.

[140] Tang CY, She Q, Lay WCL, Wang R, Fane AG. Coupled effects of internal concentration polarization and fouling on flux behavior of forward osmosis membranes during humic acid filtration. J Memb Sci 2010;354:123–33. doi:10.1016/j.memsci.2010.02.059.

[141] Subramani A, Jacangelo JG. Emerging desalination technologies for water treatment: A critical review. Water Res 2015;75:164–87. doi:10.1016/j.watres.2015.02.032.

[142] Anis SF, Hashaikeh R, Hilal N. Reverse osmosis pretreatment technologies and future trends: A comprehensive review. Desalination 2019:159–95. doi:10.1016/j.desal.2018.11.006.

[143] Oki T, Kanae S. Global hydrological cycles and world water resources. Science (80-) 2006;313:1068–72. doi:10.1126/science.1128845.

[144] Park KC, Chhatre SS, Srinivasan S, Cohen RE, McKinley GH. Optimal design of permeable fiber network structures for fog harvesting. Langmuir 2013;29:13269–77. doi:10.1021/la402409f.

[145] Lee A, Moon MW, Lim H, Kim WD, Kim HY. Water harvest via dewing. Langmuir 2012;28:10183–91. doi:10.1021/la3013987.

[146] Sharma V, Yiannacou K, Karjalainen M, Lahtonen K, Valden M, Sariola V. Large-scale efficient water harvesting using bioinspired micro-patterned copper oxide nanoneedle surfaces and guided droplet transport. Nanoscale Adv 2019;1:4025–40. doi:10.1039/c9na00405j.

[147] Comanns P, Withers PC, Esser FJ, Baumgartner W. Cutaneous water collection by a moisture-harvesting lizard, the thorny devil (Moloch horridus). J Exp Biol 2016;219:3473–9. doi:10.1242/jeb.148791.

[148] Cao M, Ju J, Li K, Dou S, Liu K, Jiang L. Facile and Large-Scale Fabrication of a Cactus-Inspired Continuous Fog Collector. Adv Funct Mater 2014;24:3235–40. doi:10.1002/adfm.201303661.

[149] Zhang L, Wu J, Hedhili MN, Yang X, Wang P. Inkjet printing for direct micropatterning of a superhydrophobic surface: Toward biomimetic fog harvesting surfaces. J Mater Chem A 2015;3:2844–52. doi:10.1039/c4ta05862c.

[150] Andrews HG, Eccles EA, Schofield WCE, Badyal JPS. Three-dimensional hierarchical structures for fog harvesting. Langmuir 2011;27:3798–802. doi:10.1021/la2000014.

[151] Garrod RP, Harris LG, Schofield WCE, McGettrick J, Ward LJ, Teare DOH, et al. Mimicking a Stenocara beetle's back for microcondensation using plasmachemical patterned superhydrophobic-superhydrophilic surfaces. Langmuir 2007;23:689–93. doi:10.1021/la0610856.

[152] Comanns P, Effertz C, Hischen F, Staudt K, Böhme W, Baumgartner W. Moisture harvesting and water transport through specialized micro-structures on the integument of lizards. Beilstein J Nanotechnol 2011;2:204–14. doi:10.3762/bjnano.2.24.

[153] Olivier J, De Rautenbach CJ. The implementation of fog water collection systems in South Africa. Atmos Res 2002;64:227–38. doi:10.1016/S0169-8095(02)00094-7.

[154] Olivier J. Fog-water harvesting along the West Coast of South Africa: A feasibility study. Water SA 2002;28:349–60. doi:10.4314/wsa.v28i4.4908.

[155] Park KC, Chhatre SS, Srinivasan S, Cohen RE, McKinley GH. Optimal design of permeable fiber network structures for fog harvesting. Langmuir 2013;29:13269–77. doi:10.1021/la402409f.

[156] Gido B, Friedler E, Broday DM. Assessment of atmospheric moisture harvesting by direct cooling. Atmos Res 2016;182:156–62. doi:10.1016/j.atmosres.2016.07.029.

[157] Ozkan O, Wikramanayake ED, Bahadur V. Modeling humid air condensation in waste natural gas-powered atmospheric water harvesting systems. Appl Therm Eng 2017;118:224–32. doi:10.1016/j.applthermaleng.2017.02.096.

[158] Milani D, Abbas A, Vassallo A, Chiesa M, Bakri D Al. Evaluation of using thermoelectric coolers in a dehumidification system to generate freshwater from ambient air. Chem Eng Sci 2011;66:2491–501. doi:10.1016/j.ces.2011.02.018.

[159] Kim H, Rao SR, Kapustin EA, Zhao L, Yang S, Yaghi OM, et al. Adsorption-based atmospheric water harvesting device for arid climates. Nat Commun 2018;9. doi:10.1038/s41467-018-03162-7.

[160] Hanikel N, Prévot MS, Fathieh F, Kapustin EA, Lyu H, Wang H, et al. Rapid Cycling and Exceptional Yield in a Metal-Organic Framework Water Harvester. ACS Cent Sci 2019. doi:10.1021/acscentsci.9b00745.

[161] Kalmutzki MJ, Diercks CS, Yaghi OM. Metal–Organic Frameworks for Water Harvesting from Air. Adv Mater 2018;30. doi:10.1002/adma.201704304.

[162] Kallenberger PA, Fröba M. Water harvesting from air with a hygroscopic salt in a hydrogel–derived matrix. Commun Chem 2018;1:28. doi:10.1038/s42004-018-0028-9.

[163] Li R, Shi Y, Alsaedi M, Wu M, Shi L, Wang P. Hybrid Hydrogel with High Water Vapor Harvesting Capacity for Deployable Solar-Driven Atmospheric Water Generator. Environ Sci Technol 2018;52:11367–77. doi:10.1021/acs.est.8b02852.

[164] Li R, Shi Y, Shi L, Alsaedi M, Wang P. Harvesting Water from Air: Using Anhydrous Salt with Sunlight. Environ Sci Technol 2018;52:5398–406. doi:10.1021/acs.est.7b06373.

[165] Wang JY, Liu JY, Wang RZ, Wang LW. Experimental investigation on two solar-driven sorption based devices to extract fresh water from atmosphere. Appl Therm Eng 2017;127:1608–16. doi:10.1016/j.applthermaleng.2017.09.063.

[166] Ji JG, Wang RZ, Li LX. New composite adsorbent for solar-driven fresh water production from the atmosphere. Desalination 2007;212:176–82. doi:10.1016/j.desal.2006.10.008.

[167] Entezari A, Ejeian M, Wang R. Modifying water sorption properties with polymer additives for atmospheric water harvesting applications. Appl Therm Eng 2019;161:114109. doi:10.1016/j.applthermaleng.2019.114109.

[168] Entezari A, Ejeian M, Wang RZ. Extraordinary air water harvesting performance with three phase sorption. Mater Today Energy 2019;13:362–73. doi:10.1016/j.mtener.2019.07.001.

[169] Li R, Shi Y, Wu M, Hong S, Wang P. Improving atmospheric water production yield: Enabling multiple water harvesting cycles with nano sorbent. Nano Energy 2020;67:104255. doi:10.1016/j.nanoen.2019.104255.

[170] Kim H, Rao SR, Kapustin EA, Zhao L, Yang S, Yaghi OM, et al. Adsorption-based atmospheric water harvesting device for arid climates. Nat Commun 2018;9. doi:10.1038/s41467-018-03162-7.

[171] Hanikel N, Prévot MS, Fathieh F, Kapustin EA, Lyu H, Wang H, et al. Rapid Cycling and Exceptional Yield in a Metal-Organic Framework Water Harvester. ACS Cent Sci 2019;5:1699–706. doi:10.1021/acscentsci.9b00745.

[172] Bui DT, Chua KJ, Gordon JM. Comment on "Water harvesting from air with metal-organic frameworks powered by natural sunlight." Science (80-) 2017;358:eaao0791. doi:10.1126/science.aao0791.

[173] Schneider SH, Root TL, Mastrandrea MD. Encyclopedia of climate and weather. Oxford University Press; 2011.

[174] Harding R, Best M, Blyth E, Hagemann S, kabat P, Tallaksen LM, et al. WATCH: Current knowledge of the terrestrial global water cycle. J Hydrometeorol 2011;12:1149–56. doi:10.1175/JHM-D-11-024.1.

[175] Prashad L. Encyclopedia of Remote Sensing: water and energy cycles. Encycl Remote Sens 2014:878–81. doi:10.1007/978-0-387-36699-9.

[176] Vörösmarty CJ, Green P, Salisbury J, Lammers RB. Global water resources: Vulnerability from climate change and population growth. Science (80-) 2000;289:284–8. doi:10.1126/science.289.5477.284.

[177] Desalination – Past, Present and Future - International Water Association n.d. https://iwa-network.org/desalination-past-present-future/ (accessed April 23, 2020).

[178] Mezher T, Fath H, Abbas Z, Khaled A. Techno-economic assessment and environmental impacts of desalination technologies. Desalination 2011;266:263–73. doi:10.1016/j.desal.2010.08.035.

[179] Vanham D, Hoekstra AY, Wada Y, Bouraoui F, de Roo A, Mekonnen MM, et al. Physical water scarcity metrics for monitoring progress towards SDG target 6.4: An evaluation of indicator 6.4.2 "Level of water stress." Sci Total Environ 2018;613–614:218–32. doi:10.1016/j.scitotenv.2017.09.056.

[180] Gassert F, Reig P, Luo T, Maddocks A. Aqueduct country and river basin rankings: a weighted aggregation of spatially distinct hydrological indicators 2013:28.

[181] WAD | World Atlas of Desertification n.d. https://wad.jrc.ec.europa.eu/waterstress (accessed April 23, 2020).

[182] Sweet SK, Wolfe DW, DeGaetano A, Benner R. Anatomy of the 2016 drought in the Northeastern United States: Implications for agriculture and water resources in humid climates. Agric For Meteorol 2017;247:571–81. doi:10.1016/j.agrformet.2017.08.024.

[183] Pielke RA, Doesken N, Bliss O, Green T, Chaffin C, Salas JD, et al. Drought 2002 in Colorado: An unprecedented drought or a routine drought? Pure Appl Geophys 2005;162:1455–79. doi:10.1007/s00024-005-2679-6.

[184] Wan Z, Wang P, Li X. Using MODIS Land Surface Temperature and Normalized Difference Vegetation Index products for monitoring drought in the southern Great Plains, USA. Int J Remote Sens 2004;25:61–72. doi:10.1080/0143116031000115328.

[185] Scanlon BR, Faunt CC, Longuevergne L, Reedy RC, Alley WM, McGuire VL, et al. Groundwater depletion and sustainability of irrigation in the US High Plains and Central Valley. Proc Natl Acad Sci U S A 2012;109:9320–5. doi:10.1073/pnas.1200311109.

[186] Simoes Vitule JR, Azevedo-Santos VM, Salete Daga V, Pereira Lima-Junior D, Barroso de Magalhaes AL, Orsi ML, et al. Brazil's drought: Protect biodiversity. Science (80-) 2015;347:1427–8. doi:10.1126/science.347.6229.1427-b.

[187] Scarlet D. VARIATIONS IN ATMOSPHERIC WATER VAPOR: BASELINE RESULTS FROM SMITHSONIAN OBSERVATIONS. J Chem Inf Model 2013;53:1689–99. doi:10.1017/CBO9781107415324.004.

[188] Chen B, Liu Z. Global water vapor variability and trend from the latest 36year (1979 to 2014) data of ECMWF and NCEP reanalyses, radiosonde, GPS, and microwave satellite. J Geophys Res Atmos 2016;121:442–62. doi:10.1038/175238c0.

[189] Nedoluha GE, Michael Gomez R, Allen DR, Lambert A, Boone C, Stiller G. Variations in middle atmospheric water vapor from 2004 to 2013. J Geophys Res Atmos 2013;118:11285–93. doi:10.1002/jgrd.50834.

[190] Lambert A, Read WG, Livesey NJ, Santee ML, Manney GL, Froidevaux L, et al. Validation of the Aura Microwave Limb Sounder middle atmosphere water vapor and nitrous oxide measurements. J Geophys Res Atmos 2007;112:1–24. doi:10.1029/2007JD008724.

[191] Read WG, Lambert A, Bacmeister J, Cofield RE, Christensen LE, Cuddy DT, et al. Aura Microwave Limb Sounder upper tropospheric and lower stratospheric H2O and relative humidity with respect to ice validation. J Geophys Res Atmos 2007;112:1–29. doi:10.1029/2007JD008752.

[192] Wetzel Seemann S, Li J, Gumley LE, Strabala KI, Menzel WP. Operational retrieval of atmospheric temperature, moisture, and ozone from MODIS infrared radiances. Appl with Weather Satell 2003;4895:168. doi:10.1117/12.466686.

[193] Borbás ÉE, Seemann SW, Stephenson G, Kern A, Li J, Menzel WP. MODIS MOD07 Temperature , Moisture , and Ozone products : Recent Updates and Validation 2005:7. doi:10.1029/2005JD006103.Acknowledgements.

[194] Frantz D, Röder A, Stellmes M, Hill J. An operational radiometric landsat preprocessing framework for large-area time series applications. IEEE Trans Geosci Remote Sens 2016;54:3928–43. doi:10.1109/TGRS.2016.2530856.

[195] Remer LA, Kaufman YJ, Tanré D, Mattoo S, Chu DA, Martins J V., et al. The MODIS aerosol algorithm, products, and validation. J Atmos Sci 2005;62:947–73. doi:10.1175/JAS3385.1.

[196] Water Vapor (1 month - Terra/MODIS) | NASA 2020.

[197] LAADS S&O [1]: MOD05_L2--61 n.d. https://ladsweb.modaps.eosdis.nasa.gov/search/order/1/MOD05_L2--61 (accessed April 23, 2020).

[198] Trenberth KE, Fasullo J, Smith L. Trends and variability in column-integrated atmospheric water vapor. Clim Dyn 2005;24:741–58. doi:10.1007/s00382-005-0017-4.

[199] Robert G. Roosen RJA. Variations in atmospheric water vapor baseline results from smithsonian observations. J Chem Inf Model 2013;53:1689–99. doi:10.1017/CBO9781107415324.004.

[200] TMY3 (NREL & DWD) - Meteonorm (en) n.d. https://meteonorm.com/en/typical-meteorological-years (accessed October 14, 2019).

[201] Henninger SK, Schmidt FP, Henning HM. Water adsorption characteristics of novel materials for heat transformation applications. Appl Therm Eng 2010;30:1692–702. doi:10.1016/j.applthermaleng.2010.03.028.

[202] Duffie B. John A. Duffie, Solar Engineering of Thermal Processes, 4th Edition ,2013 by John Wiley & Sons. n.d.

[203] Kim H, Yang S, Rao SR, Narayanan S, Kapustin EA, Furukawa H, et al. RENEWABLE RESOURCES Water harvesting from air with metal-organic frameworks powered by natural sunlight Downloaded from. vol. 356. 2017.

[204] Li R, Shi Y, Wu M, Hong S, Wang P. Improving atmospheric water production yield: Enabling multiple water harvesting cycles with nano sorbent. Nano Energy 2020;67:104255. doi:10.1016/j.nanoen.2019.104255.

[205] Kim H, Yang S, Rao SR, Narayanan S, Kapustin EA, Furukawa H, et al. Water harvesting from air with metal-organic frameworks powered by natural sunlight. Science (80-) 2017;356:430–4. doi:10.1126/science.aam8743.

[206] Li R, Shi Y, Shi L, Alsaedi M, Wang P. Harvesting Water from Air: Using Anhydrous Salt with Sunlight. Environ Sci Technol 2018;52:5398–406. doi:10.1021/acs.est.7b06373.

[207] Zhao F, Zhou X, Liu Y, Shi Y, Dai Y, Yu G. Super Moisture-Absorbent Gels for All-Weather Atmospheric Water Harvesting. Adv Mater 2019;31:1806446. doi:10.1002/adma.201806446.

[208] Ruthven DM. Douglas M. Ruthven. Principles of Adsorption and Adsorption processes. 1984.

[209] Incropera FP. Introduction to heat transfer. Wiley; 2007.

[210] Li A, Thu K, Ismail A Bin, Ng KC. A heat transfer correlation for transient vapor uptake of powdered adsorbent embedded onto the fins of heat exchangers. Appl Therm Eng 2016;93:668–77. doi:10.1016/j.applthermaleng.2015.09.057.

[211] Klein G. Principles of adsorption and adsorption processes. vol. 4. 1985.

[212] Sharafian A, Bahrami M. Adsorbate uptake and mass diffusivity of working pairs in adsorption cooling systems. Int J Heat Mass Transf 2013;59:262–71. doi:10.1016/J.IJHEATMASSTRANSFER.2012.12.019.

[213] Ramzy K. A, Kadoli R, Ashok Babu TP. Improved utilization of desiccant material in packed bed dehumidifier using composite particles. Renew Energy 2011;36:732–42. doi:10.1016/j.renene.2010.06.038.

[214] Xu G, Guan W, Shi S, Blersch D. Adsorption model development for mass transport characteristics of MFEP structure by physisorption method. Chem Eng J 2018;354:922–31. doi:10.1016/J.CEJ.2018.08.080.

[215] Kabeel AE. Water production from air using multi-shelves solar glass pyramid system. Renew Energy 2007;32:157–72. doi:10.1016/j.renene.2006.01.015.

[216] Sharafian A, Bahrami M. Adsorbate uptake and mass diffusivity of working pairs in adsorption cooling systems. Int J Heat Mass Transf 2013;59:262–71. doi:10.1016/J.IJHEATMASSTRANSFER.2012.12.019.

[217] Chakraborty A, Saha BB, Ng KC, Koyama S, Srinivasan K. Theoretical insight of physical adsorption for a single-component adsorbent + adsorbate system: I. thermodynamic property surfaces. Langmuir 2009;25:2204–11. doi:10.1021/la803289p.

[218] Panou AI, Papadokostaki KG, Tarantili PA, Sanopoulou M. Effect of hydrophilic inclusions on PDMS crosslinking reaction and its

interrelation with mechanical and water sorption properties of cured films. Eur Polym J 2013;49:1803–10. doi:10.1016/j.eurpolymj.2013.04.004.

[219] Zhou J, Khodakov DA, Ellis A V., Voelcker NH. Surface modification for PDMS-based microfluidic devices. Electrophoresis 2012;33:89–104. doi:10.1002/elps.201100482.

[220] Toepke MW, Beebe DJ. PDMS absorption of small molecules and consequences in microfluidic applications. Lab Chip 2006;6:1484–6. doi:10.1039/b612140c.

[221] Zhou J, Ellis AV, Voelcker NH. Recent developments in PDMS surface modification for microfluidic devices. Electrophoresis 2010;31:2–16. doi:10.1002/elps.200900475.

[222] Choi SJ, Kwon TH, Im H, Moon D Il, Baek DJ, Seol ML, et al. A polydimethylsiloxane (PDMS) sponge for the selective absorption of oil from water. ACS Appl Mater Interfaces 2011;3:4552–6. doi:10.1021/am201352w.

[223] Di Colo G, Carelli V, Nannipieri E, Serafini MF, Vitale D. Effect of water-soluble additives on drug release from silicone rubber matrices. II. Sustained release of prednisolone from non-swelling devices. Int J Pharm 1986;30:1–7. doi:10.1016/0378-5173(86)90129-8.

[224] Abbasi F, Mirzadeh H, Katbab A-A. Modification of polysiloxane polymers for biomedical applications: a review. Polym Int 2001;50:1279–87. doi:10.1002/pi.783.

[225] DIMETHYLSILOXANE-(60-70% ETHYLENE OXIDE) BLOCK COPOLYMER, 20 cSt | Gelest, Inc. n.d. https://www.gelest.com/product/DBE-712/ (accessed April 26, 2020).

[226] DIMETHYLSILOXANE-(80% ETHYLENE OXIDE) BLOCK COPOLYMER, 40-50 cSt | Gelest, Inc. n.d. https://www.gelest.com/product/DBE-814/ (accessed April 26, 2020).

[227] SILANOL TERMINATED POLYDIMETHYLSILOXANE, 1,000 cSt | Gelest, Inc. n.d. https://www.gelest.com/product/DMS-S31/ (accessed April 26, 2020).

[228] POLYDIMETHYLSILOXANE EMULSION, 10,000 cSt | Gelest, Inc. n.d. https://www.gelest.com/product/DMS-T41M50/ (accessed April 26, 2020).

[229] Gelest. Polydimethylsiloxane emulsion. Saf Data Sheet DMS-T41M50 2016;1.1.

[230] Fleischer CA, Koberstein JT, Krukonis V, Wetmore PA. The Effect of End Groups on Thermodynamics of Immiscible Polymer Blends. 1. Interfacial Tension. Macromolecules 1993;26:4172–8. doi:10.1021/ma00068a016.

[231] Lee MH, Fleischer CA, Morales AR, Koberstein JT, Koningsveld R. The effect of end groups on thermodynamics of immiscible polymer blends. 2. Cloud point curves. Polymer (Guildf) 2001;42:9163–72. doi:10.1016/S0032-3861(01)00399-8.

[232] Zhang QH, Chen B, Zhan XL, Chen FQ. Synthesis and solution properties of PDMS-b-PEO amphophilic diblock copolymers. Wuli Huaxue Xuebao/ Acta Phys - Chim Sin 2009;25:1075–80. doi:10.3866/PKU.WHXB20090606.

[233] Sturmayr D, Bauer J, Launay B, Kickelbick G, Hsing N, Malanoski AP, et al. PDMS-b-PEO Block Copolymers as Surfactants in the Synthesis of Mesostructured Silica: A Theoretical and Practical Approach. Organosilicon Chem. V, Weinheim, Germany: Wiley-VCH Verlag GmbH; 2008, p. 689–95. doi:10.1002/9783527619924.ch109.

[234] Davis RL, Register RA. Coatings with thermally switchable surface energy produced from poly(ethylene oxide)-poly(dimethylsiloxane) block copolymer films. J Polym Sci Part B Polym Phys 2016;54:135–40. doi:10.1002/polb.23806.

[235] Fang MY and J. Hydrophilic PEO-PDMS for microfluidic applications. J Micromechanics Microengineering 2012;22. doi:ttps://doi.org/10.1088/0960-1317/22/2/025012.

[236] Otsuka H, Nagasaki Y, Kataoka K. PEGylated nanoparticles for biological and pharmaceutical applications. Adv Drug Deliv Rev 2003;55:403–19. doi:10.1016/S0169-409X(02)00226-0.

[237] Murthy NS, Zhang Z, Borsadia S, Kohn J. Nanospheres with a smectic hydrophobic core and an amorphous PEG hydrophilic shell: Structural changes and implications for drug delivery. Soft Matter 2018;14:1327–35. doi:10.1039/c7sm02472j.

[238] Murthy NS, Wang W, Kohn J. Microphase separation in copolymers of hydrophilic PEG blocks and hydrophobic tyrosine-derived segments using simultaneous SAXS/WAXS/DSC. Polymer (Guildf) 2010;51:3978–88. doi:10.1016/j.polymer.2010.06.024.

[239] Hazer B, Ayyıldız E, Bahadır F. Synthesis of PNIPAM–PEG Double Hydrophilic Polymers Using Oleic Acid Macro Peroxide Initiator. J Am Oil Chem Soc 2017;94:1141–51. doi:10.1007/s11746-017-3020-0.

[240] Ko PT, Lee IC, Chen MC, Tsai SW. Polymer microneedles fabricated from PCL and PCL/PEG blends for transdermal delivery of hydrophilic compounds. J Taiwan Inst Chem Eng 2015;51:1–8. doi:10.1016/j.jtice.2015.01.003.

[241] UNICEF - Water, Sanitation and Hygiene n.d. https://www.unicef.org/wash/ (accessed October 14, 2019).

[242] Liang H, Abshaev MT, Abshaev AM, Huchunaev BM, Griffiths S, Zou L. Water vapor harvesting nanostructures through bioinspired gradient-driven mechanism. Chem Phys Lett 2019;728:167–73. doi:10.1016/j.cplett.2019.05.008.

[243] Entezari A, Ejeian M, Wang R. Super atmospheric water harvesting hydrogel with alginate chains modified with binary salts. ACS Mater Lett 2020. doi:10.1021/acsmaterialslett.9b00315.

[244] Pawar SN, Edgar KJ. Alginate derivatization: A review of chemistry, properties and applications. Biomaterials 2012;33:3279–305. doi:10.1016/j.biomaterials.2012.01.007.

[245] Skjåk-Bræk G, Grasdalen H, Smidsrød O. Inhomogeneous polysaccharide ionic gels. Carbohydr Polym 1989;10:31–54. doi:10.1016/0144-8617(89)90030-1.

[246] Bajpai SK, Sharma S. Investigation of swelling/degradation behaviour of alginate beads crosslinked with Ca2+ and Ba2+ ions. React Funct Polym 2004;59:129–40. doi:10.1016/j.reactfunctpolym.2004.01.002.

[247] Motwani SK, Chopra S, Talegaonkar S, Kohli K, Ahmad FJ, Khar RK. Chitosan-sodium alginate nanoparticles as submicroscopic reservoirs for ocular delivery: Formulation, optimisation and in vitro characterisation. Eur J Pharm Biopharm 2008;68:513–25. doi:10.1016/j.ejpb.2007.09.009.

[248] Li L, Fang Y, Vreeker R, Appelqvist I, Mendes E. Reexamining the egg-box model in calcium - Alginate gels with X-ray diffraction. Biomacromolecules 2007;8:464–8. doi:10.1021/bm060550a.

[249] Powell DA, Morris ER, Gidley MJ, Rees DA. Conformations and interactions of pectins. II. Influence of residue sequence on chain association in calcium pectate gels. J Mol Biol 1982;155:517–31. doi:10.1016/0022-2836(82)90485-5.

[250] Grant GT, Morris ER, Rees DA, Smith PJC, Thom D. Biological interactions between polysaccharides and divalent cations: The egg-box model. FEBS Lett 1973;32:195–8. doi:10.1016/0014-5793(73)80770-7.

[251] Plazinski W. Molecular basis of calcium binding by polyguluronate chains. Revising the egg-box model. J Comput Chem 2011;32:2988–95. doi:10.1002/jcc.21880.

[252] Sikorski P, Mo F, Skjåk-Bræk G, Stokke BT. Evidence for egg-box-compatible interactions in calcium - Alginate gels from fiber x-ray diffraction. Biomacromolecules 2007;8:2098–103. doi:10.1021/bm0701503.

[253] Fang Y, Al-Assaf S, Phillips GO, Nishinari K, Funami T, Williams PA, et al. Multiple steps and critical behaviors of the binding of calcium to alginate. J Phys Chem B 2007;111:2456–62. doi:10.1021/jp0689870.

[254] Borgogna M, Skjåk-Bræk G, Paoletti S, Donati I. On the initial binding of alginate by calcium ions. the tilted egg-box hypothesis. J Phys Chem B 2013;117:7277–82. doi:10.1021/jp4030766.

[255] Kang D, Liu Q, Gu J, Su Y, Zhang W, Zhang D. Egg-Box-Assisted Fabrication of Porous Carbon with Small Mesopores for High-Rate Electric Double Layer Capacitors. ACS Nano 2015;9:11225–33. doi:10.1021/acsnano.5b04821.

[256] Gurikov P, Smirnova I. Non-Conventional Methods for Gelation of Alginate. Gels 2018;4:14. doi:10.3390/gels4010014.

[257] Vreeker R, Li L, Fang Y, Appelqvist I, Mendes E. Drying and rehydration of calcium alginate gels. Food Biophys 2008;3:361–9. doi:10.1007/s11483-008-9087-2.

[258] Stephen AM, Phillips GO, Williams PA. Food Polysaccharides and Their Applications: Second Edition. 2016.

[259] Voo WP, Ooi CW, Islam A, Tey BT, Chan ES. Calcium alginate hydrogel beads with high stiffness and extended dissolution behaviour. Eur Polym J 2016;75:343–53. doi:10.1016/j.eurpolymj.2015.12.029.

[260] Simonetti M, Gentile V, Liggieri L, Fracastoro GV, Carrabba MG. Experimental analysis of “NAC-wall” for hybrid ventilation mode. Energy Build 2017;152. doi:10.1016/j.enbuild.2017.07.047.

[261] Earth Fact Sheet n.d. https://nssdc.gsfc.nasa.gov/planetary/factsheet/earthfact.html (accessed April 25, 2020).

Attachments

A- Comparison of air pressure drop. SiO2 packed bed versus Zeolite-SAPO34 finned coil

T1 @ 15°C					T2 @ 25°C					T3 @ 35°C				
V_{T1}	Q	σ_Q	ΔP_{exp}	$\sigma_{\Delta P}$	V_{T2}	Q	σ_Q	ΔP_{exp}	$\sigma_{\Delta P}$	V_{T3}	Q	σ_Q	ΔP_{exp}	$\sigma_{\Delta P}$
[m s^{-1}]	[m^3 h^{-1}]	[m^3 h^{-1}]	[Pa]	[%]	[m s^{-1}]	[m^3 h^{-1}]	[m^3 h^{-1}]	[Pa]	[%]	[m s^{-1}]	[m^3 h^{-1}]	[m^3 h^{-1}]	[Pa]	[%]
0.33	150	±10.5	0	-	0.33	150	±10.5	0	-	0.33	150	±10.5	0	-
0.55	245	±17.15	1.8	±11%	0.55	247	±17.29	0.8	±25%	0.56	250	±17.5	0.5	±40%
0.78	350	±24.5	3.2	±6%	0.78	350	±24.5	2.7	±7%	0.78	350	±24.5	2.1	±10%
1.02	460	±32.2	5.4	±4%	1.04	467	±32.69	4.5	±4%	1.04	465	±32.55	4.05	±5%
1.28	575	±40.25	7.6	±3%	1.28	575	±40.25	7.5	±3%	1.28	575	±40.25	7.4	±3%
1.51	680	±47.6	11.4	±2%	1.50	675	±47.25	10.5	±2%	1.51	680	±47.6	10.25	±2%

Table A1. Experimental measurements of pressure drop tests carried out on the Zeo-SAPO34 coated finned coil. [[260]]

TEST		Q	T	ρ	m	ΔP_{exp}	v	Re	ε	L	ΔP_{Ergun}	R.E.
		[m^3/h]	[°C]	kg/m3	[kg/h]	[Pa]	[m/s]	[-]	[-]	[m]	[Pa]	[%]
1	RIG	461	55.8	1.07	495	69.9	0.42	72.5	0.38	0.038	82.20	-17.6%
2	ADS	348	30.2	1.16	405	55.2	0.32	59.9	0.38	0.038	56.35	-2.1%
3	RIG	589	74.5	1.02	598	96	0.54	88.2	0.38	0.038	118.89	-23.8%
4	ADS	349	30.8	1.16	405	53.6	0.32	59.8	0.38	0.038	56.29	-5.0%
5	RIG	252	56	1.07	271	32.9	0.23	39.7	0.38	0.038	33.26	-1.1%
6	ADS	253	32.4	1.16	292	35.9	0.23	42.7	0.38	0.038	34.36	4.3%
7	RIG	325	69.5	1.03	335	41.7	0.3	49.7	0.38	0.038	48.07	-15.3%
8	ADS	227	35.8	1.14	259	29	0.21	38.6	0.38	0.038	30.01	-3.5%
9	RIG	139	51.4	1.09	151	17.8	0.13	22.7	0.38	0.038	15.37	13.7%
10	ADS	128	29.3	1.17	149	17.2	0.12	22.5	0.38	0.038	14.15	17.8%
11	RIG	147	64.6	1.05	154	17.9	0.13	21.9	0.38	0.038	15.19	15.1%
12	ADS	134	30.5	1.16	156	17.6	0.12	22.4	0.38	0.038	14.13	19.7%
13	RIG	330	55.5	1.07	355	83.4	0.3	51.8	0.4	0.078	82.19	1.5%
14	ADS	309	32.3	1.16	357	78.1	0.28	52.0	0.40	0.078	76.87	1.6%
15	RIG	370	73.2	1.02	377	94.4	0.34	55.7	0.40	0.078	96.67	-2.4%
16	ADS	324	31.6	1.16	375	83.2	0.3	55.9	0.40	0.078	85.42	-2.7%
17	RIG	254	47.6	1.10	280	57.7	0.23	40.7	0.40	0.078	56.23	2.6%
18	ADS	214	30.7	1.16	249	47.5	0.2	37.4	0.40	0.078	47.12	0.8%
19	RIG	254	70.9	1.03	261	59.1	0.23	38.0	0.40	0.078	54.55	7.7%
20	ADS	210	32.5	1.16	243	47	0.19	35.3	0.40	0.078	43.72	7.0%
21	RIG	137	54	1.08	148	28.4	0.13	22.6	0.40	0.078	25.52	10.1%
22	ADS	138	31.8	1.16	160	29.9	0.13	24.2	0.40	0.078	26.09	12.8%
23	RIG	137	66.4	1.04	142	29.3	0.13	21.7	0.40	0.078	25.24	13.9%
24	ADS	139	30.5	1.16	162	28	0.13	24.3	0.40	0.078	26.12	6.7%
CPB-18-28	RIG	313	51.5	1.09	-	175	0.36	63.0	0.41	0.14	177.7	-1.6%
CPB-18-29	ADS	295	35.5	1.14	352	168	0.34	62.5	0.41	0.14	167.2	0.5%
CPB-18-30	ADS	274	31.5	1.16	362	158	0.31	57.8	0.41	0.14	146.1	7.6%
CPB-18-31	RIG	227	50	1.09	-	111	0.26	45.7	0.41	0.14	108.8	2.0%
CPB-18-32	ADS	218	30.6	1.16	261	105	0.25	46.7	0.41	0.14	105.8	-0.7%

CPB-18-33	ADS	212	30.6	1.16	266	105	0.24	44.9	0.41	0.14	99.6	5.1%

Table A2. Experimental measurements of pressure drop tests carried out on the SiO_2 packed bed configurations [[127]]

B - Testing condition of the ADS-HX coated with Zeolite SAPO34

TEST	Time	Qa	Ta in	Tout	x in	Tw in	v	Re
-	mins	m^3h^{-1}	°C	°C	g kg^{-1}	°C	m s^{-1}	-
1	156	163	36.9	61.3	0.032	88.5	0.36	118
3	39	210	34.2	56.3	0.029	78.0	0.47	156
5	70	252	32.4	62.8	0.024	86.5	0.56	184
7	44	307	32.3	55.6	0.026	79.5	0.68	230
9	38	355	30.5	57.1	0.023	85.3	0.79	265
11	37	408	32.9	54.9	0.023	81.4	0.91	304
13	37	465	31.8	54.3	0.020	85.1	1.04	348
15	38	509	30.0	51.7	0.013	83.4	1.13	384
17	40	570	31.2	50.7	0.018	80.0	1.27	430
19	39	620	29.9	49.6	0.012	82.0	1.38	469
21	45	683	31.3	51.7	0.018	31.3	1.52	514
23	43	736	30.5	51.3	0.016	87.9	1.64	555

Table B1. Set of the air flow, air temperature, humidity and phase duration of regeneration tests of the SAPO34 ADS-HX, preparing the tests of adsorption for the hybrid ventilation mode.

TEST	Time	Qa	Ta in	Tout	x in	dx-5	dx-10	dx-20	dx-30	Tw in	v	Re
-	Mins	m^3h^{-1}	°C	°C	g kg^{-1}	g kg^{-1}	g kg^{-1}	g kg^{-1}	g kg^{-1}	°C	m s^{-1}	-
2	87	163	31.5	33.7	0.026	3.6	4.6	1.4	0.4	64.6	0.36	125
4	90	210	33.4	35.9	0.031	5.4	5.6	2.1	1.1	58.9	0.47	160
6	120	252	31.9	33.5	0.024	3.7	4.6	2.2	1.5	58.0	0.56	193
8	120	307	31.7	33.1	0.026	4.8	4.8	1.3	1.3	56.1	0.68	235
10	90	356	31.8	33.6	0.025	5.5	4.4	1.6	1.2	61.2	0.79	273
12	100	405	32.1	33.7	0.024	5.3	4.2	1.7	1.1	60.4	0.90	311
14	90	465	32.0	32.2	0.023	4.6	3.2	1.2	0.8	61.3	1.04	357
16	100	509	31.1	31.3	0.018	2.9	2.5	1.3	1.0	57.1	1.13	392
18	90	570	31.5	31.6	0.031	2.8	2.2	1.2	1.0	57.0	1.27	439
20	90	620	31.1	32.2	0.013	2.5	1.6	1.1	0.8	57.5	1.38	477
22	90	683	31.3	31.3	0.020	4.0	2.4	1.0	0.9	56.1	1.52	526
24	90	738	31.5	31.6	0.017	2.9	1.7	0.9	0.8	57.6	1.64	568

Table B2. Set of the air flow, air temperature, humidity and phase duration of adsorption test during the adsorption of SAPO34 ADS-HX without cooling

C - AWG prototype and modelling parameters

- FAN 1 - is the centrifugal fan (model G1G108-AB17-02) moving the air in the closed loop of ADS-HX. Variable velocity 0-3000 rpm (0-10V PWM) with a maximum power consumption of 43 W, air flow rate 100 m3/h, 400 Pa,
- FAN 2 - is an axial fan (model A3G300-AN02-03) variable speed up to 2500 rpm, controlled with PWM (Pulse Width Modulation) signal between 0-10 V. Operative point 1400 m3/h, 14 Pa, 26 W.
- PUMP 1 - solar pump (20 W)
- PUMP 2 - condenser pump (20 W)
- 4WAY AIR VALVE

The functioning of the component is not continuous and variable. In the table below is reported the power consumptions in each test and the evaluation of the daily electric consumptions.

6	$P_{el\ max}$ (W)		TESTS																	
			20	21	22	23	24	25	26	27	28	29	30	31	32	33	36	37	38	39
Fan 1	43	duty	100%	70%	100%	30%	100%	50%	100%	30%	100%	50%	100%	70%	100%	70%	100%	30%	100%	50%
		P_{el} (W)	43	30	43	13	43	22	43	13	43	22	43	30	43	30	43	13	43	22
Fan 2	26	duty	0%	100%	0%	100%	0%	100%	0%	100%	0%	100%	0%	100%	0%	100%	0%	100%	0%	100%
		P_{el} (W)	0	26	0	26	0	26	0	26	0	26	0	26	0	26	0	26	0	26
Hot pump	10	duty	0%	100%	0%	100%	0%	100%	0%	100%	0%	100%	0%	100%	0%	100%	0%	100%	0%	100%
		P_{el} (W)	0	10	0	10	0	10	0	10	0	10	0	10	0	10	0	10	0	10
Cold pump	10	duty	0%	100%	0%	100%	0%	100%	0%	100%	0%	100%	0%	100%	0%	100%	0%	100%	0%	100%
		P_{el} (W)	0	10	0	10	0	10	0	10	0	10	0	10	0	10	0	10	0	10
Total Power (W)			43,0	76,1	43,0	58,9	43,0	67,5	43,0	58,9	43	87.5	43,0	76,1	43,0	76,1	43	78.9	43,0	67,5
Working Time (h)			15	9	15	9	15	9	15	9	15	10	15	9	15	9	14	10	15	9
Average Power (W)			55,4		49,0		52,2		49,0		62		55,4		55,4		58		52,2	
Total Energy (kWh)			0,645	0,6849	0,645	0,5301	0,645	0,6075	0,645	0,5301	0.602	0.875	0,645	0,6849	0,645	0,6849	0.602	0.789	0,645	0,6075
Daily consumptions			1,330		1,175		1,253		1,175		1.477		1,330		1,330		1.391		1,253	

k_{air}	0.027	W $m^{-1}K^{-1}$
k_{Al}	250	W $m^{-1}K^{-1}$
$c_{p_{Al}}$	900	J $kg^{-1}K^{-1}$
ρ_{Al}	2700	Kg m^{-3}
k_{Cu}	365	W $m^{-1}K^{-1}$
$c_{p_{Cu}}$	675	J kg^{-1} K^{-1}
D_0	1.6x10^{-6}	m^2 s^{-1}
ρ_{Cu}	2700	Kg m^{-3}
r	1.5	mm
$\bar{r_p}$	11x10^{-10}	M
Pr	0.7055	-
ρ_s	1129	Kg m^{-3}
L_{bed}	65	cm
P_{atm}	1.01325	bar
H_{bed}	10	cm
d_z	3	mm
d_t	1	s
a_f	16.13/0.12/0.65^2 ~ 318	m^2 m^{-3}
A_{th}	16.13	m^2
U_{ADS}	0.58	W $m^{-2}K^{-1}$
U_{RIG}	21.05	W $m^{-2}K^{-1}$
U_L	6.9	W $m^{-2}K^{-1}$
ε_b		-
ε_p	0.35	
ρ_w	1000	Kg m^{-3}
c_{p_w}	4186	J $kg^{-1}K^{-1}$
k_w	0.6	W $m^{-1}K^{-1}$

List of parameters ad constants used for the numerical solution of the model.

D - Load cell calibration

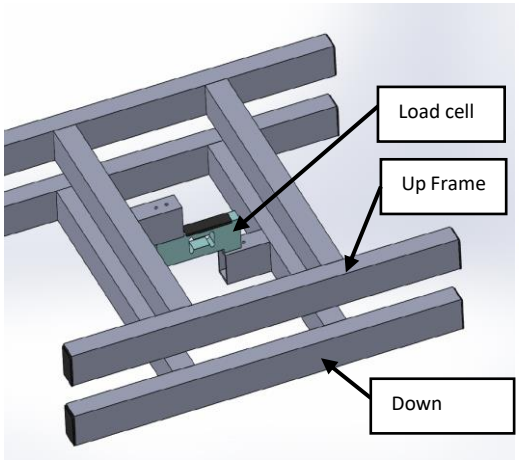

Calibration			
Element	Tare	Cumulative tare	Load cell Output
-	kg	kg	kg
Frame	0,99	0,99	0,97
1	1,084	2,0742	2,042
2	1,084	3,1580	3,102
3	1,0859	4,2439	4,17
4	1,0879	5,3318	5,238
5	1,0818	6,4136	6,307
6	1,073	7,4866	7,352
7	1,0868	8,5734	8,42
8	1,0849	9,6583	9,48
9	1,0822	10,7405	10,54
10	1,0851	11,8256	11,62
11	1,0828	12,9084	12,68
12	1,0814	13,9898	13,74
13	1,0858	15,0756	14,8
14	1,0834	16,1590	15,87
15	1,0815	17,2405	16,93
16	1,0836	18,3241	17,99
17	1,0824	19,4065	19,05
18	1,0814	20,4879	20,1
19	1,0859	21,5738	21,18
20	1,0854	22,6592	22,24
21	1,008	23,6672	23,22
22	1,9983	25,6655	25,18
23	1,9985	27,6640	27,13
24	10,6725	38,3365	37,59
25	9,1153	47,4518	46,52
26	16,0665	63,5183	62,29
27	7,852	71,3703	69,96
28	6,784	78,1543	76,58

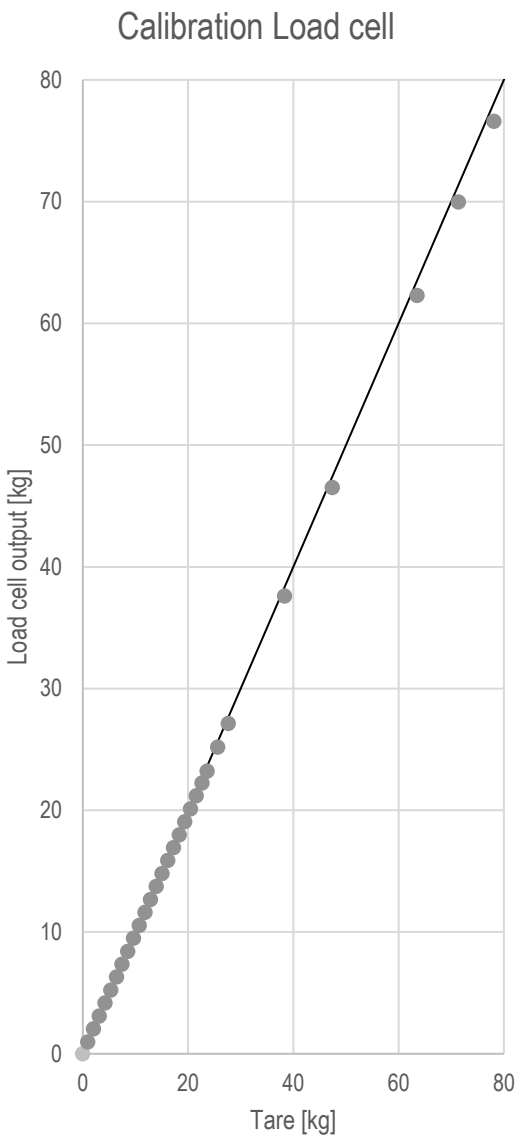

E – Air velocity measurements

	Open Loop				Closed Loop			
20%	H	sampling 1	sampling 2	sampling 3	H	sampling 1	sampling 2	sampling 3
	1	0.06	0.07	0.06	1	0.01	0	0.01
	2	0.27	0.3	0.29	2	0.28	0.29	0.26
	3	0.33	0.34	0.34	3	0.31	0.32	0.32
	5	0.31	0.32	0.34	5	0.3	0.27	0.29
	7	0.31	0.33	0.3	7	0.29	0.24	0.25
	9	0.28	0.29	0.28	9	0.27	0.25	0.26
	11	0.29	0.28	0.27	11	0.23	0.28	0.26
40%	H	sampling 1	sampling 2	sampling 3	H	sampling 1	sampling 2	sampling 3
	1	0.26	0.23	0.25	1	0	0.02	0.06
	2	0.76	0.81	0.79	2	0.63	0.67	0.93
	3	0.82	0.86	0.83	3	0.74	0.76	1.14
	5	0.86	0.85	0.86	5	0.75	0.74	1.17
	7	0.74	0.79	0.76	7	0.66	0.65	1.07
	9	0.69	0.71	0.67	9	0.57	0.6	0.94
	11	0.66	0.65	0.65	11	0.58	0.57	0.9
60%	H	sampling 1	sampling 2	sampling 3	H	sampling 1	sampling 2	sampling 3
	1	0.56	0.19	0.21	1	0.04	0.03	0.06
	2	1.21	0.18	1.22	2	0.74	0.84	0.93
	3	1.3	1.27	1.28	3	1.11	1.13	1.14
	5	1.18	1.17	1.21	5	1.15	1.18	1.17
	7	1.12	1.13	1.15	7	1.02	1.04	1.07
	9	1.07	1.08	1.09	9	0.93	0.89	0.94
	11	0.93	1.02	0.94	11	0.88	0.87	0.9
80%	H	sampling 1	sampling 2	sampling 3	H	sampling 1	sampling 2	sampling 3
	1	0.48	0.28	0.38	1	0.01	0.05	0.03
	2	1.45	1.48	1.44	2	1.1	1.08	1.07
	3	1.52	1.49	1.48	3	1.21	1.24	1.23
	5	1.44	1.45	1.46	5	1.25	1.28	1.25
	7	1.27	1.29	1.3	7	1.2	1.15	1.16
	9	1.19	1.21	1.23	9	1.12	1.06	1.13
	11	1.12	1.15	1.16	11	1.03	1.04	1.04
100%	H	sampling 1	sampling 2	sampling 3	H	sampling 1	sampling 2	sampling 3
	1	0.43	0.36	0.44	1	0.08	0.09	0.06
	2	1.76	1.74	1.76	2	1.25	1.4	1.37
	3	1.8	1.75	1.83	3	1.32	1.44	1.48
	5	1.73	1.65	1.84	5	1.42	1.46	1.49
	7	1.66	1.61	1.64	7	1.35	1.38	1.41
	9	1.52	1.57	1.54	9	1.24	1.26	1.27
	11	1.38	1.36	1.44	11	1.16	1.2	1.15

F – Estimation of measurement uncertainties

The experimental activity carried out within this research involved the use of multiple sensors for the evaluation of variables and macroscopic indicators resulting from the combination of different physical quantities. In this attachment is reported the procedure and the quantitative estimation of the errors on variables and indicators elaborated on the acquired data.

The experimental activity grounds mainly on the measurements of three parameters: the air and water temperature, the relative humidity, and the weight of the sorbent. The standard deviation for each sensor typology is recalled in the table below:

Physical variable	Symbol	Sensor type	Sensor model	Producer	Standard deviation σ[-]
Air temperature	T	IC temperature sensor	LM35CAZ	Texas Instruments	±0.5 °C
Relative humidity	RH	capacitive polymer	HIH4000	Honeywell	±3.5 %
Sorbent weight	W	load cell	AL6N-C3-100kg-3B6	Variohm	±0.002 mV/V

Table F.1: Standard deviation of the three main sensors used to measure the air temperature, the relative humidity and the weight of the sorbent material.

In the following part will be assessed the error estimation for: Pressure of vapor saturation; moisture content; vapor pressure; water uptake; equilibrium water uptake; charge level.

1) Vapor saturation pressure

P_{sat} is a non-linear function of measured air temperature T, evaluated as:

$$P_{sat} = h(T) = a \cdot \exp\left(\frac{b \cdot T}{c + T}\right) [Pa] \quad (F.1)$$

This function can be approximated with the Taylor expansion truncated at the first term:

$$P_{sat} \cong h(\bar{T}) + \left.\frac{\partial h}{\partial T}\right|_{\bar{T}} (T - \bar{T}) \quad (F.2)$$

Where $\bar{T}$ is the mean value (where x is the generic variable and $E[x]$ its average value) over n samplings of the temperature. The mathematical definition of the variance is $\sigma^2[x] = E[x^2] - (E[x])^2$, that once applied to the function h(T), becomes:

$$\sigma^2[P_{sat}] = \sigma^2[h(T)] = E[(h(T) - E[h(T)])^2] \quad (F.3)$$

Where $E[h(T)] = h(\bar{T})$. The final formula to estimate the variance is obtained substituting the approximated solution of $h(T)$ to the equation F.3:

$$\sigma^2[P_{sat}] \cong E\left[\left(h(\bar{T}) + \left.\frac{\partial h}{\partial T}\right|_{\bar{T}} (T - \bar{T}) - h(\bar{T})\right)^2\right] = E\left[\left(\left.\frac{\partial h}{\partial T}\right|_{\bar{T}} (T - \bar{T})\right)^2\right] = \left(\left.\frac{\partial h}{\partial T}\right|_{\bar{T}}\right)^2 \cdot E[(T - \bar{T})^2] = \left(\left.\frac{\partial h}{\partial T}\right|_{\bar{T}}\right)^2 \cdot \sigma^2[T] \quad (F.4)$$

$$\sigma[p_{sat}] = \sqrt{\sigma^2[p_{sat}]} \cong \left.\frac{\partial h}{\partial T}\right|_{\bar{T}} \cdot \sqrt{\sigma^2[T]} = \left.\frac{\partial h}{\partial T}\right|_{\bar{T}} \cdot \sigma[T] \quad (F.5)$$

Equation F.5 requires the mathematical development of the h(T) derivative, and the numerical evaluation at the average temperature $\bar{T}$, as in the equation F.6

$$\left.\frac{\partial h}{\partial T}\right|_{\bar{T}} = \frac{b \cdot (c + \bar{T}) - b \cdot \bar{T}}{(c + \bar{T})^2} \cdot \exp\left(\frac{b \cdot \bar{T}}{c + \bar{T}}\right) \cdot a = \frac{b \cdot c \cdot a}{(c + \bar{T})^2} \cdot \exp\left(\frac{b \cdot \bar{T}}{c + \bar{T}}\right) \quad (F.6)$$

In the table and figure below is reported the uncertainty on the saturation pressure at the different temperature value.

T °C	P_{sat} Pa	dh/dT Pa/°C	$\sigma[P_{sat}]$ Pa
10	1229	82	41
20	2341	145	72
30	4250	244	122
40	7396	395	198
50	12391	617	309
60	20059	934	467
70	31480	1373	687

Table F.2: Values of the saturation pressure, and related uncertainties, at different temperature values.

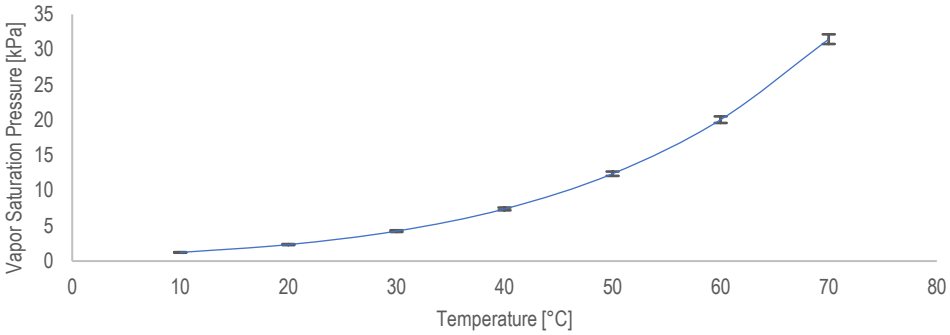

Figure F.1: Pressure of saturated water vapor and related uncertainty within the range of 10-70°C.

2) Moisture content

Moisture content (x) is a non-linear function dependent by both temperature and relative humidity measurements.

$$x = 0.622 \cdot \frac{P_{sat} \cdot \frac{RH}{100}}{101325 - \left(P_{sat} \cdot \frac{RH}{100}\right)} \cdot 1000 \left[\frac{g}{kg}\right] \quad (F.7)$$

The variance of moisture content $\sigma[x]$ will be a combined function of the single variances on temperature and relative humidity. As before, is applied the same method with the Taylor approximation, and the subsequent development of variance definition.

$$x = y(RH, P_{sat}) \cong y(\overline{RH}, \overline{P_{sat}}) + \frac{\partial y}{\partial RH}\Big|_{\overline{RH}} (RH - \overline{RH}) + \frac{\partial y}{\partial P_{sat}}\Big|_{\overline{P_{sat}}} (P_{sat} - \overline{P_{sat}}) \quad (F.8)$$

$$\sigma^2[x] = \sigma^2[y(RH, P_{sat})] = E[(y(RH, P_{sat}) - E[y(RH, P_{sat})])^2] \quad (F.9)$$

$$\sigma^2[x] \cong E\left[\left(y(\overline{RH}, \overline{P_{sat}}) + \frac{\partial y}{\partial RH}\Big|_{\overline{RH},\overline{P_{sat}}} \cdot (RH - \overline{RH}) + \frac{\partial y}{\partial P_{sat}}\Big|_{\overline{RH},\overline{P_{sat}}} \cdot (P_{sat} - \overline{P_{sat}}) - y(\overline{RH}, \overline{P_{sat}})\right)^2\right] \quad (F.10)$$

$$\sigma^2[x] \cong E\left[\left(\frac{\partial y}{\partial RH}\Big|_{\overline{RH},\overline{P_{sat}}} \cdot (RH - \overline{RH}) + \frac{\partial y}{\partial P_{sat}}\Big|_{\overline{RH},\overline{P_{sat}}} \cdot (P_{sat} - \overline{P_{sat}})\right)^2\right] \quad (F.11)$$

$$\sigma^2[x] \cong E\left[\left(\frac{\partial y}{\partial RH}\Big|_{\overline{RH},\overline{P_{sat}}}\right)^2 \cdot (RH - \overline{RH})^2 + \left(\frac{\partial y}{\partial p_{sat}}\Big|_{\overline{RH},\overline{P_{sat}}}\right)^2 \cdot (P_{sat} - \overline{P_{sat}})^2 + 2 \cdot \frac{\partial y}{\partial RH}\Big|_{\overline{RH},\overline{P_{sat}}} \cdot \frac{\partial y}{\partial p_{sat}}\Big|_{\overline{RH},\overline{P_{sat}}} \cdot (RH - \overline{RH}) \cdot (P_{sat} - \overline{P_{sat}})\right] \quad (F.12)$$

Where $\sigma_{RH,P_{sat}}[x] = 2 \cdot \frac{\partial y}{\partial RH}\Big|_{\overline{RH},\overline{P_{sat}}} \cdot \frac{\partial y}{\partial p_{sat}}\Big|_{\overline{RH},\overline{P_{sat}}} (RH - \overline{RH}) \cdot (P_{sat} - \overline{P_{sat}})$ is the covariance of x from the two variable RH and P_{sat}. These two variables can be reasonably considered as uncorrelated, then the covariance of moisture content is negligible.

$$\sigma^2[x] \cong \left(\frac{\partial y}{\partial RH}\Big|_{\overline{RH},\overline{P_{sat}}}\right)^2 \cdot \sigma^2[RH] + \left(\frac{\partial y}{\partial p_{sat}}\Big|_{\overline{RH},\overline{P_{sat}}}\right)^2 \cdot \sigma^2[P_{sat}] \quad (F.13)$$

$$\sigma[x] = \sqrt{\left(\frac{\partial y}{\partial RH}\Big|_{\overline{RH},\overline{P_{sat}}}\right)^2 \cdot \sigma^2[RH] + \left(\frac{\partial y}{\partial p_{sat}}\Big|_{\overline{RH},\overline{P_{sat}}}\right)^2 \cdot \sigma^2[P_{sat}]} \quad (F.14)$$

The derivatives of the function y(RH,P_{sat}) are:

$$\frac{\partial y}{\partial p_{sat}}\Big|_{\overline{RH},\overline{p_{sat}}} = \frac{0.622 \cdot \frac{\overline{RH}}{100} \cdot \left(101325 - \overline{p_{sat}} \cdot \frac{\overline{RH}}{100}\right) + 0.622 \cdot \overline{p_{sat}} \cdot \frac{\overline{RH}}{100} \cdot \frac{\overline{RH}}{100}}{(101325 - \overline{p_{sat}} \cdot \frac{\overline{RH}}{100})^2} = \frac{0.622 \cdot \frac{\overline{RH}}{100} \cdot 101325}{(101325 - \overline{p_{sat}} \cdot \frac{\overline{RH}}{100})^2} \quad (F.15)$$

$$\frac{\partial y}{\partial RH}\Big|_{\overline{RH},\overline{p_{sat}}} = \frac{0.622 \cdot \frac{\overline{p_{sat}}}{100} \cdot \left(101325 - \overline{p_{sat}} \cdot \frac{\overline{RH}}{100}\right) + 0.622 \cdot \overline{p_{sat}} \cdot \frac{\overline{RH}}{100} \cdot \frac{\overline{p_{sat}}}{100}}{(101325 - \overline{p_{sat}} \cdot \frac{\overline{RH}}{100})^2} = \frac{0.622 \cdot \frac{\overline{p_{sat}}}{100} \cdot 101325}{(101325 - \overline{p_{sat}} \cdot \frac{\overline{RH}}{100})^2} \quad (F.16)$$

Whit this equation is realized the table below, where $\sigma[x]$ is assessed.

T	Psat	dP/dT	$\sigma^2[P_{sat}]$	RH	x	dy/dRH	dy/dP_{sat}	σ[x]
°C	Pa	Pa/°C	Pa	%	g/kg	g/(kg*RH)	g/(kg*Pa)	g/kg
10	1229	82	1694	10	0,76	7,6E-05	6,2E-07	0,27
				20	1,51	7,6E-05	1,2E-06	0,27
				30	2,27	7,6E-05	1,9E-06	0,28
				40	3,03	7,6E-05	2,5E-06	0,29
				50	3,8	7,6E-05	3,1E-06	0,30
				60	4,56	7,7E-05	3,7E-06	0,31
				70	5,33	7,7E-05	4,4E-06	0,32
				80	6,1	7,7E-05	5,0E-06	0,34
				90	6,87	7,7E-05	5,6E-06	0,36
20	2341	145	5255	10	1,44	1,4E-04	6,2E-07	0,51
				20	2,89	1,5E-04	1,2E-06	0,52
				30	4,34	1,5E-04	1,9E-06	0,53
				40	5,8	1,5E-04	2,5E-06	0,54
				50	7,27	1,5E-04	3,1E-06	0,56
				60	8,74	1,5E-04	3,8E-06	0,59
				70	10,2	1,5E-04	4,4E-06	0,61
				80	11,7	1,5E-04	5,1E-06	0,64
				90	13,2	1,5E-04	5,8E-06	0,67
30	4250	244	14906	10	2,62	2,6E-04	6,2E-07	0,92
				20	5,26	2,7E-04	1,2E-06	0,94
				30	7,93	2,7E-04	1,9E-06	0,96
				40	10,6	2,7E-04	2,5E-06	0,99
				50	13,3	2,7E-04	3,2E-06	1,03
				60	16,1	2,7E-04	3,9E-06	1,07
				70	18,8	2,8E-04	4,6E-06	1,12
				80	21,6	2,8E-04	5,3E-06	1,17
				90	24,4	2,8E-04	6,0E-06	1,23
40	7396	395	39051	10	4,57	4,6E-04	6,2E-07	1,62
				20	9,22	4,7E-04	1,3E-06	1,66
				30	13,9	4,7E-04	1,9E-06	1,70
				40	18,7	4,8E-04	2,6E-06	1,76
				50	23,6	4,9E-04	3,3E-06	1,83
				60	28,5	5,0E-04	4,0E-06	1,91
				70	33,5	5,0E-04	4,8E-06	2,00
				80	38,6	5,1E-04	5,5E-06	2,10
				90	43,7	5,2E-04	6,3E-06	2,21
50	12391	617	95288	10	7,7	7,8E-04	6,3E-07	2,74
				20	15,6	8,0E-04	1,3E-06	2,83
				30	23,7	8,2E-04	2,0E-06	2,93
				40	32	8,4E-04	2,7E-06	3,06
				50	40,5	8,6E-04	3,5E-06	3,21
				60	49,3	8,9E-04	4,3E-06	3,37
				70	58,2	9,1E-04	5,1E-06	3,56
				80	67,5	9,3E-04	6,0E-06	3,76
				90	76,9	9,6E-04	7,0E-06	3,99

Table F.3. Evaluation of the uncertainty on the air moisture content, at different values of relative humidity, and saturation pressure of the water vapor (then different temperature)

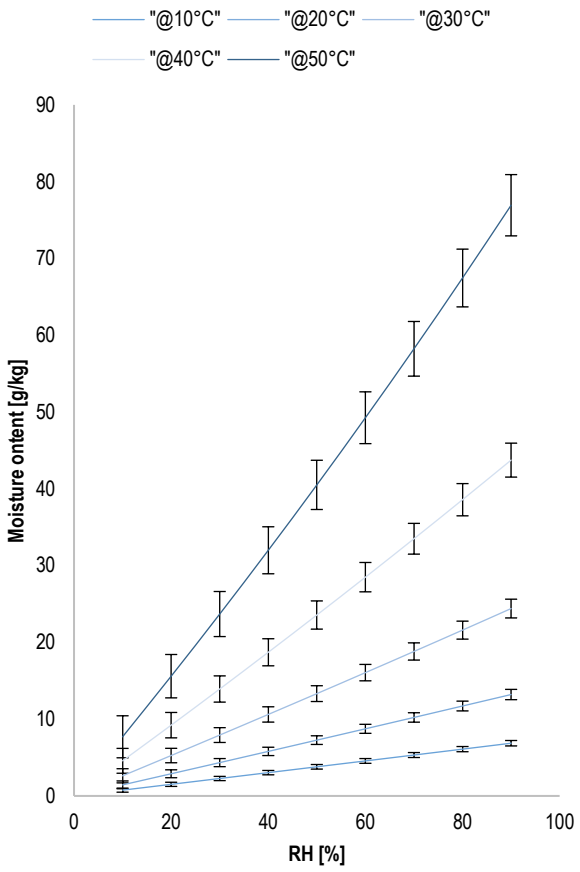

Figure F.2. The graph depicts the different moisture content, varying temperature of the humid air and relative humidity. Per each couple of (T,RH) is estimated the uncertainty on moisture content.

3) Vapor Pressure

$$P_v = RH * P_{sat} = RH * a * exp\left(\frac{b \cdot T}{c + T}\right) = f(RH) * h(T) \quad (F.17)$$

$$\sigma[P_v] = \sqrt{\left(\frac{\partial P_v}{\partial RH}_{\overline{RH},\overline{T}}\right)^2 \sigma[RH]^2 + \left(\frac{\partial P_v}{\partial T}_{\overline{RH},\overline{T}}\right)^2 \sigma[T]^2} = \sqrt{\left(P_{sat_{\overline{T}}}\right)^2 * \sigma[RH]^2 + \left(RH * \frac{b \cdot c \cdot a}{(c + \overline{T})^2} \cdot e^{\left(\frac{b \cdot \overline{T}}{c + \overline{T}}\right)}\right)^2 \sigma[T]^2} \quad (F.18)$$

T	P_{sat}	RH	Pv	dPv/dRH	dPv/dT	$\sigma[P_v]$
		0,1	0,43	4,27	0,02	0,1
		0,3	1,28	4,27	0,07	0,2
		0,6	2,56	4,27	0,15	0,2
30	4,27	0,9	3,84	4,27	0,22	0,2
		0,1	0,75	7,46	0,04	0,3
		0,3	2,24	7,46	0,12	0,3
		0,6	4,48	7,46	0,24	0,3
40	7,46	0,9	6,72	7,46	0,36	0,3
		0,1	1,25	12,54	0,06	0,4
		0,3	3,76	12,54	0,19	0,4
		0,6	7,52	12,54	0,38	0,5
50	12,54	0,9	11,28	12,54	0,56	0,5

Table F.4: Evaluation of the uncertainty on the partial vapor pressure, at different values of relative humidity, and saturation pressure of the water vapor (then different temperature)

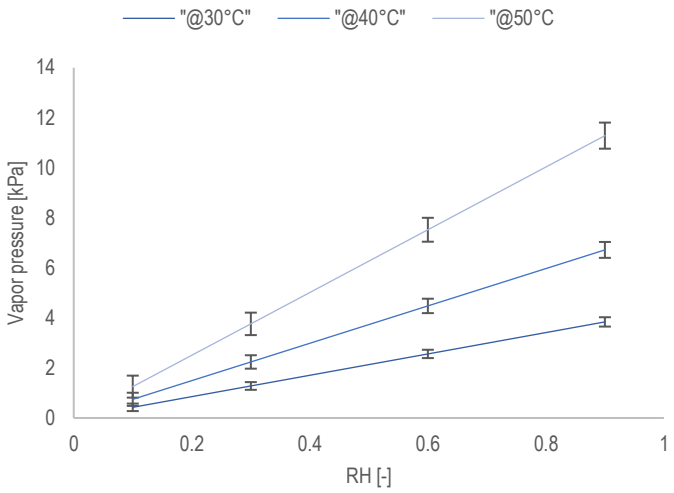

Figure F.3. The graph depicts the different partial vapor pressure, varying temperature of the humid air and relative humidity. Per each couple of (T,RH) is estimated the uncertainty on vapor pressure.

4) Water uptake and Charge Level indicator

Load cell output is P=2 ± 0.002 mV/V @ F.S. (100kg for the used model Variohm AL6N-C3-100kg-3B6). The wheatstone bridge was excited @24V DC, then the output of the load cell (P) is a linear function with slop 0.48 mV in the range of 0-100 kg, with a variance $\sigma[P]$ equal to ±0.048mV. The final value of the weight (W) will result then as:

$$W = P * \frac{100}{48} [kg] \quad (F.19)$$

The variance $\sigma[W]$ can be evaluated as done for saturation pressure, using the Taylor expansion of a generic function h(P):

$$W = h(P) \cong h(\bar{P}) + \frac{\partial h}{\partial P}\Big|_{\bar{P}} (P - \bar{P}) \quad (F.20)$$

$$\sigma[W] = \frac{\partial h}{\partial P}\Big|_{\bar{P}} \cdot \sigma[P] = \frac{100\ [kg]}{48\ [mV]} * 0.048\ [mV] = 0.1\ kg$$

The instantaneous water uptake W_i has been estimated with the equation 4.5, function of the variable W:

$$W_i = \frac{W - M_{dry\ silica} - M_{metallic\ frame}}{M_{dry\ silica}} \quad \left[\frac{kg_{H2O}}{kg_{SiO}}\right] \quad (F.21)$$

Then the Taylor expansion is:

$$W_i = h(W) \cong h(\bar{W}) + \frac{\partial h}{\partial W}\Big|_{\bar{W}} (W - \bar{W}) \quad (F.22)$$

$$\sigma[W_i] = \frac{\partial h}{\partial P}\Big|_{\bar{P}} \cdot \sigma[P] = \frac{1}{M_{dry\ silica}} \sigma[P] = \frac{1}{27} \frac{\left[\frac{kg_{H2O}}{kg_{SiO}}\right]}{[kg]} 0.1[kg] = 0.0037 \left[\frac{kg_{H2O}}{kg_{SiO}}\right] \quad (F.23)$$

The Charge Level (C.L.), is a macro-indicator evaluated starting from the instantaneous water uptake, the potential value achievable at the equilibrium:

$$C.L. = \frac{W_i}{W_{eq}}\ [-] \quad (F.24)$$

Where the equilibrium water uptake is evaluated as inverted function of equation 2.5, dependent by air thermodynamic variables, inlet air temperature and relative humidity:

$$W_{eq}(RH_{in}, T_{in}) = A_1\,T + A_2\,T^2 + A_3\,\mathrm{RH} + A_4\,\mathrm{RH}\,T + A_5\,RH\,T^2 + A_6\,\mathrm{RH}^2 + A_7\,T\,\mathrm{RH}^2 + A_8\,\mathrm{RH}^3 + A_9\,T^3 + A_{10} \quad (F.25)$$

Where the polynomial coefficients are A_1=-0.0017958; A_2=+2.8085e-05; A_3=-0.040625, A_4=+0.0015898; A_5=-1.7748e-06; A_6=+0.7411; A_7=-0.0013052; A_8=-0.37765; A_{10}=+0.044373, A_9=-1.6617e-07;

As done for the moisture content, being the C.L. a bidimensional function of W_i and W_{eq}, with the hypothesis that the two independent variables have no cross correlation (the covariance is the neglected), the uncertainty connected to the evaluation of C.L. can be calculated as:

$$CL = y(W_i, W_{eq}) \cong y(\overline{W_i}, \overline{W_{eq}}) + \frac{\partial y}{\partial W_i}\Big|_{\overline{W_i}} (W_i - \overline{W_i}) + \frac{\partial y}{\partial W_{eq}}\Big|_{\overline{W_{eq}}} (W_{eq} - \overline{W_{eq}}) \quad (F.26)$$

$$\sigma[CL] = \sqrt{\left(\frac{\partial y}{\partial W_i}\Big|_{\overline{W_i},\overline{W_{eq}}}\right)^2 \cdot \sigma^2[W_i] + \left(\frac{\partial y}{\partial W_{eq}}\Big|_{\overline{RH},\overline{P_{sat}}}\right)^2 \cdot \sigma^2[W_{eq}]} \quad (F.27)$$

However, equilibrium water uptake is still a bidimensional function of T and RH, requiring itself a specific evaluation of the variance, with a similar method. Following equation reports mathematical passages for its evaluation. Final values are reported in Table F.5 and Figure F.4

$$W_{eq} = y(RH_{in}, T_{in}) \cong y(\overline{RH_{in}}, \overline{T_{in}}) + \frac{\partial y}{\partial RH_{in}}\Big|_{\overline{RH_{in}}} (RH_{in} - \overline{RH_{in}}) + \frac{\partial y}{\partial T_{in}}\Big|_{\overline{T_{in}}} (T_{in} - \overline{T_{in}}) \quad (F.28)$$

$$\sigma\left[W_{eq}(T_{in}, RH_{in})\right] = \sqrt{\left(\frac{\partial y}{\partial T_{in}}\Big|_{\overline{T_{in}},\overline{RH_{in}}}\right)^2 \cdot \sigma^2[T_{in}] + \left(\frac{\partial y}{\partial RH_{in}}\Big|_{\overline{T_{in}},\overline{RH_{in}}}\right)^2 \cdot \sigma^2[RH_{in}]} \quad (F.29)$$

$$\frac{\partial y}{\partial T_{in}}\Big|_{\overline{T_{in}},\overline{RH_{in}}} = A_1 + 2A_2\overline{T_{in}} + A_4\overline{RH_{in}} + 2A_5\overline{RH_{in}}\,\overline{T_{in}} + 3A_8\overline{T_{in}}^2 \quad (F.30)$$

$$\frac{\partial y}{\partial RH_{in}}\Big|_{\overline{T_{in}},\overline{RH_{in}}} = A_3 + A_4\overline{T_{in}} + A_5\overline{T_{in}}^2 + 2A_6\overline{RH_{in}} + 2A_6\overline{RH_{in}} + 3A_8\,\overline{RH_{in}}^2 \quad (F.31)$$

T		RH	dy/dT	dy/dRH	σ[W_{eq}]
°C		%	[kg_{H2O}/kg_{SiO}]/[°C]	[kg_{H2O}/kg_{SiO}]/[-]	[kgH2O/kgSiO]
	0,04	0,17	-0,001308	0,189388579	0,006660762
	0,06	0,25	-0,001174	0,276428892	0,009692787
	0,10	0,39	-0,000962	0,379588388	0,013294295
10	0,15	0,51	-0,000770	0,436855393	0,01529478
	0,20	0,61	-0,000611	0,458031223	0,016034001
	0,25	0,73	-0,000435	0,453853969	0,015886376
	0,30	0,88	-0,000191	0,400166393	0,01400615
	0,04	0,17	-0,001170	0,213380846	0,007491213
	0,06	0,26	-0,001040	0,29850095	0,010460463
	0,10	0,39	-0,000835	0,398680621	0,013960063
20	0,15	0,52	-0,000650	0,453559008	0,015877893
	0,20	0,62	-0,000499	0,473532347	0,01657551
	0,25	0,73	-0,000332	0,469517512	0,016433952
	0,30	0,88	-0,000100	0,418517055	0,014648183
	0,04	0,18	-0,001129	0,239789901	0,008411611
	0,06	0,27	-0,001002	0,3225734	0,011301185
	0,1	0,40	-0,000803	0,419074651	0,014673113
30	0,15	0,52	-0,000626	0,47086681	0,016483307
	0,2	0,62	-0,000482	0,488963197	0,017115406
	0,25	0,73	-0,000323	0,484193058	0,016947527
	0,3	0,88	-0,000102	0,434365883	0,015202892
	0,04	0,20	-0,001187	0,266716746	0,009353927
	0,06	0,28	-0,001063	0,347062778	0,012158827
	0,1	0,41	-0,000870	0,439687575	0,015395216
40	0,15	0,53	-0,000699	0,488158988	0,017089139
	0,2	0,63	-0,000561	0,504102464	0,01764582
	0,25	0,73	-0,000411	0,498117593	0,017435326
	0,3	0,88	-0,000200	0,448592324	0,01570105
	0,04	0,21	-0,001346	0,292413824	0,010256583
	0,06	0,29	-0,001226	0,370531399	0,012983069
	0,1	0,42	-0,001038	0,459565837	0,016093176
50	0,15	0,54	-0,000873	0,504914959	0,017677409
	0,2	0,63	-0,000741	0,518787309	0,018161337
	0,25	0,74	-0,000598	0,51153517	0,017906226
	0,3	0,88	-0,000397	0,462020853	0,016171946

Table F.5. Evaluation of the uncertainty on the potential equilibrium water uptake, at different values of relative humidity and temperature of the air.

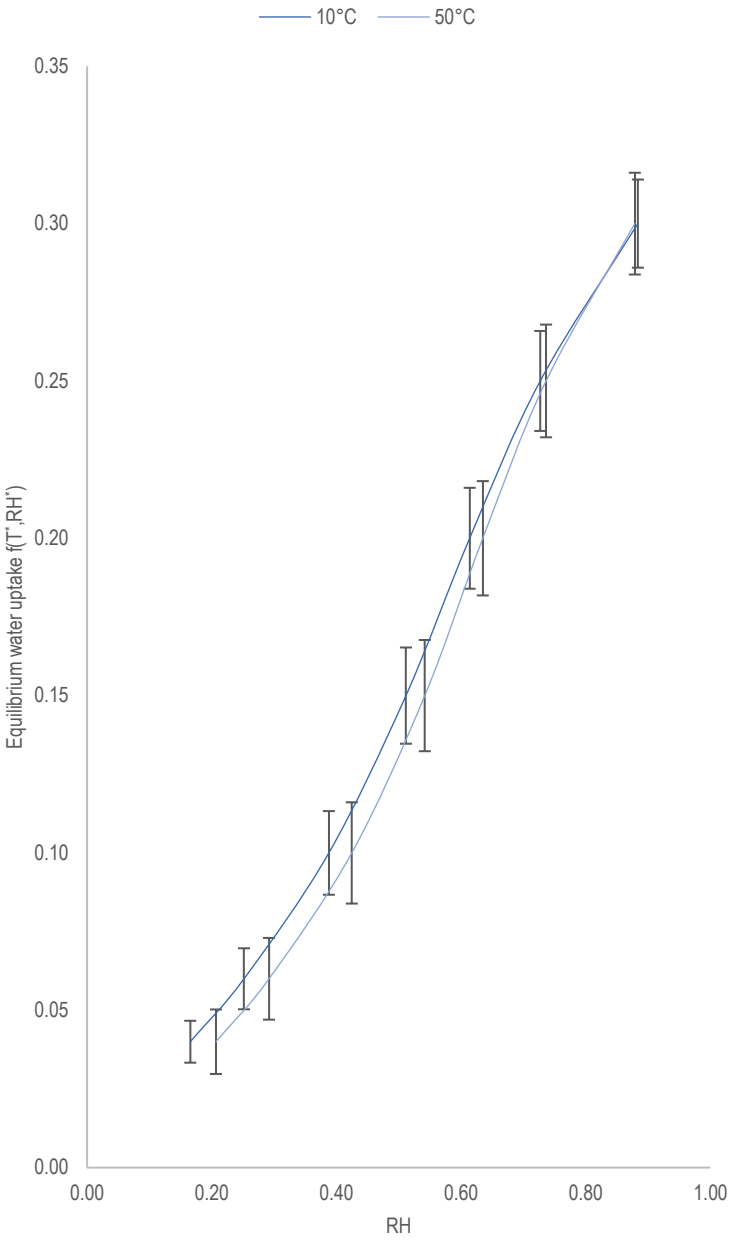

Figure F.4. The graph depicts the different water uptake values trough the equilibrium equation, varying temperature of the humid air and relative humidity. Per each couple of (T,RH) is estimated the uncertainty on the equilibrium water uptake.

Finally, the uncertainty related to the evaluation of the macro indicator C.L. can be calculated with the following equation.

$$\sigma[CL] = \sigma[y(W_i, W_{eq})] \cong \sqrt{\left(\frac{1}{\overline{W_{eq}}_{\overline{RH},\overline{T}}}\right)^2 \sigma^2[W_i] + W_i^2\,\sigma^2\left[\overline{W_{eq}}_{\overline{RH},\overline{T}}\right]} \quad (F.32)$$

Final values, at different measurements of air temperature and relative humidity, and different measurements of water uptake (starting from the load cell measurements) are reported in the table and graph below.

	Weq	RH	σ[Weq]		Weq	RH	σ[Weq]
30°C; 4%	0,04	0,18	0,008411611	50°C; 4%	0,04	0,20672	0,010257
	CL	Wi	σ[CL]		CL	Wi	σ[CL]
	0,1	0,004	0,09250000		0,1	0,004	0,0925
	0,3	0,012	0,09250005		0,3	0,012	0,0925
	0,5	0,02	0,09250015		0,5	0,02	0,0925
	0,7	0,028	0,0925003		0,7	0,028	0,0925
	0,9	0,036	0,09250049		0,9	0,036	0,09250
	Weq	RH	σ[Weq]		Weq	RH	σ[Weq]
30°C; 15%	0,15	0,51	0,01529478	50°C; 15%	0,15	0,54	0,02
	CL	Wi	σ[CL]		CL	Wi	σ[CL]
	0,1	0,015	0,02466773		0,1	0,015	0,02466
	0,3	0,045	0,02467626		0,3	0,045	0,02467
	0,5	0,075	0,02469332		0,5	0,075	0,02470
	0,7	0,105	0,02471889		0,7	0,105	0,02473
	0,9	0,135	0,02475293		0,9	0,135	0,02478
	Weq	RH	σ[Weq]		Weq	RH	σ[Weq]
30°C; 30%	0,30	0,88	0,02	50°C; 30%	0,30	0,88	0,02
	CL	Wi	σ[CL]		CL	Wi	σ[CL]
	0,1	0,03	0,01234176		0,1	0,03	0,01234
	0,3	0,09	0,01240899		0,3	0,09	0,01241
	0,5	0,15	0,01254238		0,5	0,15	0,01257
	0,7	0,21	0,01273985		0,7	0,21	0,01279
	0,9	0,27	0,01299847		0,9	0,27	0,01308

Table F.6. Evaluation of the uncertainty on the potential equilibrium water uptake, defined with the different triples of (RH*, T*, w_i)

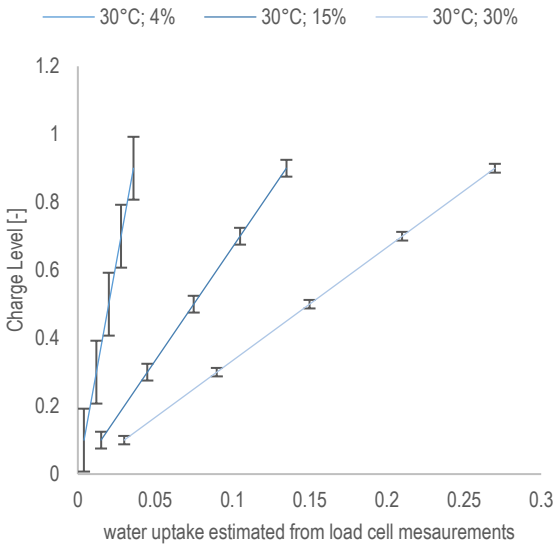

Figure F.5. The graph depicts the different Charge Level values estimated trough the equilibrium equation (@ 30°C and increasing RH corresponding to an equilibrium water uptake w_{eq} respectively of 0.04, 0.15 and 0.3) and the different instantaneous water uptakes estimated from the load cell measurements

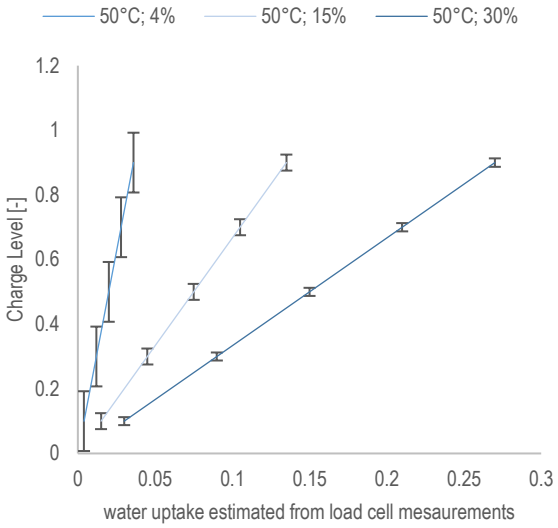

Figure F.6. The graph depicts the different Charge Level values estimated trough the equilibrium equation (@ 50°C and increasing RH corresponding to an equilibrium water uptake w_{eq} respectively of 0.04, 0.15 and 0.3) and the different instantaneous water uptakes estimated from the load cell measurements

3250